Universidad
Carlos III de Madrid
www.uc3m.es

TESIS DOCTORAL

Studies on electromagnetic turbulence and edge phenomena in fusion plasmas

Autora:
Adriana Martín de Aguilera

Directores:
Dr. Carlos Hidalgo
Dr. Francisco Castejón
Dr. Eduardo de la Cal
Dr. Boudewijn van Milligen

Tutor:
José Ramón Martín Solís

Departamento de Física, Universidad Carlos III de Madrid

Leganés, Febrero de 2017

Universidad
Carlos III de Madrid
www.uc3m.es

TESIS DOCTORAL

Studies on electromagnetic turbulence and edge phenomena in fusion plasmas

Autora:

Directores:

Firma del Tribunal Calificador:

	Nombre y apellidos	Firma
Presidente		
Vocal		
Secretatio		

Calificación:

En Leganés, de de

UNIVERSIDAD CARLOS III DE MADRID

Abstract

Doctorado en Plasmas y Fusión Nuclear
Departamento de Física

Studies on electromagnetic turbulence and edge phenomena in fusion plasmas

by Adriana Martín de Aguilera

The magnetic well depth if one of the principal actors when the stability of a confined plasma is analysed. It is the main stabilising mechanism in the TJ-II stellarator, as this is an almost shearless device. This and TJ-II's ability for changing the currents of its coils make the Spanish stellarator a perfect candidate for magnetic well studies. This thesis presents an exhaustive study on plasma performance and stability under theoretically unstable magnetic well conditions. NBI-heated reproducible plasmas were successfully produced even for the most stability adverse conditions and a link between the Alfén Eigenmodes and magnetic well depth was found.

Visible light emission at the plasma edge of the JET tokamak has been studied with an intensified fast visible camera since the installation of its ITER-Like Wall. A method to characterize the evolution of ELMs in the divertor and relate the recorded signal with other diagnostics at JET has been developed. A large Matlab library orientated to treat and share the data produced by the intensified fast visible camera has been made available to the users of this diagnostic.

To the women of my life:
my mother, my aunt and my grandmother.

A las mujeres de mi vida:
mi madre, mi tía y mi abuela.

"Non bisognava fermarsi a metà, questo era chiaro. Doveva essere una cosa che cominciava e poi finiva, senza perdersi per strada. Come un ritornello di una canzone, pensò. I bambini, di là dalla rete, continuavano a strillare. Canta, Gould. Comunque vada a finire, è il momento di cantare."

City, Alessandro Baricco

Acknowledgements

When one spends some years of her life developing a scientific work there are, at the end of the path, two kinds of acknowledgements to recall. The first one is scientific: to my supervisors, Carlos Hidalgo, who believed in me and offered me a place to work; and Francisco Castejón, for his joyful optimism, his compromise and for helping me to find a project to explore and develop. Eduardo de la Cal has taught me most of what I know about intensified fast visible cameras. I have always felt supported and respected by him and that's something I will never thank him enough. Boudewijn van Milligen, for his imaginative help with coding and data analysis; Antonio López Fraguas, who made up few new configurations for our crazy experiments, and for his contagious good mood and Marian Ochando, to whose knowledge this thesis owes a few sections. M^a Ángeles Pedrosa, Enrique Ascasíbar, Francisco Medina, Teresa Estrada, Ignacio Pastor and José María Fontdecaba have also contributed to this work.

Also, this thesis has involved more trips to the JET tokamak that I can count. I will always be thankful to CIEMAT and Carlos Hidalgo for trusting me with the manning of the intensified fast visible camera installed there: my times in England are the dearest memories I take from these years. From the people I met there, special and huge thanks to Emilia Solano, for her tireless love to Science and all of her help scientific and personal help at JET. Itziar Balboa, who also was a friend and a teacher there; Gabor Cseh, Gabor Kocsis and Ulises Losada, the fearless KL8A team and; Adrian Capel, without whom most of my analysis from KL8A would have not been possible.

The second kind of thanks one needs to give at this point is emotional: because I have not only met colleagues at CIEMAT and JET, but I have also made some wonderful friends, whose support and complicity have also been key to my job. Ulises, Fran, Álvaro, Nerea and Jose, with whom I have shared space, lunch, laughs and worries in Madrid; Raul, Giuseppe, Daniel (thanks for the open-mic nights and the ale!) and Gabor, in Oxford.

Finally, to those friends and family who don't understand a word of my work, but have been there, no matter what, in every step of the way. Facun, Alejandro and Rocío, for all the movie nights, board games and beers at La Chilostra; Jorge and Ana, for the never ending barbecues and concerts and, in spite of the distance, Fonso and Javi, for their infinite support, the 24-h availability and for their huge ability to listen. I could have never survived these years without any of you. And you know it.

One last word to thank some of the music bands that, without knowing it, walked beside me all these years: The Raveonettes, The National, Sigur Rós, Luna, The Beatles, The Jezabels, Pearl Jam and The Afghan Whigs, just to mention some. People that I will never meet, but who have helped me in an immense way.

The works here presented was partially funded by a FPU grant awarded by by the Spanish Ministry of Education (BOE resolution 245, 11/10/2010) and by CIEMAT through the contract 41EUROfusion15.

Contents

List of Figures

List of Tables

Abbreviations

ADAS	**A**tomic **D**ata and **A**nalysis **S**tructure
AE	**A**lfvén **E**igenmode
ALCATOR	**AL**to **CA**mpo **TOR**o
ASDEX	**A**xially **S**ymmetric **D**ivertor **E**xperiment
CCD	**C**harged **C**oupled **D**evice
CIEMAT	**C**entro de **I**nvestigaciones **E**nergéticas, **M**edio**A**mbientales y **T**ecnológicas
CMOS	**C**omplementary **M**etal **O**xide **S**emiconductor
DMV	**D**isruption **M**itigation **V**alve
DT	**D**euterium-**T**ritium
ECE	**E**lectron **C**yclotron **E**mission
ECRH	**E**lectron **C**yclotron **R**esonance **H**eating
ELM	**E**dge **L**ocalized **M**ode
FPS	**F**rames **P**er **S**econd
GAE	**G**lobal **A**lfvén **E**igenmode
GAM	**G**eodesic **A**coustic **M**ode
GHG	**G**reen**H**ouse **G**ases
HAE	**H**elical **A**lfvén **E**igenmode
HFS	**H**igh **F**ield **S**ide
HIBP	**H**eavy **I**on **B**eam **P**robe
ICRF	**I**on **C**yclotron **R**esonance **F**requency
II	**I**mage **I**ntensifier
ILW	**I**TER-**L**ike **W**all
ISP	**I**nner **S**trike **P**oint
ITER	**I**nternational **T**hermonuclear **E**xperimental **R**eactor
JET	**J**oint **E**uropean **T**orus

JPF	**J**ET **P**ulse **F**ile
JPN	**J**ET **P**ulse **N**umber
LCFS	**L**ast **C**losed **F**lux **S**urface
LFS	**L**ow **F**ield **S**ide
LHD	**L**arge **H**elical **D**evice
LNF	**L**aboratorio **N**acional de **F**usión
MGI	**M**assive **G**as **I**njection
MHD	**M**agneto**H**ydro**D**ynamics
NBI	**N**eutral **B**eam **I**njection
NPA	**N**eutral **P**article **A**nalyzer
NSTX	**N**ational **S**pherical **T**orus e**X**periment
OECD	**O**rganisation for **E**conomic **C**o-operation and **D**evelopment
OSP	**O**uter **S**trike **P**oint
PFC	**P**lasma **F**acing **C**omponent
PPF	**P**rocessed **P**ulse **F**ile
PSD	**P**ower **S**pectral **D**ensity
PWI	**P**lasma-**W**all **I**nteraction
RE	**R**unaway **E**lectrons
RMS	**R**oot **M**ean **S**quare
ROI	**R**egion **O**f **I**nterest
SOL	**S**crape-**O**ff **L**ayer
TF	**T**oroidal **F**ield
TFTR	**T**okamak **F**usion **T**est **R**eactor
TJ-II	**T**okamak de la **J**unta **II**
TS	**T**homson **S**cattering

Symbols

a	minor radius	m
B or $\vec{B}$	magnetic field	T
E or $\vec{E}$	electric field	V/m
I_p	plasma current	kA
I_{sat}	ion saturation current	A
n_e	electron density	m^{-3}
R	major radius	m
r_L	Larmor radius	m
T_e	electron temperature	keV
T_i	ion temperature	keV
T_{ped}	pedestal temperature	keV
V	volume	m^3
V_f	floating potential	V
W	magnetic well depth	%
W_{b4}	stored energy	kJ

ι	rotational transform	rad
ϕ	toroidal angle	$^\circ$ or rad
λ_D	Debye length	m
μ	magnetic moment	$A \cdot m^2$
ρ	normalized radious	-
σ	cross section	barns
τ_E	energy confinement time	s
θ	poloidal angle	$^\circ$ or rad

Part I

Introductory Material

Chapter 1

Introduction

> This Agreement [...] aims to strengthen the global response to the threat of climate change, in the context of sustainable development and efforts to eradicate poverty, including by:
>
> (a) Holding the increase in the global average temperature to well below 2°C above pre-industrial levels and to pursue efforts to limit the temperature increase to 1.5°C above pre-industrial levels, recognizing that this would significantly reduce the risks and impacts of climate change;
>
> (b) Increasing the ability to adapt to the adverse impacts of climate change and foster climate resilience and low greenhouse gas emissions development, in a manner that does not threaten food production;
>
> (c) Making finance flows consistent with a pathway towards low greenhouse gas emissions and climate-resilient development.
>
> *Paris Agreement, Article 2* Paris, 11 December 2015 [1]

Global warming is one of the most challenging threats humanity will face during the rest of the 21st century. Nowadays, skepticism regarding the rise of temperatures since the 19th century as a consequence of combined action of natural climate variability and pollution from human activities is small [2]. As it was stated in the United Nations Framework Convention on Climate Change that took place in Paris in December 2015 [1], solving this problem demands deep changes in the international energetic scheme,

involving a drastic reduction in the use of fossil fuels (coal, gas and oil), the main source of Greenhouse Gases.

Although wind and solar energy are expected to help to reduce drastically these emissions by 2050 [3] and other renewable energy sources, such as geothermal and marine energies, present promising prospects to significantly contribute to the global capacity for power generation in the future [4] they demand, still, large research investments to reduce their costs and to develop storage systems that allow one to overcome their intermittence. Otherwise, it will take them decades to overcome fossil fuels as the planet's main source of energy and effectively reduce the Greenhouse Gases (GHG) emission to the atmosphere.

On the other hand, nuclear fission power plants are among the lowest GHG emitters energy producers [5]. In 2014 $9,9\%$ of the energy consumed in the Organisation for Economic Co-operation and Development (OECD) countries was nuclear [6] but, despite their enhanced safety, nuclear fission technologies lack of public acceptance due to waste handling, weapons proliferation [7] or the risk of major accidents, as if has been the case after the catastrophe in Fukushima [8]. Also the limited availability of the minerals [9] used for fuelling enforces the idea that nuclear fission is not only a risky, but a temporary solution to the problem of global warming.

Some consideration about the negative impact of energy waste in our society is needed, but global access to reliable, sustainable and affordable energy sources is a key prerequisite for social and economic development. It is Science's responsibility to provide a clean and safe energy source that guarantees this development but also reduces human interferences in the Earth's climate. All this will have to happen in a world that, by 2050, is expected to consume two or three [10] times the energy it uses today. In search for it we have to look up to the sky, wonder where do the stars get their energy from, and challenge ourselves to master their source of power.

Stars are fuelled by nuclear reactions that involve the fusion of light nuclei into a heavier one [11]: the joint mass of the initial elements is slightly bigger than the mass of the product and this difference is released as its kinetic energy [12]. For such a reaction to take place, the reactant nuclei have to be close enough to overcome their electrostatic repulsion in order to allow the nuclear strong force to be the predominant interaction between them. This can only be achieved when:

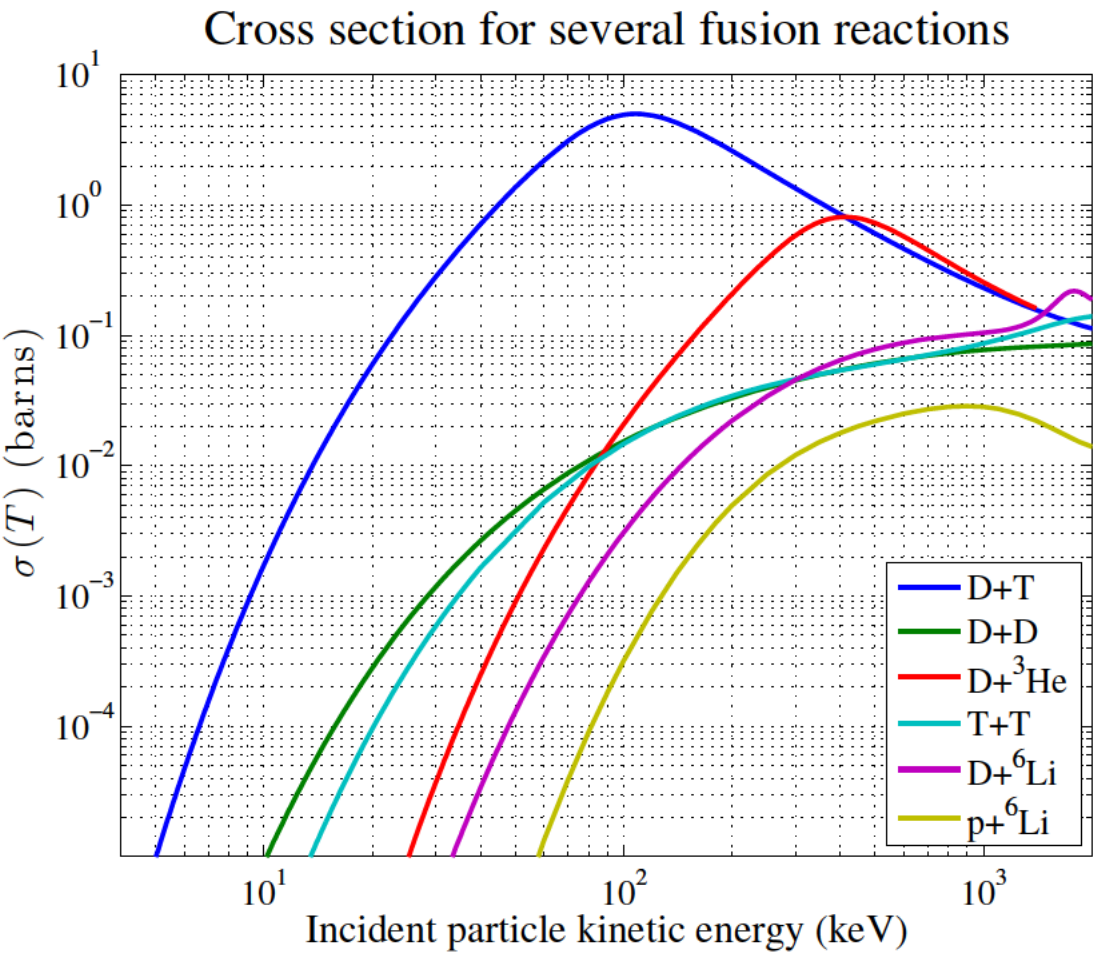

FIGURE 1.1: Cross sections versus temperature for some relevant fusion reactions. The data for these curves has been taken from the ENDF B-VII database https://www-nds.iaea.org/exfor/endf.htm

- the nuclei's kinetic energy is higher than the electrostatic repulsion, meaning that they have to be at very high temperatures;
- the amount of available ions is such that the probability of collisions to happen is relevant, which equals to saying that high density is required for a plasma to contain fusion reactions;
- particles are confined for a time significantly longer than the required for this collisions to happen.

Fig. 1.1 shows the energy conditions at which relevant cross sections for the following fusion reactions can be obtained.

$$
\begin{aligned}
D\ +\ T &\rightarrow {}^4He\,(3.5\text{ MeV}) + n\,(14.1\text{ MeV}) \\
D\ +\ D &\rightarrow {}^3He\,(0.82\text{ MeV}) + n\,(2.25\text{ MeV}) \\
&\rightarrow T\,(1.01\text{ MeV}) + p\,(3.02\text{ MeV}) \\
D\ +\ {}^3He &\rightarrow {}^4He\,(3.6\text{ MeV}) + p\,14.7\text{ MeV} \\
T\ +\ T &\rightarrow {}^4He + 2n + 11.3\text{ MeV} \\
D\ +\ {}^6Li &\rightarrow 2\,{}^4He + 22.4\text{ MeV} \\
p\ +\ {}^6Li &\rightarrow {}^4He\,(1.7\text{ MeV}) + {}^3He\,(2.3\text{ MeV})
\end{aligned}
$$

The Lawson Triple Product must exceed a given number (also called Lawson Criterion) [13]

$$nT\tau_E \geq 1,5 \cdot 10^{21}\ \text{keV} \cdot \text{s} \cdot \text{m}^{-3} \tag{1.1}$$

establishes numerically these three conditions for a fusion reaction to produce as much energy as it requires to be started and sustained. Eq. 1.1 expresses this numeric threshold for the most favourable fusion reaction (as represented in Figure 1.1): the one that combines Deuterium (${}^2H$) and Tritium (${}^3H$) to produce Helium (${}^4He$) and a neutron.

Once one solves the most obvious problem (how to reach these thermonuclear temperatures), the key issue of fusion arises: when, at millions of degrees of temperature, physical contact between the gases and any other material would mean the destruction of the latter and the dilution of the plasma, how can the mixture of gases be confined? Stars are so massive that gravity does the work for them, holding the fuel and the reaction together; but that approach cannot be used in a reactor that will only need milligrammes of fuel to operate. Fusion reactions take place when the gas is fully ionised, that is, when it reaches the plasma state. A plasma is an ionised gas where separation between ions and electrons produces electric fields that affect its particle flows, giving rise to currents and magnetic fields (this is normally called collective behaviour).

Two approaches for achieving plasma confinement are under study nowadays: inertial confinement, which explores the possibility of inducing fusion in a millimetre-sized pellet of fuel by the micro-implosions induced by a high-power laser or particle beam; and magnetic confinement, which exploits the electromagnetic nature of plasma to trap these

charged particles in the lines of an intense toroidal magnetic field, which inhibits perpendicular transport and drives the hot particles away from any material walls. In this model, the pressure ($p = nT$) gradient is counter balanced by the Lorentz force:

$$-\nabla p + \vec{j} \times \vec{B} = 0 \tag{1.2}$$

where $\vec{j}$ is the plasma's electric current and $\vec{B}$ is the external magnetic field. Eq. 1.2 illustrates the first order of local equilibrium required to obtain confinement. The electromagnetic nature of the plasma, which is the reason that allows its confinement by magnetic vessels, has also a side effect: interaction between the plasma, specially its outermost region, with the wall of this vessel is unavoidable.

This work is devoted entirely to the study of magnetically confined plasmas, which will be the only ones considered in this thesis. There are two main different conceptual designs to achieve this kind of confinement: the tokamak, which uses the plasma's induced electric current to produce part of the confinement magnetic field; and the stellarator, that avoids the generation of such a current and produces the magnetic trap through external electromagnets. A more detailed description of both approaches will be presented further in this thesis, as work on two of these devices, JET (tokamak) and TJ-II (stellarator), has been carried out.

One of the main goals of this thesis is to contribute to a better understanding of magnetic confinement, to lead to a technological improvement of it. In order to get this, we've turned our view on two topics: experimental testing of the flexibility of one of the stability factors in stellarators, the magnetic well; and the study of turbulent transport and other edge phenomena occurring in plasmas that affect greatly the equilibrium described by Eq. 1.2.

This thesis is presented in three blocks. The first one tries to compile everything that the author has considered necessary to understand the experiments and results presented in the second part. A final block analyses the results to offer some conclusions. This way Chapter 2 reminds some of the rudiments of Plasma Physics for a better understanding of Chapter 3, which presents the characteristics and differences of tokamaks and stellarators, paying special attention to the physical phenomena that have been studied in them and the technical details of the experimental devices where the presented experiments have been developed. To finish the introductory materials, Chapter 4 describes

the Physics behind the key diagnostics to this research and the specific tools employed in the course of these works.

After that, two groups of results will be presented: firstly, everything related with the magnetic well scan experiment perfomed in TJ-II (Chapters 5-6); and then, in Chapter 7, we will analyze the edge phenomena recorded by the intensified fast visible camera on JET. An extra Appendix A references the coding works required for all the analysis presented in Chapter 7. Finally, Chapter 8 lays all the findings accomplished in the course of these years, attempts to look for physical explanations to the observed phenomena, and points the remaining questions opened by this work. All the references are ordered as they appear an external links for their consulting are provided in all the available cases.

Chapter 2

Plasma Physics

The present Chapter provides a glimpse of the complexity one faces when describing plasma systems. Collective behaviour has already been mentioned as one of the main characteristics of plasmas, arising as a consequence of its electromagnetic features and the fact that a plasma can be described as a fluid. Establishing the theoretical fundamentals required to describe them and their confinement is essential before we move any further into this research.

2.1 Quasineutrality

Quasineutrality is such a fundamental property of plasmas that taking some time to refresh the concept is in order. It addresses the fact that any charge or electric potential introduced in a plasma is shielded by it, creating a sphere beyond which, global neutrality is approximately maintained. The radius of this sphere is Debye's length λ_D and it gives an estimation of radius scale in which no net charge can be found. This phenomenon will be of great interest in Chapter 4 when we present Langmuir probes, one of the diagnostics used in the course of this research, as this diagnostic involves physical contact between a electrode and the plasma.

Debye's length can be estimated assuming that the plasma is in a near-equilibrium state, being the Maxwell-Boltzmann distribution an appropriated way to describe the probability for a particle (with a q charge) to be in a specific state of energy. Using the conversion factor 1 eV = 11600 K to avoid including Boltzman's constant in all the

equations by writing temperature in energy units (we will operate this way from now on), when one takes kinetic and potential energy into account, the Boltzmann distribution function f_M looks like:

$$\int f_M \mathrm{d}v_x \mathrm{d}v_y \mathrm{d}v_z = n \quad f_M = \frac{n}{\left(\sqrt{2\pi} v_t\right)^3} \exp[-\left(mv^2/2 + q\phi\right)/T] = n_\infty \exp[q\phi/T] \tag{2.1}$$

One of these equities will be required for each species, ions and electrons, contained in the plasma. When temperature for both species is much larger than their potential energy, a Taylor expansion can be used:

$$n = n_\infty \exp[q\phi/T] \longrightarrow n \simeq n_\infty \left(1 + \frac{q\phi}{T}\right) \tag{2.2}$$

When all this is taken into Poisson equation

$$\nabla^2 \phi = \frac{e^2}{\epsilon_0}\left(n_e - Z n_i\right) \simeq \frac{e^2 n_{e\infty}\left(1 + Z T_e/T_i\right)}{\epsilon_0 T_e}\phi \tag{2.3}$$

it can be solved easily:

$$\phi\left(r\right) = \frac{q}{4\pi\epsilon_0}\frac{1}{r}\exp\left(-r/\lambda_D\right) \quad \lambda_D = \left(\frac{\epsilon_0 T_e}{e n_{e\infty}\left(1 + Z T_e/T_i\right)}\right)^{1/2} \tag{2.4}$$

where λ_D gives the limit distance at which individual charges are shielded, this means, when the plasma reaches quasineutrality.

	R (m)	n_e (m^{-3})	T_e (eV)	B (T)	λ_D (m)	r_L^e (m)	r_L^i (m)
Interestellar gas	10^{16}	10^6	1	10^{-10}	10^1	10^5	10^6
Earth's ionosphere	10^5	10^{11}	10^{-1}	$3 \cdot 10^{-5}$	10^{-2}	10^{-1}	10^0
Solar corona	10^8	10^{13}	10^2	10^{-9}	10^{-2}	10^4	10^5
Fusion experiment	1	$10^{19} - 10^{20}$	$10^3 - 10^4$	$1 - 5$	10^{-4}	10^{-4}	10^{-3}

TABLE 2.1: In order of magnitude: size, electron density, electron temperature, magnetic field intensity, Debye lenght and Larmor radious for electrons and ions. See http://www2.warwick.ac.uk/fac/sci/physics/research/cfsa/people/erwin/teaching/px384l/calculator/#info_rl for more.

For any statistical description to make sense, the amount of particles contained inside the Debye sphere must be high. Tab. 2.1 summarises temperature, density and size values of natural and laboratory plasmas [14]. For fusion plasmas this number of particles (normally called the plasma parameter) is $N_D \simeq 10^7$, while λ_D is in the order of microns.

If this condition is not satisfied, then the gas is not in plasma state, but an assembly of independent charged particles.

2.2 Describing plasmas

When facing the problem of describing a plasma system, one of the first questions that arises is which description should one use, either kinetic or a fluid theory. A plasma is a hot gas of ionised particles so, will it behave as a N amount of classical charged particles or will the gas' fluid nature be predominant? The answer lies in between: both approaches are essential for a full understanding of the physical processes that take place in this kind of systems. There are even hybrid descriptions, where ions are treated kinetically and electrons as a fluid.

2.2.1 Plasma as a collection of single particles

In a magnetically confined plasmas, ions and electrons will be immerse in a complex combination of magnetic and electric fields, so their motion equations will be subjected to the electromagnetic forces described by Maxwell equations. Understanding the trajectories that these particles will follow is crucial to get a good confinement. The most common way to describe such motions is to assume that the external fields are uniform in space and constant in time and then add the corrections that arise from adding these dependencies.

- **Uniform magnetic field: gyro-motion.** The equation of motion of any charged particle in presence of an uniform magnetic field parallel to its velocity (we shall call this direction z) is given by Lorentz equation:

$$\vec{F} = m\dot{\vec{v}} = q\vec{v} \times \vec{B} \;\rightarrow\; \begin{cases} \frac{\mathrm{d}^2 v_x}{\mathrm{d}t^2} = -\left(\frac{qB}{m}\right)^2 v_x \\ \frac{\mathrm{d}^2 v_y}{\mathrm{d}t^2} = -\left(\frac{qB}{m}\right)^2 v_y \end{cases} \tag{2.5}$$

  The solution to this system of equations is a helical movement along the z direction where the Larmor radius

$$r_L \equiv \frac{v_\perp}{\omega_c} = \frac{\sqrt{v_{xi}^2 + v_{yi}^2}}{|q|\, B/m} \tag{2.6}$$

is the radius of this helix. When the distances considered inside the plasma are larger than r_L and the times much longer than the time required to complete one of these gyro-periods, the particle's trajectories can be described by their gyro-centres. This gyro-motion is much smaller for electrons than for ions, since the latter have larger mass and slower velocities. For a magnetically confined plasma with temperature of 1keV, $r_L^{electrons} \approx 10^{-4}$ m and $r_L^{ions} \approx 5 \cdot 10^{-3}$ m. See Tab. 2.1 for more typical values.

- **Uniform magnetic and electric fields: $\vec{E} \times \vec{B}$ drift.** When an uniform electric field is added, Eq. 2.5 becomes $m\dot{\vec{v}} = q\left(\vec{E} + \vec{v} \times \vec{B}\right)$. The velocity's perpendicular component to $\vec{B}$, $v_\perp$, will behave exactly as it is described in Eq. 2.5. The presence of $\vec{E}$ affects the guiding-centre velocity as

$$\vec{v}_{gc} = v_\parallel \widehat{b} + \frac{\vec{E} \times \vec{B}}{B^2} \equiv v_\parallel \widehat{b} + \vec{v}_{\vec{E}\times\vec{B}} \tag{2.7}$$

  This $\vec{E} \times \vec{B}$ drift doesn't depend on charge or mass, so it affects the same way all the particles in the plasma, stretching and pulling the helix's circumferences.

- **Inhomogeneous magnetic field: ∇B drift.** For a magnetic field changing in scales much larger than r_L, an asymptotic expansion can be used to compute $\vec{v}$. When one assumes that the magnetic field changes perpendicularly to its own direction, like $\vec{B} = B_{gc}\widehat{e}_z + (\vec{r} - \vec{r}_{gc,i})\nabla B \widehat{e}_z$ can be taken into Eq. 2.5. The resulting correction to the gyro-centre velocity is

$$\vec{v}_{\nabla B} = \pm \frac{1}{2} v_\perp r_L \frac{\vec{B} \times \nabla B}{B^2} \tag{2.8}$$

  which changes with the particle's charge and makes the Larmor radius dependant on the magnetic field, causing a current transverse to $\vec{B}$.

- **Curvature drift.** When $\vec{B}$ is homogeneous in module but presents a R_c curvature radious, it will exert a centrifugal force on the particle $\vec{F}_{cf} = \frac{mv_\parallel^2}{R_c}\widehat{e}_r$ that will add another correction to the velocity:

$$\vec{v}_R = \frac{mv_\parallel^2}{qB^2} \frac{\vec{R}_C \times \vec{B}}{R_c^2} \tag{2.9}$$

  In fact this kind of curvature always involves a radial dependence in the modulus (normally $B_\theta \propto \frac{1}{r}$), so Eqs. 2.8 and 2.9 will always appear combined.

2.2.2 Plasma as a fluid

Although the single particle approach that we have introduced in Subsec. 2.2.1 is a powerful tool, able to describe many experimental features of plasma (as will be shown, for example, in Sec. 2.3), a fluid description is necessary to address the complexity of the plasma systems. Magnetohydrodynamics (MHD) aims to focus on the magnetic field topology of magnetically confined plasmas and was developed by Hannes Alfvén.

To begin this description, like every fluid would, plasma needs a continuity equation to express how the number of particles only changes when there is a flux and a source:

$$\frac{\partial n}{\partial t} + \vec{\nabla} \cdot (n\vec{u}) = S \tag{2.10}$$

where $\vec{u}$ represents the average velocity $\langle \vec{v} \rangle$ and S is the source and/or sink term given by edge ionisation and core fuelling. In a plasma system Eq. 2.10 will be fulfilled by mass and charge.

The distribution function $f(\vec{x}, \vec{v})$, with $n(\vec{x}) = \int f(\vec{x}, \vec{v}) d^3v$, addresses the probability of finding a particle at the point $\vec{x}$ with the velocity $\vec{v}$. While moving along the direction x_i, the particle's velocity can have components on any direction: this freedom demands the use of tensors in our description. This way, the rate of momentum exchange can be expressed as $\frac{\partial(nmu_i)}{\partial t} = -\sum_{j=1}^{3} \frac{\partial(mn\langle v_i v_j \rangle)}{\partial x_j}$. In a fluid, this momentum exchange is, in fact, the pressure, so it turns out that a pressure tensor will be required to describe plasmas as fluids:

$$P_{ij} \equiv mn\langle (v_i - u_i)(v_j - u_j) \rangle = mn(\langle v_i v_j \rangle - u_i u_j) \tag{2.11}$$

where $u_i = \langle v_i \rangle$. If $f(\vec{x}, \vec{v})$ describes a Maxwellian distribution, Eq. 2.11 becomes a diagonal matrix. $P_{ij} = nT_{ij}$, although temperature can still depend on direction. The non diagonal terms appear due to viscosity.

Taking all directions into account, moment interchange is $\frac{\partial(mnu_j)}{\partial t} = -\sum_i \frac{P_{ij}}{\partial x_i} - m\sum_i \frac{\partial(nu_i u_j)}{\partial x_i}$. Then substituting into Lorentz equation (Eq. 2.5) and using the connective derivative, one gets the momentum balance that will be referred as the equations of motion of the

individual fluids.

$$mn\left(\frac{\partial \vec{u}_\alpha}{\partial t} + (\vec{u}_\alpha \cdot \vec{\nabla})\vec{u}_\alpha\right) = mn\frac{D\vec{u}}{Dt} = nq(\vec{E} + \vec{u}_\alpha \times \vec{B}) - \vec{\nabla} \cdot \overleftrightarrow{P}_\alpha - \sum_\beta \vec{R}_{\alpha\beta} \quad (2.12)$$

The ratio of momentum loss due to collisions is proportional to relative velocity between the particles and the fluid $\vec{u} - \vec{u}_o$. If the collision frequency between two particles α and β is $\nu_{\alpha\beta}$, then the ratio of momentum loss for an element of volume due to collisions is

$$\vec{R}_{\alpha\beta} = -m_\alpha n_\alpha \nu_{\alpha\beta}(\vec{u}_\alpha - \vec{u}_\beta) \quad (2.13)$$

and should be added to Eq. 2.12 as the source/sink term. Obviously, momentum conservation implies $\vec{R}_{\alpha,\beta} = -\vec{R}_{\beta,\alpha}$.

Equations of state are also necessary to describe the heat flow by stabilishing a relationship between pressure, density and temperature. For isothermal compressions the form $p = Cn^\gamma$ can describe adiabatic processes slower than collisionality. For faster cases, anisotropy appears and components parallel and perpendicular to the magnetic field must be taken into account.

$$p_\perp = mn\langle\frac{v_\perp^2}{2}\rangle = n\langle\mu\rangle B \quad \rightarrow \quad \frac{d}{dt}\left(\frac{p_\perp}{nB}\right) = \frac{d}{dt}\langle\mu\rangle = 0 \quad (2.14)$$

$$p_\parallel = mn\langle v_\parallel^2\rangle \quad \rightarrow \quad J \approx v_\parallel L \quad (2.15)$$

Where μ is the magnetic moment and Eq. 2.14 expresses its invariability in time. Combining all these expressions with Maxwell equations, assuming charge neutrality ($n_i \approx n_e \approx n$) and considering one single fluid (e.g. meaning for density $\rho = n_i M + n_e m \approx n(M + m) \approx nM$), MHD equations can be formulated (they can be found in several textbooks like [15] or [14]).

If the ion's Larmor radius is small compared with the fluid's characteristic motion length ($r_L/L \ll 1$), pression gradient and magnetic forces have similar magnitude and Ohm's Law can be written as

$$\vec{E} + \vec{u} \times \vec{B} = \nu\vec{j} \quad (2.16)$$

where ν represents resistivity. Assuming quasineutrality, Eq. 2.16 leads to the commonly used simplified set of MHD equations:

$$\frac{\partial \rho}{\partial t} + \vec{\nabla} \cdot (\rho \vec{u}) = 0; \quad \vec{\nabla} \cdot \vec{j} = 0; \quad \rho \frac{D\vec{u}}{Dt} = -\vec{\nabla} p + \vec{j} \times \vec{B} \tag{2.17}$$

2.3 Confining plasmas

As explained in Subsec. 2.2.1, when initially moving parallel to a magnetic field a charged particle executes a helical trajectory along the line. As long as the Larmor radius is small and the field line doesn't hit the boundaries, one can say that the particle is confined. Even considering three dimensions, single particle confinement is 'just a matter of adding external forces to drive away from any wall. In toroidal geometries the conservation of the magnetic moment, as it was stated in Eq. 2.14, has great impact on particle dynamics, as it produces orbits with a radius much larger than r_R (e.g. banana orbits). But plasmas exhibit collective behaviour, they are more than a collection of single particles, because electromagnetic and other collective interactions, such as Coulomb collisions, arise. To reduce contact between a thermonuclear grade plasma, with temperatures in the 10^7K range, with the walls, we can follow two possible strategies: either to limit field lines to closed surfaces, or to increase $|\vec{B}|$ along field lines before the wall contact, so as to reflect a sufficient fraction of the energetic particles.

2.3.1 First approach: Rotational transform and magnetic moment

All the preceding single particle description exposed in Subsec. 2.2.1 can lead to think of each helix-describing particle as a magnetic dipole (a spire of r_L size) that moves along the guiding centre. So, the force such a dipole would experience under a magnetic field would be

$$\vec{F}_{\parallel} = m \frac{dv_{\perp}}{dt} = -\mu \nabla |\vec{B}| \tag{2.18}$$

where

$$\mu \equiv \frac{1}{2} \frac{v_{\perp}^2 e}{\omega_c} \tag{2.19}$$

By energy conservation this μ is constant in time, which is the basic idea behind the first attempts of confining plasmas (magnetic mirrors): an increasing value of B will force

$\vec{v}_\perp$ to grow in order to keep μ constant, implying that $\vec{v}_\parallel$ must decrease in order to keep the energy balance.

Eq. 2.9 implies that a toroidal magnetic field will effect differently the two species contained in the plasma, drifting ions upwards and electrons downwards, which would generate a vertical electric field that gives an outwards $\vec{E} \times \vec{B}$ drift (Eq. 2.7), preventing any effective confinement (one of the first attempts to toroidally confine plasma, the *bumpy torus*, was a circular distribution of magnetic mirrors that exhibited this problem). To solve this the upper and lower regions must be connected for the charge to be short-circuited: a toroidal current must be induced in the plasma (adding a new poloidal component to the magnetic field, $\vec{B}_\theta$) so that the particles are forced to circulate from one region to the other by twisting the magnetic field lines. We describe this twisting by the rotational transform angle (or field line pitch, in some texts), ι, given by

$$\frac{\iota}{2\pi} \equiv \lim_{n\to\infty} \frac{2\pi}{n} \sum_n \Delta\theta_n = \frac{d\Psi}{d\Phi} = \frac{R}{r}\frac{B_\theta}{B_\phi} \tag{2.20}$$

where R is the major radius, r the radial coordinate and B_θ and B_ζ are the poloidal and toroidal components of the magnetic field; Ψ and Φ being the poloidal and toroidal magnetic fluxes. This ι describes the twisting angle that a magnetic field line experiences after a complete turn around the magnetic axis: if we follow a field line once around the torus the poloidal angle will change by $\theta \to \theta + 2\pi\iota$. An important consequence comes from this, as if ι is a rational number ($\iota = n/m$), the field line returns over itself after m toroidal turns. If ι is irrational, the field line will never reach itself but will keep coming arbitrarily close to each point of the flux surface.

The inverse of $\iota/2\pi$ is called safety factor q and describes the number of turns required for a field line to return to an arbitrary point. In tokamaks one will often see references to q, while ι is preferred when describing stellarators. Similar expressions are also available for tokamaks [16].

The radial gradient of the rotational transform is related with the variation in direction of the magnetic field and gives the local shear of the equilibrium field:

$$s = \frac{r}{q}\frac{dq}{dr} = -\frac{r}{\iota}\frac{d\iota}{dr} \tag{2.21}$$

which plays an important role in plasma stability [17]. As a consequence of this analysis we can conclude that axisymmetric field will not be enough to confine plasma.

2.3.2 Energy confinement time and beta

Experimental confined plasmas prove that their collective behaviour overcomes any theoretical equilibrium conditions: the perturbative effect of collisions and turbulence on transport of particles and energy across the magnetic field must be addressed. Confinement time τ_E, that appeared to be a key factor in Lawson's criteria (Eq. 1.1), measures the rate at which this system loses energy [18]:

$$\tau_E = \frac{W}{P_{in}} = \frac{W}{P - dW/dt} \tag{2.22}$$

Collisions force jumps in the particles' trajectories of δ, producing diffusion with a coefficient $D \approx \delta^2/\tau_c$. For turbulence the step size is in the order of the wavelength perpendicular to the magnetic field $k_\perp^{-1}$, assuming a diffusive-like transport. All this means that τ_E is linked to D by means of the diffusive relation $\tau_E \approx a^2/D$.

Energy confinement time represents the e-folding relaxation time of plasma energy due to heat conduction. In practise it is determined experimentally by regression analysis of large databases of plasma discharges. In stellarators, in order to provide an unified scaling law, discharges from several devices were analysed to obtain the ISS04 expression [19]:

$$\tau_E^{ISS04} = 0.134 a^{2.28} R^{0.64} P^{-0.61} n_e^{0.54} B^{0.84} \iota_{2/3}^{0.41} \tag{2.23}$$

where a and R are the minor and major radius (in meters), P is the absorbed power (in megawatts), n_e the line-averaged electron density (in 10^{19} m^{-3}), B the magnetic field strength (in Tesla) and $\iota_{2/3}$ is the rotational transform at $r/a = 2/3$.

The quantity β represents the capability of a device to confine and it is given by the ratio between plasma thermal energy and magnetic field energy [20], and needs to be introduced to measure how effective the applied fields are at confining plasma pressure:

$$\beta = \frac{\langle p \rangle}{2\mu_0 B^2} \tag{2.24}$$

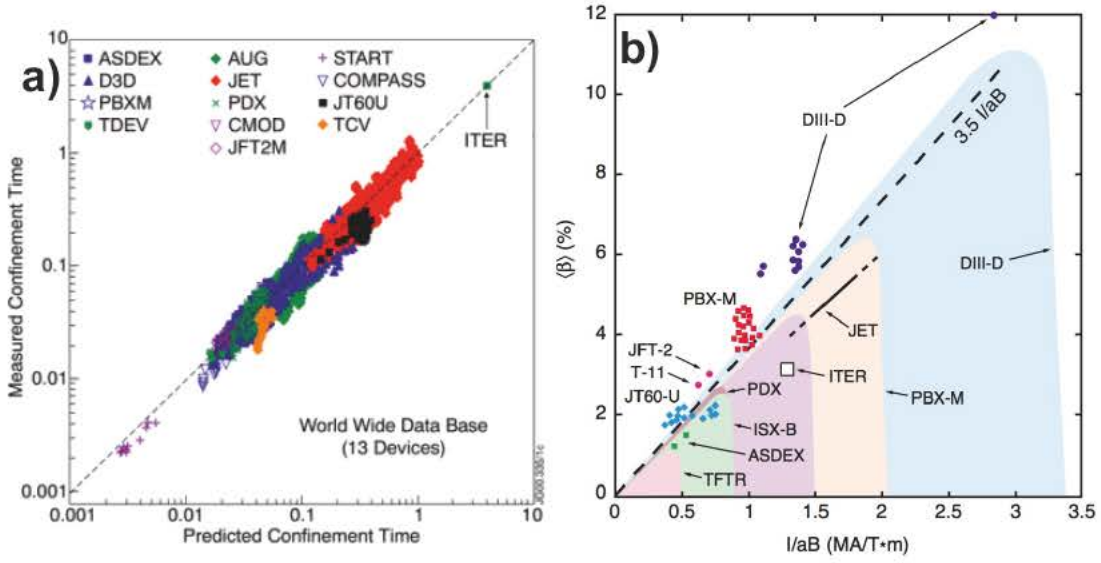

FIGURE 2.1: a) Predicted and measured confinement time (in seconds) for 13 fusion experiments. b) Normalized β or Troyon factor for some fusion experiments: $\beta_N = \beta \frac{aB_T}{I_p}$, where B_T is the toroidal magnetic field in T, a is the minor radious in m and I_p is the plasma current in MA. Credit: http://wiki.fusenet.eu/fusionwiki/index.php/Beta

High β will be mandatory for a fusion reactor to be economically profitable [21]. Normally a poloidal and toroidal components are distinguished in β to address the different components of the confining field.

2.3.3 Toroidal magnetic configuration

The magnetization of the entire plasma requires the boundary of confinement region to be topologically equivalent to a torus to prevent rapid particle transport from inside the torus to the walls [22]. As a consequence of this, the confining magnetic field cannot be uniform. A set of coordinates must be introduced to describe this system: ψ labels the flux surfaces, θ are the poloidal and ϕ the toroidal angles. The Clebsch representation gives $\vec{B}$ as an orthogonal vector to the flux surfaces:

$$\vec{B} = \nabla\psi_\theta \times \nabla G \tag{2.25}$$

where G is a function chosen to address that the poloidal flux inside the magnetic surface is $2\pi\psi_\theta$ and to exhibit periodicity in ϕ and θ. This way, the contravariant representation of $\vec{B}$ is

$$\vec{B} = q(\psi_\theta)\nabla\psi_\theta \times \nabla\theta + \nabla\phi \times \nabla\psi_\theta \tag{2.26}$$

where $q(\psi_\theta)$ is the helicity of the field line. The vector potential $\vec{B} = \nabla \times \vec{A}$ associated to this field is:

$$\vec{A} = \psi \nabla\theta - \psi_\theta \nabla\phi \tag{2.27}$$

Turning back to the equilibrium condition (Eq. 1.2) and assuming scalar pressure equilibrium $p = p(\psi)$ one gets the covariant representation of $\vec{B}$

$$\vec{B} = g\nabla\phi + I\nabla\theta + \delta\nabla\psi \tag{2.28}$$

In stellarator equilibrium, g, I and δ are functions of three variables. If the small toroidal axis (a) is much smaller than the large one (R), the plasma is circular and the plasma pressure is small compared to the magnetic field pressure, plasma beta is small $\beta = 2p/B^2 \ll 1$ and the equilibrium is given by

$$g = B_0 R, \quad \psi = \frac{B_0 r^2}{2}, \quad I = \frac{B_0 r^2}{R^2 q(r)}, \quad \delta = 0 \quad \rightarrow \quad B \simeq \frac{B_0}{R}(1 - r\cos\theta) \tag{2.29}$$

When β is high and the plasma is strongly shapped, the equilibrium must be found by solving the Grad-Shafranov equation. However, in an experimental device, like a tokamak, toroidal field is not exactly axisymmetric because it's generated by a finite number of coils. A correction must be added to the expression obtained in Eq. 2.29 for it to contain this ripple: $B = B_0(1 - r\cos\theta + \delta\cos N\phi)$, where N is the number of coils and δ, the ripple magnitude.

2.3.4 Runaway electrons

The impact of Coulomb collisions in confinement is clear in the apparition of runaways [23]: electrons that move under an electric field with $m_e \frac{d\vec{v}}{dt} = -e\vec{E} - \frac{m_e \vec{v}}{\tau_{ee}(v)}$, where $\nu_{ee} = \frac{1}{\tau_{ee}} = n_e \sigma v = \frac{e^4 \ln\Lambda}{2\pi\epsilon_0^2 m_e^2 v^3}$ is the electron-electron collision frequency, which varies as v^{-3}. If v increases, then the $\frac{m_e \vec{v}}{\tau_{ee}(v)}$ term becomes smaller and smaller and after a critical velocity, the Drecier velocity,

$$\frac{m_e v_c^2}{2e} = \frac{e^2 n \ln\Lambda}{4\pi\epsilon_0^2 E} \tag{2.30}$$

can be overcome by $|-e\vec{E}|$. Beyond this velocity threshold, electrons are increasingly accelerated and rarely suffer Coulomb collisions becoming runaways, with dangerous

consequences to the plasma facing pieces of the reactor, when escape, and storing large kinetic energy that is not in the bulk. For instance, for plasma densities in the range $n_e \approx 10^{19}$ m^{-3} and $E \approx 1$ V/m, electrons with energy larger than 5 keV will become runaway electrons.

2.3.5 Poloidal field

According to Eq. 2.9, a purely toroidal magnetic field will not be enough to confine the plasma without creating currents due to species separation. A poloidal component of $\vec{B}$ will be indispensable to achieve confinement, but the source of such field is the root of the two main different approaches to magnetically confine plasmas nowadays: the tokamak, that uses the plasma current itself to produce the poloidal magnetic field; and the stellarator, that requires of complex external coils to complete the confinement. In the course of this thesis, works have been carried out in these two kinds of devices, so a more detailed description of both concepts will be provided in Chapter 3.

Chapter 3

Confining devices

Although there are other solutions (like the reverse field pinch), magnetic confinement fusion community faces today the choice between two reactor models. Tokamaks and stellarators are not antagonistic, but the phenomena they exhibit and the problems they face are different. As in the course of this PhD, works have been carried out in the TJ-II stellarator and the JET tokamak, a description of them and the physics addressed in both cases is in order.

3.1 Tokamaks

The word *tokamak* comes from a Russian transliteration that stands for 'toroidal chamber with current', as the first of these devices were designed and developed in the Soviet Union, at the Kurchatov Institute in Moscow, in the last 50's [24]. The first approaches to thermonuclear fusion reactions and temperatures were achieved by Russian scientists at the T-4 tokamak by the end of the 60's [25], leading to the construction of new machines by other nations.

3.1.1 Tokamak equilibrium

In a tokamak, plasma equilibrium needs to address two requirements: firstly, the balance between the pressure of plasma and the magnetic forces and, secondly, shaping and positioning the plasma by external means. Although necessary, in a tokamak, the poloidal

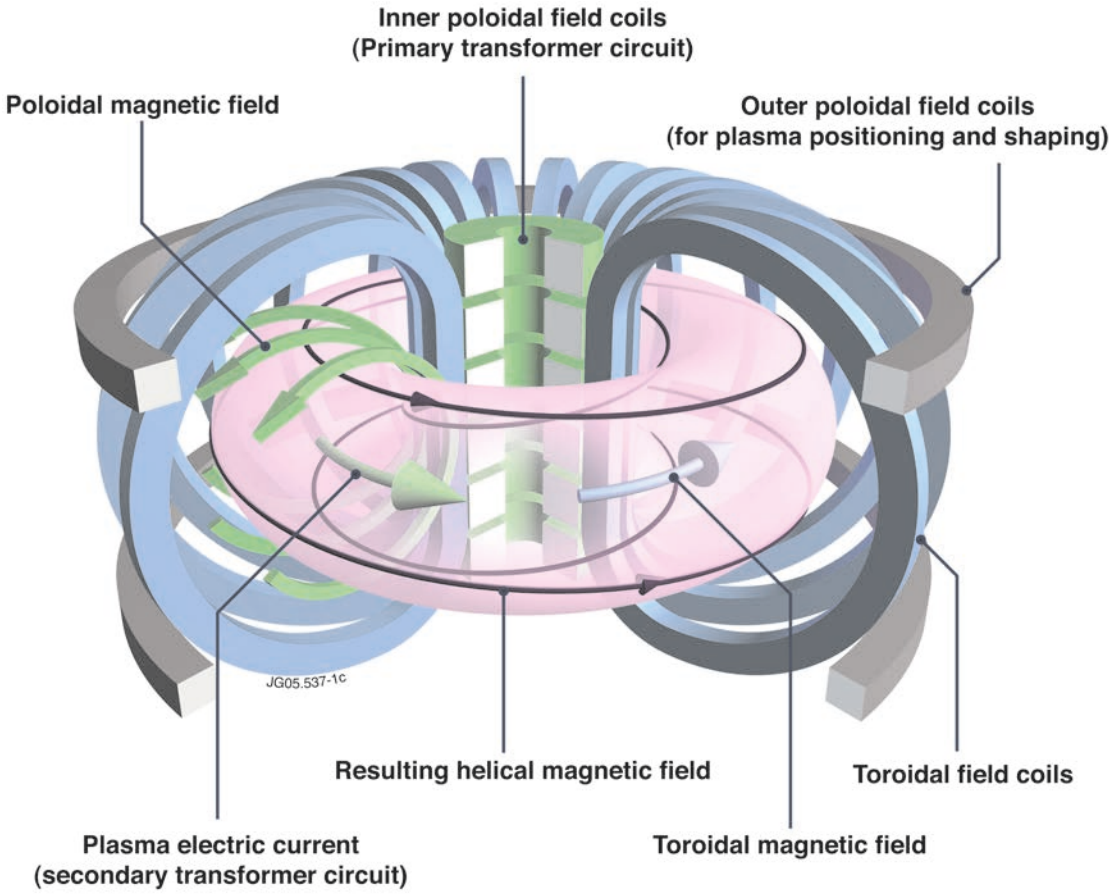

FIGURE 3.1: Diagram illustrating the tokamak concept: arrangement of magnetic field coils and the resulting magnetic field that confines the plasma. Credit: https://www.euro-fusion.org/2011/09/tokamak-principle-2/

magnetic field due to the plasma's toroidal current is typically ten times smaller than the toroidal field applied externally.

Knowing that the poloidal magnetic field will require a plasma toroidal current given by Ampere's law, that will increase with electron temperature, the plasma current will be peaked in the central region, where temperature is higher and resistivity smaller [26]. As it already did in Subsec. 2.3.1, ψ represents the poloidal magnetic flux, satisfying $\vec{B} \cdot \vec{\nabla}\psi = 0$. Using our previous cylindrical coordinate system, it turns:

$$B_r = -\frac{1}{r}\frac{\partial \psi}{\partial z}, \quad B_z = \frac{1}{r}\frac{\partial \psi}{\partial r} \tag{3.1}$$

The second Maxwell equation, $\vec{\nabla} \cdot \vec{B} = 0$, ensures that the flux function ψ is arbitrary to an addition constant chosen for convenience.

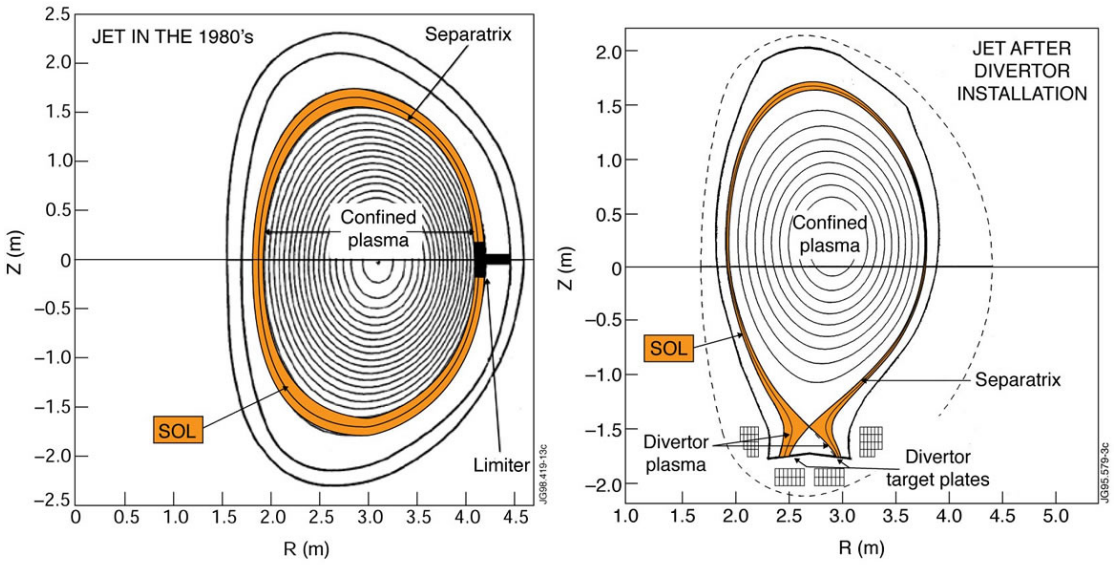

FIGURE 3.2: Schematic view of the magnetic flux surfaces at JET for limiter (left) and divertor (right) configuration. Credit: https://www.euro-fusion.org

If Eq. 3.1 is true for the flux, the symmetry of the plasma current $\vec{j}$ guarantees that it must follow a similar relationship with an f function so that

$$j_r = -\frac{1}{\mu_0}\frac{\partial B_\phi}{\partial z}, \quad j_z = \frac{1}{\mu_0}\frac{1}{r}\frac{\partial}{\partial r}(rB_\phi) \quad \rightarrow \quad f = \frac{rB_\phi}{\mu_0} \tag{3.2}$$

The equilibrium condition from Eq. 1.2 guarantees that $f = f(\psi)$, which will lead to the Grad-Shafranov equation. Writing the poloidal components of the magnetic field and current density in terms of ψ and f, the equilibrium equation turns $-\frac{B_\phi}{R}\nabla f + \frac{j_\phi}{R}\nabla\psi = \nabla p$. The forth Maxwell's equation combined with Eq. 3.1 provides a relationship between j_ϕ and ψ that leads to:

$$R\frac{\partial}{\partial R}\frac{1}{R}\frac{\partial \psi}{\partial R} + \frac{\partial^2 \psi}{\partial z^2} = -\mu_0 R^2 p'(\psi) - \mu_o^2 f(\psi) f'(\psi) \tag{3.3}$$

Which is the Grad-Shafranov equation, that can be solved numerically to extract the equilibrium flux surfaces, the plasma current density, pressure and magnetic field. This equation does not depend on the toroidal angle, ϕ, therefore tokamaks are axisymmetric.

3.1.2 Plasma-wall interaction and divertor

In spite of the refined magnetic confinement, plasma-wall interaction, and the subsequent influx of impurities in the plasma, is unavoidable. Impurities radiate and prevent the

plasma heating and they add extra electrons to the system. The Helium nuclei produced in fusion reactions will also act as impurities. The higher the atomic number, the more problematic they will be, as impurity radiation is proportional to Z^2, being Z the impurity's charge state. The particle flow to material surfaces is primarily due to transport from plasma core into the boundary or to ionisation of neutrals. In the boundary layer, plasma escapes and then interacts with the walls.

The most intuitive way to 'control' this interaction is the addition of limiters: solid surfaces that define the shape of the plasma by physically contacting the Last Closed Flux Surface (LCFS). This solution protects the vacuum chamber walls but introduces impurities in the plasma. Unfortunately no material can hold the heat load that a minute-long hot plasma would induce without delivering impurities, and a more clever solution is required: divertors, as shown in Fig. 3.2, minimise the impurity content by moving the surface interactions farther from the confined plasma to a selected area equipped with pumping and cooling, minimising the amount of impurities produced at the target from entering the confined plasma. Impurity flux is also reduced by the magnetic configuration, that forces ionising impurities resulting from residual plasma-wall interactions in the Scrape-Off Layer (SOL) to follow the field lines into the divertor.

Most of the tokamak plasmas studied in this work use a toroidally symmetric divertor, as this configuration eases the plasma's access to an enhanced energy confinement time, the H-mode.

3.1.3 H-mode and ELMs

In 1982 during NBI heating experiments in ASDEX, an abrupt transition to a higher confinement regime was found [27]. This regime is known as *High confinement mode* or H-mode. This transition is characterised by the H_α emission fall and results in a large increase in global stored energy and confinement (Fig. 3.4 c)), primarily from an increase in the edge pressure. The edge pressure (Fig. 3.3 a)) and its associated gradients grow until a MHD limit is reached. Fig. 3.3 shows temperature and pressure Thomson Scattering (TS) profiles for two moments of a high confinement pulse in JET: in blue we represent the low confinement regime (so-called L-mode) and, in green, the steep gradients for edge temperature and pressure are associated with a sudden increase of the confinement time. This behaviour has been observed in several tokamaks increasing

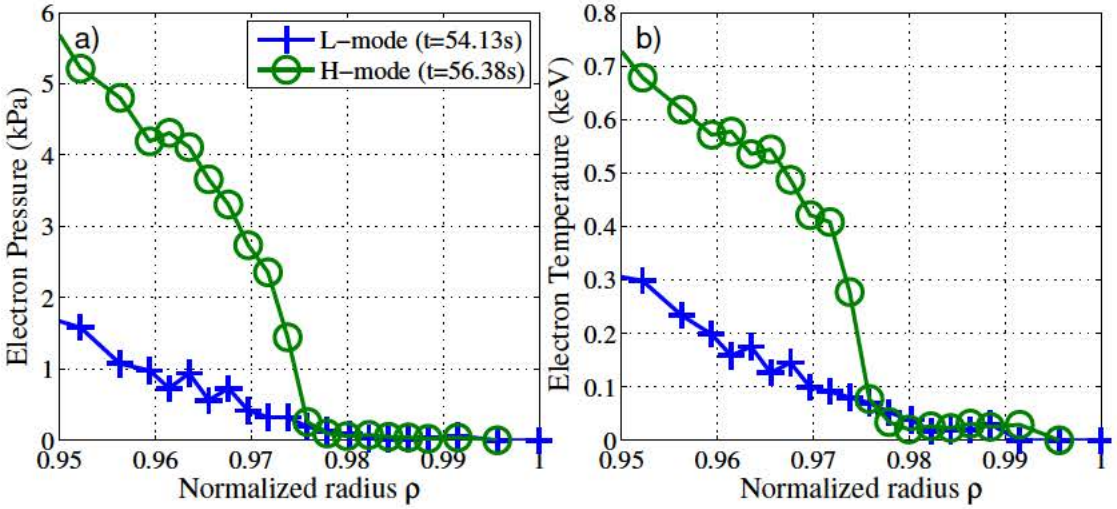

FIGURE 3.3: Thomson Scattering pressure and temperature profiles during the L and H-mode phases during the NBI-heated JET discharge JPN89372.

with density, magnetic field and machine size. Although its explanation is still unclear, mastering this confinement regime is a key factor in the development of future fusion devices like ITER.

One of the consequences of the access to the H-mode is the unavoidable apparition of ELMs: edge localised modes involving the periodic loss of particles and energy from the outermost region of plasma. These ELM instabilities cause a rapid relaxation of the edge pressure with a burst of heat flux flowing into the divertor. After the ELM burst relaxes the edge pressure, the H-mode transport barrier is re-established allowing the edge pressure and its gradients to build toward the next ELM [28]. Experimentally, ELMs manifest as a periodic growth and relaxation of the edge pressure and periodic bursts of heat flux on the walls and the divertor target, although their apparition is commonly characterised as sharp bursts in the H_α signal (see Subsec. 4.1.1) with a given repetition frequency.

ELMs are responsible of serious degradation processes in the plasma facing materials, like sputtering and large heat charges; but they also seem to provide density control and a spontaneous way to give off impurities during the H-mode [29]. Despite of that, ELMs will be problematic in ITER, as the huge power flux that they will launch to the walls will not be compatible with ITER operation.

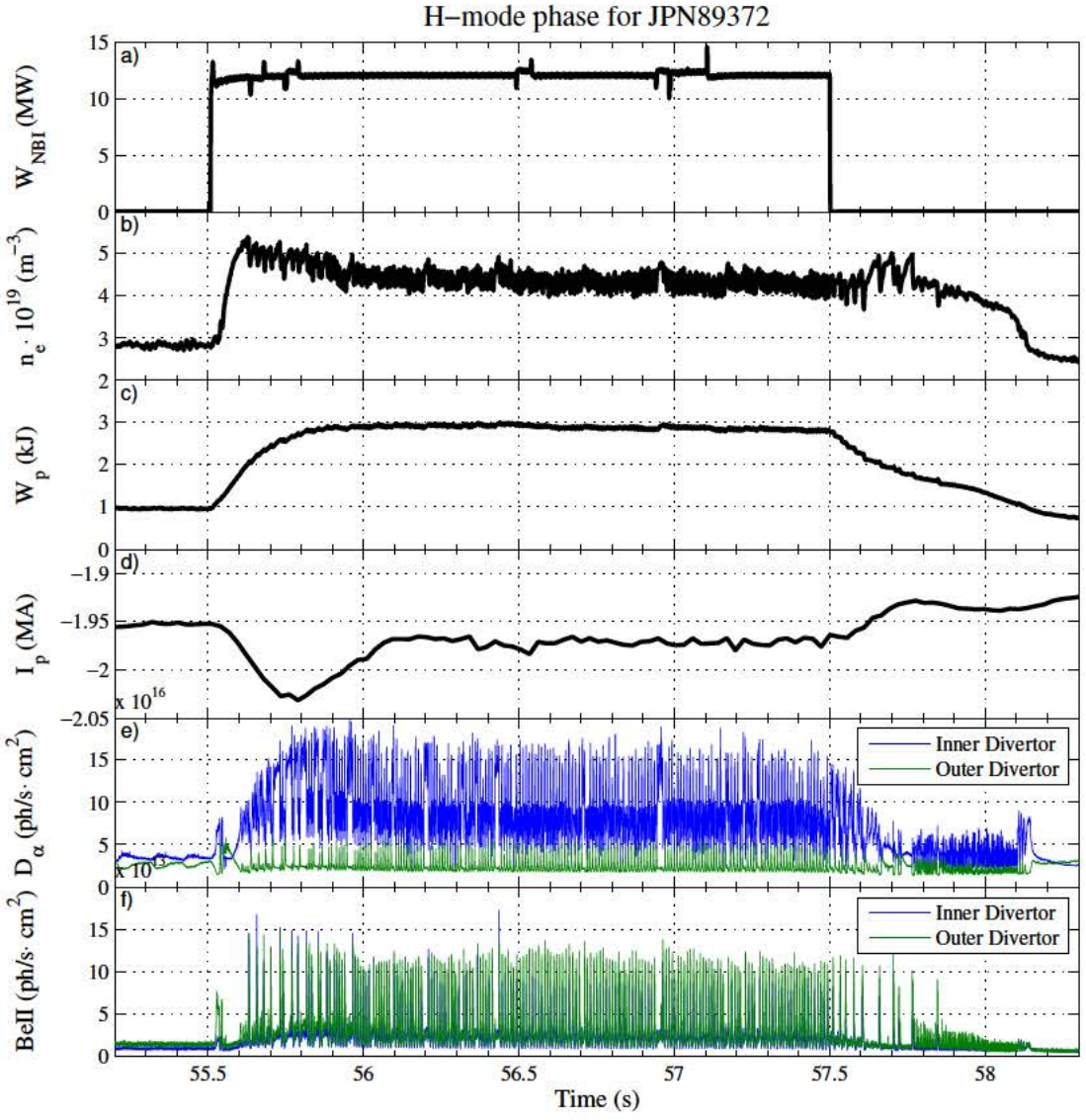

FIGURE 3.4: General plasma parameters during the L and H-mode phases during a NBI-heated JET discharge.

3.1.4 Disruptions

The contribution of the toroidal current to poloidal confinement is responsible of one of the technological advantages of tokamaks over stellarators, as it simplifies the arrangement, design and construction of the magnetic field coils. But it is also involved in one of most dangerous tokamak's weakness: disruptions. These violent events constist of a sudden destruction of the plasma confinement followed by a complete loss of the current. The mechanical stress upon the wall that this events provoke must be avoided without exceptions in future and larger tokamak fusion reactors. Nowadays, understanding, mitigating and preventing disruptions is one of the most urgent goals in the fusion

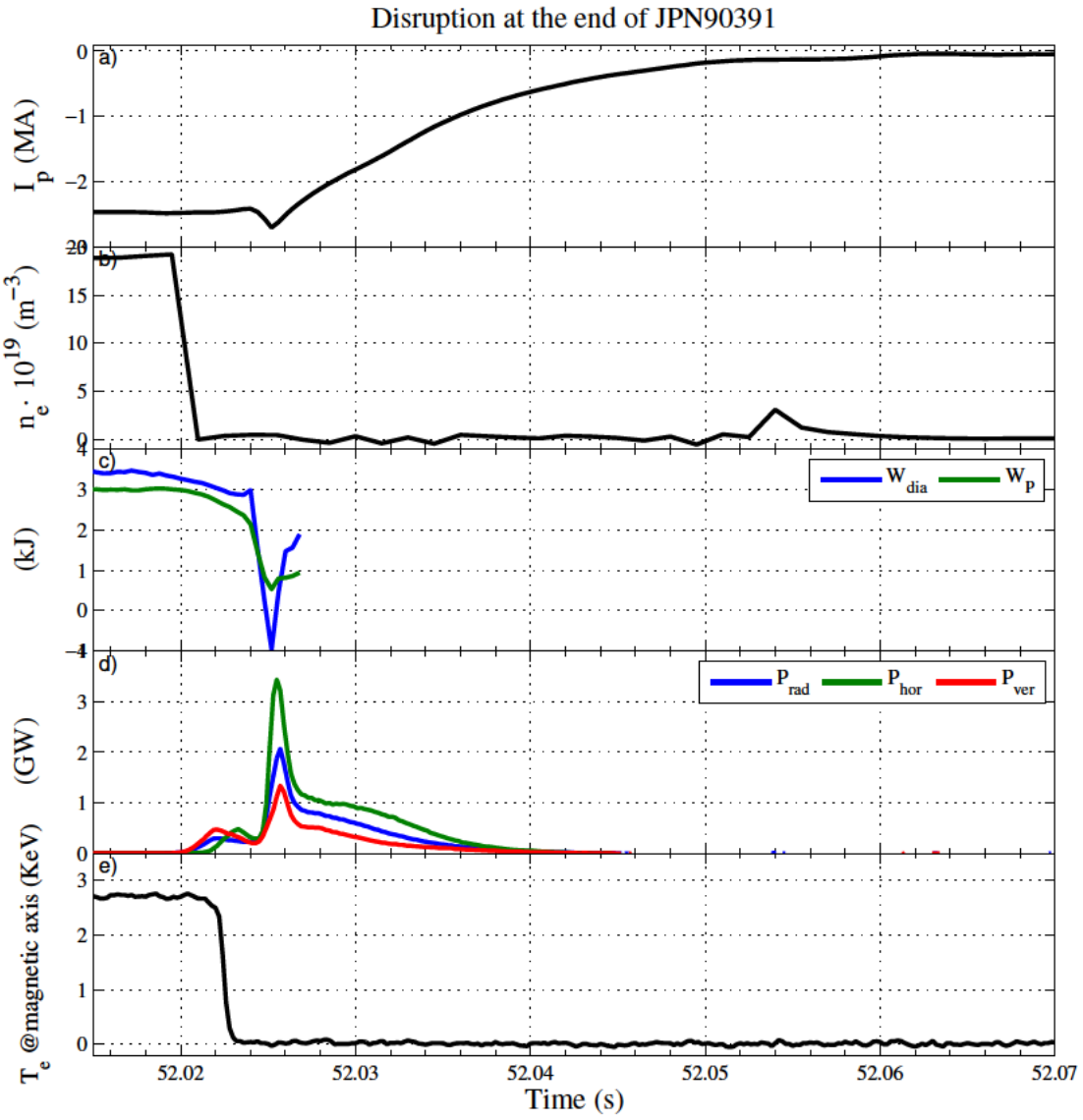

FIGURE 3.5: General plasma parameters during a disruption and current quench at JPN90391.

community.

Disruptions limit the range of operation in current and density. They can be the consequence of a MHD instability that manifests as an increase of the magnetic oscillations (precursor phase). When this instability grows, plasma temperature collapses (fast phase) and finally the plasma current abruptly decays to zero (quench phase). Fig. 3.5 shows some general plasma characteristics during a disruption at JET. As a consequence the wall surfaces suffer plasma-conducted thermal loading, $\vec{J} \times \vec{B}$ forces are induced and the toroidal plasma current turns into relativistic runaway electrons up to 20 MeV that end up hitting Plasma Facing Components (PFC's) of the wall.

Since there is not a complete physical explanation to why disruptions happen (although complex statistical analysis of large disruption databases has proved useful as a real time disruption predictor in JET [30, 31]), efficient mitigation of their harmful consequences is crucial. High pressure gas injection is now the most simple and robust method to mitigate these effects [32, 33]. When a low-Z noble gas is injected at a pressure higher than plasma pressure, it penetrates through the plasma as a neutral gas. This way part of the plasma is dissipated by radiation.

Larger tokamaks have been found to be more susceptible to the formation of runaway electrons because of the effect of avalanche or multiplications of runaways due to Coulomb collisions with the electrons of the background plasma [34] (as we mentioned in Subsec. 2.3.4 the growth rate of runaway current due to these avalanches is proportional to the toroidal electric field). Gas injection is also useful to prevent these runaways from harming the PFCs, although not all the gas species are as equally efficient as they are for disruption mitigation [35].

3.1.5 A tokamak: JET

JET, the Joint European Torus, is the world's largest tokamak in operation. It is an international experiment installed in CCFE, Culham (Oxfordshire). It was built between 1977 and 1982, and first plasmas were achieved in 1983 [36]. Some general design parameters of JET are presented in Tab. 3.1. Also, the panels in Fig. 3.6 provide some schematics on JET's design and its current outer and inner appearance.

In 1991 JET became the first magnetic confinement reactor to achieve nuclear fusion: a D-T mixture with 11% of Tritium provided 1.7 MW of fusion power [37]. Since then, small amounts of Tritium have been used in 1997, when the world record of 16 MW of fusion power was achieved [38], and 2003. A new D-T campaign is planned at JET for 2018. JET has also pioneered in the field of remote handling. Both topics, being capital for the ITER design and manning, and its size have made of JET the most suitable device to test the concepts and ideas that are planned to be used in ITER.

In 2005 the Tritium retention that occurred in JET's carbon fibre reinforced carbon (CFC) divertor made it clear that, in spite of this material's enhanced high heat load capability, such materials were incompatible with the strictly controlled ITER Tritium

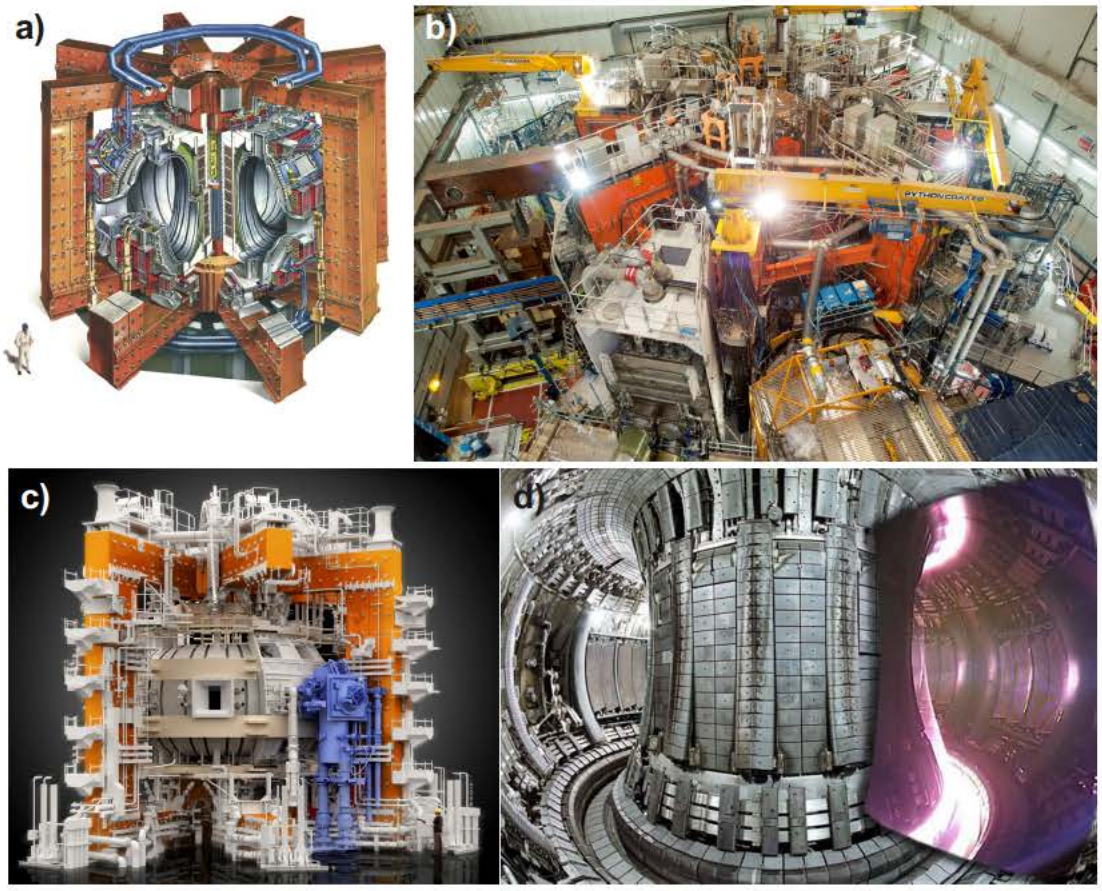

FIGURE 3.6: JET: a) 1980's Drawing of the JET machine. Credit: https://www.euro-fusion.org/2011/09/jet/. b) JET's torus hall as it was in February 2011, shortly before the beginning of the ILW experiment. Credit: https://www.euro-fusion.org/2011/09/torus-hall-6/. c) Computer generated picture showing the vacuum vessel (dark grey in the centre), surrounded by the magnetic coils. The orange coloured iron transformer core induces electric current into the plasma, the Turbo Pump station is shown in blue. Credit: https://www.euro-fusion.org/2011/01/the-most-powerful-magnetic-fusion-experiment/. d) Internal view of the JET's ITER-like wall superimposed with an image of a plasma taken with a visible spectrum video camera. Credit: https://www.euro-fusion.org.

inventory. It was decided that a different combination of materials would form ITER's facing wall and divertor, and that a test version of such a wall would be installed and tested at JET [39]. Between 2009 and 2011 JET went into a shutdown that allowed the installation of a a beryllium-clad first wall in the main chamber (to suppress carbon migration which codeposits tritium in the divertor region), CFC at the divertor strike points (to handle the highest heat loads), and tungsten for the rest of the divertor (to handle higher heat loads than beryllium can, while minimising carbon sources). This combination is commonly referred as the ITER-like wall (ILW) and it is still in operation nowadays. Fig. 3.6 d) shows an image this wall.

JET	
Major radius R (m)	2.96
Average magnetic field B (T)	3.45
ICRH power (kW)	10
NBI power (kW)	34
LHCD power (kW)	7
Plasma current (MA)	4.8
Plasma volume (m^3)	90
Minor radius a (m)	1.25 to 2.10

TABLE 3.1: JET's main parameters. Source: https://www.euro-fusion.org/jet/jets-main-features/.

Together with upgraded heating power, this ITER-Like Wall enables scientists to develop plasma scenarios that resemble as closely as possible those planned for ITER [40]. Already JET experiments have helped ITER to make the decision to begin operation with a full tungsten divertor, thus substantially reducing investment costs. These scenarios focus very special attention in the ELM [41] and disruption mitigation [42].

3.2 Stellarators

The history of stellarator research starts in 1958, shortly after the development of the firsts tokamaks, when Lyman Spitzer summarised the basic ideas required to heat and confine plasma [43]: the power source of the stars. Hence its name. As we have seen, the current-driven instabilities and the difficulty to operate on a steady state are the side effect of the relatively good plasma confinement achieved by tokamaks. By renouncing to axisymmetry, stellarators can avoid such instabilities and operate in steady state [44].

3.2.1 Plasma stability in stellarators

In a stellarator, the helical lines of force are produced by a series of coils which may themselves be helical in shape. If the toroidal curvature is ignored such a field, in vacuum, can be described by the scalar potential

$$\phi = B_0 \left[r\zeta + \sum_m \epsilon_m \frac{Rm}{n} I_m \left(\frac{nr}{R} \right) \sin(m\theta - n\zeta) \right] \tag{3.4}$$

where B_0 is the magnetic field on the axis, $R \equiv L/2\pi$, L is the axis length, r the polar radius, θ and ζ the angular variables, ϵ_n is the relative amplictude of the helical harmonic of the magnetic field with m and n periods along the short and long way of the torus [45].

A stellerator is characterised by:

- **Rotational transform** ι as we described it in Subsec. 2.3.1. Its profile consists of two components: $\iota(\rho) = \iota_{vac}(\rho) + \iota_{Ip}(\rho)$, one associated with geometry at zero plasma current and the other one, produced by the latter, which is expected to be small in comparison with the coil currents.
- **Shear** $s(\rho)$, as defined in Eq. 2.21.
- **Vacuum magnetic well** $W_0 = -U_0^{''}(\phi)\phi/U_0^{'}(\phi)$. This quantity measures the specific volume inside magnetic flux surfaces and arises from the toroidal curvature effect when the aspect ratio is not too large.
- The equilibrium (β_{eq}) and stability (β_{st}) values of the quantity introduced in Eq. 2.24.

When developing a stellarator, MHD stability and high values of β_{eq} and β_{st} (meaning efficient confinement) are mandatory. This can be achieved in two different ways:

- Large shear $s \sim l$: this way resonant surfaces aren't avoided, but their spitting can be limited. This is the case of torsatrons and heliotrons.
- Null shear $\iota(\rho) = const$: this method avoids resonances by choosing $\iota \neq n^{'}/m^{'}$, where $n^{'}$ and $m^{'}$ are the most probable numbers of possible resonances. These kind of devices are called heliacs or helias.

A description like the one provided by Eq. 3.4 allows a Hamiltonian treatment of the problem. The equilibrium solutions should be provided by minimising δQ, the functional derivative of its potential energy, against localised interchange perturbations. A detailed description for obtaining an energy functional of a magnetic field whose topological

properties obey the magnetostatic equations

$$\nabla p = \vec{j} \times \vec{B} \tag{3.5}$$

$$\nabla \times \vec{B} = \vec{j} \tag{3.6}$$

$$\nabla \cdot \vec{B} = 0 \tag{3.7}$$

is given in [46], while a stability criterion is explored in [47]. The resulting variational principle for plasma stability is expressed as the condition

$$D_M(\rho) = D_W(\rho) + D_S(\rho) + D_I(\rho) + D_G(\rho) > 0 \tag{3.8}$$

which is called Mercier Criterion [48]. This expression includes terms for the contribution to stability for many of the stellarator characteristics mentioned above: magnetic well (D_W), shear (D_S), net currents (D_I) and geodesic curvature (D_G). The complete expressions for each term can be found in [49].

3.2.2 Magnetic well depth

Being Eq. 3.8 a widely accepted criterion when the confinement magnetic field of a new stellarator is conceived, it can be said that the four parameters are of capital importance when a new stellarator and its electromagnets are designed and built. For reasons that will be explained in the next subsection, one of the goals of the thesis has been the experimental test of the importance of magnetic well towards plasma stability. It follows that special attention to the definition of this quantity and its role on plasma stability is required.

Firstly, we define the vacuum magnetic well as a quantity that measures plasma stability against short perpendicular wavelength modes driven by the plasma pressure gradient [15] as

$$\widehat{W} = 2\frac{V}{\langle B^2 \rangle}\frac{\mathrm{d}}{\mathrm{d}V}\langle\frac{B^2}{2}\rangle \tag{3.9}$$

In Eq. 3.8 D_W is a term related with perturbations that interchange magnetic flux from one region of plasma with another one (interchange perturbations) [23]. The energy Q_M

inside a magnetic tube where the magnetic flux is constant ($\Phi = \vec{B} \cdot \vec{S}$) is

$$Q_M = \int \mathrm{d}\vec{r} \frac{B^2}{2\mu_0} = \int \mathrm{d}l S \frac{B^2}{2\mu_0} = \frac{\Phi^2}{2\mu_0} \int \frac{\mathrm{d}l}{S} \tag{3.10}$$

The perturbative change of this magnetic energy δQ_M is zero when the exchanged fluxes are equal.

On the other hand, the kinetic energy of a plasma volume is

$$Q_p = \frac{nTv}{\gamma - 1} = \frac{pv}{\gamma - 1} \tag{3.11}$$

As the perturbation is adiabatic, $pV^\gamma = \text{const}$ is conserved during the interchange process. This means that the change in the plasma energy can be written as a function of the initial pressures:

$$\begin{aligned} \delta Q_p &= \frac{1}{\gamma - 1} \left(p_2' v_2 - p_1 v_1 + p_1' v_1 - p_2 v_2 \right) = \\ &= \frac{1}{\gamma - 1} \left[p_1 \left(\frac{v_1}{v_2} \right)^\gamma - p_1 v_1 + p_2 \left(\frac{v_2}{v_1} \right)^\gamma - p_2 v_2 \right] = \delta p \delta v + \gamma p \frac{(\delta v)^2}{v} \end{aligned}$$

where we have considered $p_2 = p_1 + \delta p$ and $v_2 = v_1 + \delta v$. As the second term of δQ_p will always be positive, the stability condition $\delta Q_p > 0$ reduces to

$$\delta p \delta V = \delta p \delta \int \frac{\mathrm{d}l}{B} > 0 \tag{3.12}$$

In the outward direction, plasma pressure p usually decreases so the stability condition reduces to

$$\delta \int \frac{\mathrm{d}l}{B} < 0 \tag{3.13}$$

The *specific volume* for the volume V inside the magnetic surface ψ and the flux Φ in the toridal direction inside ψ is defined as

$$U \equiv \frac{\mathrm{d}V}{\mathrm{d}\Phi} = \frac{\int \sum_i (\vec{b} \cdot \vec{n})_i S_i \mathrm{d}l}{\sum_i (\vec{b} \cdot \vec{n})_i B_i \mathrm{d}S_i} \tag{3.14}$$

When the lines of magnetic force close upon a single circuit of the torus and the magnetic flux is conserved

$$U = \oint \frac{\mathrm{d}l}{B}$$

If the lines of magnetic force close after N circuits, then

$$U = \frac{1}{N}\int_N \frac{\mathrm{d}l}{B} \tag{3.15}$$

so the specific volume can be considered to be an average of $1/B$ and the dependence of U with B is inverse. Applying the stability condition for interchange instability from Eq. 3.13

$$\frac{\mathrm{d}U}{\mathrm{d}\Phi} = \frac{\mathrm{d}^2 V}{\mathrm{d}\Phi^2} < 0 \tag{3.16}$$

Returning to the definition given for the magnetic well in Eq. 3.9, a configuration has favourable stability properties if

$$p'(V)\hat{W} > 0 \tag{3.17}$$

We are primarily interested in configurations in which the pressure decreases away from the magnetic axis, so that $p'(V) < 0$. Thus, systems with negative magnetic well $\hat{W} < 0$ are favourable for confinement. Remembering that the mean value of the magnetic field can be written as $\overline{B} = \overline{L}\frac{\mathrm{d}\Phi}{\mathrm{d}V}$, the variation of the specific volume between the magnetic axis U_0 and the plasma edge U_a can be considered, which is called *magnetic well depth*

$$W = -\frac{\Delta U}{U} = \frac{U_0 - U_a}{U_0} \tag{3.18}$$

Defining W this way we can make clear that $\Delta U/U$ is subject to the stability condition that we found in Eq. 3.13: such systems tend to confine plasma in regions of lower B, suppressing pressure gradient driven instabilities, as they make it difficult for the plasma to move to the regions with higher B. An easier way to put it is remembering that B should grow in average on the outer regions of the magnetic vessel, opposing to the plasma's tendency to expand by bounding it to the magnetic field lines.

3.2.3 A stellarator: TJ-II

TJ-II is a heliac-type stellarator installed and operating at the National Fusion Laboratory (LNF) in CIEMAT, Madrid (see Fig. 3.7 a)). It was built between 1991 and 1996 and is the third magnetic confinement device hosted by this institute [50]. TJ-II consists of a toroidally directed central conductor, about which spirals a set of 32 toroidal field (TF) coils. It produces a bean shaped plasma whose magnetic axis follows the twisting

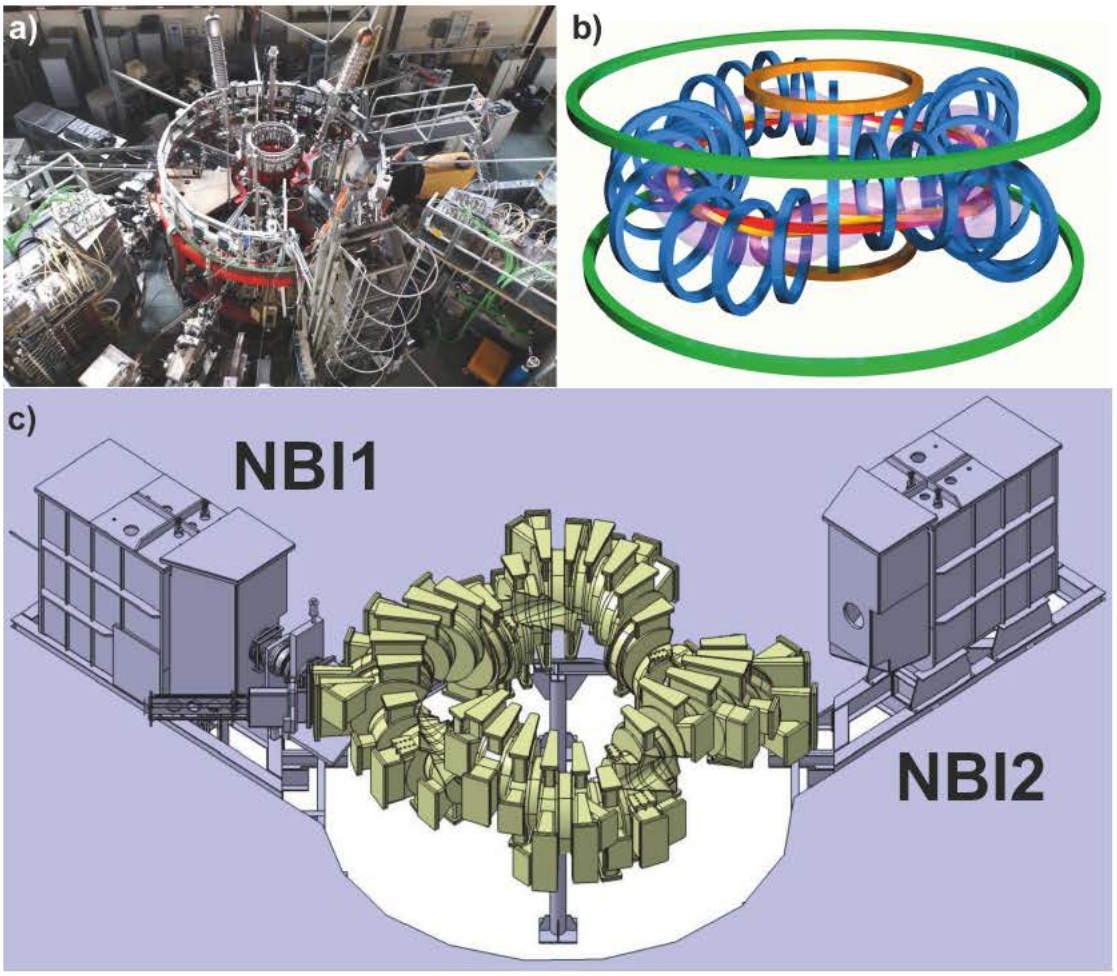

FIGURE 3.7: a) TJ-II top view. Photograph taken in 2013 by Boudewijn van Milligen. Credit: http://www.fusion.ciemat.es/tj-ii-2/virtual-tour/. b) TJ-II Coils. Red: central (CC). Yellow: helical (HC). Blue: toroidal (TF). Green: vertical (VF). Brown and green: radial (RC). Credit: http://wiki.fusenet.eu/wiki/TJ-II:Coil_system. c) TJ-II's vacuum vessel and the two NBI injectors. Left: NBI1 (co-directed); right: NBI (counter-injection). Credit: http://wiki.fusenet.eu/wiki/TJ-II:Neutral_Beam_Injection.

of the TF coils. The position of the plasma is controlled by two circular coils (VF) that add a vertical magnetic field of $\approx 5\%$ of the TF strength. The central conductor (hard core) consists of two parts: a circular coil (CC) centered at the major axis and an helical winding (HC) wrapped around it, responsible of the high degree of flexibility. A schematic drawing of each of these coils and the expected plasma is presented in Fig. 3.7 b). The currents in these windings can be controlled separately, which provides one of TJ-II's main characteristics: its flexibility, meaning the availability of a wide range of rotational transforms, while keeping a low magnetic shear [51]. Tab. 3.2 offers some general design and operational data of TJ-II.

TJ-II's flexibility translates in more than 100 accessible magnetic configurations, that

TJ-II Design Parameters	
Major radius R (m)	1.5
Average magnetic field B (T)	1
Resonant magnetic field at $\rho = 0$ (T)	0.95
Number of periods	4
ECRH power (kW)	2×300
NBI power (kW)	2×600
TJ-II Plasma Parameters	
Rotational transform at magnetic axis $\iota/2\pi$	0.96 to 2.5
Minor radius a (m)	0.10 to 0.25
Shear (%)	-1 to 10
Magnetic well depth (%)	0 to 6

TABLE 3.2: TJ-II's main parameters.

are labelled as a series of three numbers, indicating the absolute current (in hundreds of Amperes) in each set of coils: CC_HC_VF (the current through the TF coils is adjusted to provide the magnetic field $B_0 = 1$ T). We will use this notation extensively in Chapters 5 and 6. TJ-II was designed according with the Mercier criterion exposed in Eq. 3.8, but the very low shear and zero current leaves the stability to perturbations depending almost exclusively on the magnetic well and the geodesic curvature [52]. For TJ-II, the term D_W in Eq. 3.8 has a stabilising effect and D_G is always destabilising, so the stability criterion is, in fact, a competition between them.

TJ-II is capable of producing a plasma discharge of up to 1s (although often 0.25s discharges are used) every 5 minutes. Each of these pulses normally begins with an ECR heating phase with two 53.2 GHz gyrotrons that deliver ≈ 300 kW in the second harmonic of the X mode each [53]. Plasmas can reach densities around $1 \cdot 10^{19}$ m^{-3} with electron temperatures of about 1keV. There are two NBI injectors available for the following heating phase. They can produce ≤ 300 ms pulses of neutral hydrogen accelerated to 40 keV which is injected in the same direction with respect to the magnetic field in one of the cases (co-directed, NBI1) and in the opposite direction in the other (counter-injection, NBI2) [54]. The location of both injectors with respect to the vacuum vessel can be consulted in Fig. 3.7 c). Although TJ-II operation normally involves ECRH plasma breakdown and further heating as first discharge phases, some of the experiments carried out between 2014 and 2015 could use only NBI, being the injectors enough to create plasmas with reproducible parameters [55],

Chapter 4

Experimental techniques: Diagnostics

As in any experimental work several diagnostics have been necessary to provide data from the plasmas presented in this memory, both in JET and in TJ-II. Most of them are common to magnetic confinement devices, and the basics of their operation will be briefly explained as we present the data extracted from them along Part II. But in the course of this work, the manning and analysis of data from two plasma edge diagnostics, Langmuir probes and intensified fast visible cameras, has been of major importance. The present Chapter will provide some insight on the physical mechanisms behind these diagnostics, necessary for an informed analysis of the data extracted from them; and will put the specific systems used in this work in the context of the magnetic confinement devices where they are installed.

4.1 Fast imaging of plasmas

4.1.1 Recycling, atomic and molecular processes and visible radiation at the plasma boundary

In most tokamaks the pulse length is at least an order of magnitude longer than the replacement time. Thus, on average, each plasma ion goes to the divertor target plate and returns to the plasma a few times during the discharge. This process is called

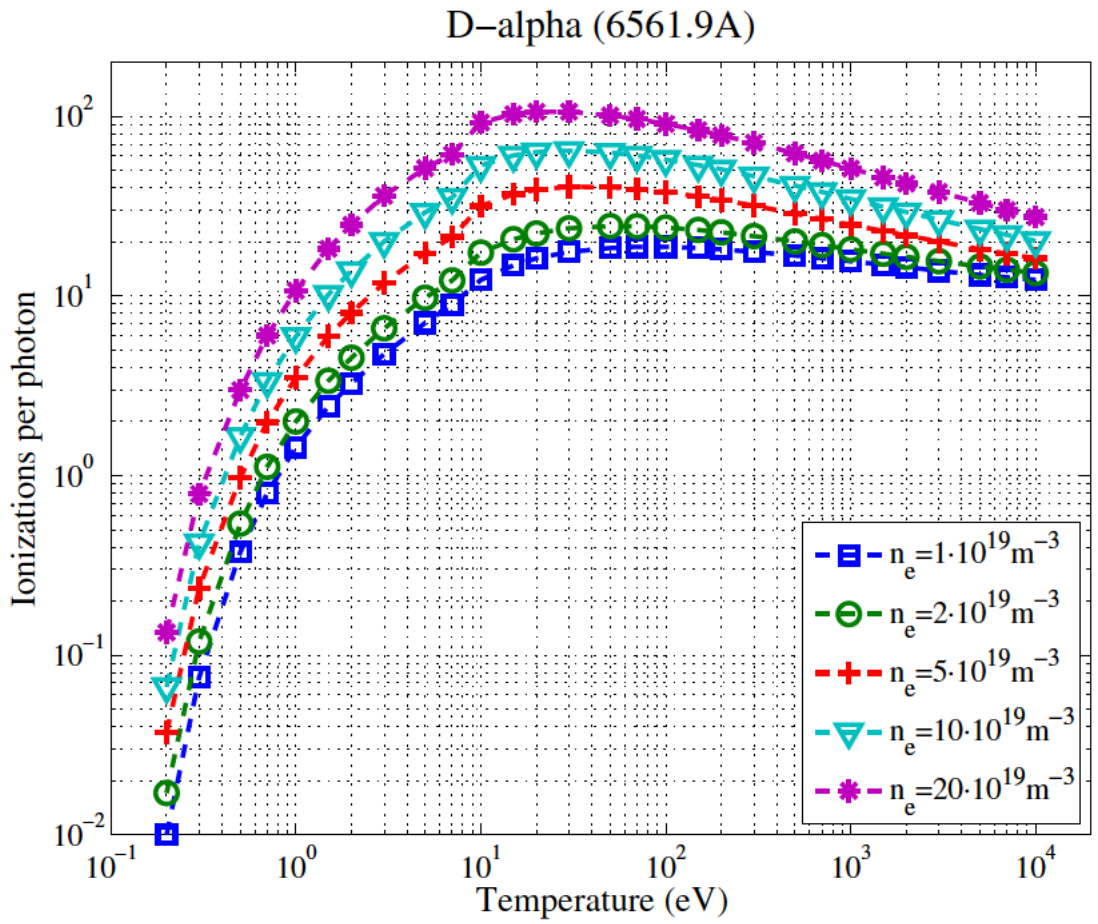

FIGURE 4.1: Ionizations per photon versus temperature for several densities in the D_α radiation wavelength ($\lambda = 6561.9$ Å). Data extracted from the Atomic Data and Analysis Structure (OPEN-ADAS) database http://open.adas.ac.uk/

recycling. Recycled particles normally enter the plasma as neutrals to be ionised again, but in divertor configurations most of the ionisation takes place in the vicinity of the target, making the process of re-trapping the recycled ions slightly more complicated than in limiter configurations.

Due to material defects, plasma fuel atoms can come to reside uniformly at the facing wall surface by diffusion, to be released from the surface as recombined molecules. The concentration of hydrogen in intrestitial sites $C(x,t)$ can be described as

$$\frac{\partial C}{\partial t} = D\frac{\partial^2 C}{\partial x^2} - k_{st}C(C_{T0} - C_t) + k_t C_t + S(x) \tag{4.1}$$

where D is the diffusion coefficient, C_t is the concentration of hydrogen in traps, C_{T0} is the concentration of traps, k_{st} is the rate coefficient for entering the traps, k_t is the thermal desorption coefficient and $S(x)$ is the range profile of the implanted ions.

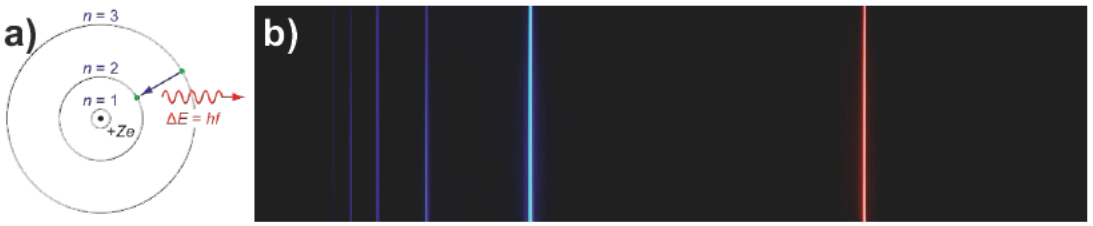

FIGURE 4.2: a) In the simplified Rutherford Bohr model of the hydrogen atom, the Balmer lines result from an electron jump between the second energy level closest to the nucleus, and those levels more distant. Shown here is a photon emission. Credit: JabberWork for www.wikipedia.org. b) The visible hydrogen emission spectrum lines in the Balmer series. H-alpha is the red line at the right. The two leftmost lines are considered to be ultraviolet as they have wavelengths less than 400 nm. Credit: Jan Homann for www.wikipedia.org.

In steady state, the ion flux to the solid is balanced by reflection (around 30% with Carbon and 60% for Tungsten) and by the recombination outflow. The latter gives place to atomic and molecular reactions, as the incoming hydrogen isotopes from the wall meet the energetic electrons and ions of the plasma boundary. The same applies to impurities, producing electronic excitations, ionisations and charge interchanges that lead to emission of radiation and cooling the edge of the plasma. The relative reaction rates of these processes are function of plasma density and temperature.

The neutral flux is given by

$$F(r) = F(a)\left(1 - \int_r^a \frac{n_e(r)\langle\sigma\nu\rangle}{\nu_0} dr\right) \tag{4.2}$$

where $F(a)$ is the initial flux and $\langle\sigma\nu\rangle$ is the reaction rate and can be determined by the local electron temperature and density. This means that the penetration into the plasma of recycled particles and impurities depends on its temperature and density.

The photon efficiency is the number of photons emitted in an atomic transition, like an ionisation. This amount is known for several species so absolute measurements of radiation enable the influx of ions to be directly calculated and related to temperature and density by Eq. 4.2. Both ionised impurities and recycled fuel emit photons as a result of their arrival to the plasma periphery. The analysis of such emissions can help to understand temperature and density at the plasma edge.

In the case of Hydrogen (or Deuterium), this recombination equilibrium results, in around 50% of the cases, in an ion being eventually excited by plasma collisions and undergoing a $3 \rightarrow 2$ transition (see Fig. 4.2 a)). This is the H_α transition, the first of

the well-known Balmer series, whose visible lines is shown in Fig. 4.2 b). The frequency of the emitted photon is described by the Plank relation $\Delta E = h\nu$ and can be calculated with:

$$\frac{1}{\lambda} = \Re\left(\frac{1}{n_f^2} - \frac{1}{n_i^2}\right) \tag{4.3}$$

where $\Re$ is the Rydberg constant and n_i, n_f are respectively the initial and final energetic levels. The inverse of the photon efficiency for Deuterium at different values of density and temperature is shown in Fig. 4.1.

4.1.2 Fast visible cameras and image intensifiers

As we have seen in the previous subsection, recycling and ionisation of impurities in the areas where the plasma is close to the facing wall, will emit visible photons, and the amount of these will be related with density and temperature. Also, the wall's parts physically touching the plasma, like the divertor and limiters, will be at a such high temperature that, according to the Wien displacement law

$$\lambda_{\max} = \frac{b}{T_{body}} \tag{4.4}$$

they will emit some light in the visible bandwidth. This emission is traditionally called the Blackbody radiation and involves the wavelength peak λ_{max}, the temperature of the material T_{body} and the Wien constant b. Therefore collecting this light, even if part of it doesn't come exactly from the plasma, looks like a non-invasive method to learn about density and temperature on plasma edge. Fast recording of these images, with and without H_α filters, has been used since the dawn of tokamak research [56].

The fast development that digital imaging has experienced in the last two decades has renewed the impulse on this kind of observations: commercial devices up to 10^6 frames per second of recording speed allow, nowadays, the recording of two dimensional fast events. This has led to the installation of fast cameras in Alcator C-Mod [57], NSTX [58], ASDEX-U [59], JET [60], TJ-II [61], LHD [62] or DIII-D [63]. The issues addressed by such devices goes from edge turbulence [64], dust [65, 66], disruption runaway electrons [67], electron temperature and density [61] or pellet ablation [59].

Additionally, fast tracking of specific impurity or Bremsstrahlung emissions requires the use of optical filters, that reduce drastically the amount of light delivered to the

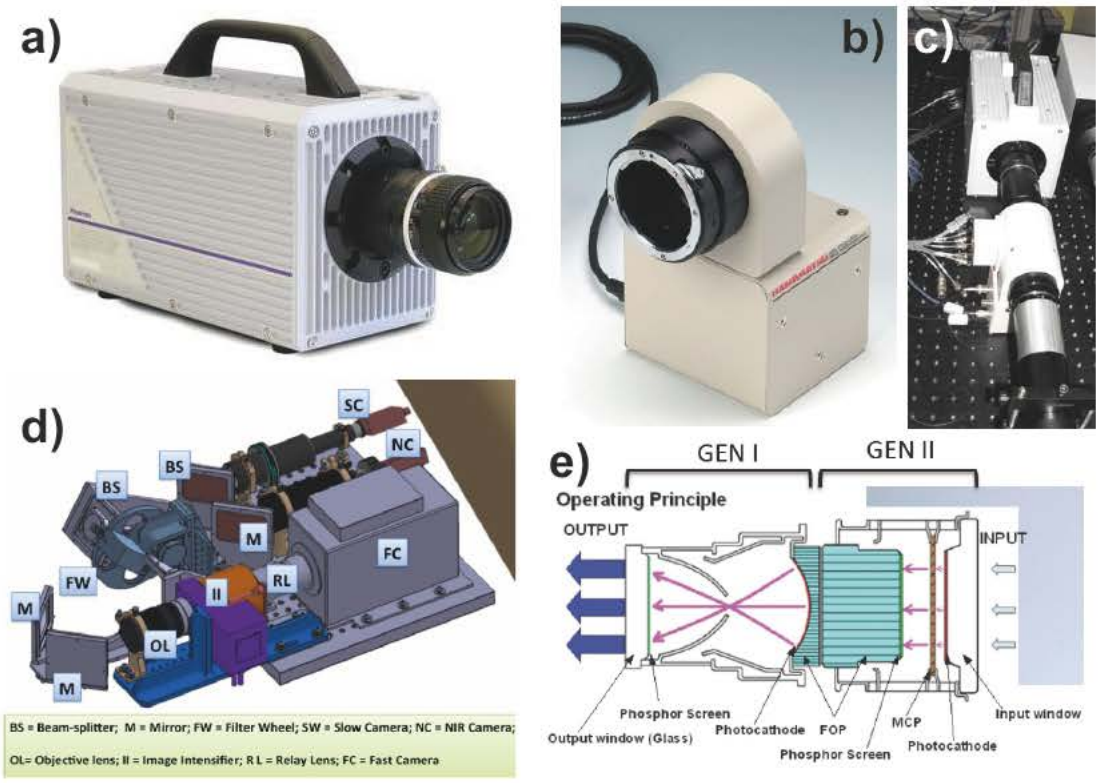

FIGURE 4.3: a) Photron Fastcam APX-RS. Credit: http://photron.com/. b) Hamamatsu Image intensifier unit C9548-03. Credit: http://www.hamamatsu.com/jp/en/C9548-03.html. c) Intensified fast visible camera as it is installed in TJ-II. Courtesy of Eduardo de la Cal. d) Schematic of the components and their distribution of the intensified fast visible camera at JET. Courtesy of Eduardo de la Cal. e) Two step II (Image Intensifier) operating principle. Courtesy of Eduardo de la Cal.

camera's sensor. Image intensifiers are devices capable of intensifying an image at high gain and high-speed gating. This makes them suitable to capture phenomena that occur in extremely short periods of time. These devices can increase the camera's sensitivity, allowing recording phenomena in the range of $1\mu s$ in low light conditions [61].

Digital imaging is, basically, the process of converting light into electric charge to be processed as an electronic signal on a sensor with the help of an appropriate optics. There are two technologies to take into account for this task:

- **CCD** (Charged Coupled Device) In these sensors pixels are represented by p-doped MOS (Metal Oxide Semiconductor) capacitors. These capacitors are biased above the threshold for inversion when image acquisition begins, allowing the conversion of incoming photons into electron charges at the semiconductor-oxide interface; the CCD is then used to read out these charges.

- **CMOS** (Complementary Metal Oxide Semiconductor) Consists of an integrated circuit containing an array of pixel sensors, each pixel containing a photodetector and an active amplifier. They reach higher speeds because of the relative ease of parallel readout of a voltage matrix when compared with the sequential charge-to-voltage required to acquire the CCD output.

It follows that CMOS technology is, at the moment, the most adequate for fast visible imaging. Also, its enhanced resistance against radiation damage makes these kind of sensors more adequate for our purposes, specially at JET.

In the course of these works two almost-twin intensified fast visible cameras have been manned: one in TJ-II [61] (see Fig. 4.3 c)), where basic training on the system has been implemented; and one in JET [60] (presented in Fig. 4.3 d)), where manning and experimental assistance has been provided between the campaigns C30 and C37. The technical specifications of the diagnostic are the same in both cases. The components of the diagnostic are the following:

- **Photron Fastcam APX-RS** (see Fig. 4.3 a)) Uses a 10-bit CMOS sensor (although it produces 8-bit videos) with 17 μm pixels. It can go up to 250 kHz with the sizing limitations presented in Tab. 4.1. It allows minimum exposure times of 1 μs. In our case, it has been used with a commercial camera lens of f1.4 and 135mm of focal distance.

Frame Rate (fps)	Max resolution (px W×H)	Max record (fr)	Max record time (s)
3000	1024×1024	2048	0.68
5000	768×768	3641	0.73
10000	512×512	8192	0.82
30000	256×256	32768	1.09
100000	384×48	116508	1.16
250000	128×16	1048576	0.42

TABLE 4.1: Frame rates and resolutions available for the Photron Fastcam APX-RS. Credit: http://photron.com/.

- **Hamamatsu Image intensifier unit C9548-03** (see Fig. 4.3 b)) It is a two-step II (Image Intensifier) suitable for high speed cameras. It can provide luminous gain of around $3.3 \cdot 10^3$. Fig. 4.3 e) provides a diagram of the operating principle of these devices: photons are converted into electrons in a photo cathode by photoelectric

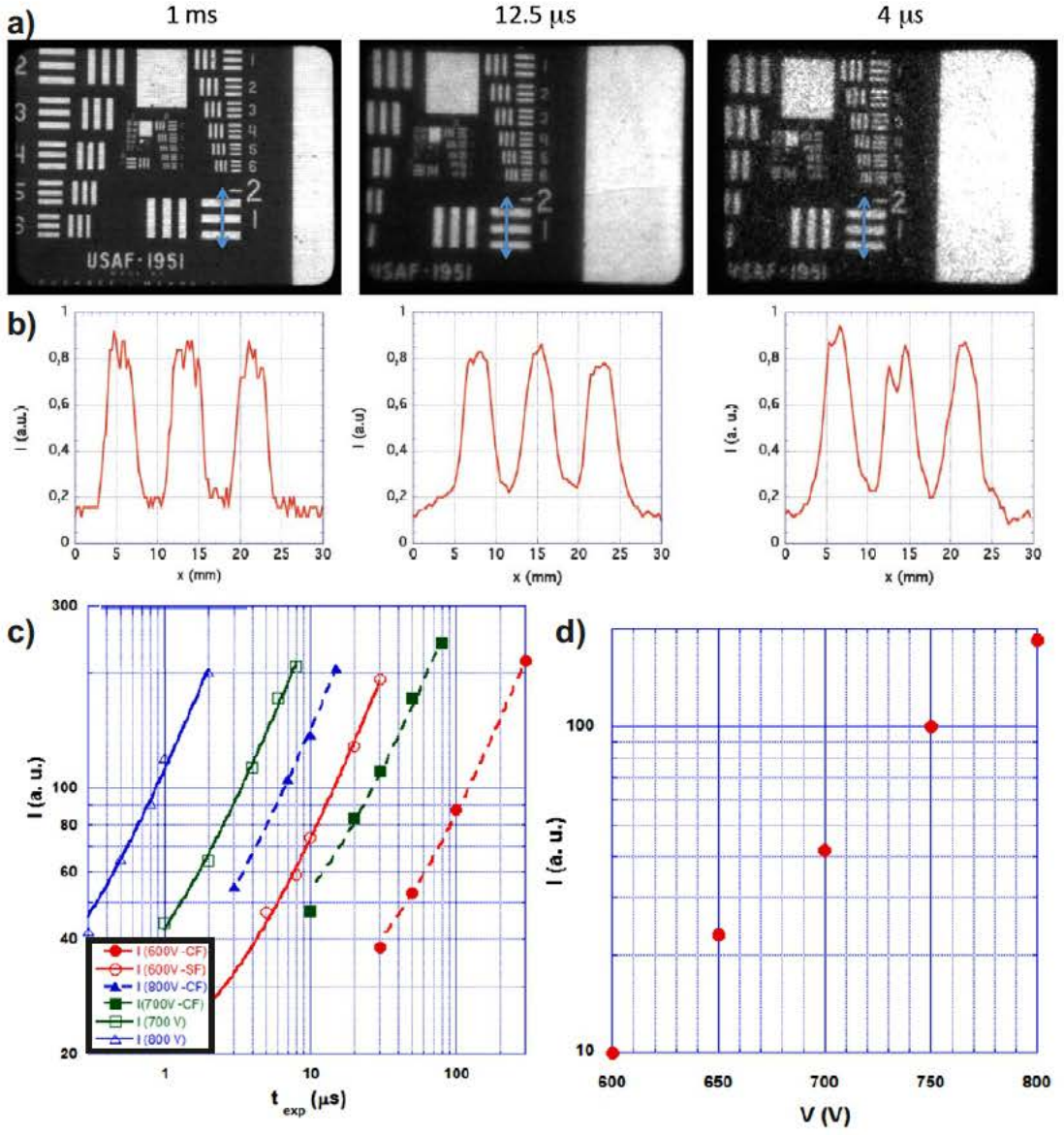

FIGURE 4.4: For the II installed on TJ-II: a) Test target images without II (left), and with intensifier at 700 V (centre) and 800 V (right). b) Intensity profiles along the vertical arrows crossing the three horizontal stripes of the upper images. c) Response curves for three possible values of voltage at the II vs. exposure time. The signal level was the mean value of the histogram obtained of a same rectangle of the image containing about 1000 pixels for all the different conditions. Linear regression coefficient is higher than 0.997 in all the cases. c) Camera output signal as a function of the II voltage V. The dependence is exponential and the gain rises by a factor of 20 when increasing the voltage from 600 V to 800 V. Courtesy of Eduardo de la Cal.

effect and then emitted to be subjected to a multiplying electric field. The resulting electrons, finally, hit a phosphor screen so they are converted back into photons. All these processes imply the loss of a fraction of the initial light signal, but the final value is greatly increased (see examples and the behaviour of gaining in Fig. 4.4, from [61]).

- **Filter wheel** Both systems make use of bandpass filters to track impurities, puffing gases or Bremsstrahlung emission. Changing them in TJ-II is simple, but the access protocol to the torus hall in JET is much stricter, so filters are available through a remotely controlled filter wheel. Filters can be exchanged via a Newport NCS200 engine from one pulse to another. A list of the used filters is provided in Tab. 4.2

Species	Wavelength (nm)	FWHM (nm)	Transmission (%)
D_α	656.19	1.00	55
Be II	527.10	1.00	55
Bremsstrahlung	538.35	3.00	61.61
Ar II	610.90	1.00	55

TABLE 4.2: Optical filters used for the fast visible camera at JET. See https://www.andovercorp.com/products/bandpass-filters/semi-custom-bandpass-filters/ for more information.

4.1.3 Visible light in JET: KL8A

A fast visible camera was installed on JET in 2007 [60] and, during the shutdown required to the installation of the ILW (see Subsec. 3.1.5) the system was upgraded with the image intensifier (II) and a filter wheel [68]. According to JET's naming system, it is normally tagged as KL8A, and this is how we will refer to the intensified fast visible camera at JET from now on. Fig. 4.5 is devoted to location of KL8A: at JET's octant 8, using a midplane endoscope (named KL7 WAV in Fig. 4.5 a) and shown in the b)-c) panels). This way, the divertor, one inner limiter and three outer ones can be seen when the larger available frame is considered (panels d) and e)). As the size of the limiters, antennas and the distance between the inner and the outer wall is known, the matching shown in Fig. 4.5 e) can give us an idea of the spatial resolution of KL8A with the optics currently installed:

$$1 \text{ px}^2 \approx 4 \text{ cm}^2 \tag{4.5}$$

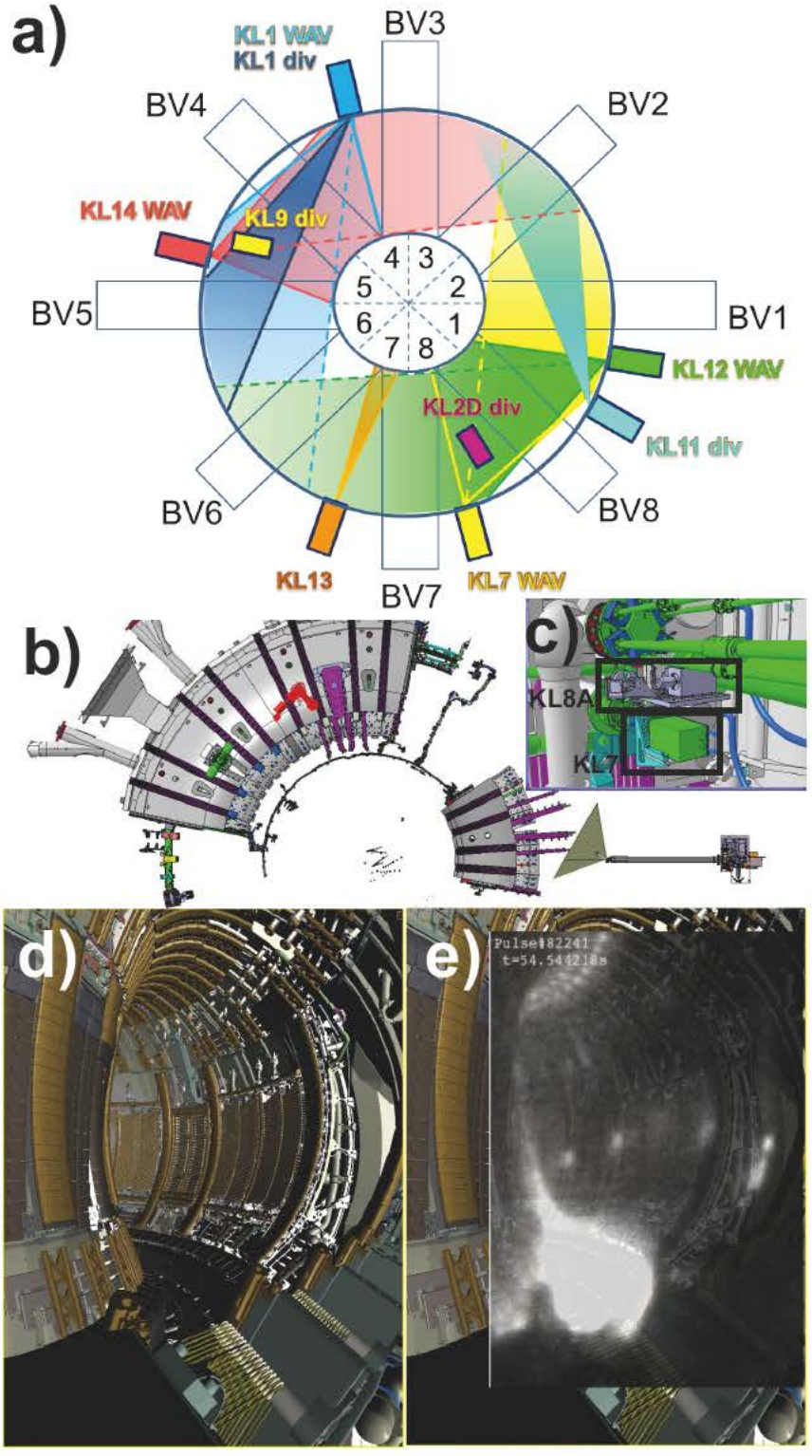

FIGURE 4.5: a) Schematic representation of the viewing systems fields of view. KL8A is installed on the KL7 endoscope. Credit: Valentina Huber. b) KL7 endoscope at JET-ILW. Courtesy of David Price. c) Close up of KL8A's system. d) Wide view of JET's ILW from the KL7 endoscope, at octant 8. Credit: http://users.euro-fusion.org/openwiki/index.php/JET_viewing_systems. e) Frame from KL8A superimposed to the model from c).

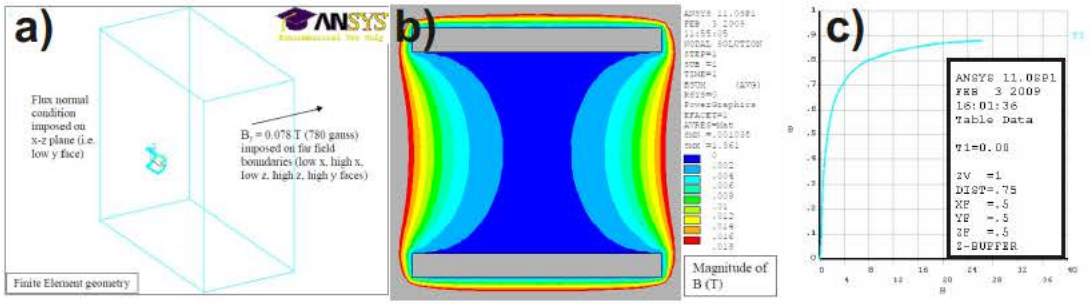

FIGURE 4.6: Design of a magnetic shield for JET's II. a) Finite element problem in ANSYS. b) Contour plot showing magnetic field inside shielded region on x-z plane. c) Magnetisation Curve for MμShield. Courtesy of Eduardo de la Cal.

for naked lens recording (where *px* stands for *pixel*). Filters introduce extra noise, reducing the spatial resolution.

The installation of the II implied an extra detail to keep in mind. TJ-II's II, as it was shown in Fig. 4.3 c), is mounted on an optical table more than one meter away from the vacuum vessel, enough not to consider the machine's magnetic fields. This is not the case in JET, where the II will experience a magnetic field of around 0.7 Tesla during operation, not to mention the sudden changes in plasma current that occur during disruptions (see Fig. 3.5 a) for an example). As we explained in the previous Subsection, the GEN I of the II consists of a portion of space where electrons are accelerated by an electric field between two plates (Fig. 4.3 e)): if an extra magnetic field is applied, Lorentz Force acts, twisting the electron's trajectory. This translates as a rotation in the produced frames, specially during disruptions (for more information about how to correct this effect see Appendix A.4). To avoid (partially) this effect a magnetic shield was designed using ANSYS to be built in μ-metal (see Fig. 4.6).

Since its installation, KL8A has performed as a promising diagnostic for the following experimental fields at JET-ILW:

- **Breakdown studies** Although the amount of emitted light in this stage is low, KL8A can provide 1-10kHz 2D information about the evolution and position of the forming plasma [69]. See Fig. 4.7 a).
- **Disruption mitigation** Filtered and unfiltered data of mitigation gas injection during the disruption can be recorded at a maximum speed of 22kHz. These results will be explored more deeply in Sec. 7.3.

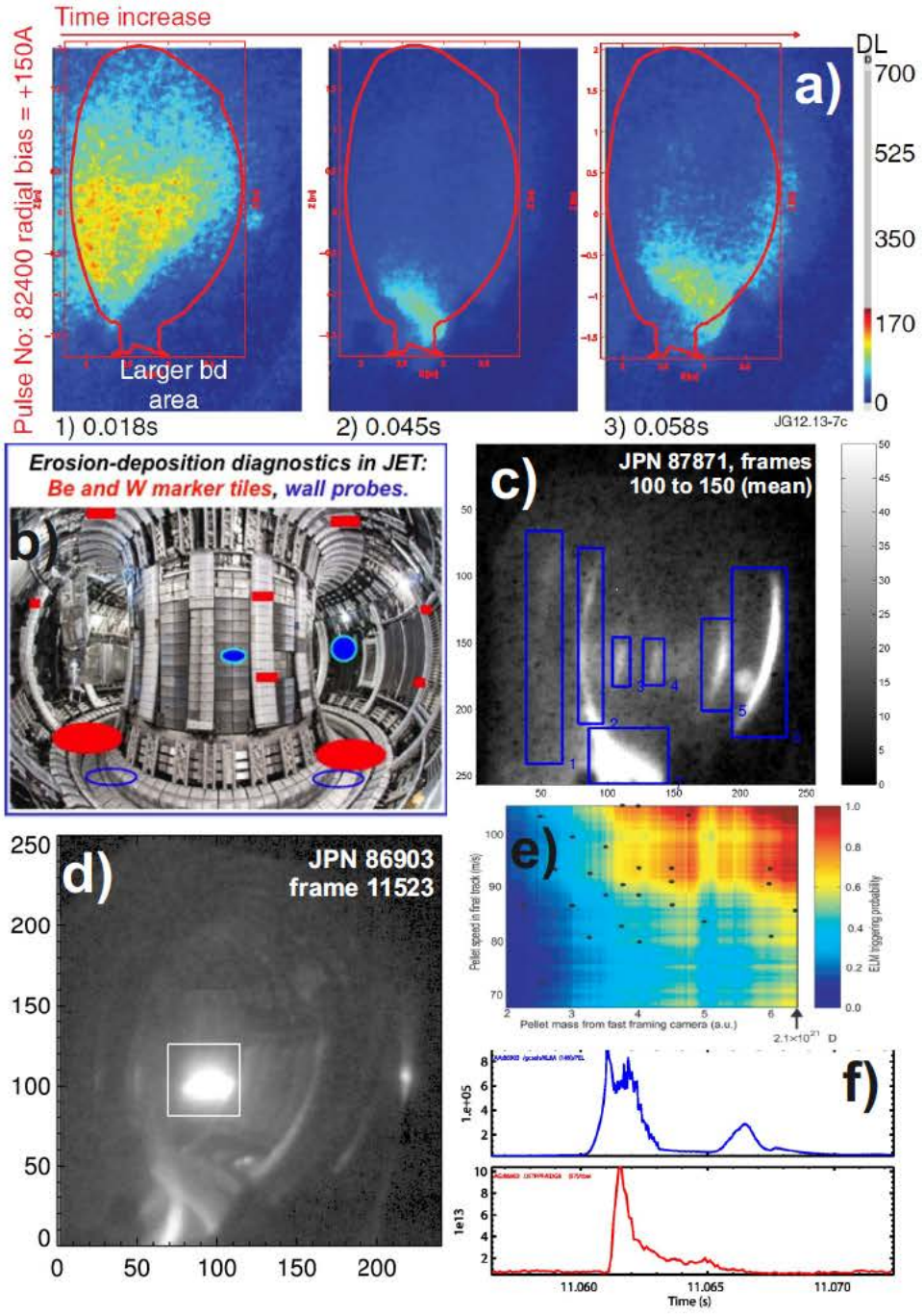

FIGURE 4.7: Some examples of the use of KL8A in the course of the experimental campaigns in JET-ILW. a) Analysis of a standard breakdown presented by Albanese *et al* in NF 52 (2012). KL8A can provide unfiltered data of the position of the plasmoid cloud in the initial stages of a JET pulse. b) A number of diagnostics can trace Beryllium in JET-ILW c) and KL8A can provide filtered images to track this material, for example, when the ICRH antennas are used. d) Image of a pellet entering the plasma. f) KL8A has an uncanny ability to detect the arrival of pellets, as they are injected directly in front of its field of view, and the fast framing allows to catch their ablation process. e) Pellet (pacing size) ELM triggering probability as a function of pellet speed and mass. The triggering probability approaches unity for pellets approaching the initial design values. Taken from Lang *et al* NF 53 (2013)

- **Beryllium sources and transport** The understanding of material migration, and thus the dynamical process of material erosion, transport and deposition, is one of the key issues for the safe operation of future fusion reactors. In JET-ILW, deposition and fuel inventory are strongly reduced (by a factor of 20) in comparison to JET-C, while Be is the main element of co-deposits in the divertor. Extensive work on the obtention and analysis of BeII filtered data has been performed. See Fig. 4.7 b)-c).

- **ELMs in the divertor** The two dimensional data provided by KL8A can be used to help modelling the particle and impurity sources in the divertor during ELMy phases. The diagnostic can achieve speeds higher than 30kHz for this task. Extensive analysis of this data will be presented in Sec. 7.2.

- **Pellet monitoring** KL8A is one of the few diagnostics in JET that can confirm that injected pellets have actually reached the plasma. This allows to check pellet integrity and ELM triggering as a consequence of injection [70]. See Fig. 4.7 d)-f).

- **Hot spot tracking** Analysing evolution in time of light emitted by the outer wall poloidal limiters can help to identify and prevent hot spots in the inner vessel.

4.2 Langmuir probes

When considering measuring electrostatic properties of a plasma at its edge, Langmuir probes come as the conceptually simplest approach that one can think of: touching it with an electrode. Normally this is done with an array of various electrodes (or pins, as we will call them from now on) to be inserted at known positions of the plasma edge. When doing this, quasineutrality, as we defined it in Sec. 2.1, needs to be kept. So this probes' operating principle is based on the I-V characteristic of the current flowing into the pin's surface in contact with the plasma as a function of the potential drop in the Debye sheath [71].

There are two basic quantities that we can measure with Langmuir probes:

- **Ion Saturation Current** I_{sat} When a large negative potential V is applied to the pin, the total current into the probe's wall

$$I = \frac{1}{2} A e n_p \sqrt{\frac{T_e}{m_i}} \left[\sqrt{\frac{m_i}{2\pi m_e}} \exp\left(\frac{eV}{T_e}\right) - 1 \right] \tag{4.6}$$

  becomes

$$I_{i,sat} = \frac{1}{2} A e n_p \sqrt{\frac{T_e}{m_i}} \tag{4.7}$$

  where A is the area of the pin in contact with the plasma.

- **Floating potential** V_f If the pin is unbiased (without extra current), simply left to float electrostaticalty, won't exactly measure the plasma potential (V_p) due to the electric field generated in the sheath. The measured potential is normally negative, as electrons have higher mobility to reach the pin faster than the ions. To obtain a relationship between the measured V_f and the plasma potential, one has to consider that the ion and electron current cancel each other:

$$V_f - V_p = \frac{T_e}{e} \ln\left(\frac{1}{2}\sqrt{\frac{2\pi m_e}{m_i}}\right) \tag{4.8}$$

  which leads to the common approximation $V_f - V_p \approx -3.3\frac{T_e}{e}$ in the sheath. Plasma potential can only be measured via floating potential if the electron temperature is known.

When arrays of these pins are used in several poloidal and radial positions, extra quantities can be obtained:

- **Drift velocity** $v_{E\times B}$ As we defined it in Eq. 2.7, depends on the electric and magnetic fields. Given that $\vec{E}(\vec{r}) = -\vec{\nabla} \cdot V(\vec{r})$, several poloidal or radial measurements of the floating potential will allow us to extract the potential's gradient without needing to know the electron temperature (we assume that the temperature gradient is much smaller than the potential one).

- **Fluctuating** $\vec{E} \times \vec{B}$ **flux** Γ Given that $\Gamma = \frac{\tilde{n}\tilde{E}_\theta}{B}$, substituting Eq. 4.7 and neglecting the incluence of electron temperature fluctuation,

$$\Gamma = C_I \frac{I_{sat}}{B} \frac{\tilde{V}(\theta_2) - \tilde{V}(\theta_1)}{d_\theta} \tag{4.9}$$

where C_I may be considered constant as long as the electron temperature doesn't change abruplty and d_θ is the distance between two poloidally separated values of the floating potential.

- **Electron density gradient** ∇n_e Again, when clearing n_e from Eq. 4.7 and we consider two different radial positions, we can deduce the density gradient:

$$\nabla n_e = C_I \frac{I_{sat}(\rho_{outer}) - I_{sat}(\rho_{inner})}{d_\rho} \tag{4.10}$$

where C_I is, again, constant as long as T_e is so and d_ρ is the radial distance between the two values of saturation current.

4.2.1 Langmuir arrays in TJ-II

During the course of these thesis, Langmuir probes have been a key diagnostic for our research in TJ-II. Two access points are available for Langmuir probe arrays in TJ-II, at almost opposite toroidal positions (see Fig. 4.8 a)-c)) [72]. Four different arrays have been used at these positions:

- **Bottom - 2D** (See Fig. 4.8 d)) This was the array installed at the bottom position between 2012 and 2013. It provided two floating potential profiles with four points each and a third one (central) with six pins. $d_\theta = 2$ mm and $d_\rho = 3$ mm.
- **Top - 2D** (See Fig. 4.8 e)) It was installed between 2012 and 2013 and then, again, in mid-2015. It provided two V_f profiles of five pins each and a three pin profile of I_{sat} (central). $d_\theta = 3$ mm and $d_\rho = 5$ mm. This is the only array that has allowed us reliable extraction of particle flux and density gradient values.
- **Bottom - Rake** (See Fig. 4.8 f)) Installed from 2013 in advance, this array provided one single eight-point V_f profile with a really small spatial resolution $d_\rho = 1.7$ mm
- **Top - Rake** (See Fig. 4.8 g)) This array was installed between 2013 and 2015. It provided ten radial points of V_f and the possibility to measure I_{sat} and two poloidal positions of V_f to extract Γ and ∇n.

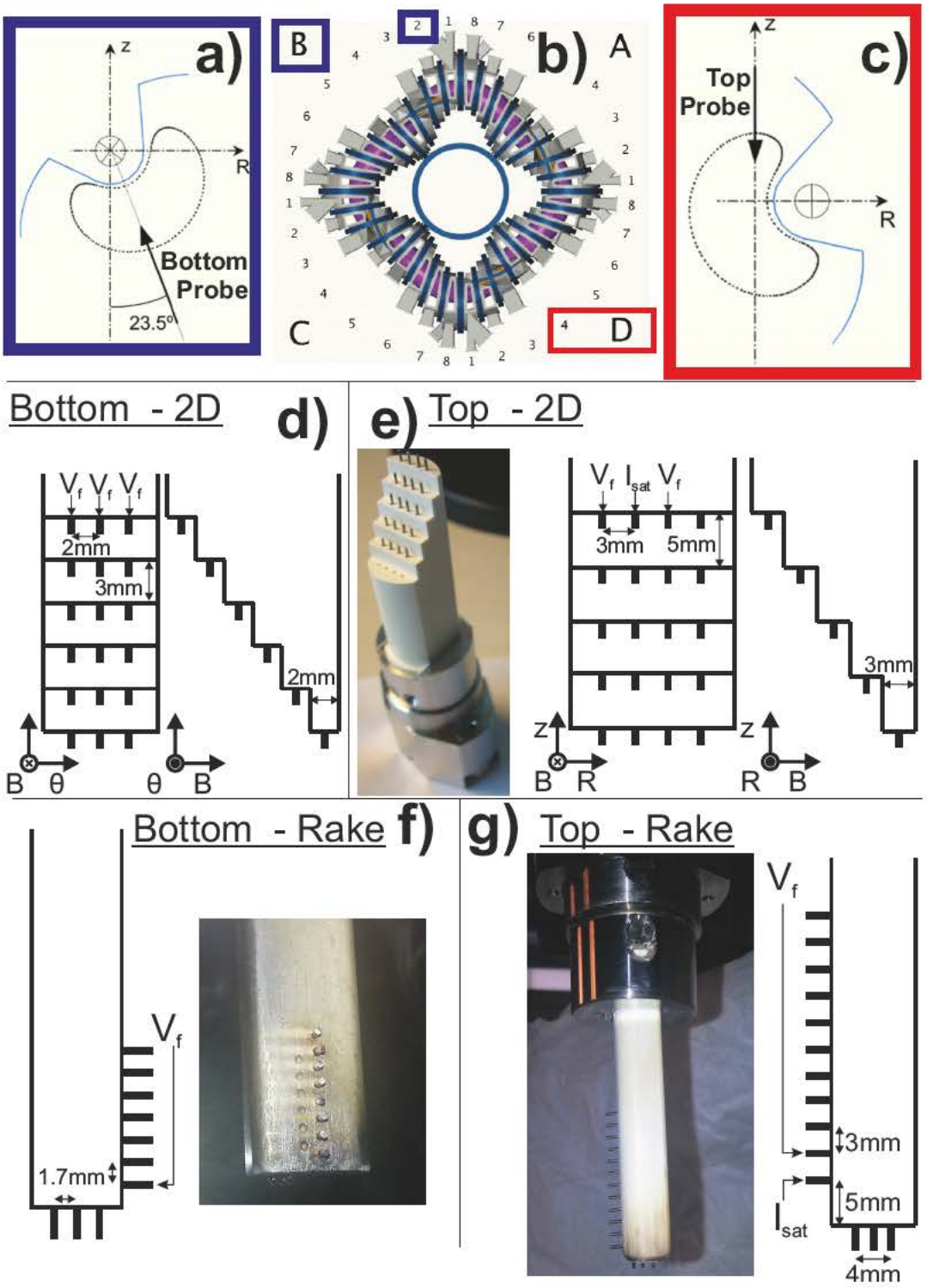

FIGURE 4.8: Langmuir probe arrays in TJ-II. a) Bottom probe access position at $\phi = 195°$. b) Schematic top view of TJ-II with the sector positions and the probe locations in red an blue. c) Top probe access point at $\phi = 38.2°$. d) Basic scheme of the 2D probe installed at the bottom position. d) Basic scheme and photography (before installation) of the 2D probe installed at the top position. e) Basic scheme and photography (installed) of the rake probe installed in the bottom position. f) Basic scheme and photography (after removal) of the rake probe installed on the top position.

The array's position can be modified from one shot to another, although reciprocating capabilities haven't been used in this work. Each pin's absolute position in TJ-II's vacuum chamber can be related to a normalised radial position in the plasma using VMEC simulations [73] to extract the closed field lines for the configuration in use.

Part II

Results

Chapter 5

Magnetic Well scan in TJ-II [1]

5.1 Description of the experiment

The magnetic well scan experiment consists in the exploration of plasma performance in situations with, theoretically, Mercier-unstable magnetic well conditions in order to quantify, experimentally, the relevance of this parameter in future stellarators. The questions this experiment attempted to answer and the strategies followed to pursue such answers are the following.

1. Can stable and reproducible plasmas be obtained when the magnetic well depth is reduced, even to negative values at the plasma edge (magnetic hill) and theoretically Mercier-unstable situations? For that, two sets of configurations with decreasing magnetic well have been designed and explored. Fig. 5.1 rows 1-2 outline the basic properties of the magnetic configurations involved in each family.

2. How does magnetic well affect the quality of confinement, defined by stored energy and energy confinement time?. A set of diamagnetic loops has been used to measure the stored energy [75] and compute experimental values of τ_E. Should the magnetic well be taken into account when scaling laws like the ISS04 presented in Eq. **??** are computed?

3. Are there any effects on electromagnetic turbulence when the magnetic well is reduced?. Edge electrostatic and magnetic turbulence has been measured using

[1] This chapter contains and extended version of the results published in [74]

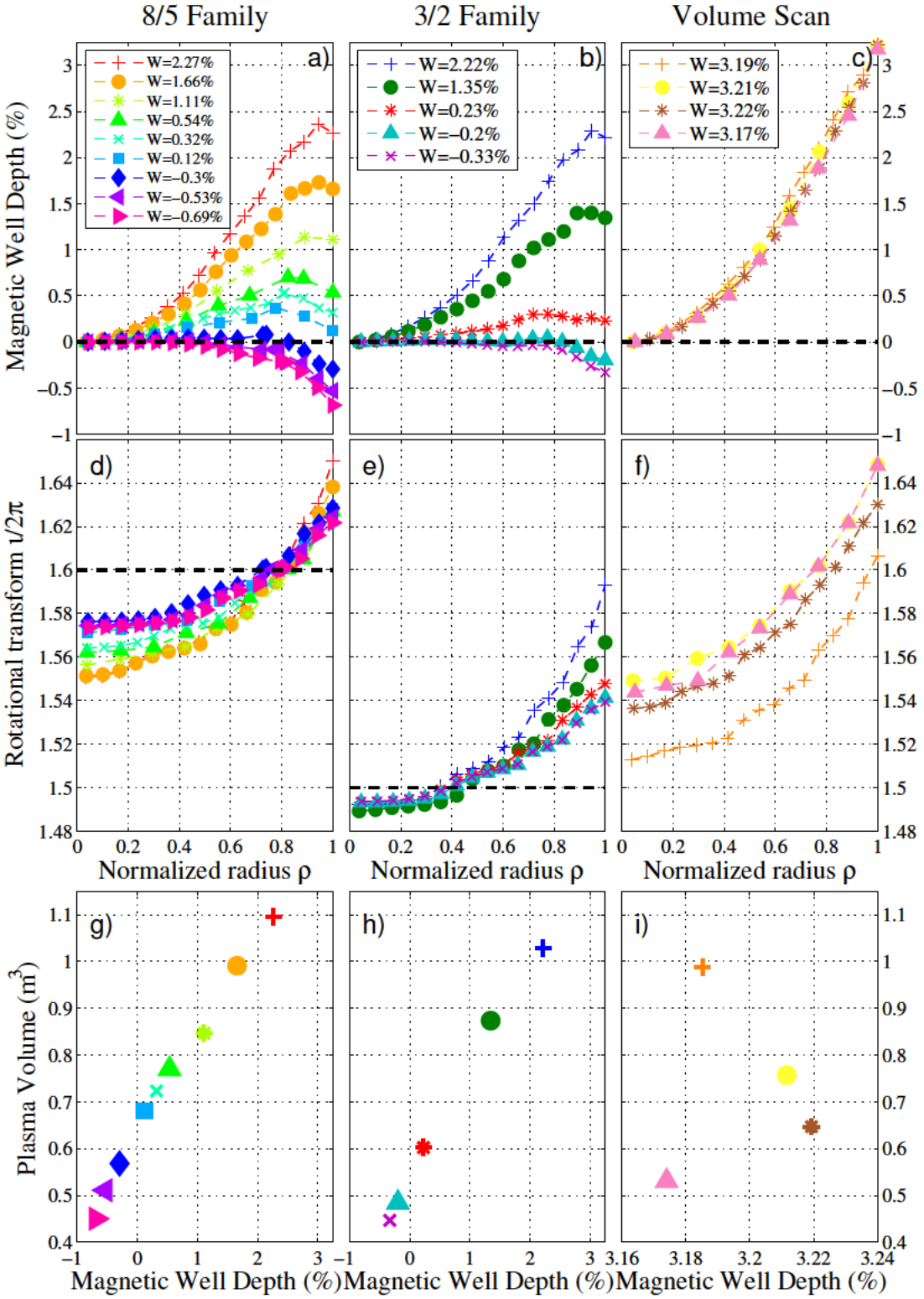

FIGURE 5.1: Magnetic well depth (row 1) and rotational transform (row 2) profiles for the three magnetic configuration families explored during the magnetic well scan experiment. Each column represents a group of magnetic configuration. Plasma volume against magnetic well is represented for each family in row 3.

Langmuir probes [76, 77]. Mirnov coils, Doppler reflectometer, bolometer arrays and HIBP characterised turbulence in the inner regions.

4. Is it possible to separate any effects observed during the magnetic well scan from the unavoidable decrease in plasma volume it implies?. Fig. 5.1 g) and h) prove that, in TJ-II, reduction of magnetic well depth at the edge involves a drastic decrease in plasma volume. A third family of magnetic configurations (Fig. 5.1 column 3) was designed to explore the effects of reducing plasma volume while avoiding any effect on their magnetic well profiles.

5. Can flux-gradient relationship at plasma edge be affected by the changes in the magnetic confinement configuration?. Again, a Langmuir probe array as the one described in Sec. 4.2, where radial measurements of floating potential and saturation current, has allowed measurement of fluctuating values of $\vec{E} \times \vec{B}$ flux and electron density gradient along plasma edge.

The experimental steps here described will be explained profusely in the following sections. First of all, a deeper consideration of the magnetic confinement configurations chosen for the magnetic well scan experiment is in order. From now on, we will refer to the magnetic well depth (as it was defined in Eq. 3.18 from Subsec. 3.2.2) simply as *magnetic well* or W.

5.1.1 8/5 Family

When the magnetic well scan was first planned (early 2013), a family of magnetic configurations was chosen so that, using the so-called 'standard configuration' for TJ-II (labelled as 100_44_64, as we explained in Subsec. 3.2.3) as a reference, the magnetic well depth was reduced from a fully Mercier-stable situation to magnetic hill conditions (Fig. 5.1 a)). Nine magnetic configurations were chosen to exhibit a rational value of their rotational transform profiles around $\rho \approx 0.8$, just like the 100_44_64 configuration has. Being this value $n/m = 8/5$ (Fig. 5.1 d)), we came to call this set '8/5 Family'.

Using configurations with similar ι profiles guarantees that any change in the plasma's properties can be attributed to the magnetic well. In this particular family, locating the rational near the plasma edge also had the objective of exploring the effects of magnetic well on stability using Langmuir probes.

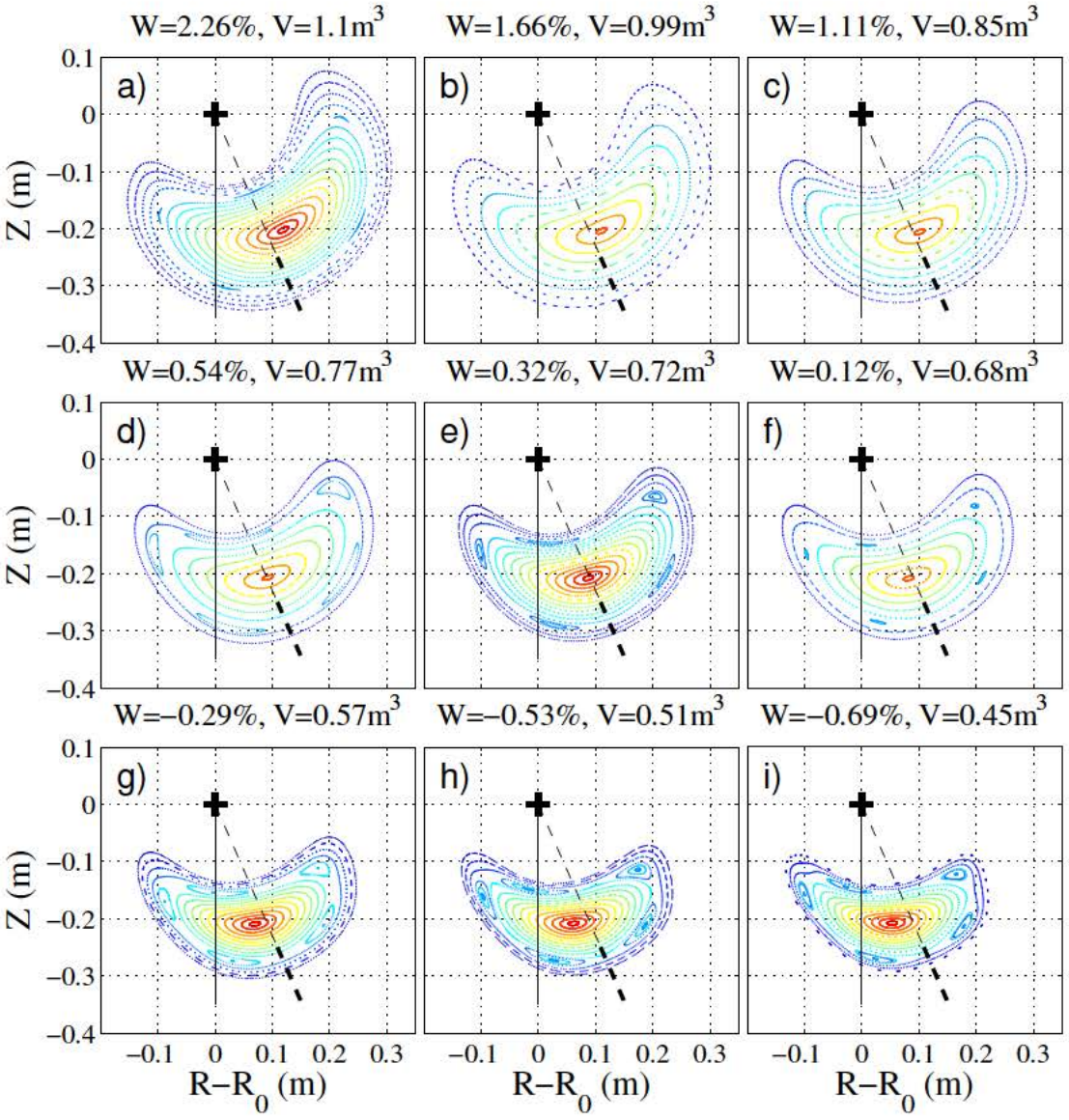

FIGURE 5.2: Magnetic field lines for the 8/5 Family at the $\phi = 15°$ toroidal position. The magnetic island is created artificially by introducing a magnetic perturbation. The dotted line represents one of the Langmuir probes trajectory.

Technical details of each of the nine magnetic configurations forming it can be found on Table 5.1. Although TJ-II operators commonly characterise any magnetic configuration by its maximum magnetic well depth (Tab. 5.1 column 7), in this work we will use its value at the plasma edge to name configurations (column 6) for explanatory reasons (to remark the importance of the cases where magnetic well becomes negative around plasma edge, as it was already used in Fig. 5.1 a) and b)).

Fig. 5.2 shows the Poincaré plots of the magnetic field lines of the nine configurations of the 8/5 Family at the toroidal slice $\phi = 15°$, which is the angular position where one of the Langmuir probes (the one at the bottom access point) is located (as explained

Label	$-I_{CC}$	$-I_{HC}$	I_{TF}	I_{VF}	$W_{\rho=1}$	W_M	V (m^3)	R (cm)
100_44_64	10.028	4.413	27.307	6.437	2.27	2.40	1.096	19.3
100_44_70	10.002	4.403	27.250	7.026	1.66	1.70	0.991	18.3
100_44_77	9.982	4.390	27.186	7.688	1.11	1.10	0.867	17.1
100_44_84	9.955	4.380	27.127	8.350	0.54	0.70	0.771	16.1
099_44_87	9.946	4.372	27.098	8.686	0.32	0.54	0.723	15.6
099_44_90	9.937	4.374	27.069	9.021	0.12	0.35	0.680	15.2
100_43_99	10.018	4.293	27.069	9.900	−0.30	0.04	0.568	13.9
100_42_104	10.006	4.181	27.134	10.400	−0.53	0.02	0.511	13.1
100_41_109	9.995	4.069	27.200	10.900	−0.69	0.00	0.450	12.3

TABLE 5.1: 8/5 Family Technical characteristics. Electric current values (columns 2 to 5) in kA, magnetic well depth is expressed in % at the plasma edge (column 6) and at its maximum value (column 7). All the data were obtained by g3d simulations and they are used as operation guide in TJ-II http://intranet-fusion.ciemat.es/fileshare/TJII_operation_documents/_ConfigurationData/Datos_de_Operacion_20140623.pdf.

in Sec. 4.2). Fig. 5.1 g) and Fig. 5.2 show how plasma volume falls in the most Mercier-unstable cases: the configuration with the lowest magnetic well, 100_41_109, not only is less than half of the standard configuration in size; but exhibits a different, less symmetric, shaping as well. As it was pointed in Subsec. 3.2.2, this deformation of the magnetic field lines is intimately related with the decrease in the magnetic well depth.

5.1.2 3/2 Family

Label	$-I_{CC}$	$-I_{HC}$	I_{TF}	I_{VF}	$W_{\rho=1}$	W_M	V (m^3)	R (cm)
101_38_62	10.055	3.821	27.379	6.209	2.22	2.20	1.031	18.7
101_38_71	10.103	3.773	27.323	7.139	1.35	1.40	0.874	17.2
102_37_90	10.199	3.677	27.210	9.000	0.23	0.30	0.602	14.7
104_35_100	10.352	3.525	27.149	10.000	−0.20	0.04	0.485	12.8
104_35_104	10.413	3.464	27.125	10.400	−0.33	0.00	0.447	12.3

TABLE 5.2: List of magnetic configurations forming the 3/2 Family and their technical characteristics.

The next step in the experiment was the examination of a new different family of magnetic configurations (Fig. 5.1 b)) with a different choice of rotational transform profiles (Fig. 5.1 c)). In this family the five configurations exhibit a rational value of $\iota = n/m = 3/2$ near $\rho \approx 0.4$, so we will call it the '3/2 Family'. This second set of magnetic configurations isn't as extensive as the 8/5 Family because the goal we wanted to achieve by exploring them wasn't proving the viability of the lowest magnetic well configurations which, as we will show in the following sections, had already been probed by

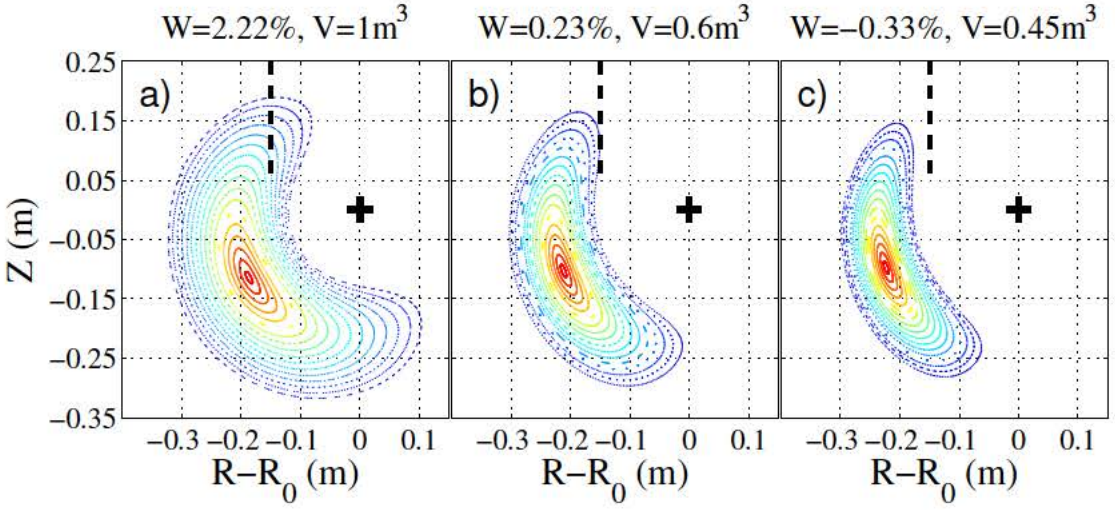

FIGURE 5.3: Poincaré plots of magnetic field lines for three selected configurations from the 3/2 Family at the $\phi = 37.5°$ toroidal position. The dotted line represents one of the trajectory of the other Langmuir probe, 'Top', located at sector D.

the 8/5 Family; but to explore the relationship between magnetic well, magnetic island location, and plasma performance. Tab. 5.2 summarises the technical characteristics of the configurations involved in this second magnetic well scan.

Fig. 5.3 depicts the magnetic surfaces for three of the five configurations in this family. The chosen section is, in this case, the toroidal position of the Langmuir array installed in TJ-II's top probe at top access point (see Fig. 4.8 from Subsec. 4.2.1) to point out the difference between the data acquired with this probe and the one obtained using the bottom probe. Here we can see again how decreasing the magnetic well depth does not only affect plasma volume, but actually deforms its shape. Fig. 5.2 proves that such deformation doesn't affect the bottom array's ability to access the plasma's outer region; while Fig. 5.3 c) makes clear that when the magnetic well is dramatically low, the top array is unable to physically touch the plasma. This situation happens both for the 8/5 and the 3/2 families and is crucial to understand and interpret any data obtained from the probe arrays installed in this position.

5.1.3 Volume scan

Finally, the experimental scheme was completed by mid-2015 with the exploration of a set of four magnetic configurations with very similar and Mercier-equilibrium favourable magnetic well profiles (Fig. 5.1 c)) but a severe decrease in plasma volume (Fig. 5.1

Label	$-I_{CC}$	$-I_{HC}$	I_{TF}	I_{VF}	$W_{\rho=1}$	W_M	V (m^3)	R (cm)
100_40_64	10.027	4.011	27.461	5.415	3.19	3.20	0.988	18.3
071_45_53	7.128	4.462	28.890	5.276	3.21	3.20	0.757	16.0
065_43_49	6.457	4.342	28.040	4.945	3.22	3.20	0.647	14.8
054_43_45	5.391	4.315	28.267	4.510	3.17	3.20	0.531	13.4

TABLE 5.3: List of magnetic configurations forming the Volume Scan Family and their technical characteristics.

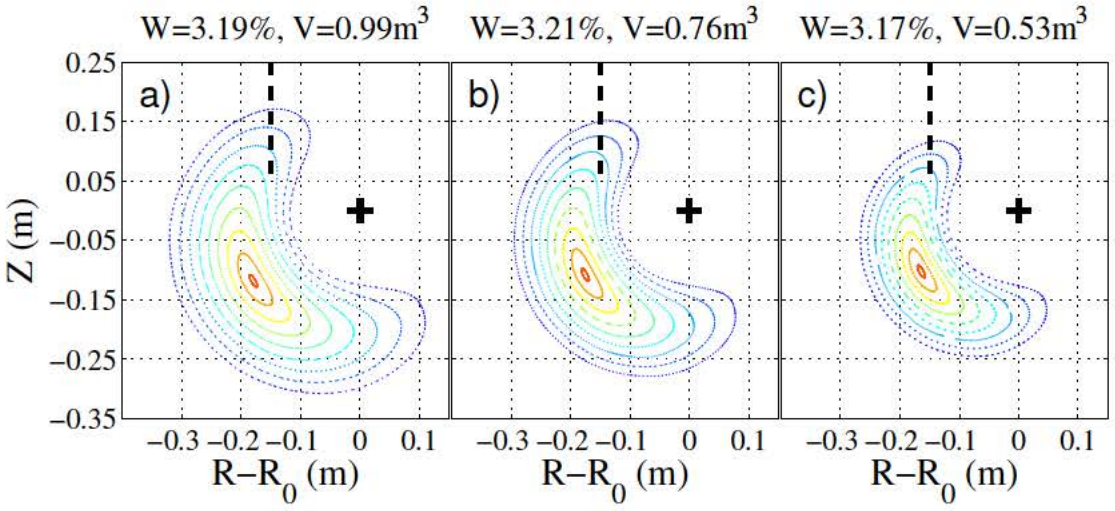

FIGURE 5.4: Poincaré plots of magnetic field lines for three selected configurations from the Volume Scan Family at the $\phi = 37.5°$ toroidal position. The dotted line represents one of the Langmuir probes trajectory.

i)), in a similar range as in the two previously explored families. It was not possible to find configurations that met these demands and exhibited similar rotational transform profiles (Fig. 5.1 f)).

Fig. 5.4 shows the Poincaré plots of the magnetic field lines for some of these configurations, proving (Fig. 5.4 c)) that in this case the decrease in plasma volume doesn't imply any change in plasma shaping, allowing full range of plasma edge exploration even for the top Langmuir array. Operating in this family of configurations allows us to distinguish the impact of the change of volume in the confinement from any effect produced by the magnetic well.

5.1.4 Experimental history

In TJ-II the first attempt to investigate the characteristics of transport close to instability thresholds related with magnetic well was carried out in 2001 [78]. Back then a family of three magnetic configurations (non-related with TJ-II's standard configuration) swapped

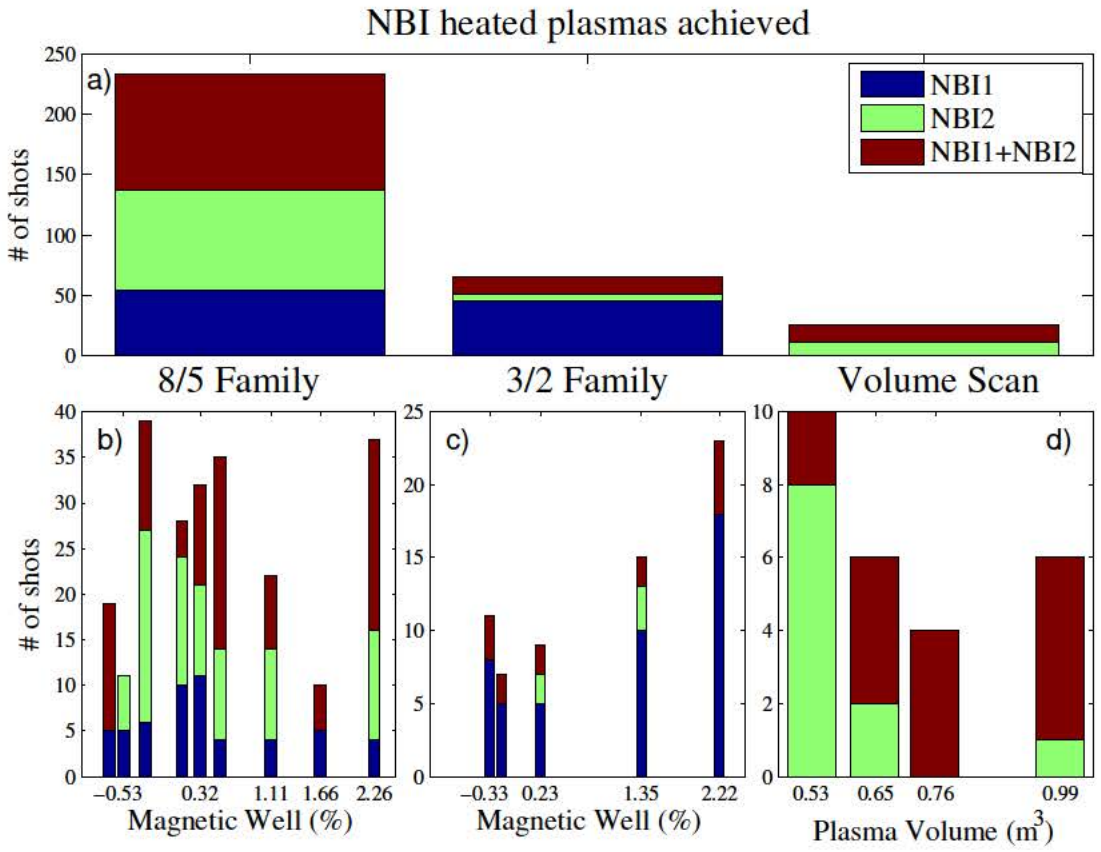

FIGURE 5.5: Number of shots achieved during the 19 experimental sessions involved in the magnetic well scan experiment.

values of magnetic well between 2.3% and −2.1% at the plasma edge. The plasmas studied in that paper were produced by ECR heating and, although Langmuir probes showed an increase of edge turbulence as the well was reduced, significant differences in Thomson-scattering measured electron temperature and density could not be found. So that first approach to this problem suggested that confinement was not affected by magnetic well.

Our magnetic well scan experiment compiles a TJ-II pulse database containing more than 450 plasma shots. Of that, roughly, 350 achieved NBI heating successfully. Because of their higher density, improved energy confinement and stiffer pressure profiles, we will focus our analysis on the successful NBI phases.

The results here presented summarise the work extracted from 19 experimental sessions that took place between February 2013 and May 2015. The first attempt to explore the first six configurations of the 8/5 Family aimed to analyse the effect of decreasing magnetic well on the edge electrostatic turbulence measured with Langmuir probes. The

unexpected results (reproducible plasmas achieved even for well depths less than 0.5% at the plasma edge) encouraged us to look for even more Mercier-unstable accessible configurations and to involve a wider range of diagnostics in order to have a better understanding of them.

Although TJ-II granted us the ability to change configurations during the same plasma shot [79], figures 5.2 and 5.3 suggest that this way to proceed wouldn't have been an appropiated course of action. The reason for this was the expected mutability for the shape and the position of the LCFS of the studied plasmas. This way we had no guarantee of reliability for some of our diagnostics that, like HIBP or Langmuir probes, require precise positioning for each configuration. This is why every plasma was confined only in a single magnetic configuration. Nevertheless, some evolution of the rotational transport in a single shot happened due to plasma current.

Fig. 5.5 shows of the amount of TJ-II shots involved in every step of the experiment. In order to ensure the reproducibility of the most Mercier-unstable plasmas and to accommodate the needs of the extra diagnostics added to the experiment, the 8/5 Family is the most widely explored of the three presented. Also, as it has been explained in Subsec. 3.2.3, different analytical treatment is required for the cases where the two neutral beam injectors at TJ-II were active from the ones where only one of them was used.

Some of the results presented in this Chapter, mostly regarding to the 8/5 Family, have been published in [74] and [80].

5.2 Theoretical calculations

A theoretical prediction of the Mercier stability property was evaluated for one of the configurations in the 8/5 Family that exhibits magnetic hill. 100_42_104, which has a magnetic well value in the edge of $W = -0.53\%$, therefore it is supposed to be unstable even for low pressure plasmas, was chosen. The configurations with shallower magnetic well are even more Mercier-unstable. As we will show in the following sections, we still obtain stable plasmas in such a configuration experimentally as well as in those with theoretically worse stability properties, which is an important result. Two types of

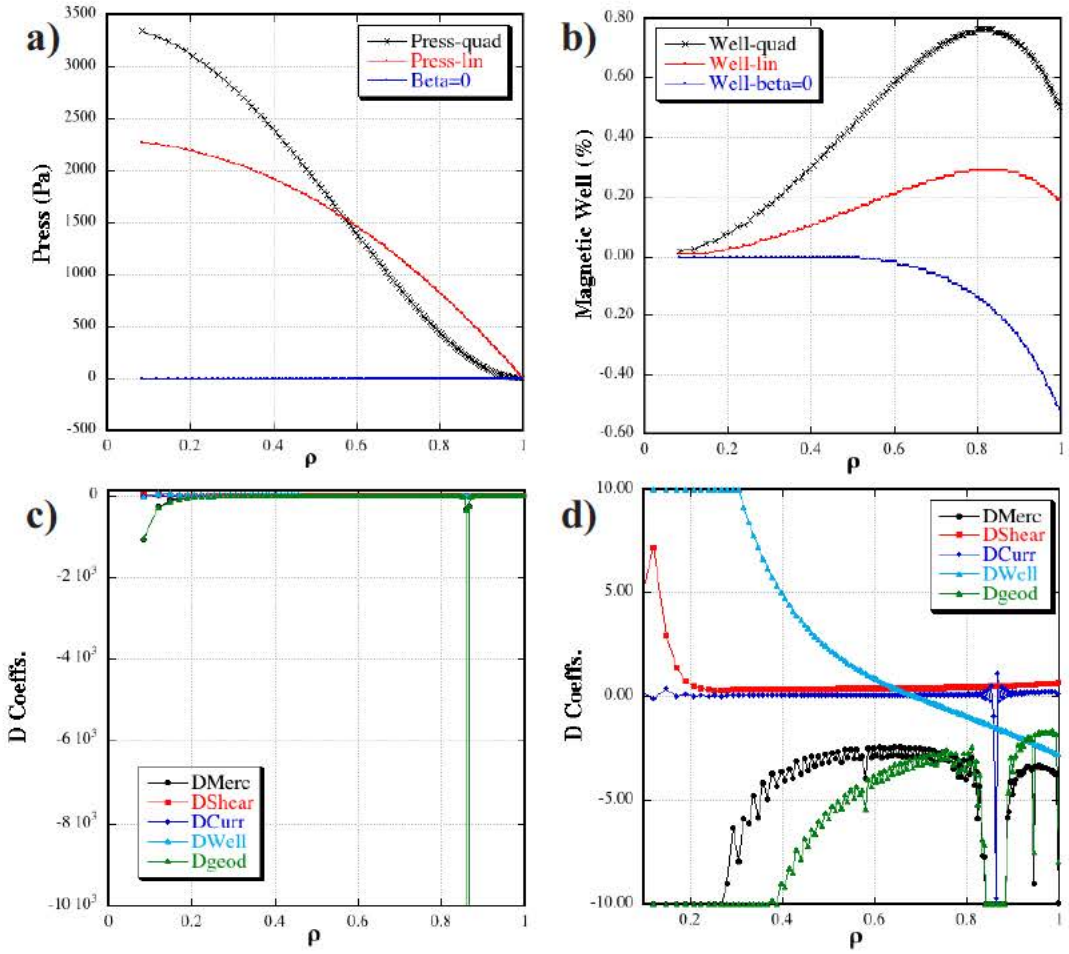

FIGURE 5.6: For the 100_42_104 configuration, with $W = -0.53$ % a) Pressure profiles with the radius used in the calculations. b) Magnetic well profile calculated when the previous pressure profiles are taken into account. c) Calculated Mercier coefficients for the linear pressure profile. d) Zoom on the c) panel to explore the behaviours of the Mercier terms and the $\iota/2\pi = 8/5$ resonance area. Credit: Francisco Castejón.

pressure profiles are used for the calculations, linear and quadratic with the normalised magnetic flux (see Fig. 5.6 a), where $s = \rho^2$).

When equilibrium is calculated using VMEC [73], it is observed that the magnetic well is increased with plasma pressure and becomes larger for the quadratic profile, as expected from the definition of magnetic well given in Eq. 3.18.

We perform the Mercier criterion calculation for the case of the linear pressure profile, i.e., for $p(s) = p(0)(1-s)$, and and $\langle\beta\rangle \approx 0.3\%$, which is of the order of the values we have used in our experiments. The Mercier coefficient of Eq. 3.8, D_{Merc}, is negative along the whole minor radius and shows a large minimum at the position of the $\iota/2\pi = 8/5$ resonance, showing that the mode is strongly unstable, as can be seen in Fig. 5.6 c).

Here, the largest instability appears at the rational values of the rotational transform when the configuration is Mercier-unstable. One would expect that the mode grew at that position, although the magnetic topology of nested magnetic surfaces estimated by the VMEC code cannot show any change. The effect of this mode on global stability can be limited, since the fraction of the profile affected is small.

We perform a zoom of the Mercier coefficients (see Fig. 5.6 d)) in order to explore the effect of the different terms. The large minimum is dominant, showing some radial extension: the most unstable region is close to the resonance and its influence on the global stability will depend strongly on the actual radial extension of the magnetic island. It can be seen that the Mercier coefficient D_{Merc} is negative along the whole minor radius, which implies that the plasma is unstable everywhere, despite of the fact that the magnetic well is positive in the inner radii. Having a detailed look on the figure, it is seen that the shear and the current terms are very small, as expected, while the most destabilising term is the geodesic curvature. Therefore, as it has been pointed previously, Mercier stability in TJ-II is an interplay between the stabilising magnetic well and the destabilising geodesic curvature. For this family of configurations, the geodesic curvature term becomes more and more negative (destabilising) as the magnetic well decreases, so the latter is a good label for the definition of the stability: the more positive the magnetic well term, the more stable the configuration. In fact, the magnetic well and the geodesic curvature are related, as has been shown for instance in reference [81].

Once we have taken a Mercier-unstable configuration with magnetic hill to check if this theoretically unstable configuration can confine stable plasmas, we have found that the plasma is Mercier unstable even in the inner radii, where the magnetic well term is positive. Experiments have been performed to explore the effect of such instability on TJ-II plasmas.

5.3 Confinement

The first approach to the experimental data consisted in analysing any possible dependence between stored energy and magnetic well or plasma volume. For that, all the hot NBI phases of all shots from each family were scanned in search for the stored energy achieved at three common values of line averaged electron density for NBI heating at

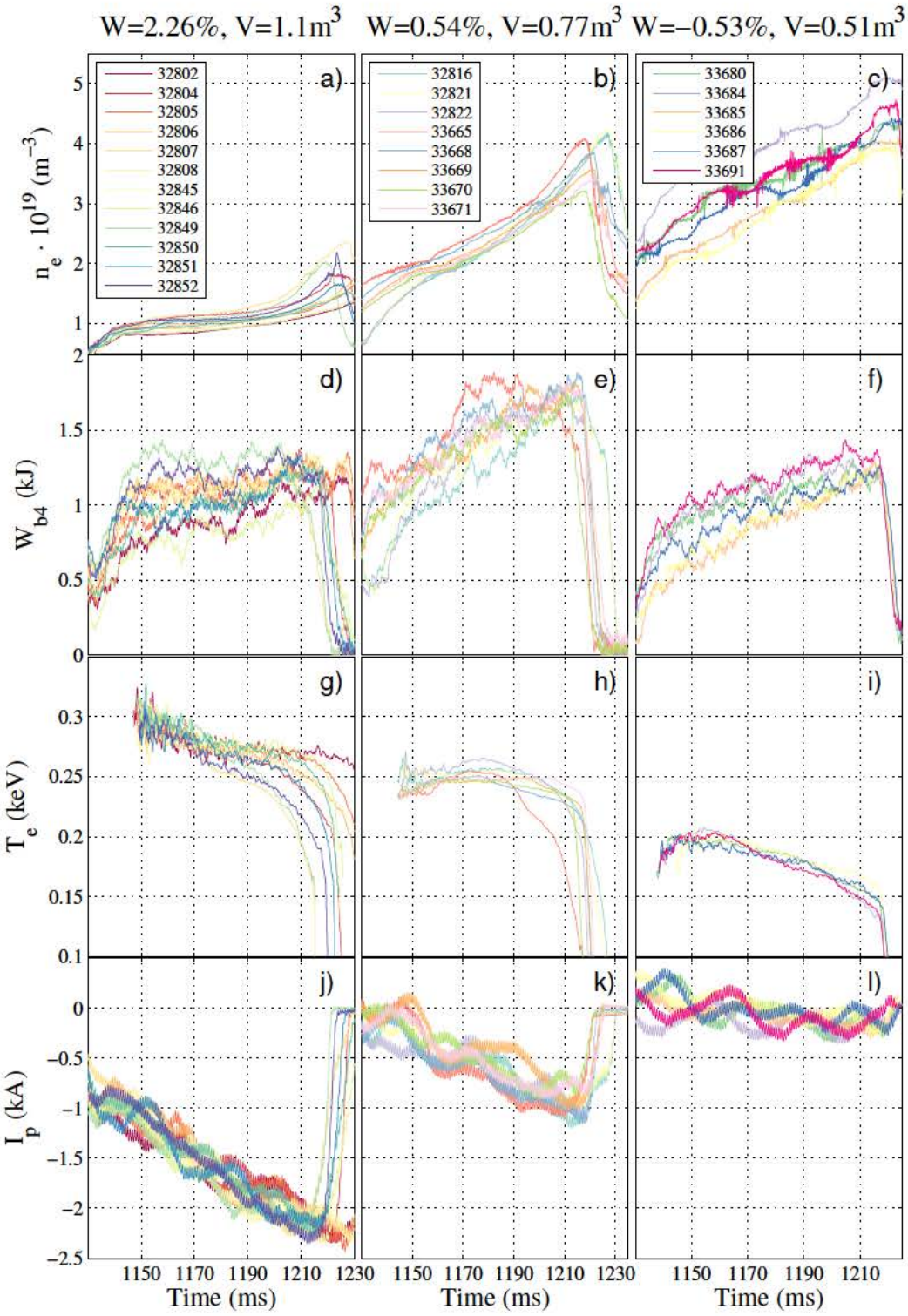

FIGURE 5.7: General plasma parameters for the NBI-heated phase of selected shots (only NBI counter-injection beam used) of three configurations of the 8/5 Family. Each column represents one configuration: column 1 takes data of the 100_44_64 'standard' configuration; column 2, the 100_44_84, with low magnetic well value on the plasma edge; and column 3, 100_42_104, one of the magnetic hill configurations. Row 1 represents line averaged electron density; row 2, stored diamagnetic energy; row 3, soft X-ray electron temperature (data courtesy of Francisco Medina) and row 4, plasma current (data courtesy of José María Fontdecaba); all versus time.

TJ-II. The first two rows in Fig. 5.7 show such time traces for some pulses in the 8/5 Family.

These results are summarised in Fig. 5.8. Firstly, panel c) seems to make clear that stored energy decreases with volume: quite a logical result, as the Volume Scan Family reduces the amount of plasma available almost to one half in its smaller configuration. This is consistent with the ISS04 scaling law [19], that throws the dependence $\tau_E \propto a^{2.28}$, which is almost proportional to the plasma volume in TJ-II, where the major radius is constant ($R_0 = 1.5m$).

The configurations of the 8/5 Family present decreasing volume as the magnetic well decreases. Experiments do not show any lowering in the stored energy until configuration 99_44_87, with less than three quarters of the standard configuration's original volume and less than 0.5% of magnetic well depth along the minor radii. One might say that, for high density values, the low-but-positive magnetic well configurations seem to achieve higher values of stored energy than the standard configuration.

Very few shots from the 3/2 Family reached high densities. The plasmas confined under these configurations did not only show little dependence between stored energy and magnetic well, but they seem to reach higher values of stored energy at the most Mercier-unstable configuration.

For a better understanding of these results, the same data appears in the second row (panels d)-f)) of Fig. 5.8 dividing, for each configuration, the stored energy by its plasma volume. This way the average density of stored energy is defined, excluding the volume dependence and making it easier to compare the points obtained for each configuration. When we represent this density of stored energy the clearest result comes from the Volume Scan (Fig. 5.8 f)), where 54_43_45, the configuration with the lowest plasma volume, can store about an 80% of the energy per cubic meter of the largest volume case. Density of stored energy falls with plasma volume, but this dependence is weak.

When magnetic well decreases with volume, the 8/5 Family has three configurations with intermediate values of magnetic well (between 1.11 and 0.32%) that actually confine better than the standard configuration. When the magnetic well turns negative, density of stored energy starts to decrease but no catastrophic events are seen. Again, in the

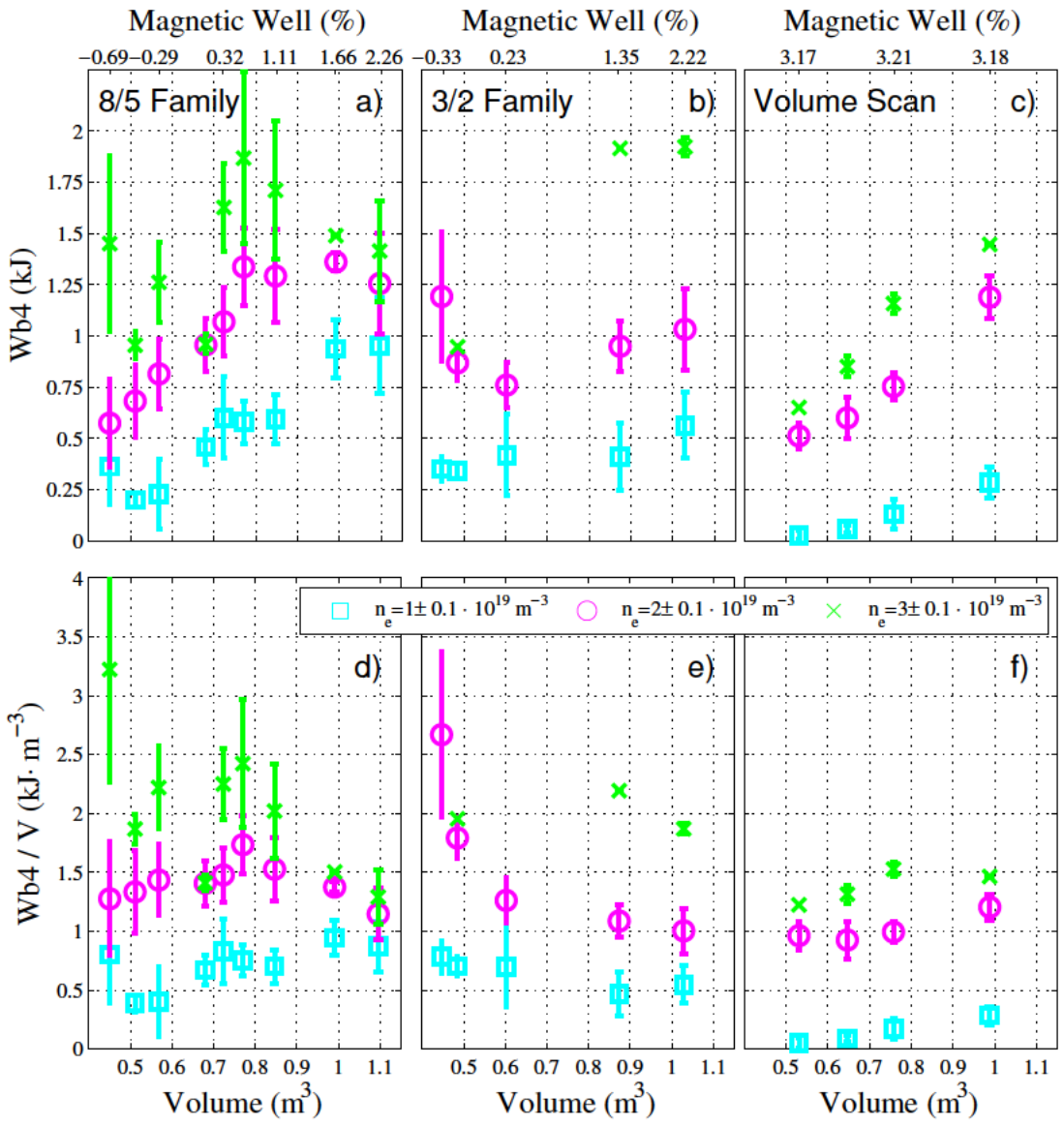

FIGURE 5.8: Stored diamagnetic energy vs. Plasma volume and magnetic well for three values of electron density at NBI phases. Each column in figure represents one of the three families of magnetic configurations used during the experiment. In the upper row, each panel contains experimental values of stored energy vs. Volume, while magnetic well is also addressed at the upper x-axis. The reason for this kind of representation is the null change of magnetic well along the volume scan, making any plot vs. Magnetic well illegible in this family of configurations. This way, the same axis have been used for all the panels, easing comparison between families. The lower row compiles the same experimental results, but dividing the stored energy by the plasma volume in order to obtain a 'density of stored energy' that allows better comparison between configurations, excluding the obvious effect of volume on confinement.

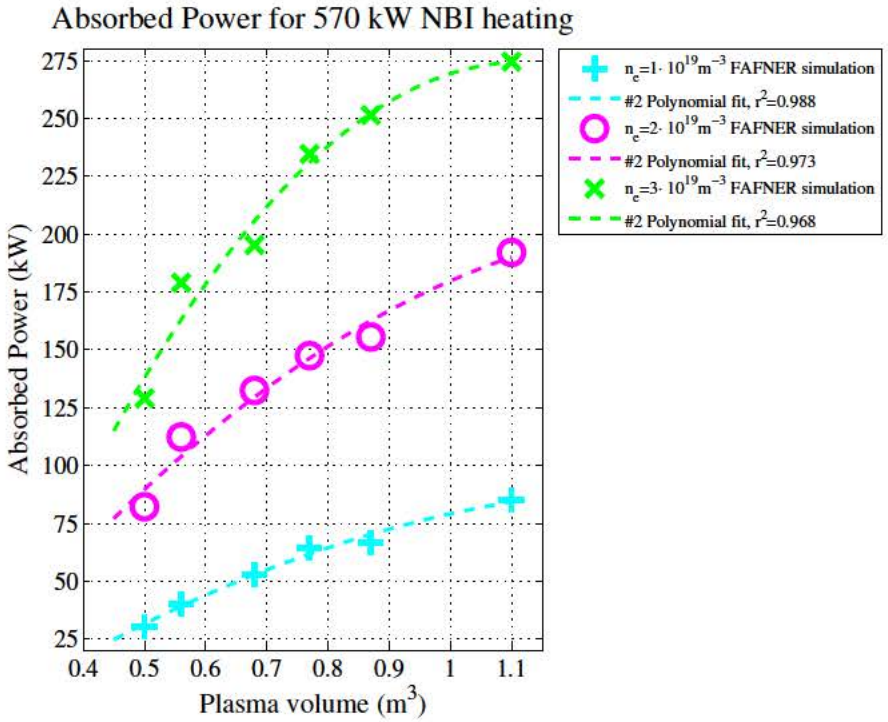

FIGURE 5.9: Absorbed power vs. Plasma volume and electron density. The points represent FAFNER simulations to obtain the fraction of 570 kW of NBI heating absorbed at different plasma volumes and core densities. The lines represent the parabolic fits that will be employed to estimate the absorbed power in the non-simulated cases.

3/2 Family the lowest magnetic well values seem to be the most favourable for energy storing.

For a better characterisation of the confinement parameters, we turn back to the energy confinement time, as it was presented by Eq. 2.22 in Subsec. 2.3.2:

$$\tau_E^{ISS04} = 0.134 a^{2.28} R^{0.64} P^{-0.61} n_e^{0.54} B^{0.84} \iota_{2/3}^{0.41}$$

The energy confinement time computation involves the stored energy, its time derivative and the power absorbed by the plasma. Among these three quantities, an estimation of the fraction of the NBI heating power is actually delivered to each magnetic configuration seems like the most difficult to obtain, as no experimental data related to it is available.

The Monte-Carlo code FAFNER [82] allowed us to obtain estimations for the fraction of absorbed power by different plasma volumes and at different core densities. Not all the volumes explored during the experiment were taken into the simulation, so a parabolic fit was necessary to address many of the studied configurations. Fig. 5.9 collects these results for the three values of electron density considered.

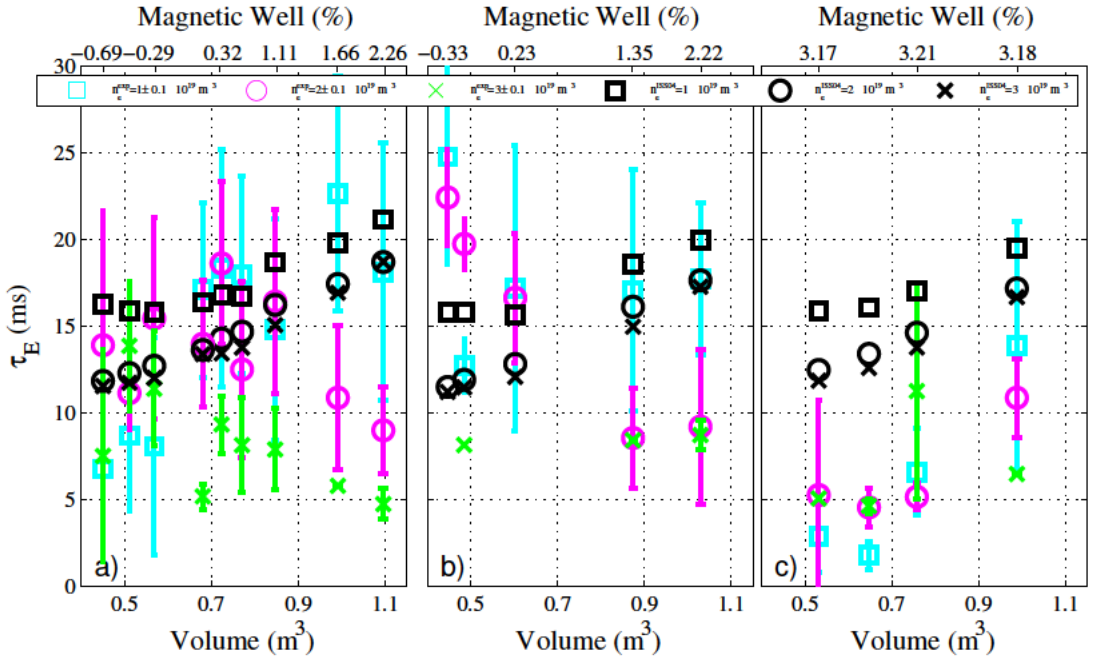

FIGURE 5.10: Energy confinement time vs. Plasma volume and magnetic well for three electron densities at NBI phases. As in the previous figures, each column represents a family of configurations. The three electron densities explored have been labelled using the usual colour map to represent experimental values of energy confinement time. Black variants of the same symbols provide equivalent quantities predicted by the ISS04 database.

Having, this way, all the data required to compute experimental values of the energy confinement time for each of the magnetic configurations, τ_E can be computed according to its definition in Eq. 2.22. These results are plotted, using the usual colour map for density, in Fig. 5.10. In principle, experimental τ_E seems to decrease with plasma volume (Fig. 5.10 c)) and magnetic well. Although, again, some configurations seem to exhibit an enhanced performance, both in the 8/5 (Fig. 5.10 a)) and the 3/2 (Fig. 5.10 b)) families. This is consistent with the results observed in Fig. 5.8, as the same data sets were used.

Again, from Subsec. 2.3.2, Eq. 2.23 addresses the dependence of energy confinement time with line density, radius, absorbed power, and rotational profile; all of them parameters that have been explored in these experiments. For each family of configurations the parameters that will affect the ISS04 value of τ_E are:

- **Minor radius** a. This is the strongest dependence, so smaller plasmas (which correspond with low values of magnetic well) will have lower confinement times.

- **Density** n_e. In principle, for similar heating power, higher densities will lead to larger confinement times.

- **Absorbed power** P. Smaller plasmas will absorb less power, so decreasing the plasma volume increases the confinement time, as predicted by the empirical scaling law Eq. 2.23. But, on the other hand, P also depends (grows with) on density, so for higher values of n_e, this factor will tend to make τ_E smaller.

These dependencies are key to understand the ISS04 predictions, although the database employed to obtain Eq. 2.23 didn't take magnetic well into account. The experimental points that TJ-II provided to this database [19] included $\iota_{2/3}$ values comparable to the ones from our experiments, but only achieved ECR heating phases and densities one order of magnitude lower than the ones that we have explored. For the moment, no clear dependence on $\iota_{2/3}$ is found in NBI plasmas [83].

The τ_E^{ISS04} values predicted by Eq. 2.23 have been added to Fig. 5.10 using the same symbols that have been used to label densities in the previous figures, but in black. In general, τ_E^{ISS04} seems to be in agreement with the experiment for the lowest density taken into account (which is the most similar to the densities employed in [19]). The case with better agreement between the experiments and the database is the Volume Scan (Fig. 5.10 c)), which shows the dependence of confinement time with volume, which also happens in the magnetic well scan.

5.4 Temperature

Electron and ion temperatures are the next plasma quantities whose dependence with magnetic well we are interested in understanding. We have used three experimental diagnostics available in TJ-II to track its evolution along our scan.

- **Charge Exchange Neutral Particle Analyser** The CX-NPA is able to measure the energy spectrum of plasma ions for a given position [84]. The ion temperature can be extracted from that spectrum if we assume a Maxwellian distribution function. The analiser is located at the $\phi = 175°$ toroidal position. Ion temperature profiles tend to be flat along the covered radius span (ρ between 0.3 and 0.8) [85],

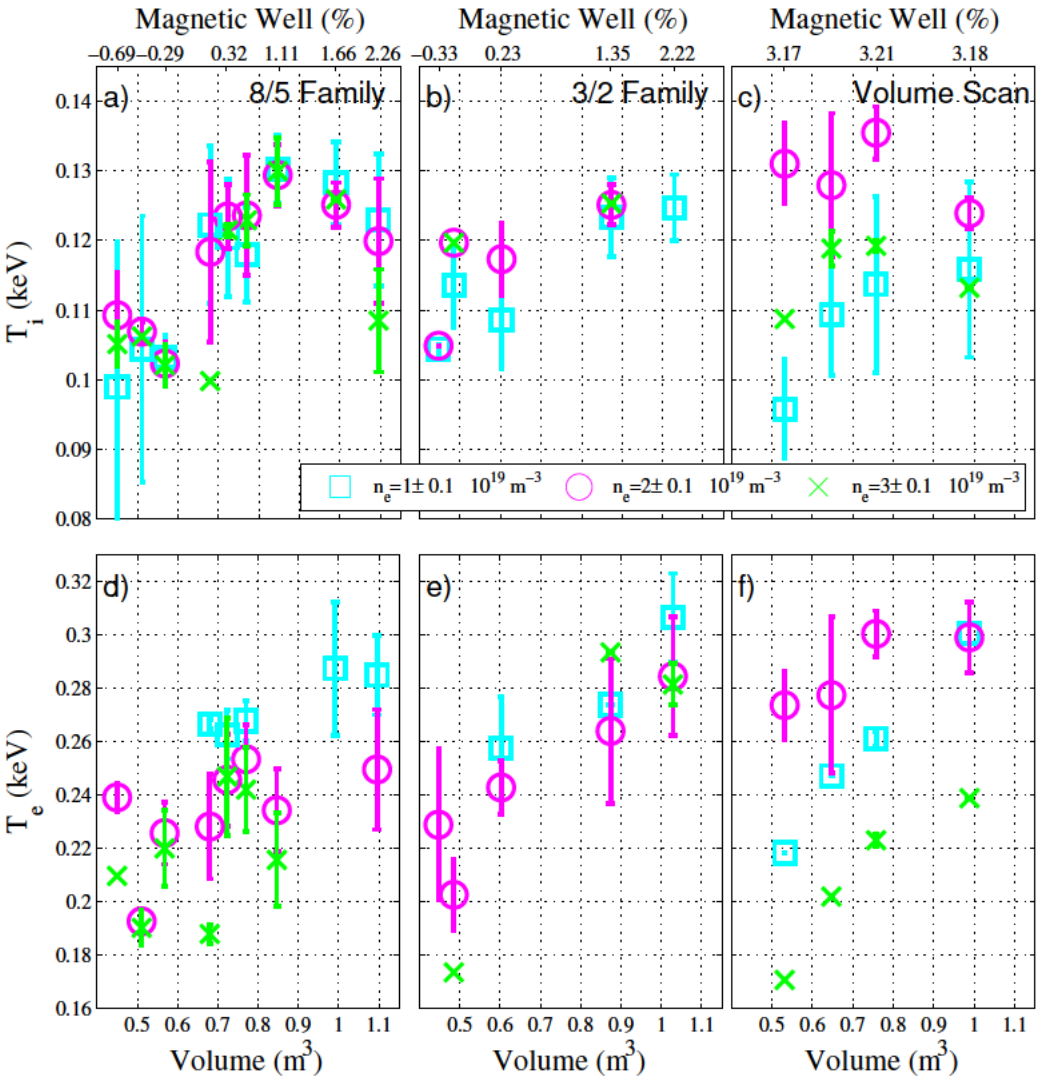

FIGURE 5.11: Electron and Ion temperature vs. Plasma volume, magnetic well and electron density at NBI phases. As in the previous figures, each column represents a family of configurations. Three electron densities have been explored and labelled using the usual colour map to represent experimental values of energy confinement time. Row 1 compiles ion temperatures at plasma core measured by TJ-II's NPA (data courtesy of José María Fontdecaba). Row 2 represents core electron temperature computed from ECE measurements (data courtesy of Francisco Medina). All the x axes are set to volume values, although the corresponding upper axes include magnetic well values for the families belonging to each configuration.

which is the range of applicability of the temperatures summarised in Fig. 5.11 a)-c).

- **Electron Cyclotron Emission** As long as the electron distribution function is Maxwellian, the measurement of the second harmonic of electron cyclotron emission allows the characterization of electron temperature for NBI-heated phases [86]. The measurements are performed on the HFS in the horizontal midplane (between sectors C4 and C5, $\phi = 315°$). Using the same database and density limits as in the previous section, Fig. 5.11 d)-f) compiles the cases where T_e was measured for each of our experimental families.

- **Thomson Scattering** A high-resolution Thomson Scattering system is installed at sector D2 ($\phi = 14.5°$). The device can provide ≈ 200 points (the exact number depends on the magnetic configuration) of electron density, temperature and pressure [87]. A selection of the available profiles is presented in Fig. 5.12. The density profiles have been chosen, among the plasma pulses where they could be reconstructed, to exhibit similar values (panels a)-c)) to ease comparison between temperatures for different configurations (panels d)-f)).

Although temperature is, in principle, an intensive property, Fig. 5.9 made it clear that, for the same NBI heating power, the absortion ratio depended drastically on plasma volume. In agreement with this, along the Volume Scan electron temperature appears to decrease as the volume does (both for ECE and TS data), although the impact seems minor for $n_e \approx 2 \cdot 10^{19} m^{-3}$. Ion temperature doesn't seem to reduce so dramatically when the volume is lowered, specially as density rises.

Regarding the magnetic well scans in the 3/2 Family, which presents clear decreases in both ion and electron temperatures as the well is reduced, seems to be more significant for T_e but shows no clear dependence on density. The TS data are not so clear but hints slightly higher values of electron temperature for the larger well configurations (although no TS profile is available from the 104_35_104 configuration.) The analysis is more complicated when we examine the 8/5 Family: electron temperature data are not as clear as in the other two families, but from the ECE measurements one could think that for high densities ($n_e \approx 2 - 3 \cdot 10^{19} m^{-3}$) some low-but-positive magnetic well configurations (100_44_84 and 99_44_87) can reach ion and electron temperatures as high as the standard configuration. Note that in the previous section both figures

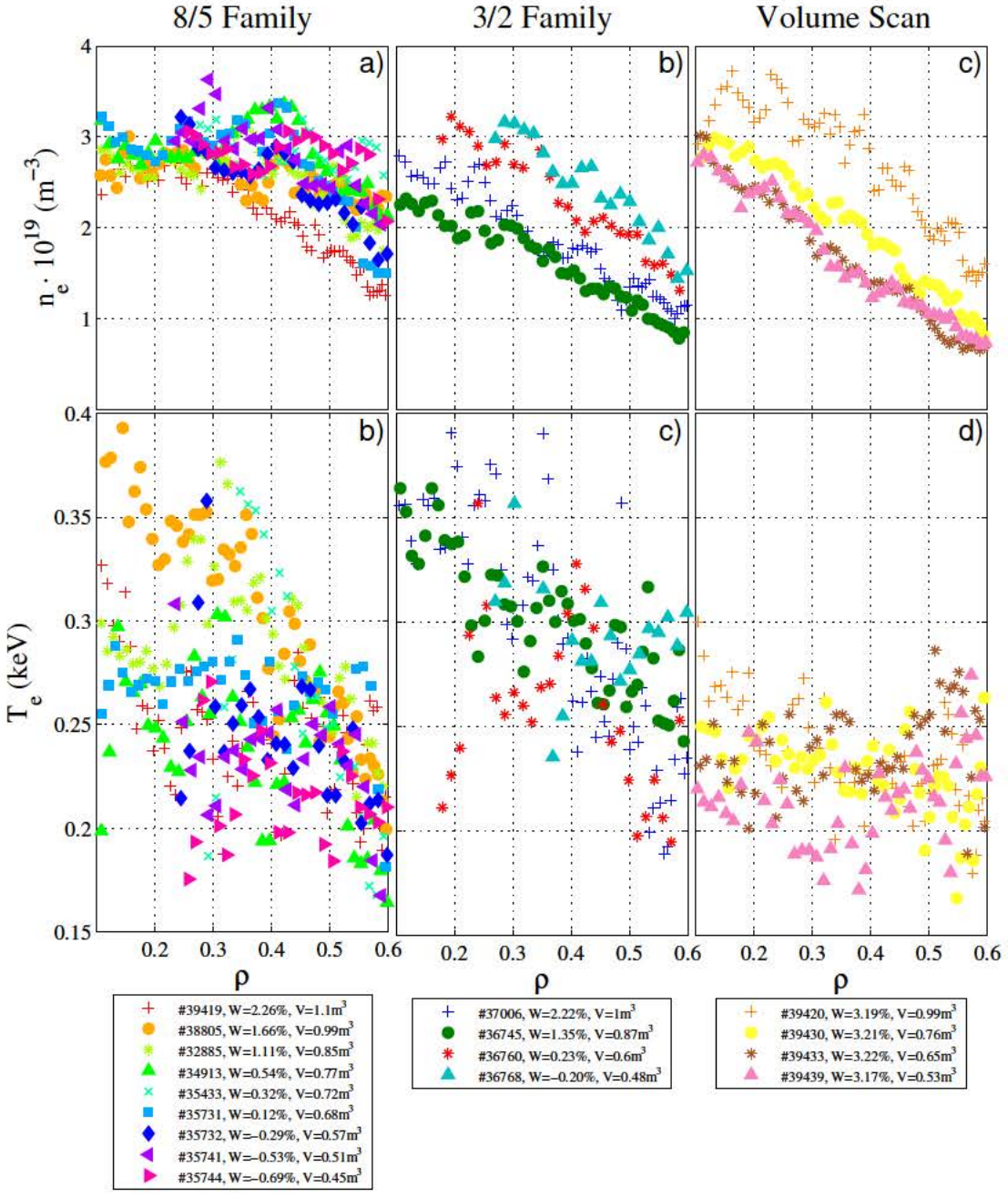

FIGURE 5.12: Thomson profiles. Row 1 presents selected (similar) electron density profiles for each of our experimental families. Row 2 provides the electron temperature profiles for the same plasma pulses. Data courtesy of Ignacio Pastor.

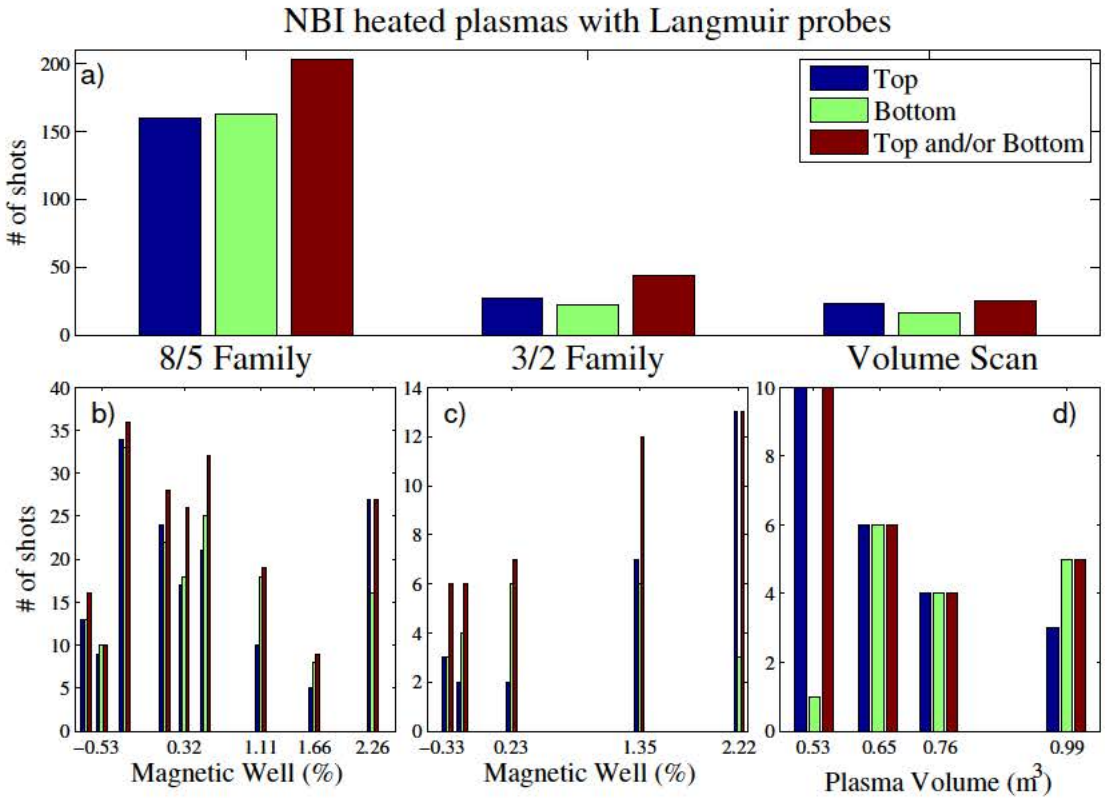

FIGURE 5.13: Summary of the achieved NBI-heated plasmas where one or the two Langmuir probes were active and operating correctly.

5.8 d) and 5.10 a) suggested a similar improvement of confinement for the same group of configurations. The temperature falls drastically for the cases where magnetic well becomes negative at plasma edge (being this effect much clearer in the ion temperature).

5.5 Shear layer position

Moving ahead in our inspection of Mercier-unstable conditions, plasma periphery is the following subject to be explored. The reason for this is, mainly, to confirm the existence of a complete plasma profile in spite of the adverse Mercier stability conditions, which include the pressure of unstable low order resonance. Our approach to this matter is checking if the plasma boundary (defined by the shear layer) lays where estimations like the ones from figures 5.2 - 5.4 predict. Langmuir probes are our diagnostic selected to study the outer region of the plasma. The shear layer is the surface where the electric field changes its sign; it determines the effective confinement radious. Radial

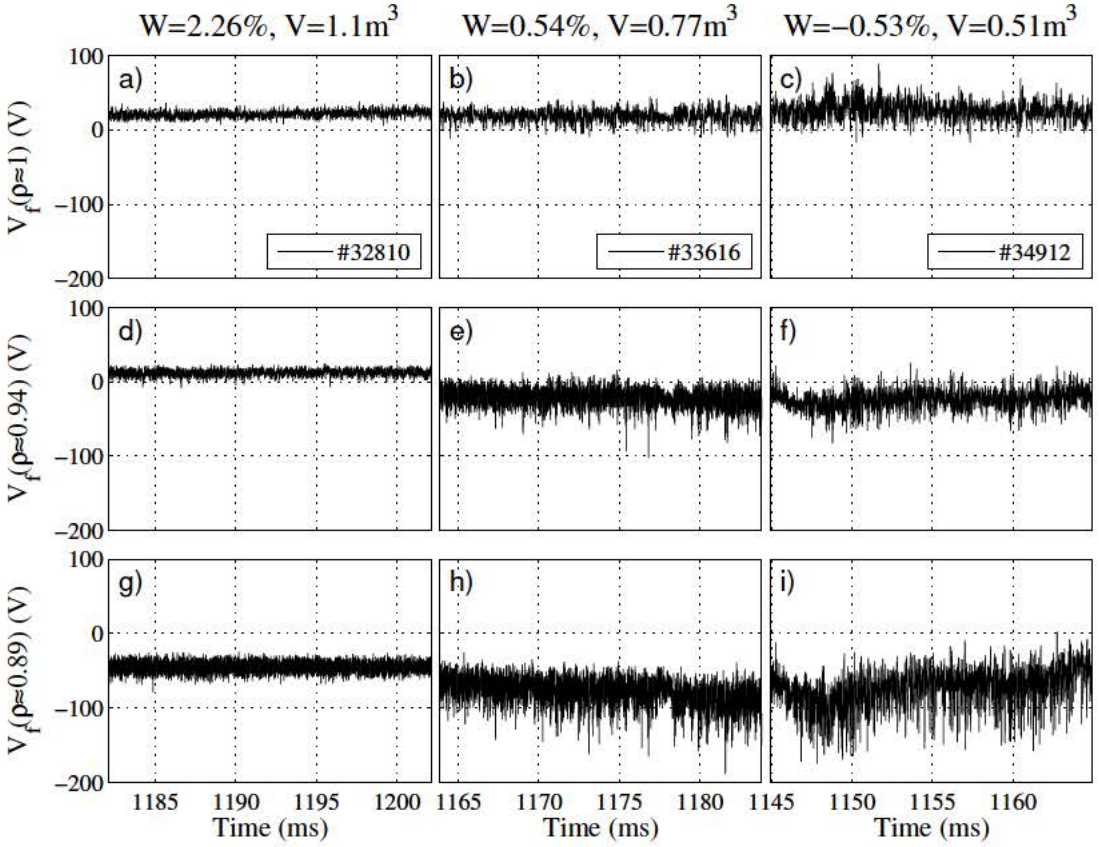

FIGURE 5.14: Raw data from the bottom Langmuir probe array. For three selected shots from representative configurations from the 8/5 family, we show the floating potential values measured at three equivalent positions of the normalised radius ρ. In the three cases a time lapse of 20 ms has been chosen once the discharge reaches a density of $n_e = 2 \cdot 10^{19} m^{-3}$.

measurements of the floating potential at the plasma edge can measure the shear layer and, hence, the plasma boundary position [88].

From the original experimental database only in a fraction of the plasma pulses could be characterised with data from the Langmuir probes. They are located, as it has been explained in Sec. 4.2.1, in different toroidal and poloidal positions. That section also introduced a method to correlate the absolute position of each pin to the plasma radius which becomes crucial for this experiment, where constant changes in the size of the plasma make mandatory for us to know the distance of the probe arrays to its surfaces.

This way, the raw data from the measured floating potential can be arranged, as in Fig. 5.14, in equivalent positions, for an easier comparison. From this kind of representation we can deduce that, as expected, floating potential becomes negative as we go inner into the plasma; and that higher values of signal fluctuation are observed when the magnetic well is reduced. In order to obtain detailed profiles of the floating potential along the

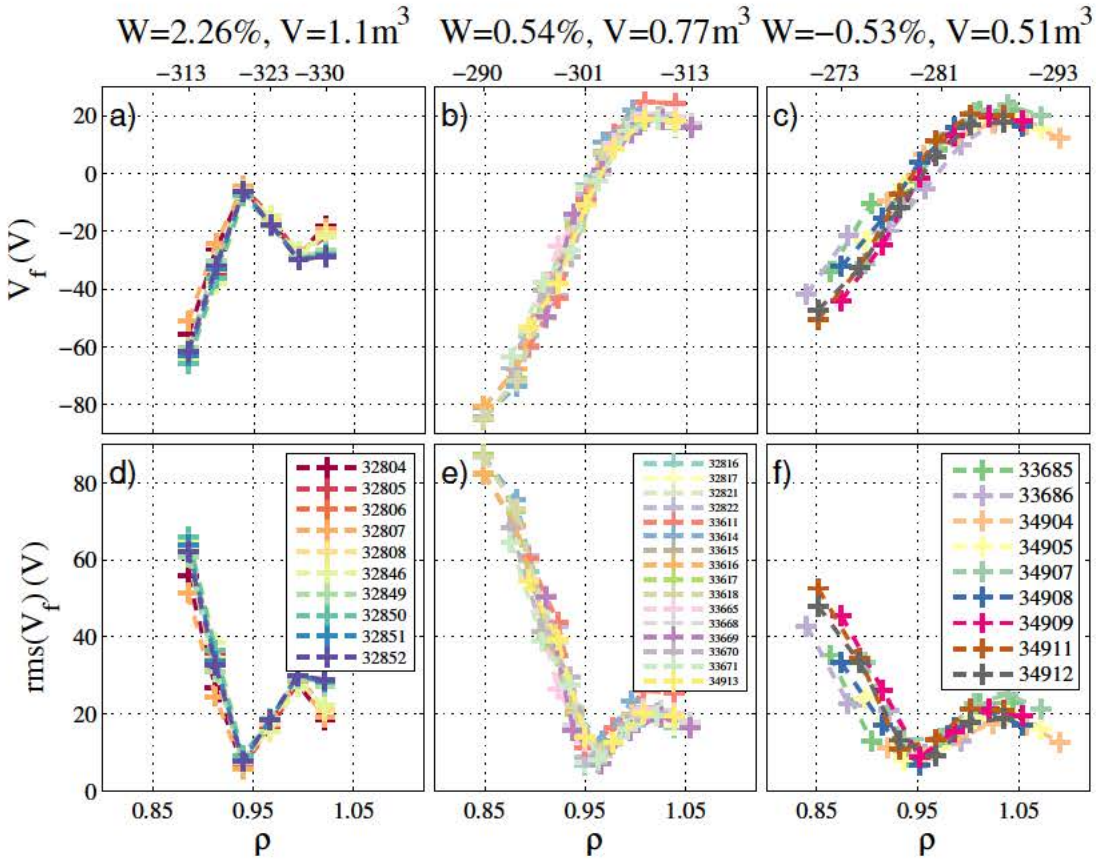

FIGURE 5.15: Floating potential profiles extracted from several reproducible shots from the bottom Langmuir probe array. For three selected representative configurations from the 8/5 family, in row 1 we show the reconstructed floating potential profiles versus normalised radius ρ (lower x axis). All the three cases average the periods where the discharges reach densities around $n_e = 2 \cdot 10^{19} m^{-3}$. Row 2 extracts the RMS of the signals, for the same plasma pulses and periods of time. The upper x axes represent, in mm, the absolute z position of the pins, changing between configurations.

plasma edge, several NBI-heated plasmas were obtained with similar density conditions for each configuration, changing slightly the position of the Langmuir probe arrays.

Fig. 5.15 shows three of these profiles extracted for representative configurations in the 8/5 Family at the bottom position. The obtained profiles are not only reproducible, but also exhibit not distortion from the Langmuir probe array position, meaning that the array is set at a safe distance so it doesn't act as a limiter for the last magnetic surfaces. The first row makes very clear how the change of sign in the radial electric field can be detected by simply finding the maxima at $V_f(\rho)$, since $\frac{\partial V_(\rho)}{\partial \rho} = 0$ implies a change of sign.

We build the floating potential profiles using a set of measurements on reproducible plasmas (more than eight for the 8/5 Family, quite less in the other two cases). Then,

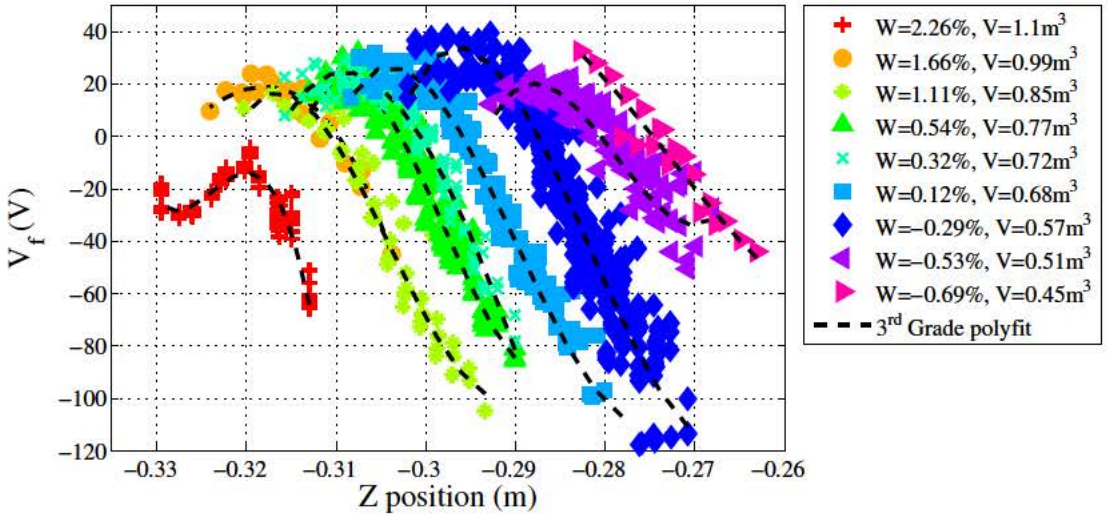

FIGURE 5.16: Floating potential profiles for all the configurations of the 8/5 Family at the bottom position. The abscissa represents the pins' position in the TJ-II frame of reference, in meters. The dotted black lines are the polynomial fits obtained for each profile. Data extracted for density around $n_e = 2 \cdot 10^{19} m^{-3}$.

we fit these profiles using a third grade polynomial for each configuration and density. The goal of using such a fit is not the physical description of the behaviour of the floating potential, but to get a tool to estimate the point where it reaches its maximum value for each magnetic configuration, which corresponds to the shear layer position.

Fig. 5.16 represents the result of this process when applied to the profiles obtained for each magnetic configuration of the 8/5 Family by the arrays installed at the bottom access point. Of the nine configurations explored only the last one, 100_41_109, with magnetic hill and negative magnetic well along all the plasma radius, fails to show a canonical profile, with an absolute maximum that we can detect. The dotted black lines represent the 3^{rd} grade polynomial fits.

The process represented by figures 5.15 and 5.16 has been carried out with Langmuir probe arrays for the three families at the two Langmuir probe access points available in TJ-II different rates of success. Tab. 5.4 summarises the outcome of this process.

Once the experimental values of the shear layer are extracted, they can be compared to the LCFS position computed using VMEC. Fig. 5.17 compiles these comparisons for the three experimental families for bottom-obtained floating potential profiles. The 1:1 matching between predictions and experiments was expected for the Volume Scan (Fig. 5.17 c)), as the constantly high magnetic well guaranteed a stable and well defined plasma edge following Mercier criterion. A similar relation is observed for most of the

	Bottom Probe	Top Probe
8/5 Family	All configurations explored with 2D and rake probes. Only 100_41_109 was unable to produce reproducible profiles.	Most configurations explored with 2D probe (some rake results are inconclusive) except 100_41_109. Negative magnetic well at plasma edge translates in steeper profiles, more difficult to analyse.
3/2 Family	All configurations explored with rake arrays, although only few shots (2-4) provided clear profiles for analysis.	After several attempts to use the rake array, proper profiles could only be obtained for 101_38_62. It was not possible to use these results in the next sections.
Volume Scan	Promising results were obtained with a rake array for the first two configurations of this family, but a failure in the probe's positioning system made it impossible to extract any usable profiles for configurations 65_43_49 and 54_43_45.	The four configurations were successfully explored with a 2D array. Reproducible profiles easily obtained in all the cases.

TABLE 5.4: Summary of the rate of success at the floating potential profile extraction for each magnetic configuration family and studied position.

8/5 Family configurations except for 101_38_62, the most Mercier-unstable of them. Fig. 5.17 a) seems to confirm that, in spite of the unfavourable Mercier stability conditions, fully developed hot plasmas are achieved even in the presence of the 8/5 rational. One could expect that the unstable 8/5 rational located at the edge affected the plasma size which did not happen to be the case. The 1:1 matching isn't so clear when this analysis is applied to the 3/2 Family (Fig. 5.17 b)): the high volatility in the floating potential profiles obtained during this experiment can either be an instrumental issue or the fact that for this family of configurations the plasma edge isn't fully developed when the Mércier stability is compromised. The experimental conditions of these plasmas were not good, since strong plasma currents were developed, since these plasmas were created exclusively using NBI.

When this analysis was attempted for the data obtained from the top access point, the results were slightly different. To begin with, a nice 1:1 matching between prediction and experiment was obtained again during the Volume Scan (Fig. 5.18 b)), as the Poincaré

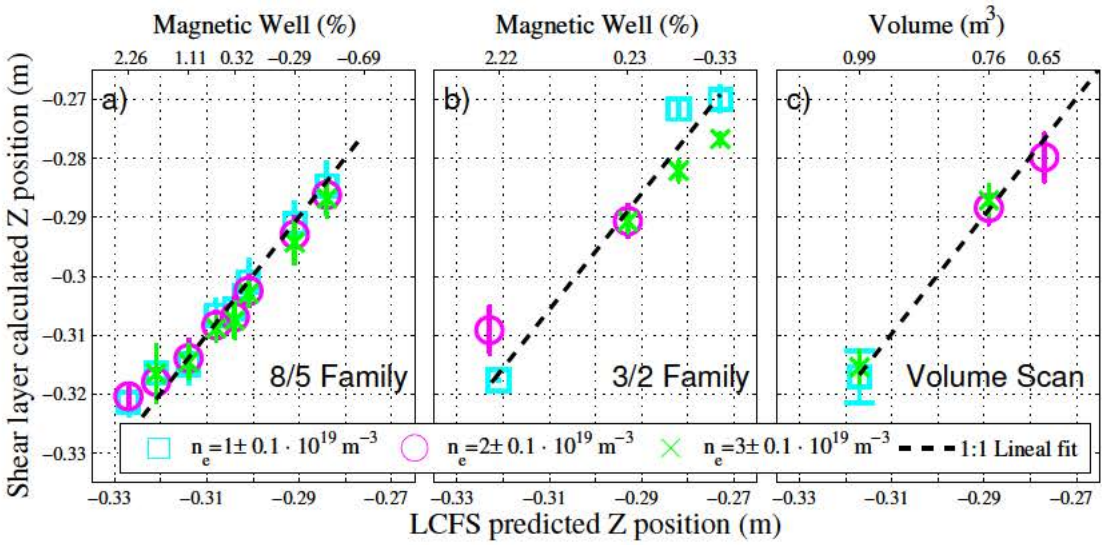

FIGURE 5.17: For the bottom access point, the result of the shear layer position calculated using the experimental floating potential profiles is presented for each family. The abscissa represents the LCFS position extracted from VMEC simulations. On the upper x axes magnetic well and plasma volume values for each LCFS predicted position are provided. Note that for this position smaller plasmas imply bigger (less negative) z values for the LCFS. Only eight of the nine configurations from the 8/5 Family are presented in a), as 101_38_62 failed to provide V_f profiles with a clear maximum. Only three of the four configurations of the Volume Scan are represented in c) because, as it has been explained in Tab. 5.4, a problem in the probe's positioning system prevented us from fully exploring the two smaller configurations. The dotted lines are the 1:1 ($y = x$) fit.

plots from Fig. 5.4 guaranteed that, even when the volume was reduced, the probe array could physically touch the plasma. Fig. 5.3 hinted that this would be a problem when the volume and the shape of the plasma are such that the Top probe does not reach it properly, casting doubts on the measurement results. Deviations from the 1:1 fitting as the well was reduced for the 8/5 Family (Fig. 5.18 a)) are shown for the smaller configuration, for which measurements are less accurate. It was not possible at all to extract the shear layer positions for the 3/2 Family configurations (except for 101_38_62, the one with the most favourable Mercier-stability conditions).

For the 8/5 Family measurements taken from the top access point seem reliable even for magnetic well values as low as $W = -0.29\%$, although the greater amount of data and lower dispersion of the results make it wiser to use data extracted from the bottom access point for any follow up analysis whenever is possible, at least for this family of configurations.

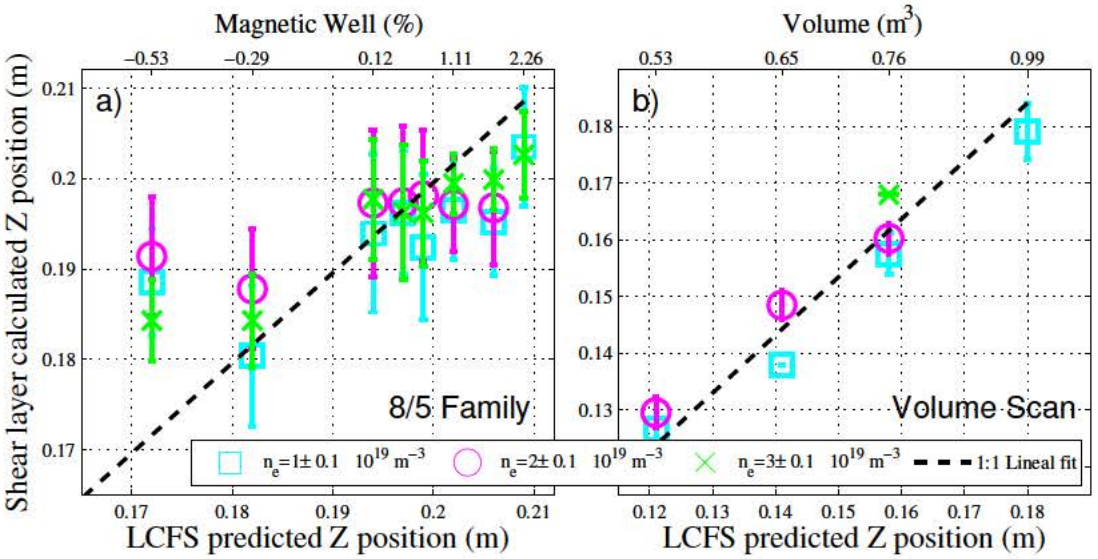

FIGURE 5.18: For the top access point, the result of the shear layer position calculated using the experimental floating potential profiles is presented for the 8/5 Family and the Volume Scan (no relaiable data available from the 3/2 Family in this case). As in the previous figure, abscissa represents the predicted LCFS position. On the upper x axes some magnetic well and plasma volume values corresponding to the LCFS values. Note that for this case smaller plasmas imply smaller z values for the LCFS. Only eight of the nine configurations from the 8/5 Family are presented in a), as there isn't data from 101_38_62 at this access point. Again, the dotted lines are the 1:1 ($y = x$) fit.

5.6 Poloidal velocity

One of the quantities accessible to Langmuir probe measurements is, as we presented in Sec. 4.2, the poloidal component of the $\vec{E} \times \vec{B}$ drift described in Eq. 2.7 as

$$v_\theta = \frac{E_r}{B} = \frac{1}{B}\frac{dV_f}{dr} \tag{5.1}$$

Given experimental data as the one used to plot Fig. 5.16, an estimation of the poloidal velocity can be obtained as the slope in a linear fitting of the $V_f(z)$ points inside the shear layer. This way

$$v_\theta \approx \frac{\Delta V_f}{\Delta z}\frac{1}{B} \tag{5.2}$$

experimental values of v_θ can be obtained from the floating potential profiles, as shown in Fig. 5.19. Similar non-monotonic behaviours can be seen in the cases of the 8/5 Family and Volume Scan. Velocity increases up to a given value of the radius and then decreases towards the LCFS. The velocity seems to be higher for higher densities. No clear correlations can be extracted from the 3/2 Family.

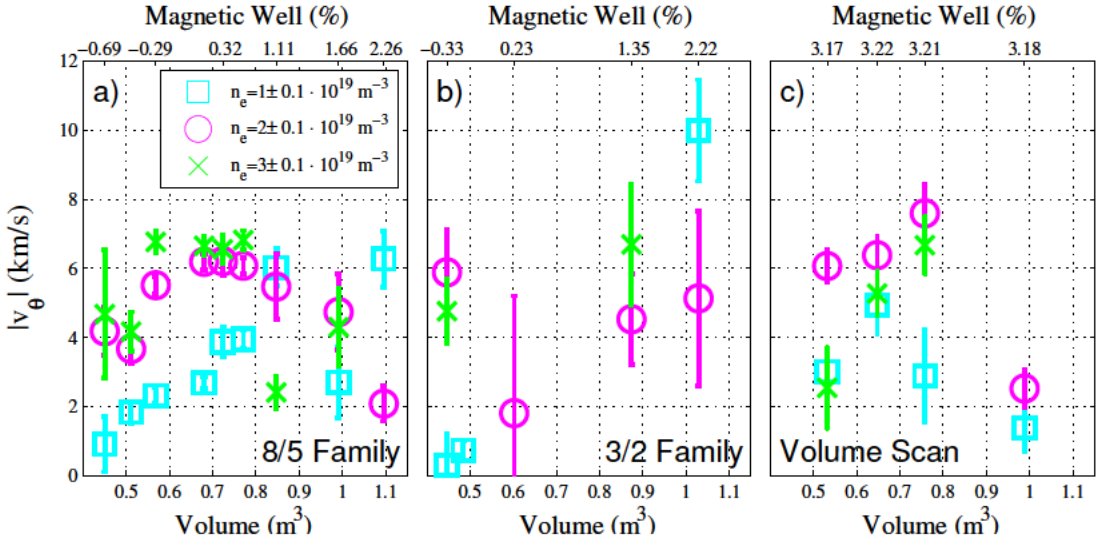

FIGURE 5.19: Poloidal velocity measured as the slope in a linear fit on the inner ($\rho \leq 0.95$) section of the floating potential profiles presented in Sec. 5.5

5.7 Turbulent particle flux and density gradient

The dynamical coupling between density gradients and particle transport has been experimentally proven to be an important self-regulation mechanism between plasma transport and gradients in several fusion devices [89]. This was done by computing the expectation value of the flux conditioned on the gradient. Further studies in TJ-II have led to the development of a technique for detecting the causal relationship between these fluctuating signals [90]. Although these quantities show great sensitivity to radial position and electron density, it was always found that the mean size of the turbulent flux events was minimal in the proximity of the most probable density gradient, and that the mean size of the flux events increased for both negative and positive excursions for the most probable gradient value, so that the resulting flux versus gradient curve attains an asymmetric 'U' shape.

A similar analysis could be carried out with the data extracted from the Top - 2D (see Subsec. 4.2.1 and Fig. 4.8 e)) for the 8/5 Family and the Volume Scan; in order to investigate the possibility that the dynamical coupling between gradients and transport is somehow connected to the magnetic well and its effects on electromagnetic turbulence (that will be thoughtfully explored in the following Chapter). Fig. 5.20 summarises the results of such analysis, presenting the expected turbulent flux for a given value of

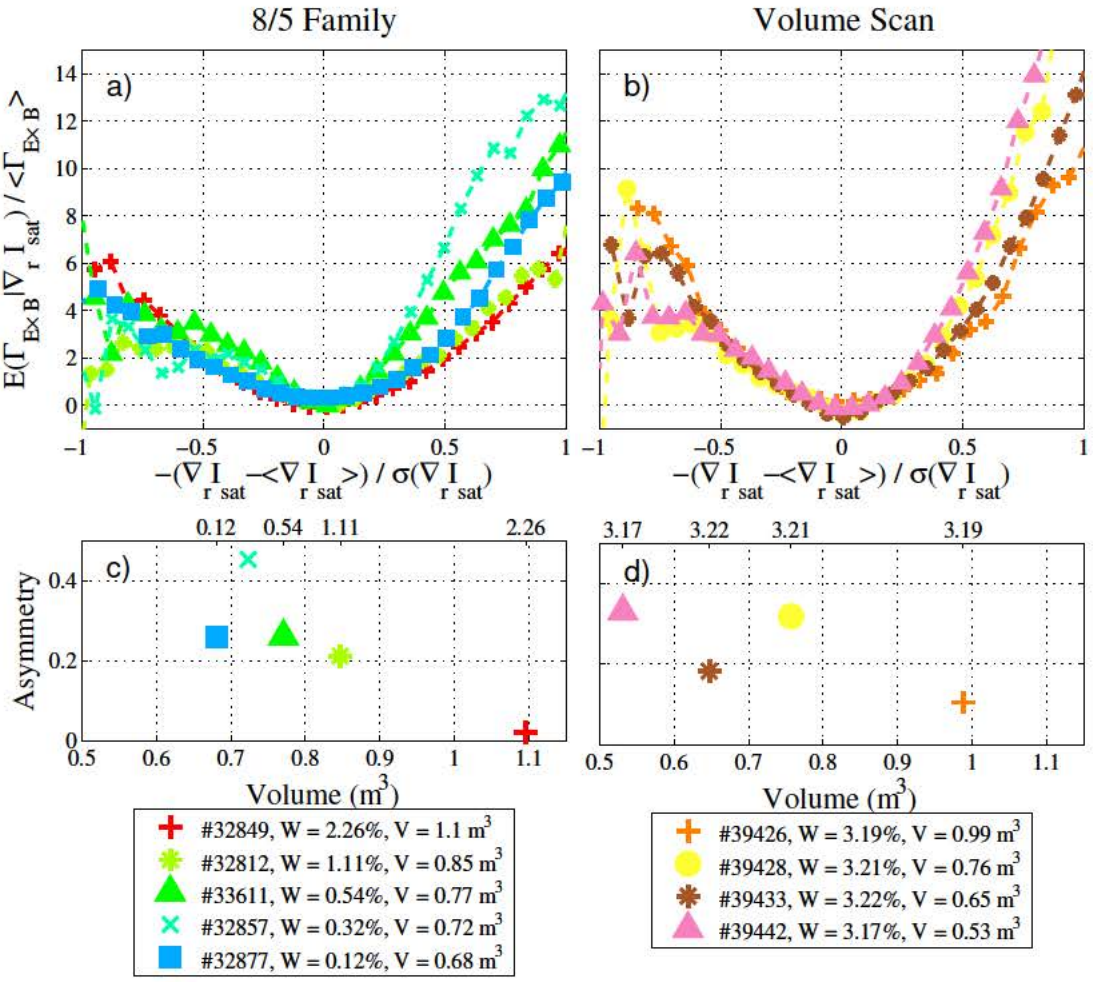

FIGURE 5.20: a) and b) Dependence of the expected value of turbulent flux for a given value of fluctuating density gradient with magnetic well and volume for $\rho = 0.89 \mp 0.01$ for the 8/5 Family and the Volume Scan versus $(\nabla_r I_{sat} - < \nabla_r I_{sat} >)/\sigma(\nabla_r I_{sat})$. The values have been measured at the plasma edge for the configurations accessible to the Top probe (see Fig. 5.18). As explained in Fig. 5.4, all the configurations in the Volume Scan are accessible for the mentioned probe. c) and d) Asymmetry of these curves as a function of plasma volume and magnetic well.

fluctuating density gradient, defined as

$$E(\Gamma|\widetilde{\nabla n}) = \int \Gamma p(\Gamma|\widetilde{\nabla n}) d\Gamma = \int \Gamma \frac{p(\Gamma, \widetilde{\nabla n})}{p(\widetilde{\nabla n})} d\Gamma \tag{5.3}$$

where $p(\widetilde{\nabla n})$ is the total probability of obtaining $\widetilde{\nabla n}$. This quantity has been computed in the vicinity of $\rho = 0.89 \pm 0.01$ for selected shots from the Volume Scan and the configurations from the 8/5 Family that could be accessed with this Langmuir probe array.

The 'U' shape of these conditional expectation values as function of the gradient implies

that not only negative gradient values above its mean value, but also those below it lead to an increased mean fluctuating flux. The gradient fluctuates around the mean or most probable gradient with a probability of distribution that decays exponentially fast for excursions from this mean gradient. Similarly, the total probability for the flux, $p(\Gamma) = \int p(\Gamma, \widetilde{\nabla n}) d\widetilde{\nabla n}$ is a peaked distribution around the most probable value of the flux. Fig. 5.20 a) shows that the shape of the curves varies gradually: lower magnetic well appears to imply larger events for similar gradient excursions.

To facilitate understanding of this variation, we introduce a quantifier of the asymmetry for such curves as:

$$A = \frac{\sum E(\Gamma|\widetilde{\nabla n})[-\widetilde{\nabla n}/\sigma(\widetilde{\nabla n})]}{\sum E(\Gamma|\widetilde{\nabla n})} \tag{5.4}$$

Fig. 5.20 c)-d) show how this quantity seems to depend more clearly on the magnetic well than on the plasma volume, giving account of the lower variation of the conditional expectation curves when only the plasma volume is reduced.

Chapter 6

Electromagnetic turbulence[1]

Once the to access Mercier-unstable configurations with good quality plasmas is surprisingly demonstrated, we introduce turbulence studies to try to describe and explain this behaviour. Electrostatic and magnetic turbulence have been measured in different radial positions, giving special attention to the 8/5 Family.

6.1 Edge electrostatic turbulence

Following up with the results presented in Sec.5.5, Langmuir probes are also a suitable diagnostic for measuring electrostatic turbulence. Once the mean value of the floating potential is substracted, the RMS of these signals (like the ones shown in Fig. 5.15 d)-f)) can be taken as a measure of the electrostatic turbulence level [88]. Again, this analysis has been completed for three representative values of line density at different positions near the plasma edge. Fig. 6.1 summarises this analysis: the first row shows the RMS of the V_f signal around the shear layer position. Fig. 6.1 a) shows that electrostatic turbulence level depends weakly of magnetic well, but decreases as the well increases, as it is seen clearly how electrostatic turbulence is always greater than the one exhibited by the standard configuration (100_44_64). A drastic increase in the electrostatic turbulence is only observed in 100_41_109, the lowest magnetic well case of all the explored. Fig. 6.1 c) proves that, as expected, no relation between plasma volume and the electrostatic turbulence can be drawn. Unfortunately Fig. 6.1 b) gives

[1]The results presented in this chapter were published in [80].

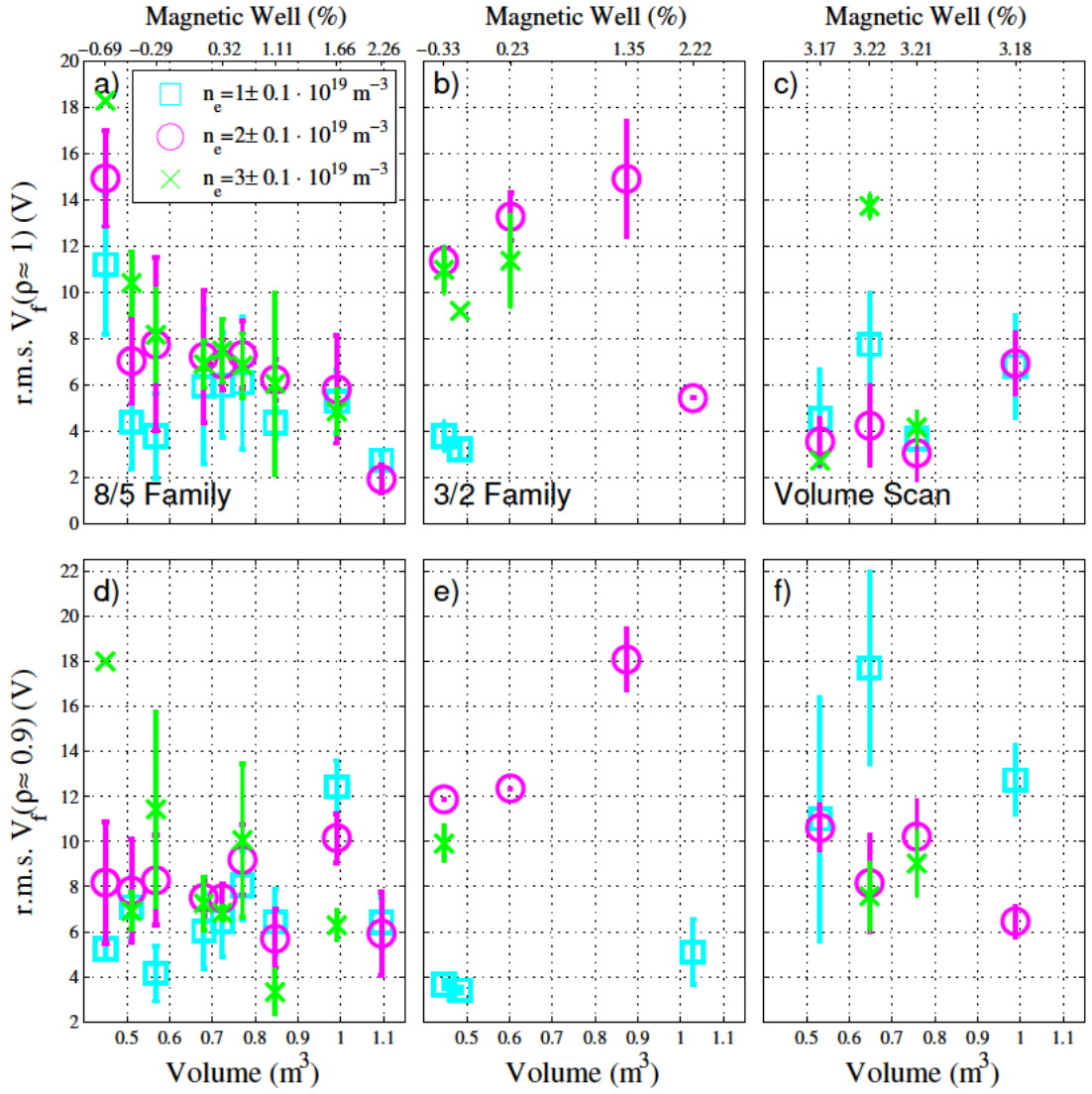

FIGURE 6.1: Electrostatic turbulence at plasma edge measured as the RMS of the floating potential. Row 1 presents the data around $\rho \approx 1$ and row 2, $\rho \approx 0.9$. For families 8/5 and 3/2 these results come from the array at the bottom position. The volume scan case has been analysed using the array from the top access point.

no conclusive information about the 3/2 Family, because of the low reproducibility of the floating potential profiles in this block of experiments.

The second row, Fig. 6.1 d)-f) provides similar results at a slightly inner position. It is clear that in this position the RMS analysis shows no obvious dependencies from these data. Nevertheless, a similar analysis can be carried out without selecting specific density values by computing the Fourier spectrum of the V_f signals. Analysing larger arrays of data instead of the portions selected by the density values throws a clearer result: Fig. 6.2 a)-b) show clearly how the high magnetic well configurations exhibit lower levels of electrostatic turbulence and how this quantity grows steadily as the Mercier conditions

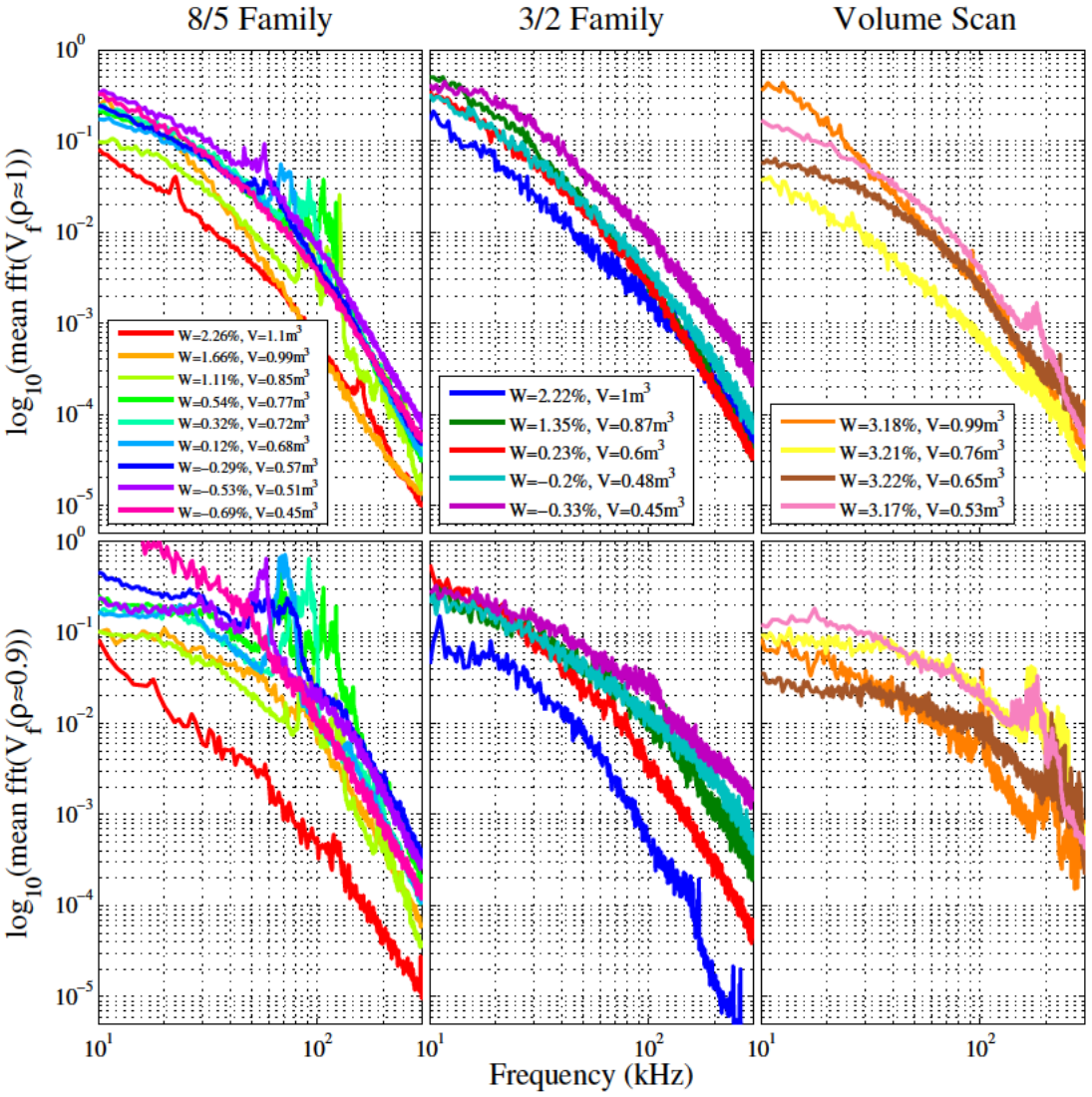

FIGURE 6.2: Electrostatic turbulence at plasma edge measured as Fourier spectrum of the floating potential power. The pin positions and probe access points are the same as in Fig. 6.1.

become theoretically more unstable. Fig. 6.2 c), hints again that no clear relationship between electrostatic turbulence and plasma volume can be found. Similar trends are found when the same analysis is applied to pins located around $\rho \approx 0.9$: increasing turbulence as the magnetic well is reduced and, for Family 8/5, the appearance of modes whose frequencies (between 100 and 50 kHz) seem to depend on the value of the magnetic well 6.2 d). A further much detailed analysis of these modes will be presented in Sec. 6.4. This weak dependence of the turbulence level on magnetic well does not seem to have any effect on confinement.

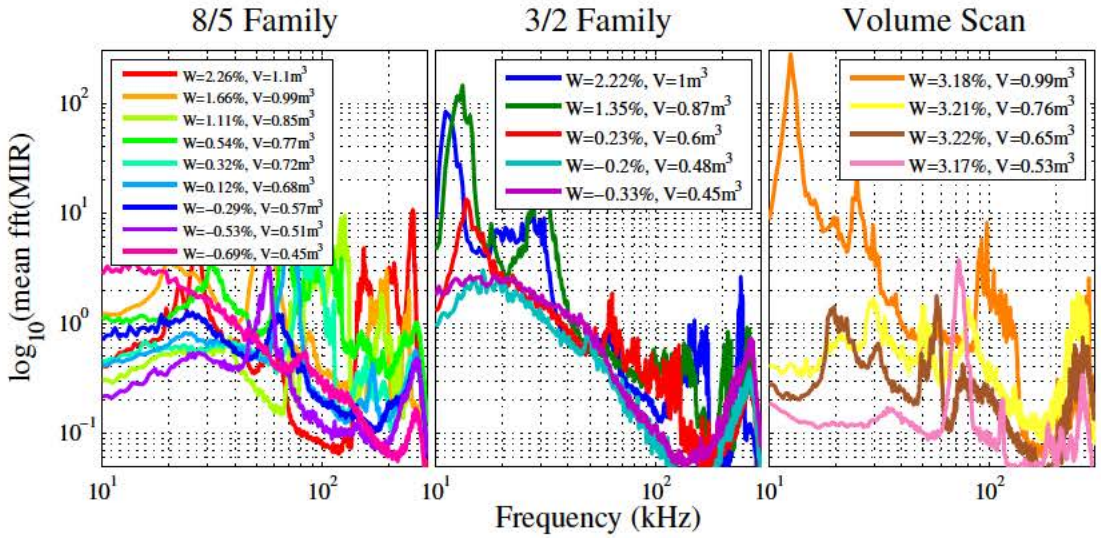

FIGURE 6.3: Magnetic turbulence at plasma edge measured as the Fourier spectrum of the Mirnov coil power.

6.2 Magnetic turbulence

Mirnov coils can detect magnetic fluctuations in the outer part of the plasma (typically $\rho \geq 0.3$ depending on the amplitude of the mode). Fig. 6.3 provides our first approach to the magnetic turbulence analysis by providing the Fourier spectrum of the Mirnov coil signals for each configuration. These plots show, again, the presence of modes whose frequency happens to depend on the value of the magnetic well. In order to perform a deeper exploration of these modes we have used Mirnov coils in combination with HIBP [91], allowing measure the mode's position.

HIBP can measure the electrostatic potential, the detected probing beam current I_{tot} (which is an increasing function of density) and their fluctuations along the whole radius in most of the configurations [92]. The mode is localised radially by scanning the sample volume position of the HIBP along the minor radius and calculating the coherence between the HIBP and the Mirnov coil signals. The area of the statistically significant coherence will indicate the position of the mode. Fig. 6.4 shows the spectrograms of the Mirnov coil signal (top panel) together with the coherence between Mirnov signal and I_{tot} and electrostatic potential measured by HIBP. The bottom panel shows the corresponding radial position of HIBP sample volume, where negative radius means high field side (HFS) and positive one means low field side (LFS), and the temporal evolution of I_{tot}, being a proxy for the radial profile of the plasma density. Note that the local maxima of I_{tot} are located symmetrically at $\rho = \pm 0.5$ while the local minimum

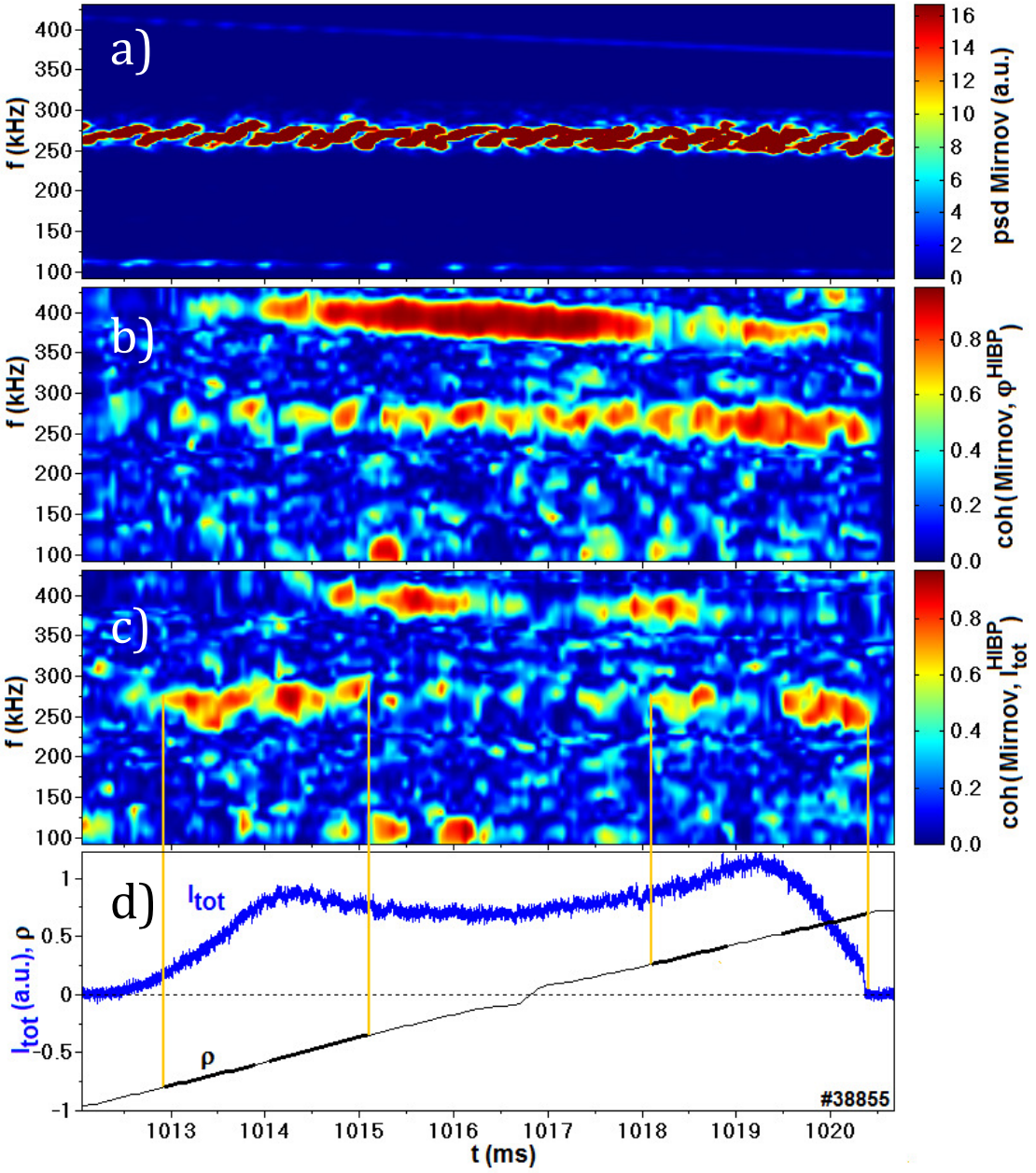

FIGURE 6.4: a) Time evolution of the Mirnov coil signal spectrogram. b) Coherence spectrogram between Mirnov coil and electrostatic potential measured by HIBP. c) Coherence between Mirnov coil and total beam current I_{tot}, representing electron density. d) Bottom box: temporal evolution of I_{tot}, representing radial profile of electron density, effective radius of the measurement, positive means LFS and negative HFS. Credit: TJ-II's HIBP Group.

is located at $\rho = 0$. $I_{tot}(\rho = -0.5) < I_{tot}(\rho = 0.5)$ due to the attenuation factor at the longer trajectories of the probing beam passing the area of higher densities at the HFS. The maximum coherence between Mirnov and these two HIBP signals show the location of the modes. Note that the density perturbations due to the modes are more pronounced in the area of the density gradient, positive for $|\rho| < 0.5$ and negative for $|\rho| > 0.5$, and almost vanishing near the area of the local extrema $|\rho| \approx 0.5$ and $\rho \approx 0$.

Contrarily, the potential perturbations are more extended radially. In this particular case the steady frequency mode with $f \approx 400$ kHz is located at the radial positions $0.6 \geq \rho \geq -0.6$, the chirping mode with f$\approx$ 250 kHz is located at the radial positions $0.75 \geq \rho \geq -0.75$. Note that the chirping mode in potential is more pronounced in the LFS, so has an antiballooning structure [93]. The shot of Fig. 6.4 corresponds to the configuration 100_44_64, with the largest magnetic well $W = 2.36\%$.

6.3 Spatial structure of the turbulence

The broadband turbulence is measured in some configurations of the 8/5 Family by Doppler reflectometer [94] in this configuration scan at the interval $0.7 < \rho < 0.85$. A set of reproducible discharges in the same configuration with wave vector scans is performed to probe the turbulence level at different perpendicular wave vectors and at given positions (see Fig. 6.5 a), where the probed wave vectors for several magnetic configurations are plotted). The turbulence level is, therefore, obtained at the radial positions where the wave is reflected and for the chosen wave vectors in plasmas with different magnetic wells. Fig. 6.5 b) shows the turbulence level at the same positions, wave vectors and configurations of Fig. 6.5 a), conserving the symbol and colour code. Finally, all the points are plotted together in Fig. 6.5 c), showing a single spectrum of perpendicular wave vector for all of the cases. The fact that no appreciable differences can be found between the different configurations means that the wave vector spectrum is the same, for the same values of densities, in all of the cases. Therefore, the spatial structure of the turbulence is the same, even if the magnetic well has changed.

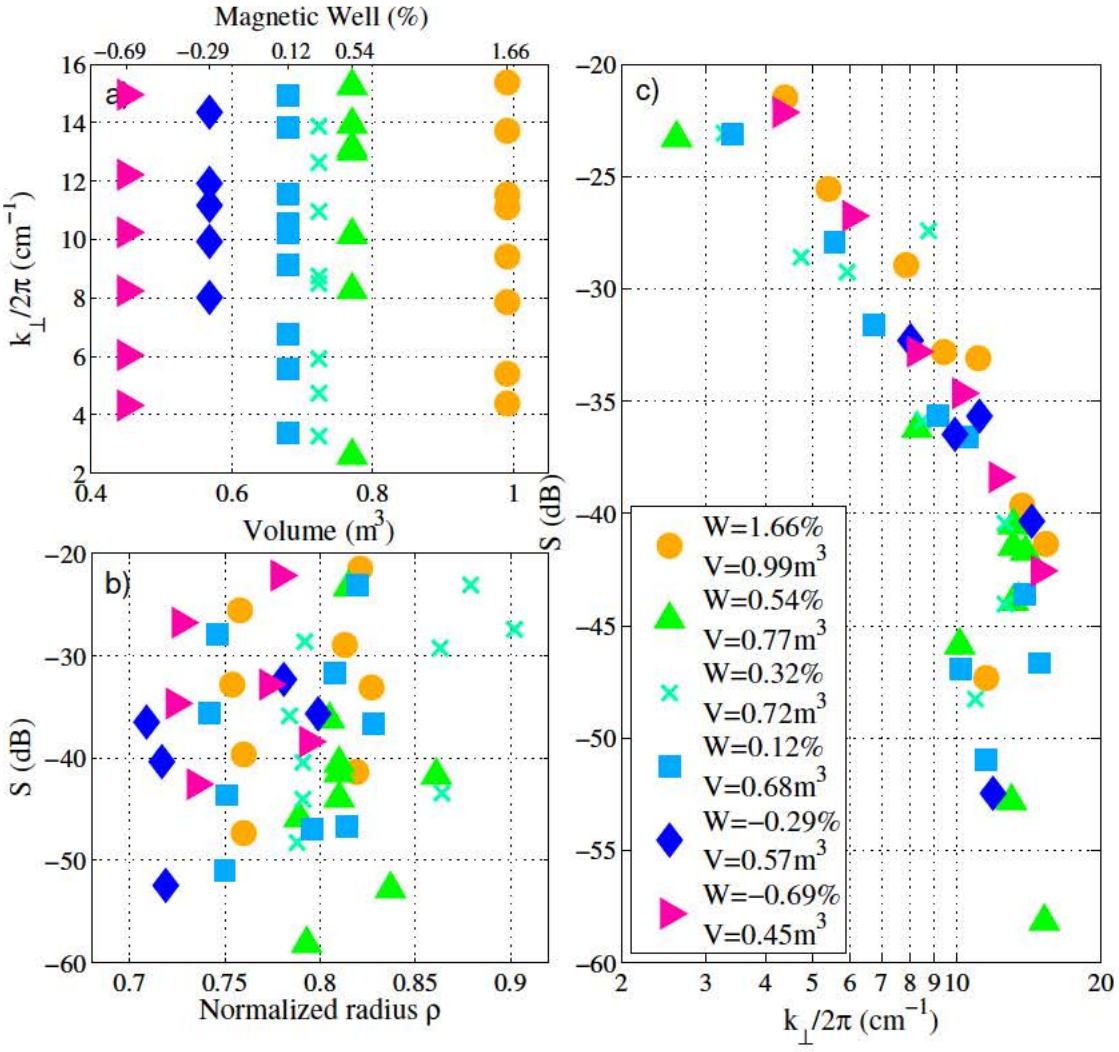

FIGURE 6.5: Spectrum of the wave vector measured by Doppler reflectometry on configurations from the 8/5 Family. a) Wave vectors explored. b) Turbulence level at different radial positions, wave vectors and magnetic configurations. c) Spectrum of wave vector for all the configurations and positions. Data courtesy of Teresa Estrada.

6.4 Coherent mode spectra

Figures 6.2 a) and 6.3 a) show the presence, for the 8/5 Family, of coherent modes with frequencies decreasing as the magnetic well did so. These modes are of Alfvénic nature, as we will demonstrate. In principle, the Alfvén frequency

$$2\pi f_A = k_\parallel v_A \approx \frac{B}{\sqrt{M\mu_0 n_e}} |m\iota - n| \tag{6.1}$$

depends on the electron density n_e, the average ion mass M, the rotational transform ι and the poloidal and toroidal numbers of the mode, m and n. Given the density and

current conditions, the model proposed in [95]:

$$\iota(\rho) = \iota_{vac}(\rho) + C(\rho)I_p \tag{6.2}$$

can be used. In Eq. 6.2 a simple relationship between the real rotational transform profile, its vacuum value and the plasma current is established as long as the perturbation driven by the current is not too large. $C(\rho)$ is a function that depends weakly on the radius for $\rho > 0.3$ [96]. This approximation allows us to write the Alfvén frequency as

$$2\pi f_A = \frac{B}{\sqrt{M\mu_0}} \frac{|m\,(C(\rho)I_p + \iota_{vac}(\rho)) - n|}{\sqrt{n_e}} \backsim \pm \frac{|I_p|}{\sqrt{n_e}} \tag{6.3}$$

Plotting $\pm\frac{|I_p|}{\sqrt{n_e}}$ and comparing it with the power spectral density (PSD) of our signals should tell us if the behaviour of the coherent modes matches this quantity. With this purpose we present the figures 6.6-6.8. In them we offer a summary of the results of the analysis of the spectrum of the Langmuir probes (around $\rho \approx 0.9$) for being the ones to provide a stronger signal and the Mirnov coils.

For the 8/5 Family a clear set of coherent modes with frequencies decreasing from 150 kHz to 50 kHz appears both in the magnetic (Fig. 6.6 a)) and electrostatic spectra (Fig. 6.6 b)). The frequency and strength of these modes decrease with magnetic well until it vanishes completely for 100_41_109, the most Mercier-unstable configuration of the family. Such a phenomena is not observed when a similar analysis is performed upon shots from the 3/2 Family, were Alfvénic modes are observed between 50 and 150 kHz in the Mirnov coils (Fig. 6.7 a)), although almost no trace of them can be found in the electrostatic spectrum (Fig. 6.7 b)). Finally the Volume Scan family shows EM modes, probably of Alfvénic nature, although no dependence between their frequency and the plasma volume can be extracted. This points to a relationship between mode frequency and magnetic well observed in the 8/5 Family that needs further exploration.

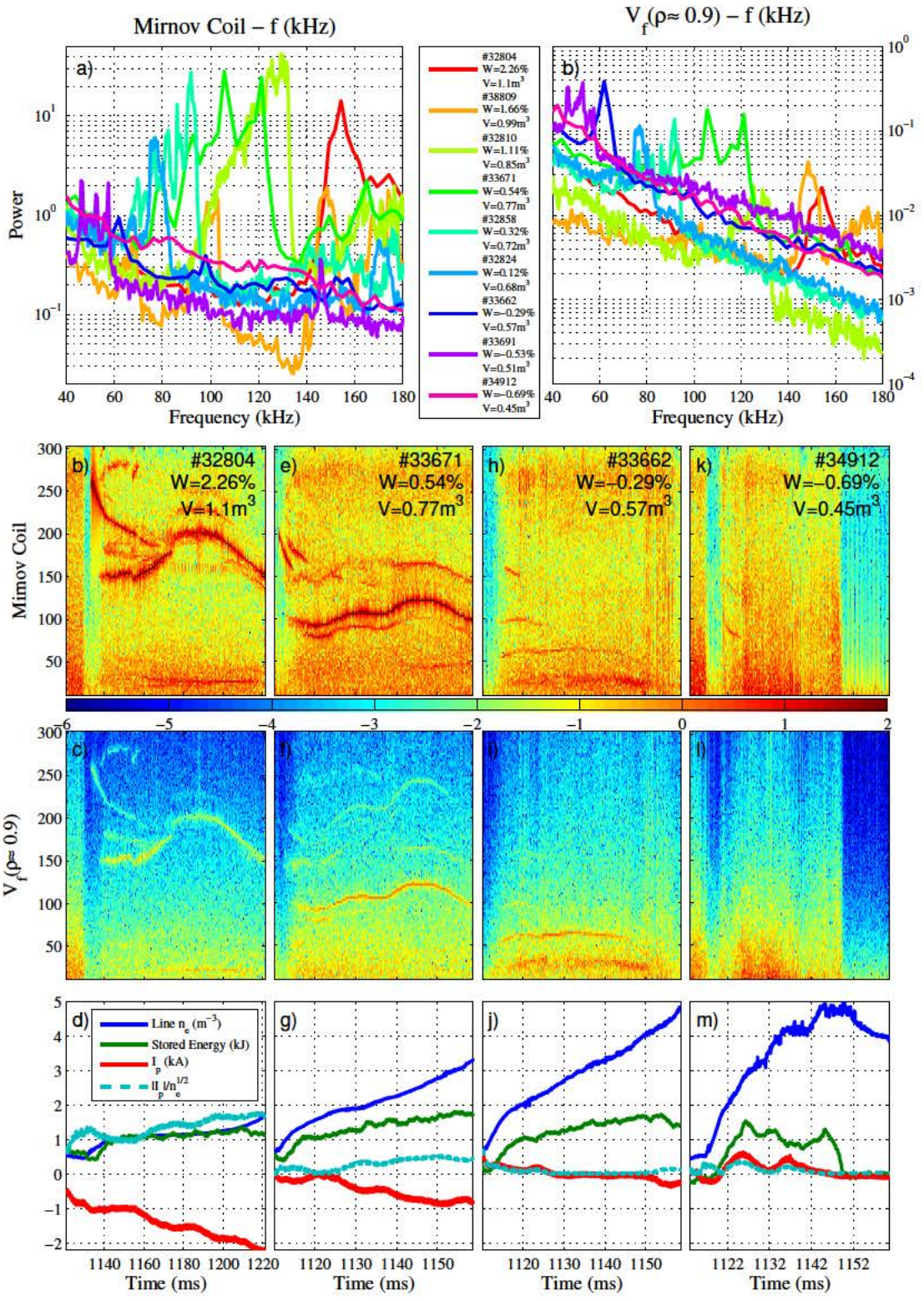

FIGURE 6.6: For selected shots of the 8/5 Family with NBI counter-injection. Row 1: Fourier spectrum for a) Mirnov coils b) Floating potential around $\rho \approx 0.9$. Row 2: Mirnov coil PSD for four shots from different configurations. Row 3: V_f PSD for the same plasma pulses and configurations. The same colour bar applies to rows 2 and 3. Row 4: General plasma parameters vs. time during the mentioned pulses.

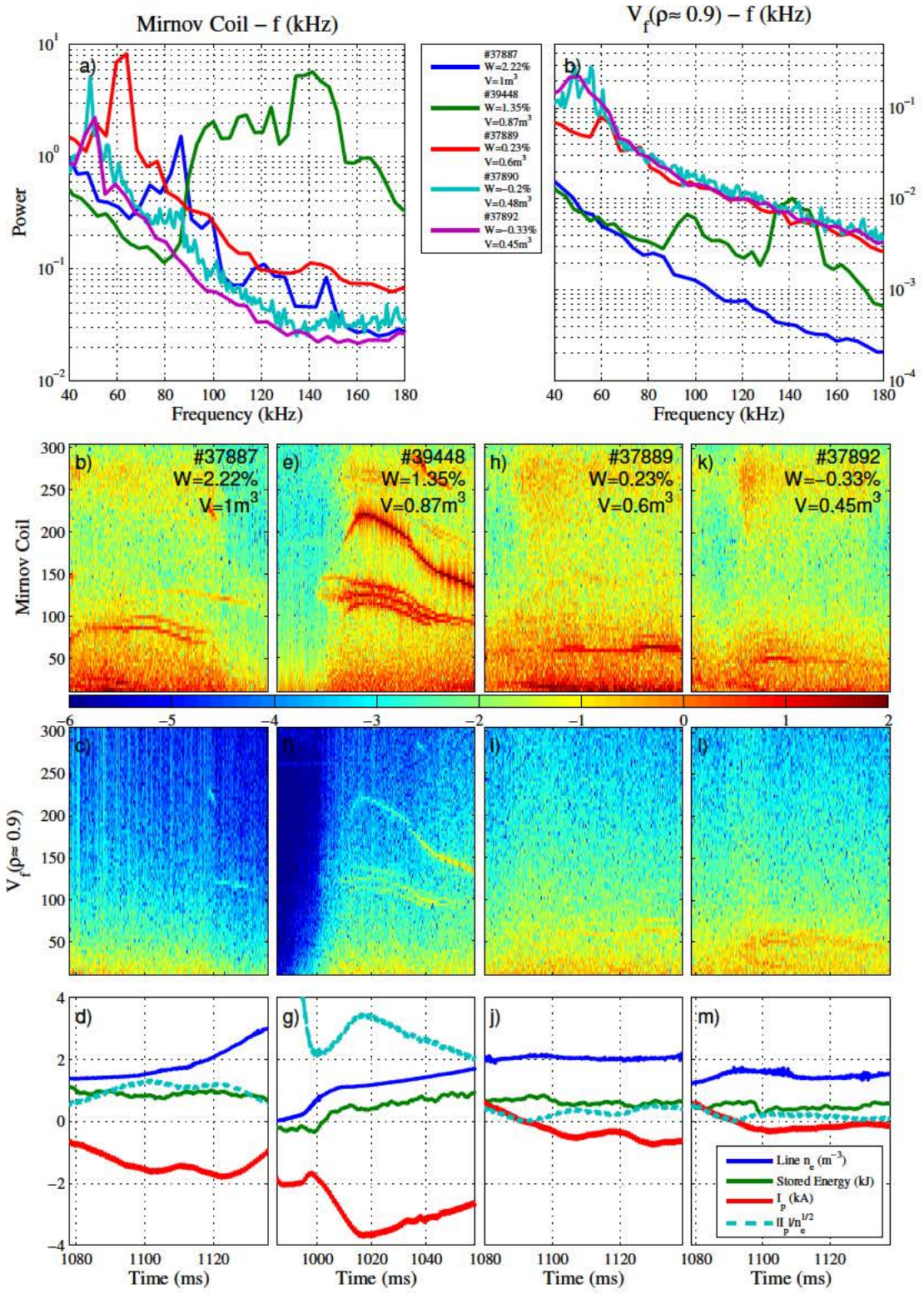

FIGURE 6.7:]
Electromagnetic spectra for selected shots of the 3/2 Family with NBI counter-injection.

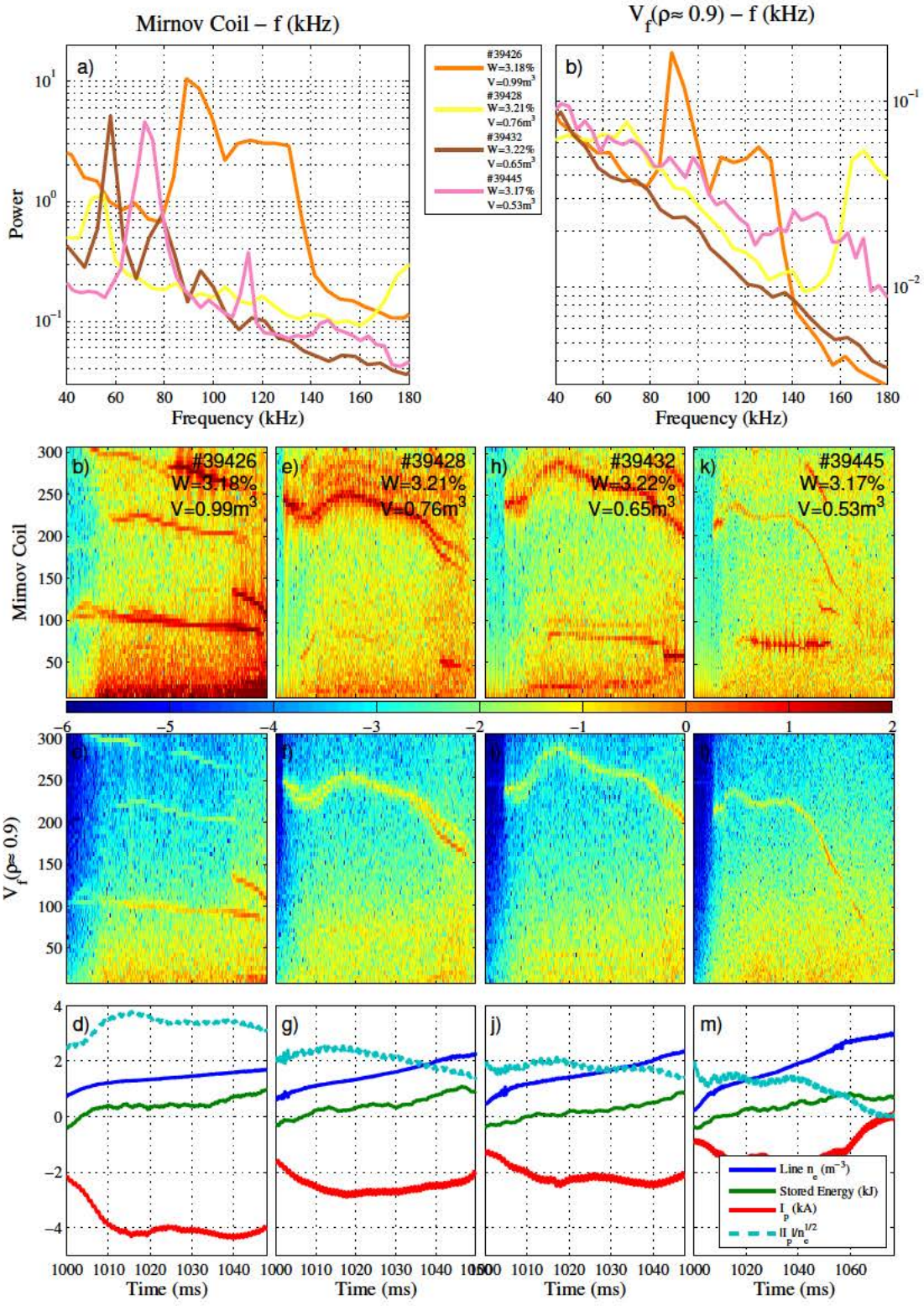

FIGURE 6.8: Electromagnetic spectra for selected shots of the Volume Scan with NBI counter-injection.

6.5 Modes for the 8/5 Family

6.5.1 Low frequencies (up to 20 kHz)

The onset of an oscillation at $f \approx 10 - 20$ kHz happens in several cases, showing that the rational creates a rotating island (see [97] for the effect of a rotating island) mainly in configurations with low magnetic well or magnetic hill, although this behaviour is not systematic and depends on the plasma characteristics. For instance, the behaviour of the island depends strongly on plasma current, which is able to move the resonance outwards in the plasma, when it takes negative values, or to inner positions for $I_p > 0$. The change of the position of the resonance with respect to the vacuum one is given by $\Delta\rho \approx 0.1$. The onset of the island could have influence on the Alfvénic spectrum [98], since the structure of magnetic field is modified and new gaps can appear in the continuum. The effect of resonances on the Alfvén spectrum has been shown in [99]. The toroidal current that appears experimentally is the sum of the bootstrap current and the one driven by the NBI system.

6.5.2 Intermediate frequencies

In the case of counter-NBI, a mode of no-Alfvénic nature appears in the configurations with intermediate magnetic well. This mode happens at frequencies close or less than $f \approx 40$ kHz. Fig. 6.4 shows the characteristics of this mode in the configuration 100_44_87, with middle magnetic well value $W = 0.32\%$, measured with HIBP and bolometers. The mode can be detected both in the potential and in the density signals. The location of the mode is around $\rho \approx 0.8$, in the HFS, with a width $\Delta\rho \approx 0.3$ as can be seen in the bottom panel of Fig. 6.4. This mode is not of Alfvénic nature, since does not evolve with the density but co-exists with an Alfvén Eigenmode (AE), so we conjecture that it could be a Geodesic Acoustic Mode (GAM). The GAM-candidate mode has a constant frequency over the radii $0.3 < \rho < 0.8$ and appears in both potential and density spectra, being more pronounced in the potential.

Linear gyrokinetic calculations on TJ-II show that a GAM appears at frequencies $f \approx$ 50 kHz [100]. Nevertheless, those calculations predict also a strong collisionless damping of this type of modes in the high ripple and high ι TJ-II configurations, which should

prevent their appearance in those plasmas. Reference [101] shows the possibility that GAMs could be driven by fast particles or fast particle driven modes, which is a feasible explanation for the presence of this mode in TJ-II plasmas.

These modes are detected only in the configurations with intermediate values of the magnetic well. The reason for this is not clear but it could be due to the fact that the AEs appear in the appropriated frequencies to drive the modes, despite of the damping. With the available data we could not extract clear conclusions on the dependence of frequency with configuration. Further research is needed to elucidate if this is really a GAM and which mechanism is acting for the mode to survive.

6.5.3 High frequency modes

Despite of the fact that the vacuum rotational transform is very similar in all the cases, Fig. 6.6 a)-b) probes that, for counter-NBI injection, the mode structure changes drastically when decreasing the magnetic well, showing a non-monotonic behaviour of the amplitude, and a decrease of the typical frequencies. The influence of the plasma characteristics, i.e. current and density, are also taken into account to describe these modes by using, both in equilibrium calculations with VMEC code and spectral calculations. Fig. 6.6 shows the onset of the Alfvén mode for four configurations with counter-NBI, the first one with deep magnetic well, the second with an intermediate value and the last ones presenting magnetic hill. The modes are of Alfvénic nature in all the cases, as it is possible to detect the frequency dependence on current and density given by Eq. 6.3 in all the cases but the last one (with highly negative magnetic hill). These trends are not observed when the other NBI (co-NBI) injector is used.

6.6 Comparison with simulations

As it has been stated above, the frequency changes observed from one configuration to another one must be attributed to the changes in the magnetic configuration, as it is shown by calculations performed with the codes STELLGAP and AE3D [102], which can justify the strong frequency variation as well as the spatial location during the magnetic well scan. We will obtain all the possible modes and will check which of them are destabilised in our experimental conditions. The fact that only some of the modes

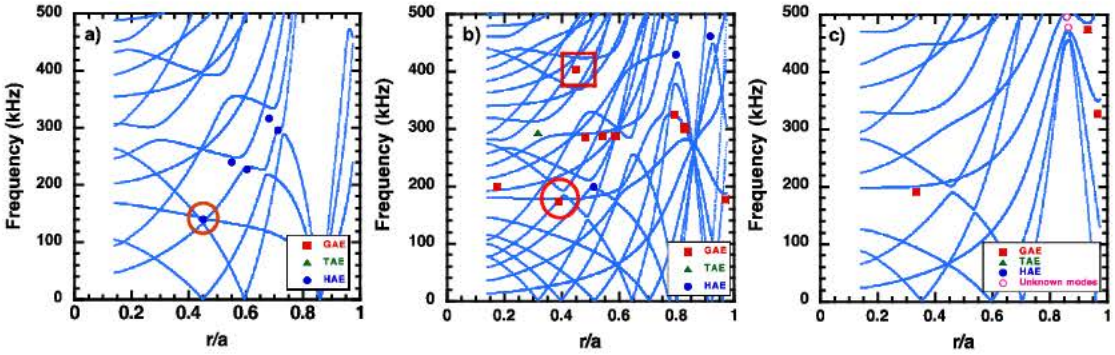

FIGURE 6.9: Calculations of the continuum spectrum with STELLGAP and of the mode position and type with AE3D for the configuration 100_44_64, with deep magnetic well ($W = 2.27\%$); for the families a) $N_f = 0$, b) $N_f = 1$, and c) $N_f = 2$. The plots show the possible frequencies and positions of the experimentally found modes, shown in Fig. 6.6, which are marked with circles. No mode is marked in the $N_f = 2$ family, since none corresponds to the measured characteristics. It is also marked with a square the mode appearing in Fig. 6.4, with frequency f ≈ 400; kHz at $\rho \approx 0.45$, belonging to family $N_f = 1$.

are destabilised is related with the actual population of fast particles: fast ions are able to resonate only with some of the possible modes of the spectra.

We consider the experimental conditions of the cases shown in Fig. 6.6, including the current and the density profiles when performing the calculations. The current profile is assumed to be given by Spitzer resistivity. Fig. 6.9 shows the calculations performed with STELLGAP and AE3D for the configuration 100_44_64, with magnetic well $W = 2.27\%$ for three families of modes $N_f = 0$, 1, 2. The symbols in the figure plotted on the continuum spectrum mark the frequency and the radial position of the modes, given by the maximum of the amplitude estimated by AE3D. The nature of the modes is also shown. All these modes, which could be potentially destabilised by the presence of fast ions, can be compared with the experimental results, regarding the frequency and the radial position. We can then consider the mode of Fig. 6.6 row 1 and compare with calculated ones in Fig. 6.9. We see that the possible modes that are destabilised are a Helical Alfvén Eigenmode (HAE) located at $\rho \approx 0.45$ of family $N_f = 0$ (see Fig. 6.9 a), where the possible mode is marked with a circle) or a Global Alfvén Eigenmode (GAE) at $\rho \approx 0.4$ belonging to the family $N_f = 1$ (see Fig. 6.9 b), marked with a circle). These positions are in qualitative agreement with HIBP measurements, as estimated by the same procedure shown in 6.4. No coincidence is found in the family $N_f = 2$.

In order to characterise the modes appearing in the configuration 99_44_87 (with magnetic well $W = 0.32\%$), we follow the same procedure and compare Fig. 6.6 row 2 with

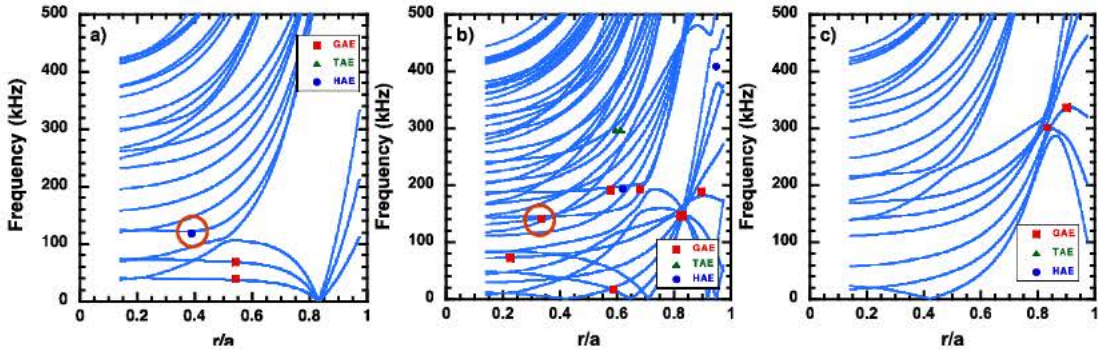

FIGURE 6.10: The same as Fig. 6.9 for the configuration 99_44_87 with intermediate magnetic well ($W = 0.32\%$). No possible destabilised modes are found in the family $N_f = 2$, while a GAE belonging either to family $N_f = 0$ or $N_f = 1$ is found (marked).

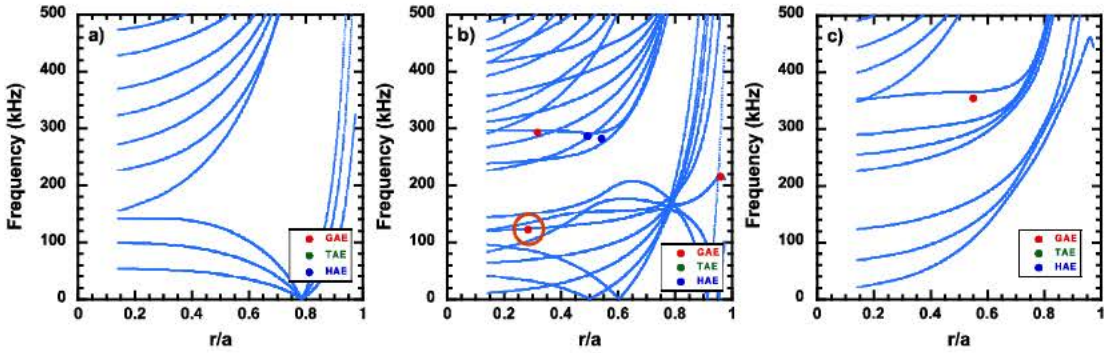

FIGURE 6.11: The same as Fig. 6.9 for the configuration 100_42_104, with magnetic hill ($W = -0.69\%$). No modes appear in families 0 and 2. The possible experimental GAE is marked in the family $N_f = 1$

the calculations of shown in Fig. 6.10. The mode that appears in the configuration could be a HAE whose maximum is located close to $\rho \approx 0.45$, belonging to the family $N_f = 0$ or it could be a GAE with maximum located close to $\rho \approx 0.3$, belonging to the family $N_f = 1$. The position is in qualitative agreement with HIBP measurements, which show pretty wide modes.

Finally, the properties of the modes that appear in configuration 100_42_104 (with magnetic well $W = -0.53\%$) can be explored similarly, taking into account figures 6.6 row 3 and 6.11. Considering the frequency that appears in former and the location of the mode measured by HIBP, we see that the mode that appears could be a GAE at $\rho \approx 0.3$ of family $N_f = 1$. The calculated location is in qualitative agreement with HIBP measurements ($\rho \approx 0.3$) but the calculated frequency is too high in comparison with the experimental results.

On top of that, we can identify the high frequency mode $f \approx 400$ kHz that appears in Fig. 6.4. Having a look on Fig. 6.10 b) we see that the mode is located closer to

the centre and, hence it is a GAE belonging to $N_f = 1$, whose maximum is located at $\rho \approx 0.45$ (marked in Fig. 6.9 b) with a square).

Chapter 7

Visible light analysis at JET-ILW with fast visible cameras[1]

Since its installation in 2008 [60], CIEMAT has been responsible for the intensified fast visible camera at JET. Of the several JET-ILW experiments where manning and data have been provided as part of the fast visible camera operation team, two fields have been investigated intensively in the course the C30-C36 campaigns. Both are key tasks in the path of understanding the behaviour of a large tokamak with Beryllium walls and a tungsten divertor: ELM dynamics in the divertor and disruption mitigation gas tracking. But before we extract any results, we will seek for a complete interpretation of the data provided by the fast visible camera. Fig. 7.1 shows the evolution of a typical ELM recorded by KL8A: the provided frames are small and blurry, and the low light settings necessary to extract a non-saturated image of the strike points prevent us from a clear image of any other part of the vacuum chamber. A method to locate and understand the light sources that we aim to analyse is necessary, and we will describe it in the opening section of this Chapter.

7.1 Correlating KL8A with other visible light diagnostics

In spite of the enhanced time resolution that KL8A can provide, there are two features the diagnostic lacks:

[1] A general outline of the first results obtained with the intensified fast visible camera at JET was presented in [68]

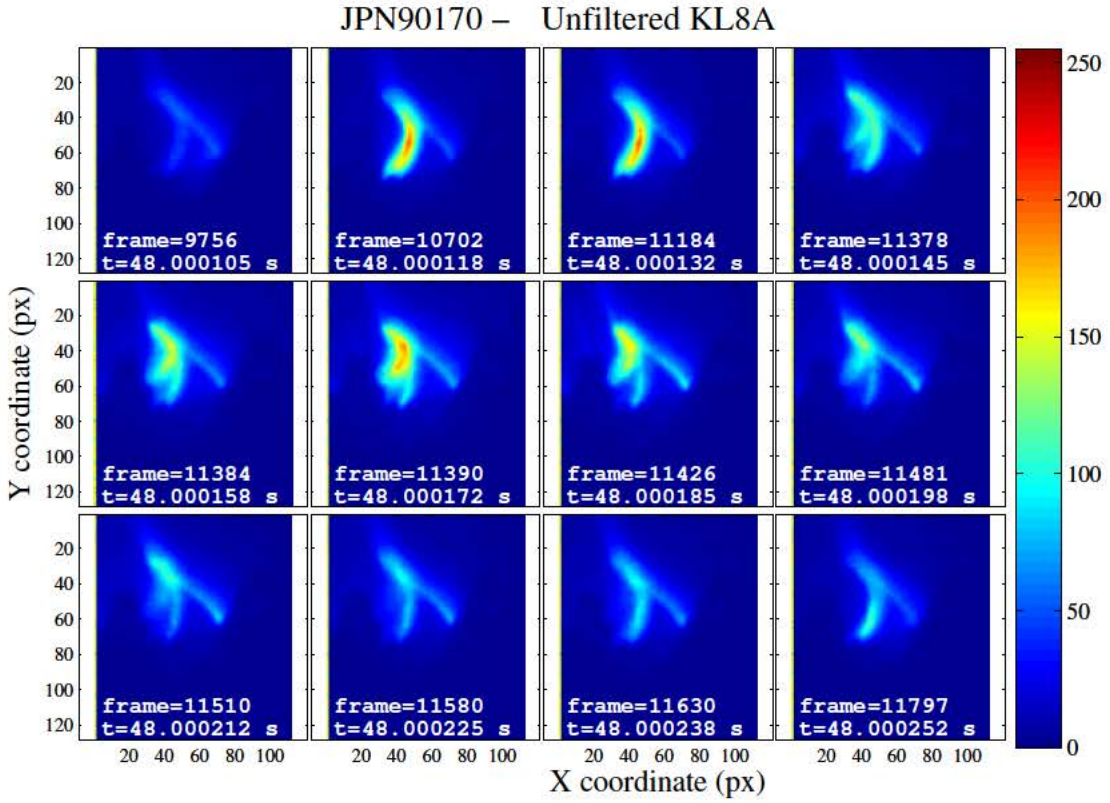

FIGURE 7.1: Example of an ELM from JET Pulse Number (JPN) 90170 on the divertor recorded with unfiltered lens by KL8A. Recording parameters: f = 75kHz, gain = 630V, exp = 3μs. Pedestal temperature $\approx$ 0.8keV. The same colour map and limits has been selected for all the shown frames. The false colour has been (and will be) used for better visualisation.

1. High spatial resolution, which reduces the sharpness and definition of the objects captured.

2. Absolute calibration, preventing us from using the ionisations per photon rate exposed in Fig. 4.1 to extract information about absolute fluxes on the SOL.

This is why relating KL8A's signals with other diagnostics looking at the divertor in JET seems like a reasonable first step before we extract any isolated conclusions from them.

7.1.1 D_α spectroscopy

There are twenty spectroscopy channels looking at the divertor, ten at the inner region and other ten at the outer one (see Fig. 7.2 a)-c)). With a 10 kHz sampling frequency, they allow tracking the D_α emission and several impurities, like Tungsten or Beryllium

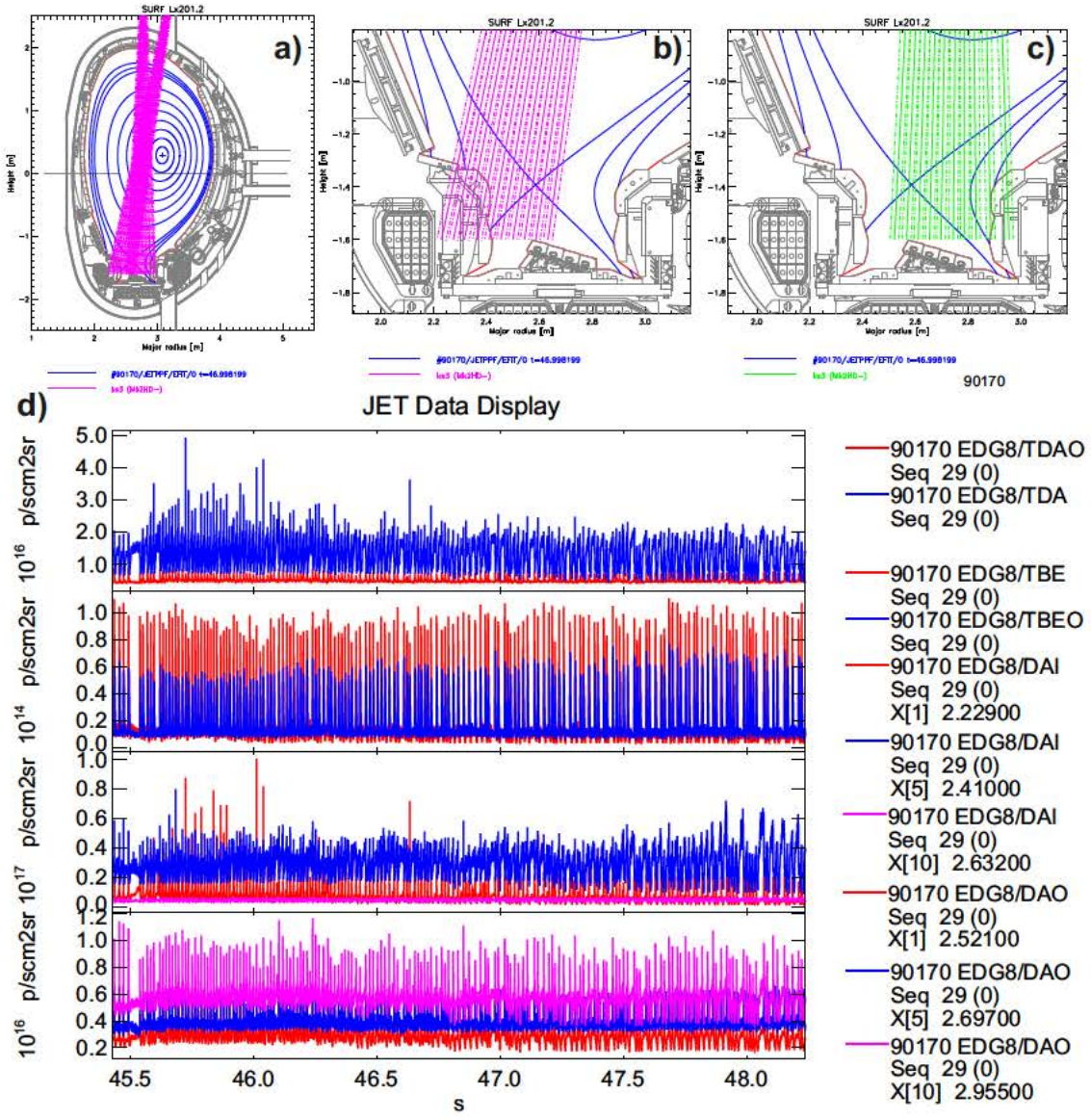

FIGURE 7.2: a) D_α spectroscpy channels for JET's divertor. b) Detail view of the ten D_α channels assigned to the inner part of the divertor. c) Similar view for the ten spectroscpy channels corresponding to the outer region of the divertor. d) From the JET data display tool, integrated D_α and BeII inner and outer divertor signals and selected D_α channels from both sectors of the divertor during an ELMy phase from JPN90170.

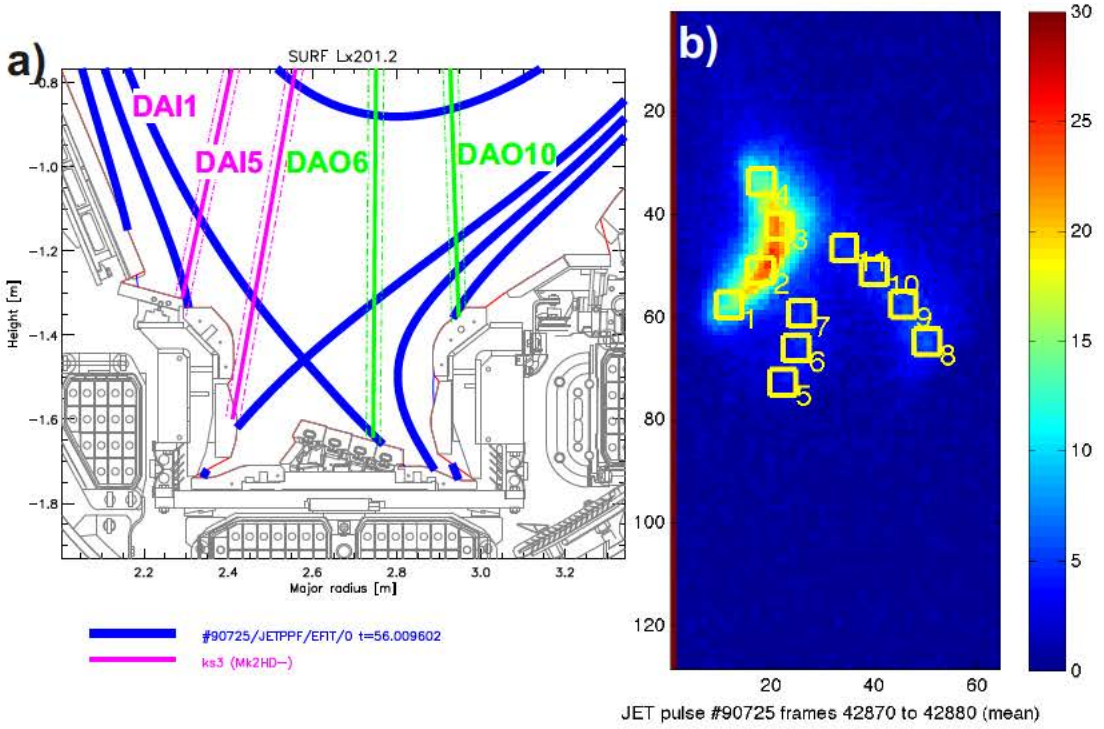

FIGURE 7.3: For JPN90725 a) Diagram of the magnetic surfaces, divertor, strike points and D_α selected spectroscpy channels at the beginning of KL8A's recording time window. b) Ten-frame average taken from KL8A recording with 5x5px ROIs along the divertor. Recording parameters: fps=25kHz, gain = 640V, exp=2μs

(whose spikes are, at the moment, currently used as the ELM detector at JET-ILW). These signals allow tracking the recycling emission with a time resolution lower than the provided by the fast visible camera, but with more accuracy to locate the sources of this light at the divertor. Spectroscopy signals are calibrated, so they are the natural diagnostic to compare and support KL8A's data.

A systematic method has been developed to compare fast visible recordings with D_α spectroscopy. The idea behind it is to search for the spectroscopy channels that behave more similarly to the time traces generated by the fast visible camera. It has been successfully tested in $\approx$ 15 ELMy phases from different experiments recorded between 2013 and 2016 phases at JET with several recording conditions. JPN90725 will be used as an example in the following figures, to illustrate the steps that our method follows:

1. Select, draw and analyse the regions of interest (ROIs) in the fast visible camera data (see Fig. 7.3 b)). The functions presented in the Appendix A.2.2 allow us to draw time traces of the three clear sources of light at the divertor during the

ELMy phases: the inner and outer strike points and the upper region of the inner divertor, around tile 1.

2. A simple ELM detector separates the signals in ≈10 ms time windows by applying a threshold to the integrated BeII signal in the inner divertor (the peak in the particle influx produced by the ELM produces erosion and heat in the walls, which translates as a sharp spike in the BeII signals). Fig. 7.4 shows one of these ELMs (usually each video contains from tens to hundreds of ELMs): integrated signals are presented in panels a)-c), d) contains some individual D_α channels, e) the three ROIs selected from KL8A and f) a heat map from an horizontal line going through the three areas of interest. Panels d) and e) behave in a very similar way, although sampling frequency in KL8A is 2.5 times higher than in the spectrometers.

3. To address mathematically the similar behaviour observed in Fig. 7.4 d)-e) we turn to correlation functions: the time traces form the three ROIs are compared, ELM by ELM, with the ten channels in each spectrometer. Fig. 7.5 provides the correlation analysis for the ELM presented in Fig. 7.4: both signals are compared and sequentially shifted in time. The correlation coefficient becomes large and positive when the compared signals behave in a similar manner, negative when they exhibit opposed phases and null when they are unrelated. We will assume that the D_α channel that exhibits a larger correlation around $\Delta t \approx 0$ with a ROI's time trace, corresponds to the ROI's location in KL8A's sensor. This way, in Fig. 7.5, the ROI taken from tile 1 (KL8A2) corresponds to the signals DAI1 (channel 1 in the inner divertor); the one from the inner strike point (KL8A6), with DAI5 and the one from the outer strike point (KL8A9), with DAO6 (from the outer strike point channels).

4. The analysis presented in Fig. 7.5 is applied to each ELM recorded by KL8A, and the resulting correspondences are extracted and saved so they can contribute to a final statistics that will throw a correspondence between the spectroscopy channels and the ROIs at KL8A's frames for the studied shot. Fig. 7.6 shows two sets of histograms resulting of these analysis: row 1 (panels a)-c)) contains the final correspondences for JPN90725, the plasma that we have used in this example: the correspondences in the inner region of the divertor are more conclusive than the one from the outer region, as the levels of light recorded by KL8A in the latter were low.

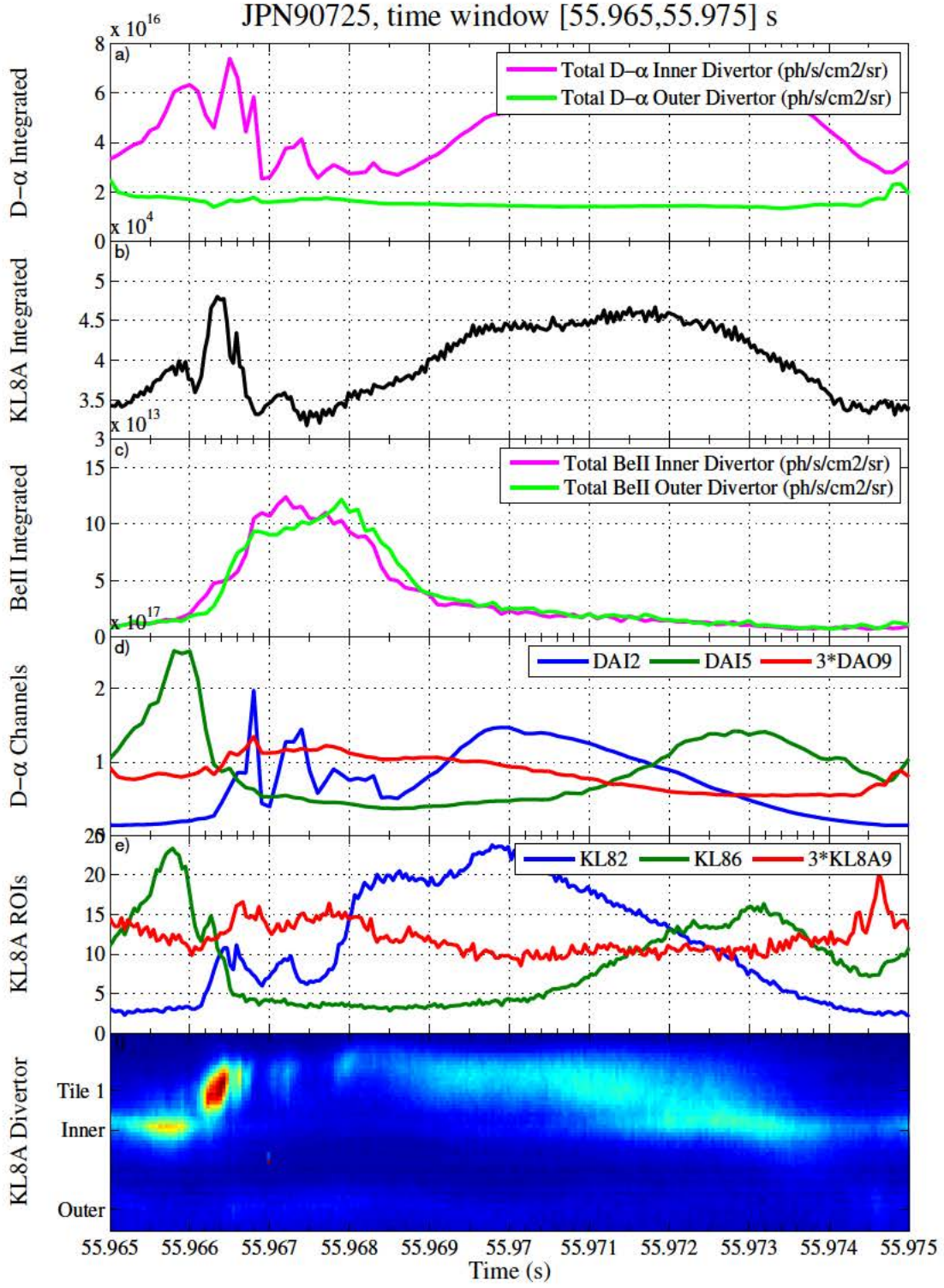

FIGURE 7.4: For JPN90725 visible light signals for a standard ELM. a) Integrated D_α. b) Integrated light on KL8A's sensor. c) BeII traces, commonly used as ELM triggers in JET-ILW and plotted as a guarantee that an ELM is been selected. d) Three D_α channels. e) Selected ROIs from KL8A, averaged. f) 2D map of light across the divertor recorded by KL8A. Estimated positions for the strike points and the upper region of the divertor are offered on the y-axis.

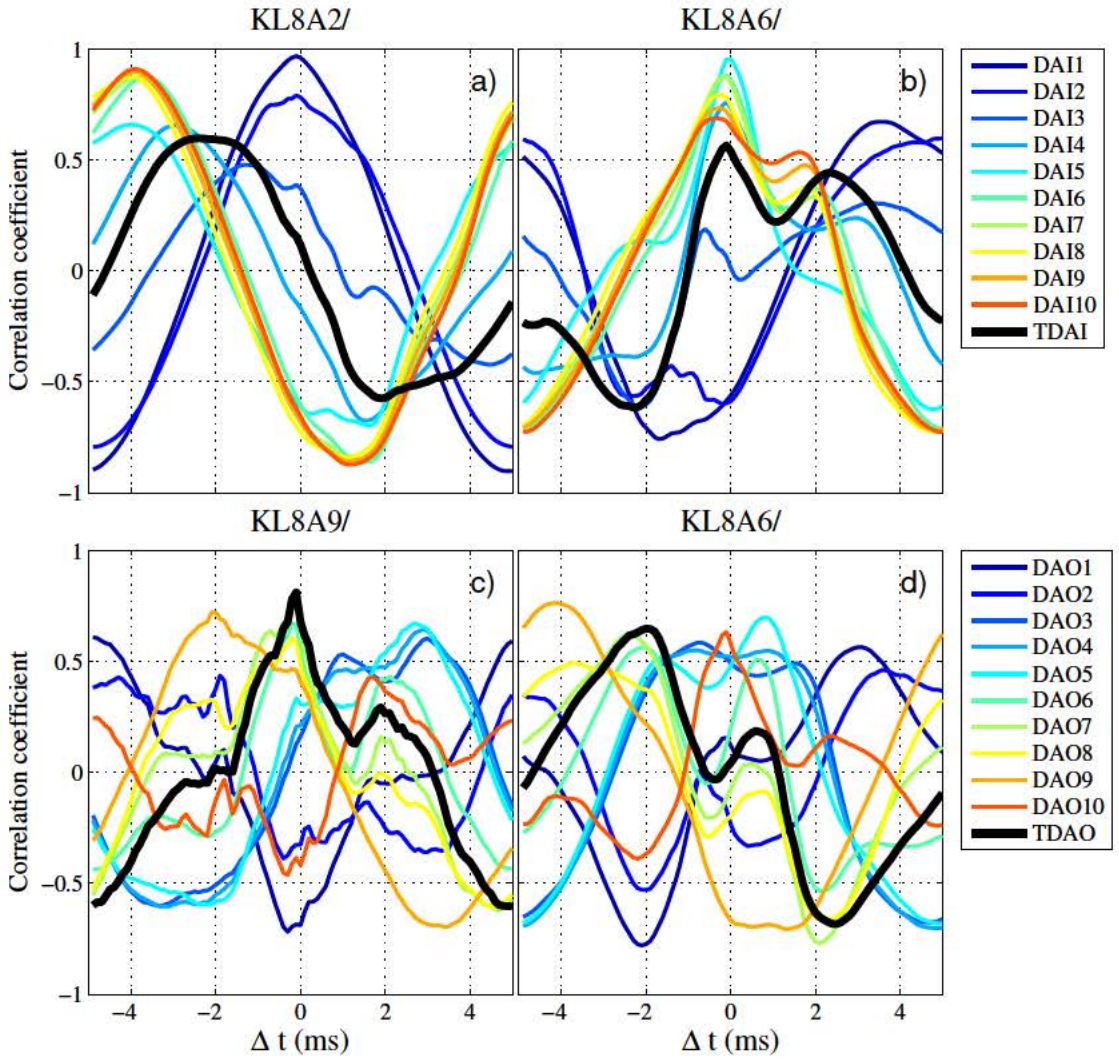

FIGURE 7.5: For the ELM from JPN90725 presented in Fig. 7.4, correlation analysis between the D_α channels and three KL8A ROIs. Each panel compares one of KL8A's ROIs (indicated in the title) with the ten D_α channels and the integrated signal from each part of the divertor vs. Δt.

Row 2 from Fig. 7.6 presents the same results for a different plasma, JPN90157, throwing a slightly different result. Does this discrepancy undermine the reliability of our method? On the contrary, it confirms KL8A's sensitivity to the location of the strike points. Fig. 7.7 a) shows the magnetic surfaces for the two pulses that we are considering, at the time of recording. It is clear that the strike points are differently located for both shots, changing slightly the shape of the emission observed by the fast visible camera (see panels b) and c)), and making them correspond to different spectroscopy channels. This way we have proved that, not only these two diagnostics can be used in a complementary way but that the fast visible camera is able to resolve different strike points at the divertor as well despite its low spatial resolution.

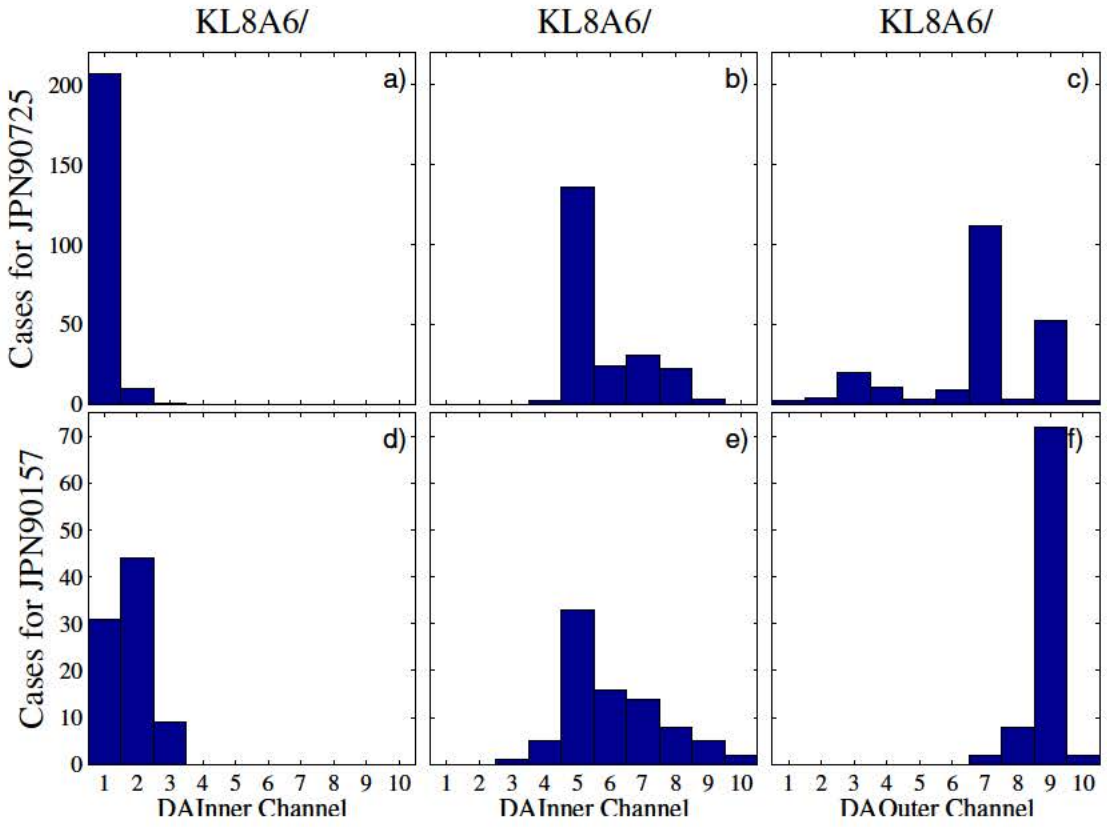

FIGURE 7.6: Total D_α-KL8A correlation results for: row 1) JPN90725 row 2) JPN90157. The bars represent the number of times each D_α channel has been selected as the maximally correlated with the corresponding ROI from the fast visible camera.

7.1.2 High resolution filtered cameras

During the close down that allowed installing the ILW, a new set of high resolution cameras focused on the divertor was installed as well in JET. A new endoscope with optimised divertor view was developed (see Fig. 4.5 a), 'KL11 div') in order to monitor the specific impurities arriving to it [103]. A system of four digital CCD cameras, each combined with two filter wheels and with a high spatial resolution of around ≤ 2 mm at the object plane. In 16 bit mode, the cameras have a maximum frame rate of 32.768 fps which corresponds to an exposure time of ≈ 30.5 ms. The exposure time can be shortened down to 75 microseconds leading to stroboscopic recording. Carbon, Beryllium, Tungsten, Neon, Argon, Nitrogen and several spectral Deuterium emissions can be tracked by combining filters and cameras. The resolution of the images produced is 1000×1000 px.

Fig. 7.8 a) shows, using external illumination, KL11's camera set view of the divertor.

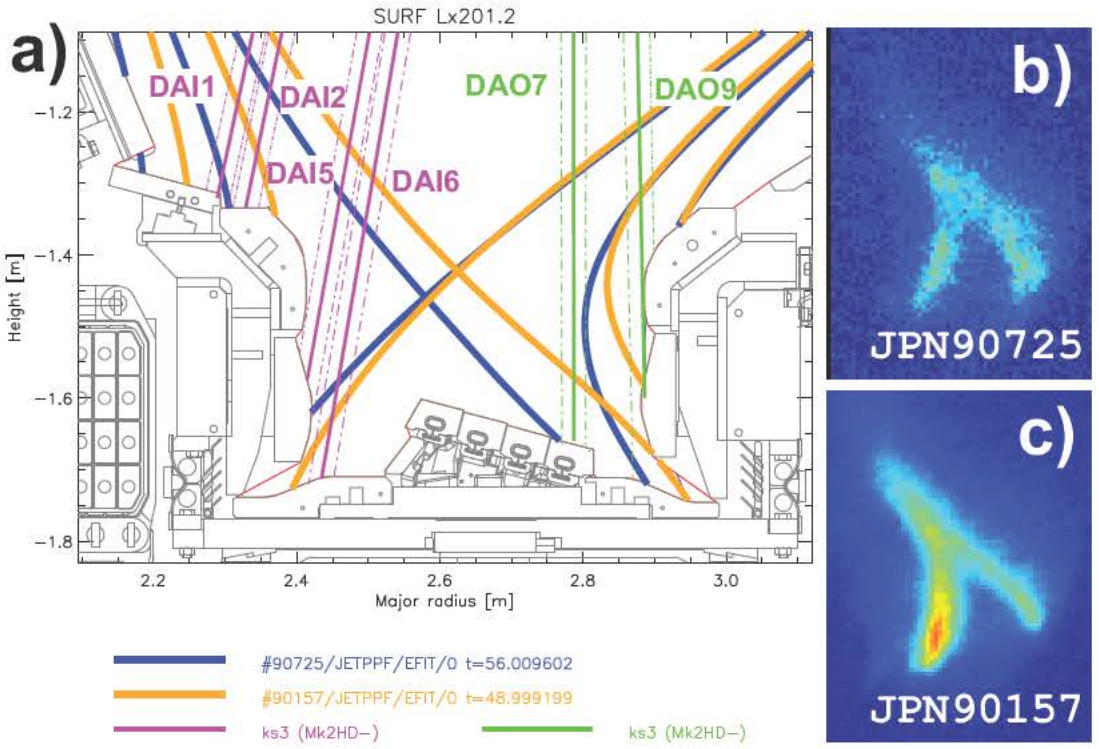

FIGURE 7.7: a) JET divertor. In blue, magnetic surfaces for JPN90725 at the time recorded by KL8A. In orange, magnetic surfaces for JPN90157 under similar conditions. In magenta, some spectroscpy channels from the inner divertor and, in green, some from the outer divertor branch. b) A frame from an inter-ELM phase recorded by KL8A during JPN90705. c) A frame from an inter-ELM phase, JPN90157. Colour limits adapted in both cases for a better visualisation.

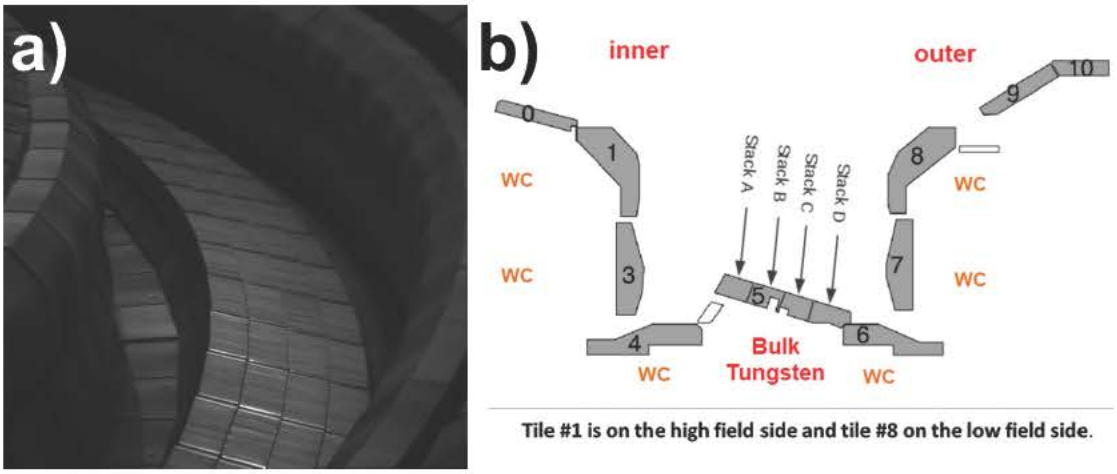

FIGURE 7.8: KL11 spectroscopy. a) KL11-E1DD (one of KL11 four cameras) with IVIS lights on, no filter (27/05/2011). b) Divertor cross-section (pre-ILW, but similar) with tiles numbered from 0 to 8 (from high field side to low field side). Credit: http://users.euro-fusion.org/openwiki/index.php/KL11_spectroscopy.

Although the point of view is not exactly equal and it is on a different toroidal position, KL11's view is very similar to the divertor section seen by the KL7 endoscope (where KL8A is installed). KL11's huge spatial resolution and the similar point of view make it the more suitable camera system at JET to balance out one of KL8A's weaknesses: its inability to provide a precise location of the fast events it records. Again, a systematic method has been developed to establish an educated connection between the images produced by these two systems. These are the conceptual steps taken:

1. As all camera systems in JET, the KL11 cameras recordings can be visualised using Juvil (a custom-developed software tool for video analysis) on JET's JAC system (the Unix servers for JET data analysis that can be connected remotely). The easier way to download these data externally is via `users.euro-fusion.org/avihost/`. The diagnostic's logbook (it can be found in `http://users.euro-fusion.org/openwiki/index.php/KL11_spectroscopy`) will provide information about the filters installed on each camera for each shot. For comparison with KL8A's recordings, D_α filtered videos are preferred.

2. KL11 records the complete JET plasma pulse, while KL8A is limited to small portions of the shot. Also, each frame from KL11 will typically be equivalent to $\gg 100$ frames recorded by KL8A. This means that:

   (a) Only the few frames recoded by KL11 during KL8A's time window will be considered.

   (b) An averaged KL8A image (see Appendix A.2.1) needs to be created for each of KL11's frames.

   This way now we have a common time vector for both diagnostics. Fig. 7.9 shows a D_α filtered frame from KL11 and the 'equivalent' average from KL8A frames during the same time window.

3. Our next step consists in comparing these frames in size and position: each KL11 frame has a constant size of 1000×1000 px, while KL8A's are normally changed to accommodate the experiment settings: in general, frames with ≈ 100 px per side are produced. Fig. 7.9 is a clear example of the differences between the images that we want to compare. So, we need to:

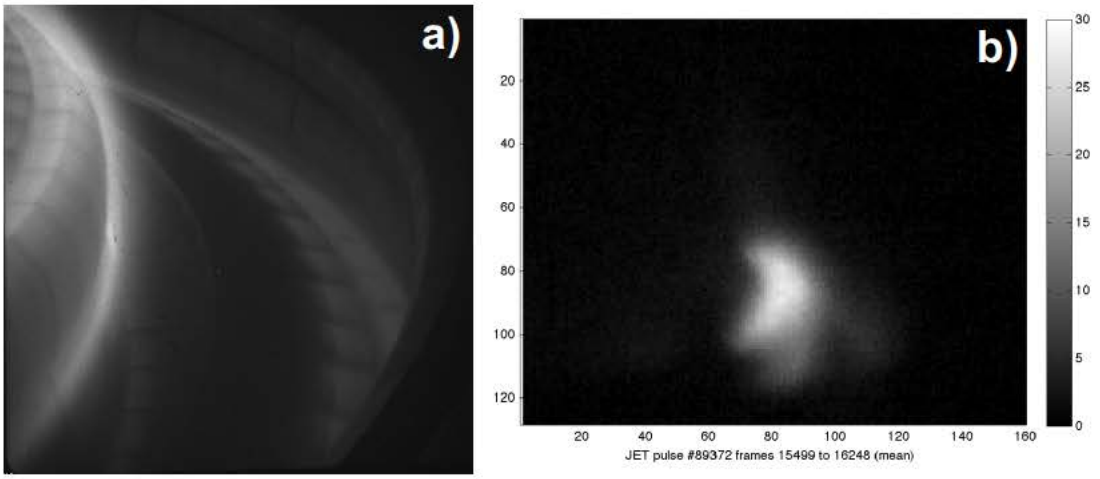

FIGURE 7.9: Comparing two visible cameras. For JPN89372 ELMy phase a) KL11-E1DD (D_α filter) frame 464. The original size of this image is 1000×1000 px. b) KL8A averaged between t=56.12s and t=56.15s. The size of these frames is 160×128 px. This video was recorded at a 25kHz speed with 2μs of exposure time and 650V of gain at the II.

(a) Crop: decide which squared area inside Fig. 7.9 b) corresponds with the view in a).

(b) Resize: KL8A's crop is much smaller than KL11's original frame: we will use Matlab's `imresize` function to enlarge the selected crop from KL8A's average.

(c) Align: as important as the size of the crop obtained from KL8A is its relative position respect the original frame.

As we did in the previous section, we will use the correlation function to compare the images produced by both diagnostics: for each KL11 frame, crops with variable sizes taken from several relative positions to the original size will be extracted from KL8A's average, resized and compared with KL11's using `corr2`, a Matlab function that computes a 2D correlation when provided with two matrices of the same size.

4. This 2D-correlation coefficient is computed sequentially for several ($\geq$ 100) cropping combinations on each frame. Fig. 7.10 provides an example of the result of such analysis upon one frame from KL11: X and Y axes represent, in pixels, the position of the Southwest corner of the considered crops on the original KL8A average and the colour code expresses the value of the correlation coefficient between the considered crop in each position and KL11's original frame. This process is repeated for 25 possible square sizes. It takes between 7 and 8 minutes to extract

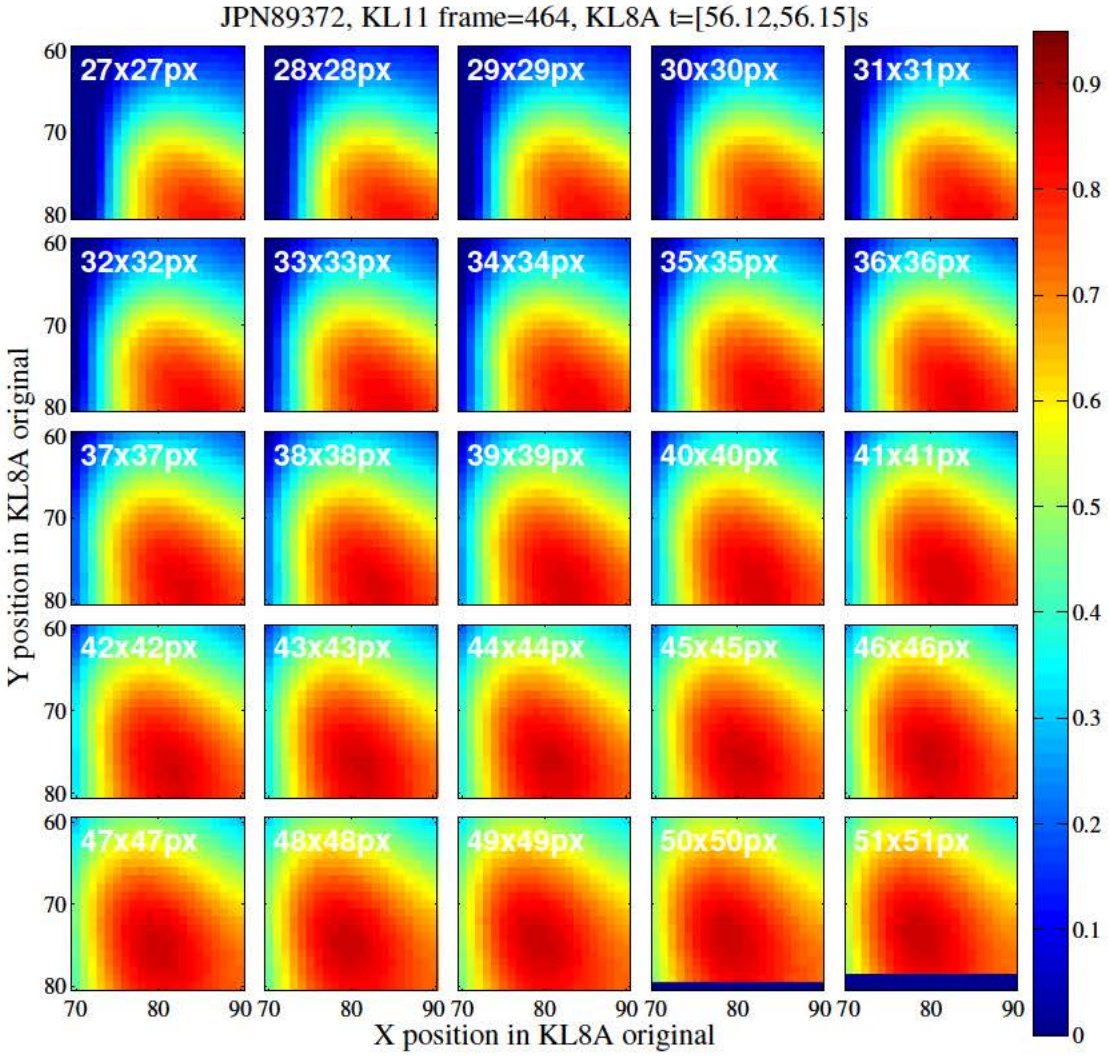

FIGURE 7.10: Example of the correlation analysis between frame 464 from KL11-E1DD (D_α filter) and a sequence of crops taken from the averaged KL8A equivalent image. The colour code represents the correlation coefficient obtained for each combination of dimensions and positions.

an analysis like the one shown in Fig. 7.10 when executed on a six-core processor PC running Windows 10 with 8GB of RAM memory, although a high amount of sizes and positions have been shown in this example for communication reasons.

5. From the analysis shown in Fig. 7.10 an optimal combination of size and coordinates for the crop on KL8A's average can be extracted by searching the largest value of the correlation coefficient among all the attempted alignments. This process can be repeated along for all the KL11 frames recorded in the same time window as KL8A, so an informed decision about the crop's dimensions and position can be made. As an example, Fig. 7.11 shows the final histograms after analysing 27 frames for JPN89372: clearly a squared crop with 49 px per side

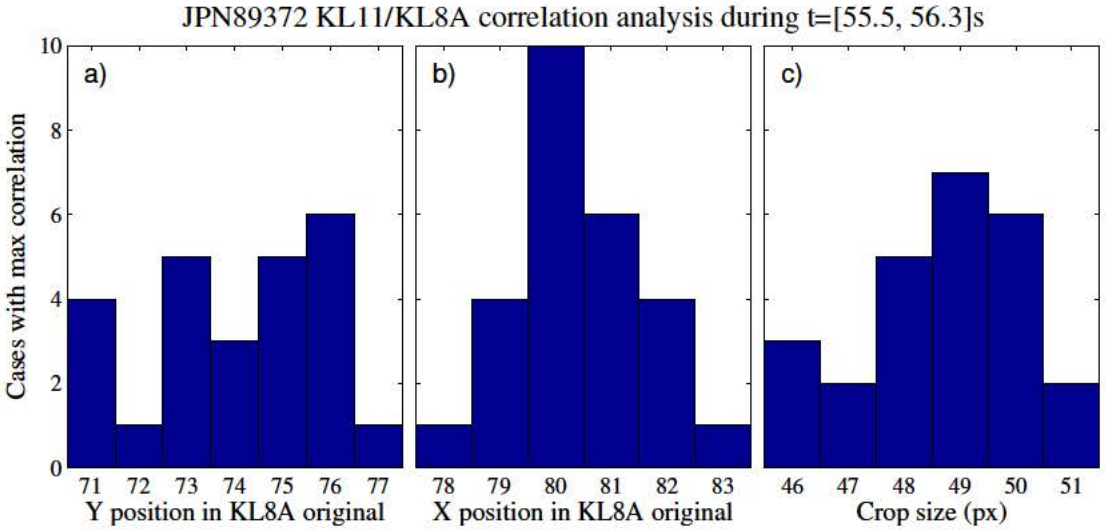

FIGURE 7.11: Final result for the correlation analysis between KL11 and KL8A for JPN89372. The bars on each panel represent the number of frames where a crop position or size (respect KL8A's original dimensions) has exhibited the highest correlation coefficient when compared with the original frame from KL11.

located on px 80 along the horizontal direction and 75 along the vertical one will be the most suitable candidate to analyse the evolution of visible emission from the divertor both with high time and spatial resolution.

This method is a powerful tool to increase KL8A's positioning capability: by addressing them to the KL11's frames, the ROIs that we define and use for analysis in KL8A and the events that we detect with them can be specifically related with clear positions at the divertor.

7.1.3 Combining three diagnostics

Finally, we will use Fig. 7.12 as an example of how KL8A can improve the analysis of data coming from the divertor focused spectrometers and cameras by combining the information obtained from each diagnostic. As we have done in the previous subsection, we will use For JPN89372 between 56.12 and 56.15 s (time corresponding to KL11's frame number 464) to illustrate the joint results:

a) The results shown in Fig. 7.11 lead to a cropped version of KL8A's frames that can be superimposed over KL11's. This also allows us to have a more comprehensive knowledge of how the 5×5px ROIs that we define for KL8A match with the divertor

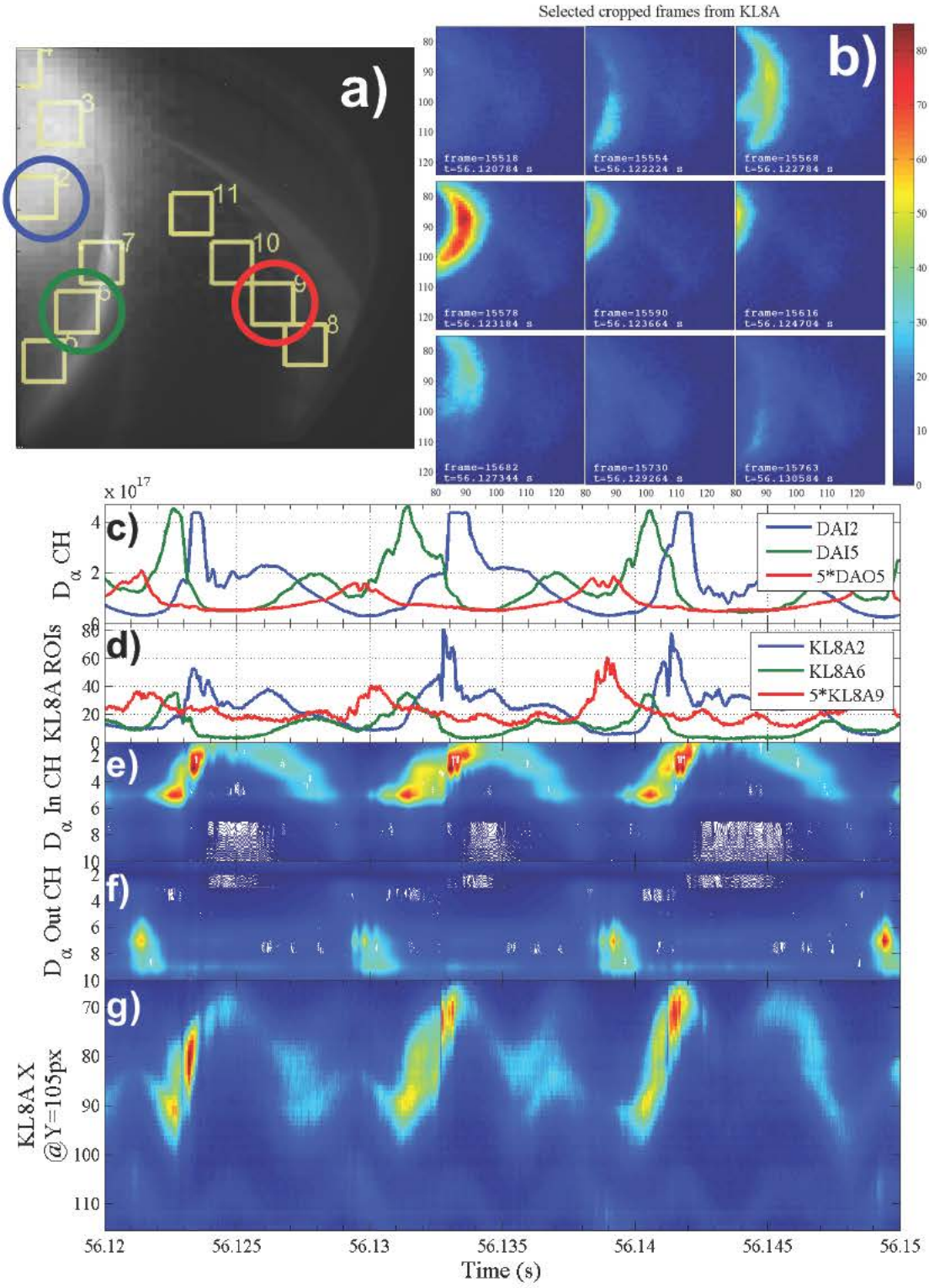

FIGURE 7.12: For JPN89372 t = [56.12, 56.15]s, an example of how the high resolution filtered camera KL11, the intensified fast visible camera KL8A and the spectroscopy channels looking at the divertor can be combined after correlation analysis.

tiles and positions, as they can also be transported to the high-res frames from KL11. This way the blurry images obtained by KL8A can be related to actual positions in the divertor.

b) KL11's time resolution is not enough to resolve ELMs. In this example, in the time that takes to record a D_α filtered frame in KL11, three ELMs take place: KL8A is the only way to track this emissions two-dimensionally. This KL8A video was recorded at a 25kHz speed with 2μs of exposure time and 650V of gain at the II.

c) The correlation analysis between KL8A and the spectroscopy signals that was explained in Subsec. 7.1.1 has also been applied to this plasma pulse. We show in this panel the time traces of the three D_α channels that obtained a higher correspondence respect the ROIs selected in KL8A. The signal from the outer divertor has been multiplied by five for a better visualisation. The time limits, for this and the next panels, are those imposed by the 30ms exposure time in KL11.

d) Averaged time trace of three representative ROIs from KL8A. The location of these ROIs is remarked (with conserved colour code) in the a) panel. Again, the signal from the outer region of the divertor has been increased for a better comparison with the ones from the inner part.

e) Contour plot (2500 lines considered) composed by the ten D_α channels looking at the inner divertor.

f) Similar to the previous panel but using the channels looking at the outer region of the divertor. Keep in mind that some of the channels from each set cover equivalent areas in the central divertor, although they 'see' different columns of plasma.

f) Heat map obtained by plotting the evolution in time of light intensity along a horizontal line (between px 65 and px 115 on the x direction) selected to intersect with the light emitted by both strike points at the divertor and its upper region (y coordinate set at 105 px).

In this example we see that the agreement between the three diagnostics is satisfactory, although KL8A can provide extra information about the innermost area of the divertor (tiles 1 and 0 in Fig. 7.8 b)) that is not covered neither by KL11 or the spectrometers.

7.2 ELMs on the divertor

The installation of the ILW in JET changed drastically the ELM scenario in this tokamak. Type-III ELM regimes with an energy loss rate in range $\Delta W_{ELM}/W_{ped} \approx 10-20\%$ that took around 1 ms to reach the minimum pedestal temperature were observed with the Carbon wall (JET-C, from now on) and much slower ($\approx$ 2 ms for the lower pedestal temperature) benign Type-I ELMs with $\Delta W_{ELM}/W_{ped} \approx 7-12\%$ are the predominant phenomena in H-mode plasmas with the ILW [104, 105]. Only when seeding is employed to cool the divertor, pedestal heights and energy losses for ELMs in JET-ILW become similar to the ones observed in JET-C. This is explained by the effects of slow transport events that didn't occur with JET-C and that seem to be avoided with impurity seeding [106]. Experiments in JET-ILW also showed how the L-H transition power threshold P_{thr} is strongly dependant on the plasma shape and divertor configuration (location of the strike points) [107]; and complete plasma detachment from the divertor targets can provide stable operation with the ILW [108].

All these results lead to the same conclusion: study of the radiation emitted by the excited Deuterium atoms at the divertor can shed light on several key processes related with the H-mode, impurity transport and ELM dynamics at JET-ILW. Fig. 7.1 shows a typical ELM recorded by the intensified fast visible camera. Our goal in this part of the work is to characterise the evolution of the visible emission from the strike points once the pedestal temperature drops and study with a high time-resolution the recovery process after the ELM.

7.2.1 Charaterization of ELM's light signature[2]

Once we have made sure that we can understand and locate KL8A's recordings from the divertor, it is time to study what we see there when the pedestal temperature suddenly drops and then slowly recovers. In the course of our explanations along Subsec. 7.1 we have shown two examples of ELMy phases in figures 7.4 and 7.12. In both cases the arrival of the ELM follows the same sequence:

[2]This work is included as part of a larger scale study in [109], that has already been submitted for publication at the date of deposit of this thesis.

1. A sudden increase of emission intensity at the inner strike point shortly before the ELM.

2. A subsequent fast reduction of emission at that same point.

3. Appearance of a new source of light at the upper region of the divertor. The emission from this location is the brightest of the sequence.

4. The top part of the divertor slowly decreases its intensity.

5. The inner strike point slowly regains luminosity.

Obvious questions arise: is this behaviour always to be expected for ELMs in JET-ILW? And, whatever the answer to that question is, what does this dynamics correspond to? In this section we will try to provide a description of the phenomenology that is observed in the divertor during ELMs so, after that, we can relate it with other physical quantities involved.

In order to characterise the relationship between the time evolution of the three sources of light that we are considering, we will use, once again, correlation functions: when compared, ELM by ELM, the trace in the inner strike point with the emission registered around tile 3, the time delay between their two spikes can be obtained and treated statistically. Similar treatment can be given to the outer strike point, although the signal in this region is usually much lower and noisy and, hence, more complicated to deal with. The same analysis can be implemented upon the D_α channels as a control.

We have encountered four situations:

- **Type-I ELMs** (See Fig. 7.13 for a typical example of these ELMs and their light signature). As we mentioned above, slow ELMs are predominant at JET since the ILW was installed. The sequence outlined above describes them fairly, with the addition of a long ($\approx$ 6 ms) secondary peak of D_α emission around tile 1 after the ELM-crash. Regarding the time delay between the emission from the inner strike point and the first spike of D_α on the up-divertor region, it is normally $\geq$ 1 ms, although very long ELMs can exhibit delays up to 3ms (like JPN90725). When comparing the time traces from KL8A's ROIs with the pedestal temperature (T_{ped}), the one corresponding to the inner strike point shows the more similar behaviour

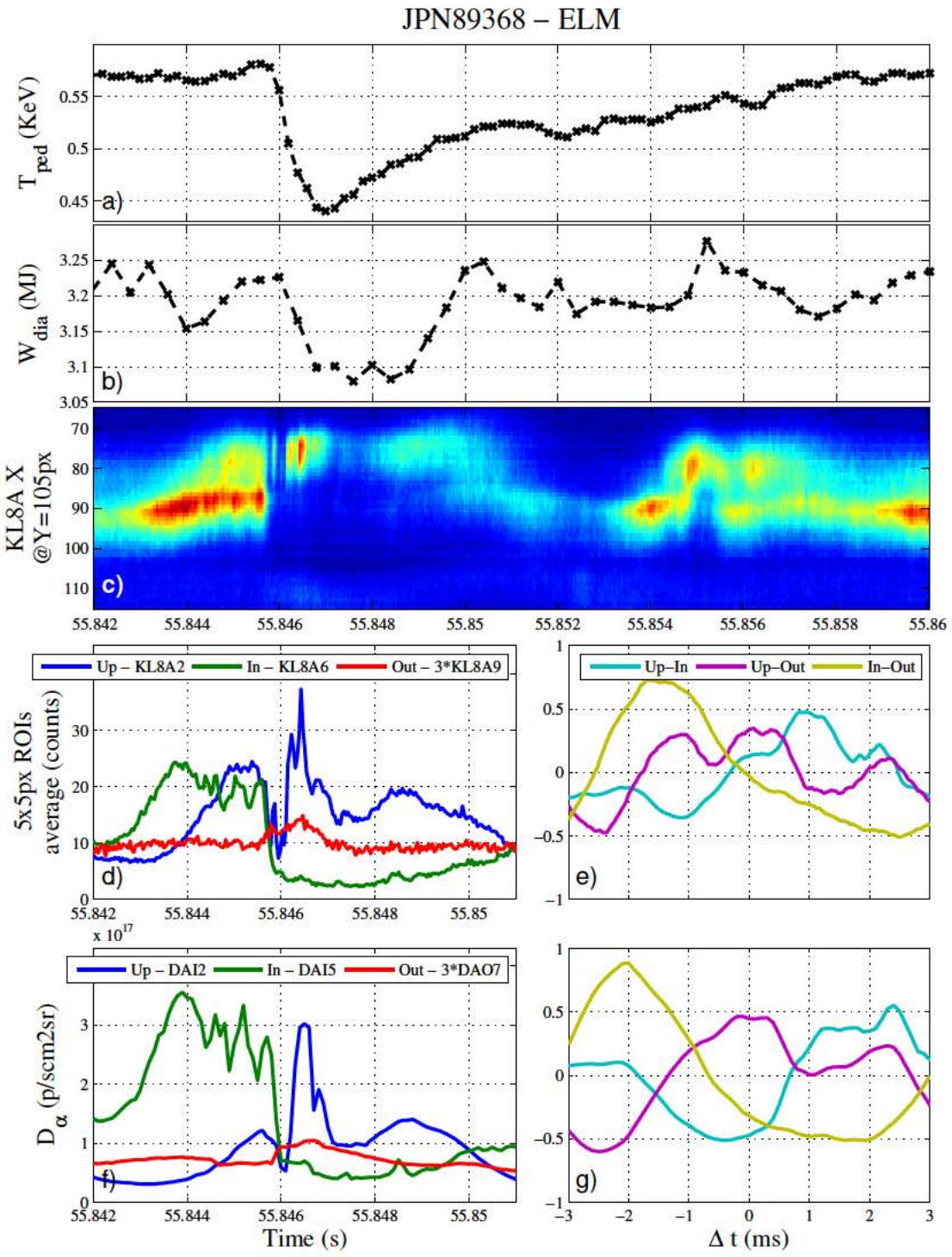

FIGURE 7.13: Type-I ELM from JPN89368 (from experiment M15-13). See Tab. 7.1. The KL8A video corresponding to this ELM can be accessed from https://drive.google.com/open?id=0B9AIoGs2odhNcDFMWHZVMGNEYjQ. a) Pedestal temperature, taken as channel 36 from the fast ECE array (ppf/kk3/te36). b) Diamagnetic energy. c) Complete ELM across the divertor recorded by KL8A. d) Time traces for three representative ROIs from KL8A, only first half of the ELM, when most of the dynamics in the inner strike point and the upper region of the divertor are represented. The signal from the outer strike point is multiplied by three for a better visualisation. e) Correlation coefficient for the tree possible combinations for the curves presented in d). f) Equivalent D_α spectroscopy channels. g) Correlation coefficient for the three spectroscopy signals from f).

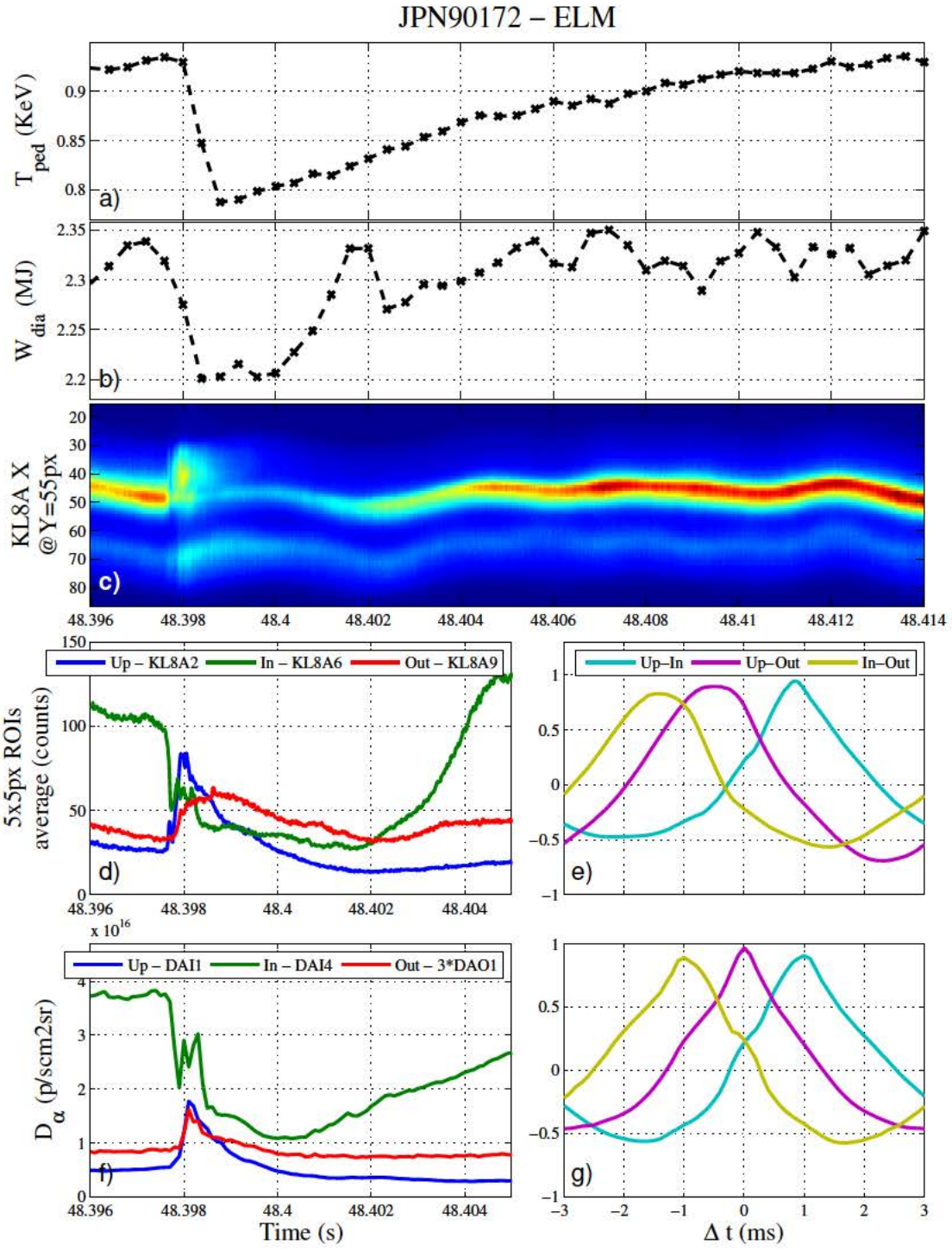

FIGURE 7.14: Ne-seeded ELM selected from JPN90172 (from experiment M15-02). See Tab. 7.1. The KL8A video corresponding to this ELM can be accessed from https://drive.google.com/open?id=0B9AIoGs2odhNWTNIVEZ5endRQnc. a) Pedestal temperature, taken as channel 92 from the fast ECE array (`ppf/kk3/te92`). b) Diamagnetic energy. c) Complete ELM across the divertor recorded by KL8A. d) Time traces for three representative ROIs from KL8A (only first half of the ELM). e) Correlation coefficient for the tree possible combinations for the curves presented in d). f) Equivalent D_α spectroscopy channels. g) Correlation coefficient for the three spectroscopy signals from f).

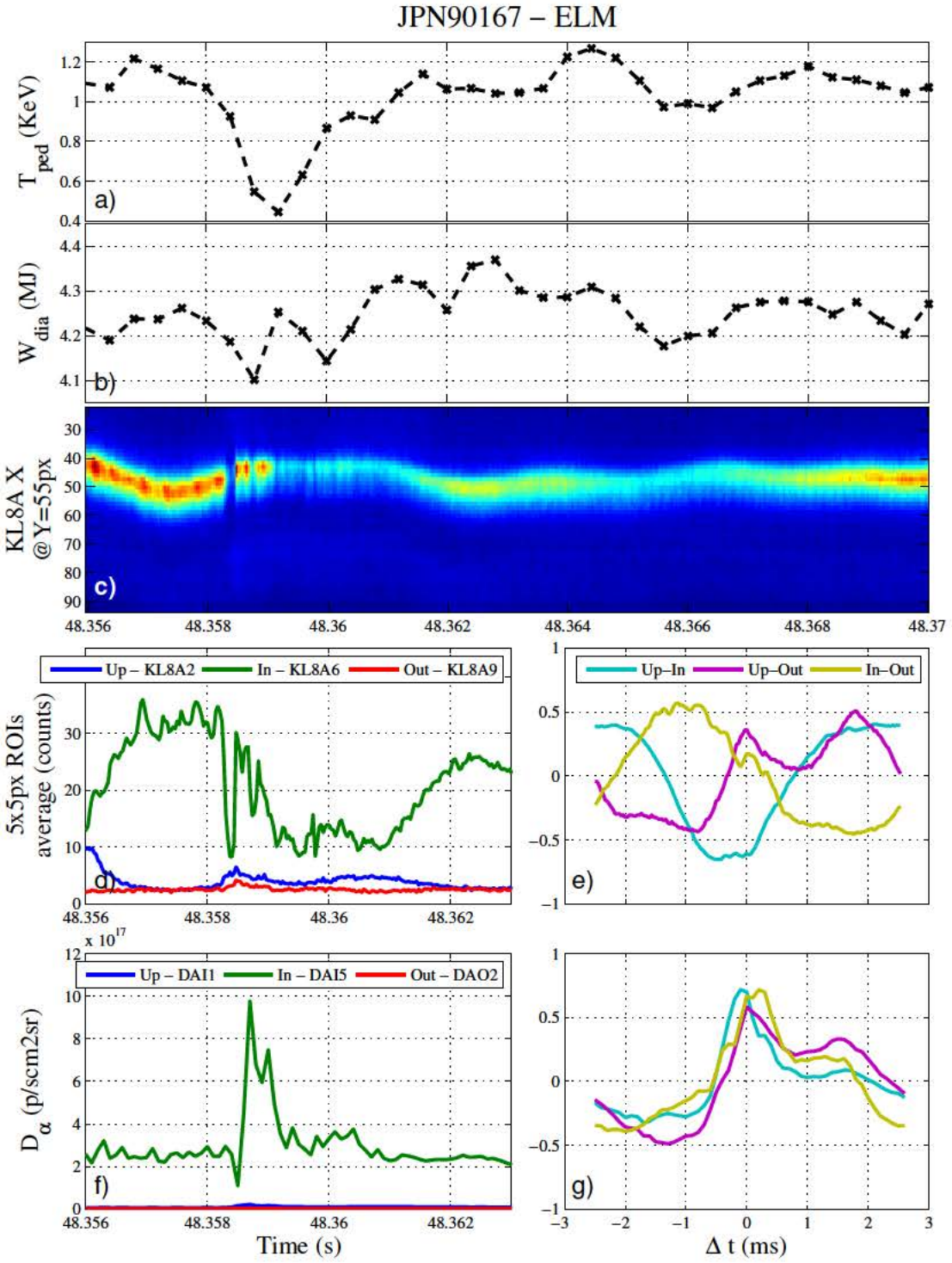

FIGURE 7.15: ELM selected from JPN90167 (from experiment M15-02). See Tab. 7.1. The KL8A video corresponding to this ELM can be accessed from https://drive.google.com/open?id=0B9AIoGs2odhNVUJSZk54Z3RYQXM. a) Pedestal temperature, taken as channel 56 from the fast ECE array (`ppf/kk3/te56`). b) Diamagnetic energy. c) Complete ELM across the divertor recorded by KL8A. d) Time traces for three representative ROIs from KL8A (only first half of the ELM). e) Correlation coefficient for the tree possible combinations for the curves presented in d). f) Equivalent D_α spectroscopy channels. g) Correlation coefficient for the three spectroscopy signals from f).

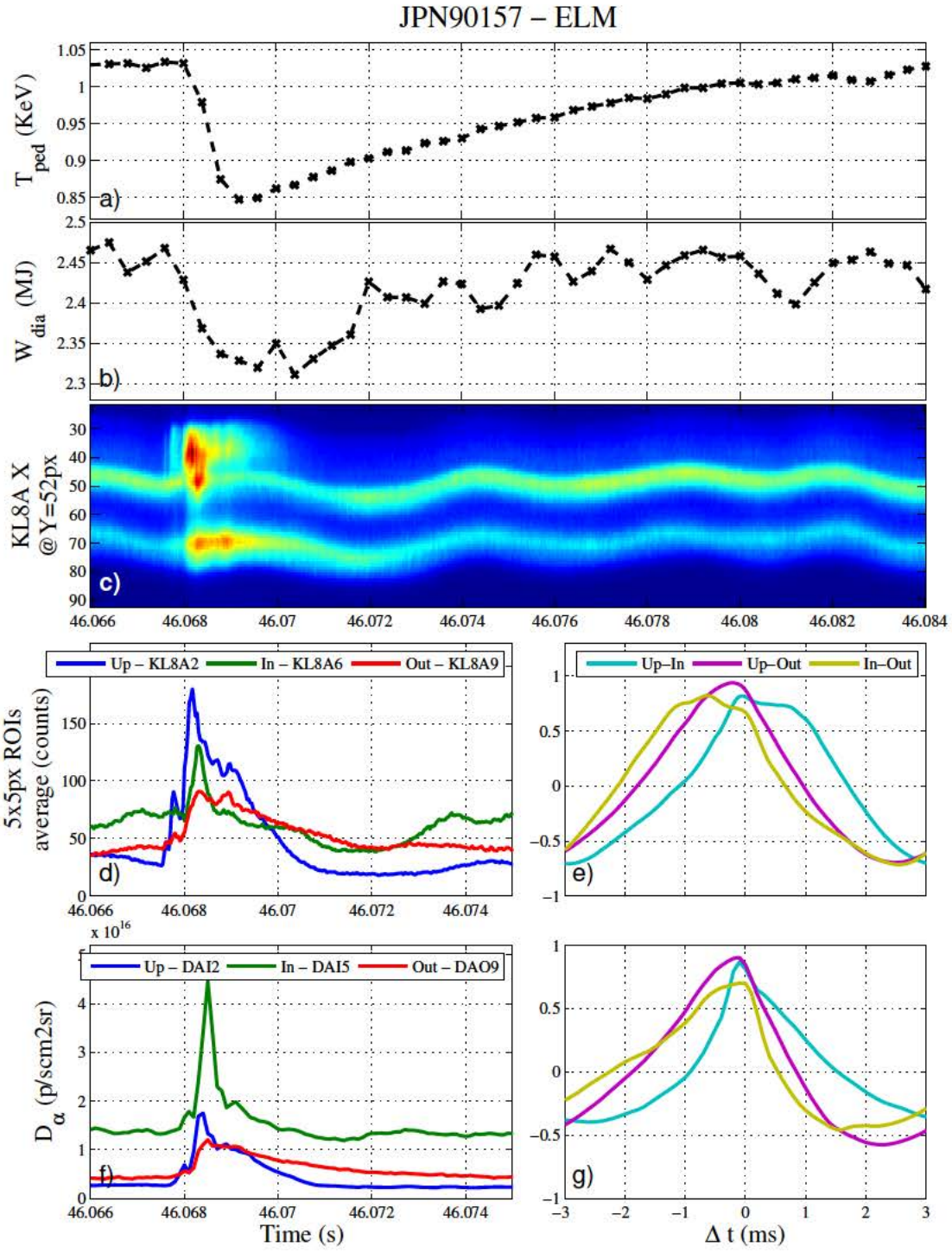

FIGURE 7.16: ELM selected from JPN90157 (from experiment M15-02). See Tab. 7.1. The KL8A video corresponding to this ELM can be accessed from https://drive.google.com/open?id=0B9AIoGs2odhNRFVhUFF1S2IzRlk. a) Pedestal temperature, taken as channel 92 from the fast ECE array (`ppf/kk3/te92`). b) Diamagnetic energy. c) Complete ELM across the divertor recorded by KL8A. d) Time traces for three representative ROIs from KL8A (only first half of the ELM). e) Correlation coefficient for the tree possible combinations for the curves presented in d). f) Equivalent D_α spectroscopy channels. g) Correlation coefficient for the three spectroscopy signals from f).

(no only decreasing drastically at the beginning of the ELM, but also at the rate of recovery). In these cases, T_{ped} only stabilises back once emission from the upper region of the divertor has decreased back to pre-ELM levels.

- **Ne seeding** (See Fig. 7.14 for a typical example of these ELMs and their light signature). It has to be mentioned too that when the divertor is cooled via Ne seeding, ELMs become faster, resembling to the ones observed with the Carbon wall. This translates in an accelerated version of our signals: the decay of the emission from the inner strike point is fast, but the recovery is so as well; and the slowly weakening cloud from the upper region becomes a bright and short spike, without the characteristic secondary emission peak observed in longer ELMs. The time between two events in the inner strike point and the upper region is, for these cases, between 0.5 and 1 ms. The similarity between the time trace from the inner strike point and T_{ped} remains.

- **High temperature and confinement.** In these cases the cloud from the upper region of the divertor disappears and very low signals are registered both in the spectrometers and the fast camera. The ELM presented in Fig. 7.15 taken from JPN90167 is a very clear example of the absence of radiation at the upper region of the divertor. Although attempted, the signal in this case is so weak apart from the inner strike point (this also happens in de D_α time traces) that no interpretation from the correlation analysis is possible.

- **High Z.** When impurities have reached the plasma, the ELM signature changes drastically: the three sources of light burst simultaneously like we show in Fig. 7.16, taken from JPN90157. The secondary peak of D_α emission from the area around tile 1 is present in these cases, but it is much shorter ($\approx$ 1 ms) than in impurity free plasmas.

Table 7.1 summarises the characteristics of the plasma pulses shown in figures 7.13-7.16.

After the first JET-ILW campaigns it was shown that about 1/3 of global fuel retention was located in tiles 1 and 0 (see Fig. 7.8 b)), as the major fraction of eroded Be particles from the main chamber are co-deposited near this region. This ratio of D retention might be the explanation of the significant D_α emission that we observe near that area: the surface is apparently heated during the ELM-crash, outgassing D particles from the Be

	General			KL8A		
JPN	$B_T(T)$	$I_P(MA)$	$P_{NBI}(MW)$	fps(kHz)	$t_{exp}(\mu s)$	gain(V)
89368	2.33	1.97	12.6	25	2	650
90172	1.9	1.4	17	75	3	630
90167	3.35	2.4	16	30	2	630
90157	1.9	1.4	14.2	30	4	630

TABLE 7.1: Characteristics of the pulses used in this subsection. General plasma parameters taken from JET's physics summary http://data.jet.uk/.

co-deposits [109] during the subsequent ≈ 5 ms. Secondary D_α emissions after the ELM-crash have also been observed in ASDEX-U [110] and were explained as a retardation of pedestal recovery due to volumetric particle reservoir.

The here presented study of the KL8A fast camera has contributed to the ongoing understanding of the recycling dynamics during ELMs that a affects global confinement in JET [109].

7.2.2 Beryllium erosion and migration

The study of impurity migration, specially Beryllium arrival and deposition on the divertor, was one of the main reasons that led to the installation of the image intensifier and the filter wheel on the fast visible camera. From the spectroscopy signals we know that we should expect the BeII emission to be approximately three orders of magnitude less intense than the D_α line emission (see Fig. 7.17 c)-f) for an example). So the questions that we need to answer are:

- Given that optical filters are not ideal, a small portion of undesired light will be transmitted through them, if the intensity is too high. Assuming that the II settings for BeII-filtered recording will be much higher than those for D_α emission, will we be forced the filter's limits and see nothing but the emission from other lines close to the one they were designed for, marginally transmitted emission?
- If successful at filtering BeII line emission, will our system retain any of its time resolution capabilities in order to provide a more accurate signal than the one given by the spectrometers?

To answer these questions we will analyse KL8A's performance when the BeII filter is set for ELM visualisation on the divertor. We will compare two ELMy phases, one

Be-filtered (JPN83585) and the other with naked lens conditions (JPN90725) (see Tab. 7.2 for the pulse settings and Fig. 7.17 for the results).

	General				KL8A		
JPN	$B_T(T)$	$I_P(MA)$	$n_e(m^{-3})$	$P_{NBI}(MW)$	fps(kHz)	$t_{exp}(\mu s)$	gain(V)
90725	2.3	2.0	12	17	25	2	640
83585	2.7	2.5	20	12	2	500	800

TABLE 7.2: Characteristics of the pulses used in this subsection. General plasma parameters taken from JET's physics summary http://data.jet.uk/.

The first impression that we get from these results is that, as suspected, very long exposure times and voltages are necessary at the II for KL8A to provide a meaningful signal/noise ratio when the BeII filter is installed. This reduces the sampling frequency to 2-5kHz, much less than the spectrometer's capability (10kHz). From Fig. 7.17 e) we also deduce that the complex D_α emission dynamics observed in the strike points and the upper part of the divertor is no where to be seen when the BeII line is traced. After a careful analysis upon a handful of ELMy phases, similar to the radial correlation process that we presented in the previous subsection, we can say that the spike in the BeII emission happens simultaneously in all the spectroscpy channels, although in some cases its width on the outer strike point (OSP) may be larger than in the inner strike point (ISP). With a much lower time resolution, that is exactly what the time traces extracted from a BeII-filtered KL8A video show (see Fig. 7.17 b).

This leaves only with study emission from the limiters (one of the straightforward beryllium sources at JET-ILW) as the ELM evolves along the SOL as a potential feature of Be-filtered recordings. The reduced light signal conditions limits this kind of analysis, normally, to the outermost limiter in KL8A's field of view (see Fig. 7.18). Parallel tracking of BeII emission at the divertor strike points and along the limiter could provide information about poloidal transport during the ELM-crash. This areas, like the antennas installed on the outer wall, are out of reach for the spectromerter's field of view. Unfortunately using the BeII filter doesn't only limit the time resolution, but adds noise and grain to the final frames, making spatial tracking even more difficult. At the moment we don't have enough BeII-filtered data to extract conclusions from an analysis like the one presented in Fig. 7.18 b)-d).

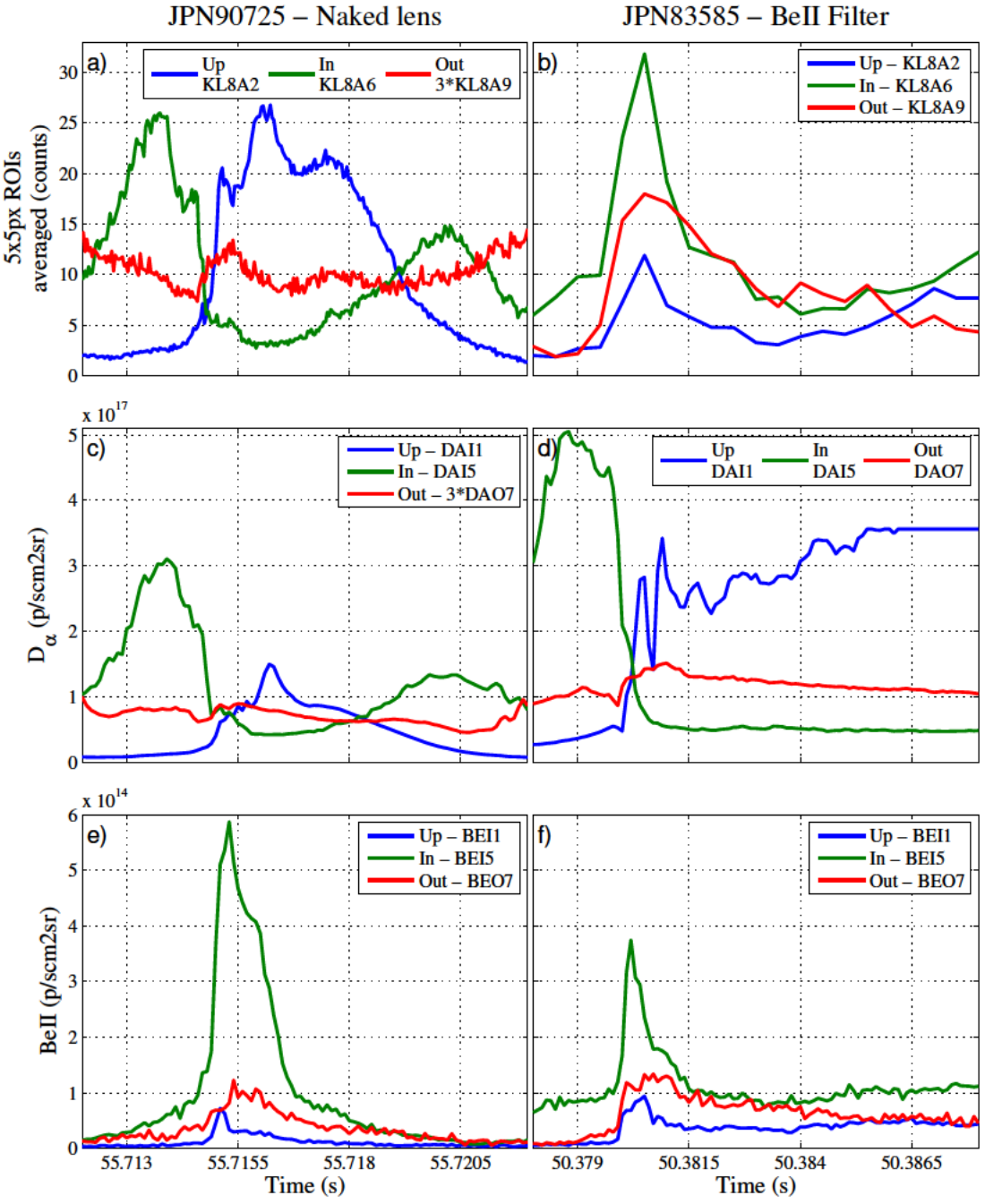

FIGURE 7.17: Comparison between naked lens and BeII filtered recording. Column 1) Typical ELM selected from JPN90725. a) Contains the usual KL8A time traces, generated using 5x5px ROIs recorded without filtering. c) Shows the equivalent D_α spectroscopy channels obtained in Subsec. 7.1.1. e) Time traces for the BeII line emission taken from the same spectroscopy channels used in c) for the D_α line. Column 2) ELM from JPN83585. b) KL8A time traces taken from the BeII-filtered video. d) D_α emission taken as the typical channels obtained from the KL8A-spectroscpy correlation analysis. f) BeII spectroscopy.

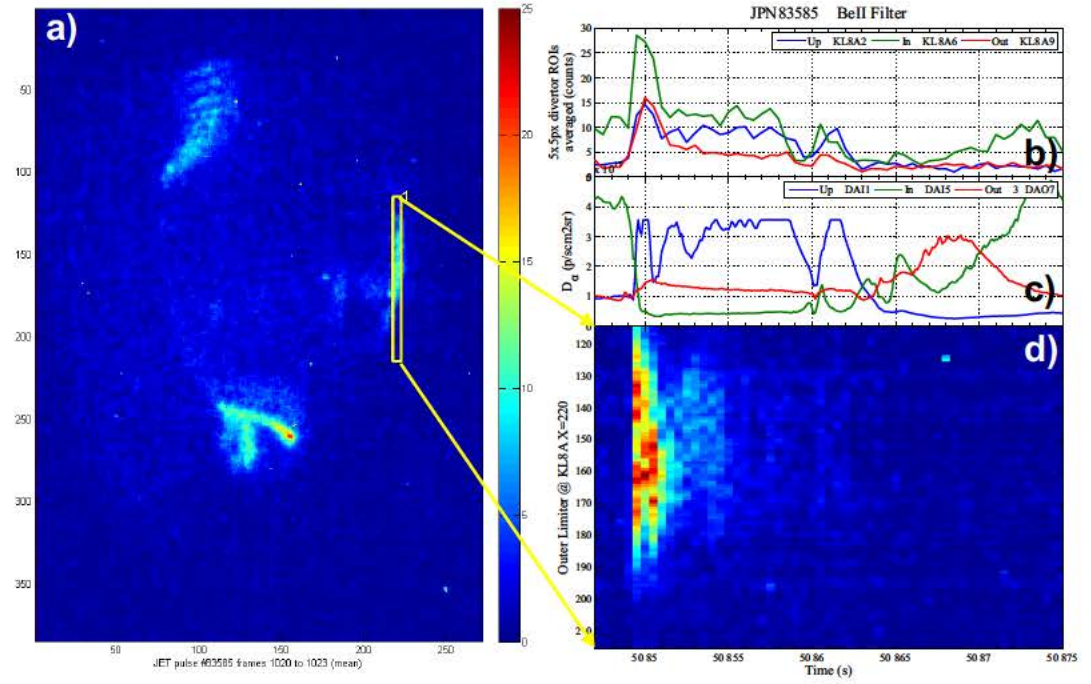

FIGURE 7.18: BeII-filtered ELM in one of the outer limiters

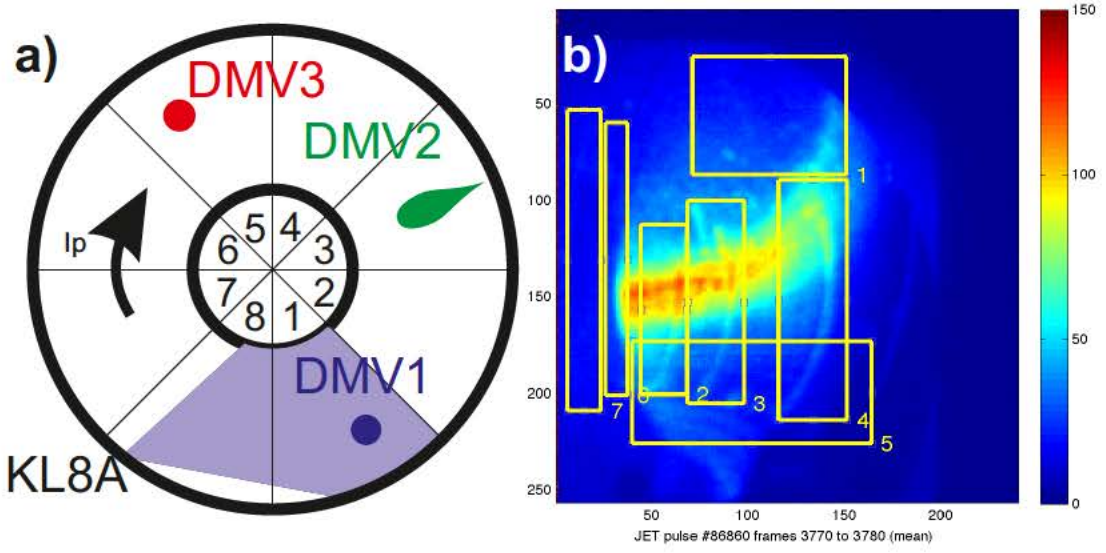

FIGURE 7.19: a) Schematics of the location of the DMV gas valves respect KL8A's field of view. b) Mitigation gas injection during the disruption at JPN86860 and the ROIs that we will typically use for disruption analysis.

7.3 Disruptions

The installation of the ILW in JET revealed that the wall material not only affected the disruption properties, but also changed the conditions under which plasmas became disruptive. The ILW reduced radiating impurity during the disruption, leading to low radiation during the current quench, long current decay times and high heat loads

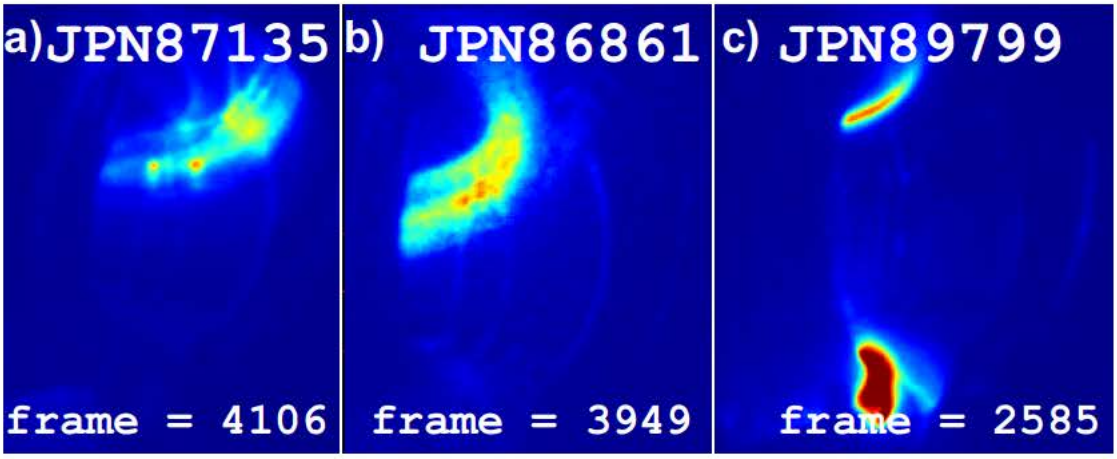

FIGURE 7.20: Gas injection valves in action. a) DMV1 b) DMV2 c) DMV3.

caused by the conduction of magnetic energy to PFCs [42]. Since 2008 three Massive Gas Injection (MGI) valves have been installed at different locations in JET, two injecting mitigation gas from upper vertical ports (DMV1 and DMV3) and one horizontally (DMV2). The efficiency of disruption mitigation depends significantly of the conditions of the injected gas: pressure, gas mixture and injection sequence have been studied intensely in the ILW campaigns. The fast visible camera was proposed as a useful tool to identify the arrival of the mitigation gas into the vacuum chamber and track its distribution inside the plasma right before the current quench. In principle, only direct view of the DVM1 valve injection can be tracked by the camera (see Fig. 7.19 a)).

7.3.1 Mitigation gas arrival time

Detecting the arrival time of the mitigation gas on KL8A's field of view is an easy task, given the ROIs presented in Fig. 7.19 b), which will be the pattern used for disruption analysis, and the position of each valve. We can estimate optimal ROIs for gas detection when each valve is used. For example, Fig. 7.20 a), which frames gas injection from the DMV1, makes it clear that the ROIs labelled in Fig. 7.19 b) as "1" and "4" will be the first to detect an increase in D_α emission by the colder gas. The rest of the examples from Fig. 7.20 provide clear locations to analyse the gas injection from each valve.

Knowledge of the precise moment when the valve starts the gas injection, its pressure and the time of flight of the gas along the tube (this amount changes drastically from one DMV to another) allows us to provide estimated arrival times for the mitigation gas on each disruption successfully recorded by KL8A. Fig. 7.21 helps to understand that

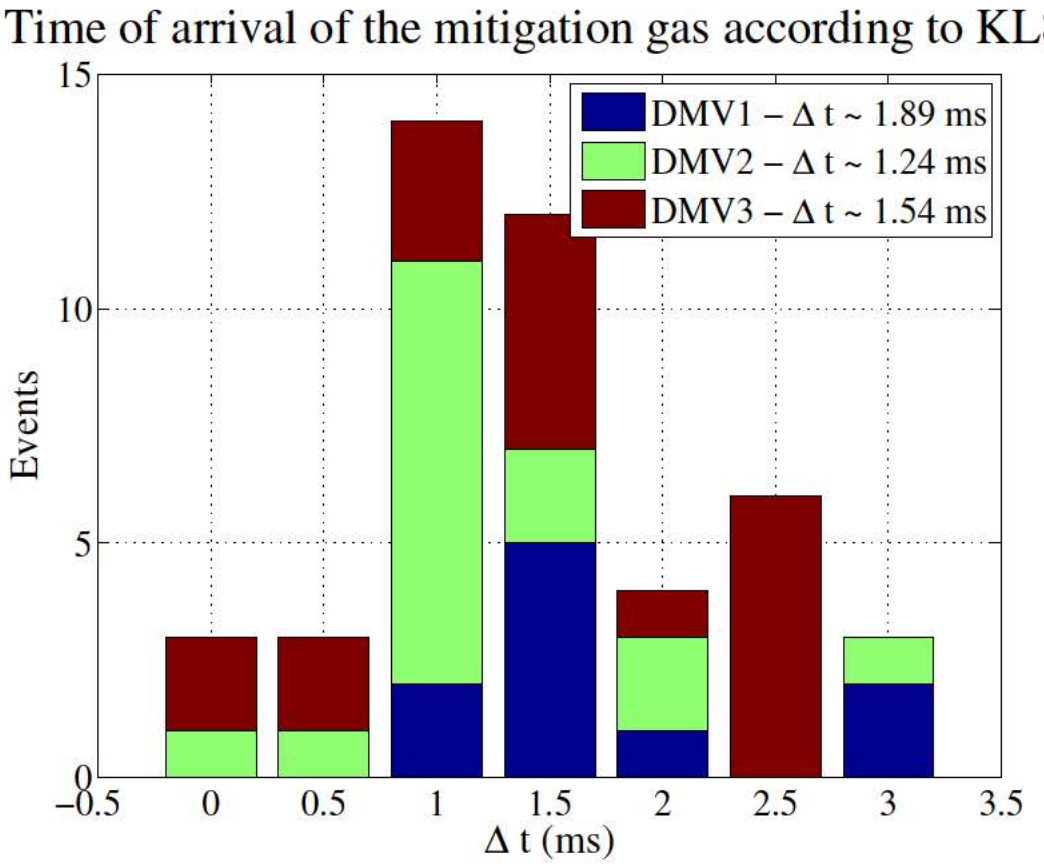

FIGURE 7.21: Detection time for each mitigation valve once the time of flight along the tube has been subtracted in each case. Statistics obtained from a database containing 45 fast-recorded disruptions.

the time of delivery for each valve changes drastically and that, in fact, the injection system that is physically closer to KL8A's point of view is the slowest to deliver the mitigation gas to the plasma.

7.3.2 Runaway electrons[3]

Fast visible imaging at JET has also proved useful at tracking the cloud of runaway electrons that can be one of the most dangerous consequences of disruptions. The interaction between these electrons and the plasma has been interpreted as synchrotron emission when observed in DIII-D [67]. When observed in JET the position of this interaction cloud is correlated with the expected position of the runaway beam.

[3]These results have been published as part of the study presented in [35]

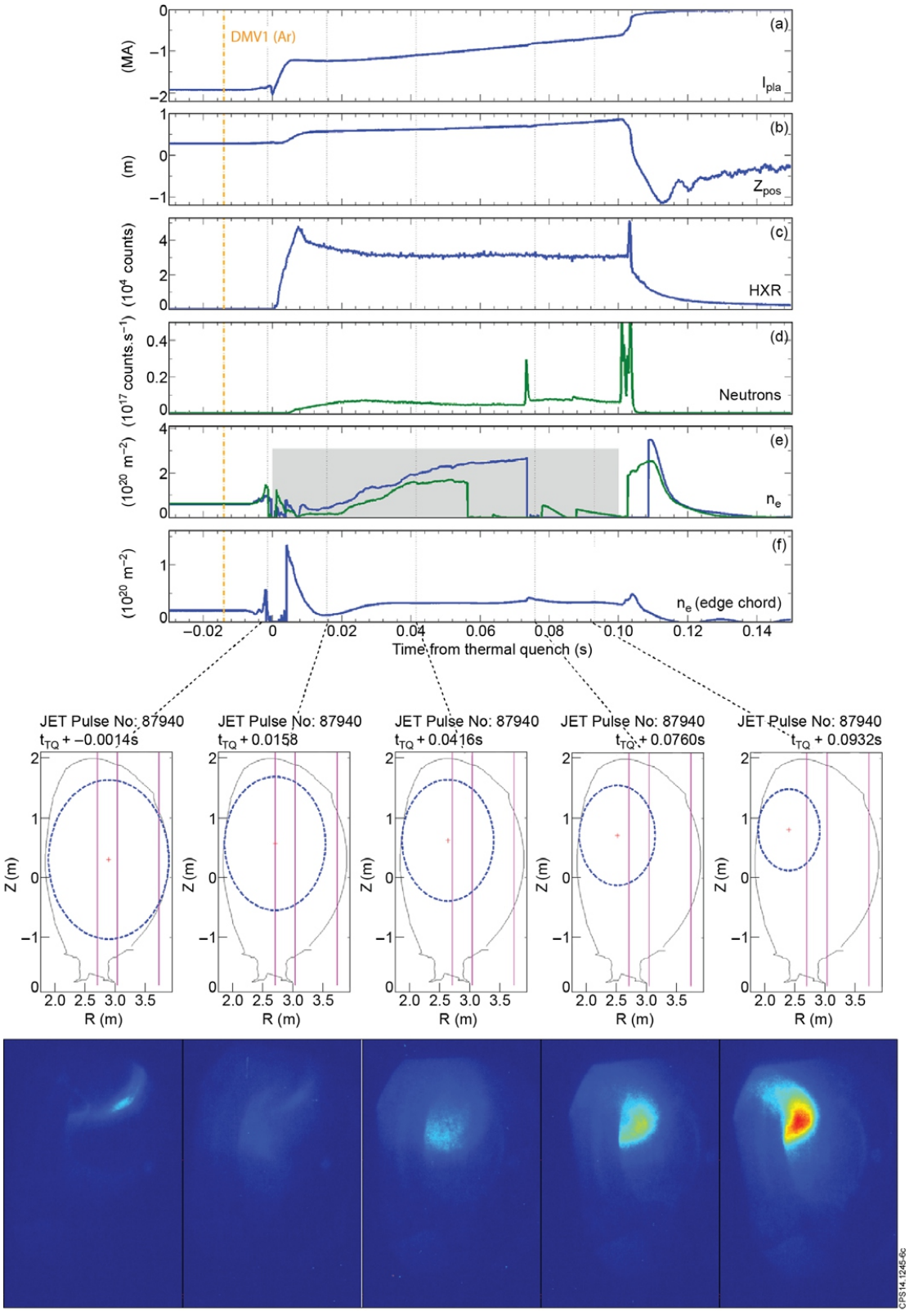

FIGURE 7.22: Runaway beam scenario example for JPN87940. Credit: Reux et al in NF 55(9) (2015), 93013. http://doi.org/10.1088/0029-5515/55/9/093013

Part III

Conclusions

Chapter 8

Conclusions

8.1 Summary of conclusions

Two clear lines of work have been developed in the course of this research. The first one, developed fully at TJ-II, has tested the limits of the Mercier Criterion, one of the notions that is commonly applied when the toroidal confinement and, hence, the electromagnets, of a magnetic confinement device are designed. TJ-II's unique capability to modify the magnetic well depth while keeping unaltered rotational transform profiles and low shear has been the key of this experimental test. From this analysis we have learnt the following lessons.

- Hot and reproducible plasmas can be achieved, not only for configurations with magnetic hill (those with positive but decreasing outwards) for $\rho > 0.8$, but for confinement conditions where the magnetic well depth is negative along the whole plasma radius. Theoretical calculations of the Mercier coefficients for one of these negative depth configurations supported the notion that such plasmas would be Mercier unstable. Their unexpected existence, stability and reproducibility is one of the most important achievements of this research.

- Decreasing the well depth has no negative effect on the stored energy or the confinement time, apart from the obvious loss of volume when the low well configurations were explored. Not only that, but for configurations with the 8/5 rational close to the plasma edge and magnetic hill confinement is actually improved.

- The International Stellarator Scaling Law predicts a dependence between confinement time and plasma volume, which is satisfied by our plasmas.

- Ion and electron temperature only shows a clear decrease when the well depth reaches negative values and, even in that case, it is difficult to separate this effect from the volume reduction that the magnetic well scan implies. Thomson scattering measurements suggest that electron temperature cannot peak up around the plasma core for magnetic hill and negative well.

- Langmuir probes have proved not only the existence of a clear, stable and reproducible plasma edge, but also have found the shear layer position to remain where VMEC simulations predicted to be as long as the magnetic well depth $W > -0.5\%$. Also poloidal $\vec{E} \times \vec{B}$ velocity, measured as the slope of these floating potential profiles, only decreases when magnetic well depth becomes negative.

- The clearest effects of the deterioration of the stability are seen on electromagnetic turbulence. Electrostatic turbulence at the plasma edge, measured as the RMS of the Langmuir signals increases by a factor of three as soon as the magnetic well depth is reduced from the standard configuration, although this measurement of turbulence doesn't grow drastically from that point until $W < -0.5\%$. We can conclude that edge electrostatic turbulence depends strongly on the magnetic well, although its effect doesn't become catastrophic until very low and negative values of well depth are reached.

- The spectrum of the wave vector, measured using the Doppler reflectometer, does not depend on the magnetic well depth, showing that the turbulence has the same spatial scale at the radial positions in the interval $0.7 < \rho < 0.85$.

- The typical frequencies of the Alfvén modes that appear in the co and counter-NBI heating tend to decrease with the magnetic well, as do their radial positions. Calculations with STELLGAP and AE3D have shown a reasonable agreement between the measurements and the simulations, with the exception of the calculated frequency of the mode that appears when $W < -0.5\%$, which happens to be too high. The frequency of this mode has a relationship with the magnetic well depth, but doesn't show any dependence with changes in the plasma volume.

- A mode is found at intermediate frequencies in the cases of intermediate values of the well. This mode is not of Alfvénic nature and can be considered as a candidate to GAM, despite of the strong damping that the calculations predict for GAMs in TJ-II.

- These findings show that although the effect of magnetic well is very limited in the general confinement properties, it is important on the characteristics of electromagnetic turbulence. In particular, the changes in Alfvén spectrum can affect the fast ion transport.

The second line of work explored has had a much clearer instrumental character, as it has required intensive manning and development of analysis tools for a visual diagnostic, like the intensified fast visible camera installed on JET by CIEMAT. Regarding this field, our main achievements have been:

- Development of a complete set of tools that enables handling data from the diagnostic from external computers, independent from JET's computing cluster.

- A user-friendly interface that allows playing videos from the fast visible camera, synchronise them with other plasma signals and extract high quality videos and frames.

- The rotation and vibration, specifically the ones occurring during the current quench that follows disruptions, have been addressed. A simple algorithm for the detection of these displacements has been created promising results during several current quench phases.

- The lack of an absolute calibration for the diagnostic has been eluded by the creation of a systematic method to relate the intensified fast visible data with other two well established diagnostics at JET: line spetroscopy and high resolution filtered cameras. This method has been used to prove that, despite the diagnostic's low spatial resolution, local changes, like the strike point position, can be traced with high time resolution.

- Since the installation of the ITER-Like Wall, a study of ELM D_α emission dynamics has been carried out. The result is the detailed charaterization of the ELM

phenomenology in order to help to understand the process of outgassing of Deuterium particles from the Beryllium deposits located at the innermost region of JET's Tunsgten divertor.

- We have also shown the problems the diagnostic faces when filters are used. We will propose some actions in the light of these findings in the next Section.

- Massive gas injection for disruption mitigation can be clearly traced by the intensified fast visible camera, providing insight on the time required for the mitigation gas to affect the plasma and spread out across it.

8.2 Remaining questions and future work

A full explanation of the achievement of theoretically Mercier-unstable plasmas remains elusive. The results reported in this thesis strongly suggest that stability calculations, as those presently used in the optimisation criteria of 3-D devices, might miss some stabilisation mechanisms. The dynamical coupling between density gradients and particle transport are a candidate for, at least, a partial explanation. Our observations have shown that fluctuations are self-regulated in such a way that the most probable density gradient minimises the size of the radial turbulent transport events, suggesting an interpretation of the improved stability of stellarators at beta regimes based on the self-organization of transport gradients.

The results from the Volume Scan helped to discriminate the effect of volume reduction and magnetic well depth modification; but the different behaviour between the two rotational transform families has not been explained. It is still unclear whether the exclusive use of NBI heating to induce the plasma breakdown induced abnormally large plasma currents that modified the magnetic configurations or the different behaviour is a consequence of the much deeper location of the rational 3/2 (around $\rho \approx 0.4$) than the 8/5. A last set of plasma pulses should be attempted in TJ-II to re-explore the configurations from this family both with ECR and NBI heating. If the different behaviour of the 3/2 Family was finally attributed to the rotational transform, then a third family of configurations (taking 100_69_72 as a starting point for its confection) would need a the treatment that we have shown in this work. Only that way a clear relationship between the magnetic well term in the Mercier criterion, plasma stability

and electromagnetic turbulence could be established for different values of resonances in the plasma.

Ultimately, extra literature research for a way to connect these experiments with plasma triangulaity in tokamaks would provide a much wider understanding of the Mercier criterion and its consequences.

There is a great amount of work left to be done on the fast visible camera. Contributing to modelling ELMs on the divertor is the ultimate goal of most of the analysis presented in sections 7.1 and 7.2. Understanding the flux of particles on the divertor is the necessary next step in this research. Work is been currently done to add Langmuir probes measurements from the divertor, so a better understanding of the relationship between D_α emission, temperature and flux can be obtained.

As well, an absolute calibration of the system is necessary. Only that way the constantly changing light conditions at JET (that imply tuning the camera settings frequently) will be analysed independently of the recording settings. The photon equivalence of our system would allow to deduce local ionisation rates.

Finally, the continuity of the image intensifier needs to be reconsidered: at the moment this image intensifier is responsible for the uncontrolled rotations of the image in the sensor, and comparison with recordings prior to its installation confirms that its use implies a considerable loss of image quality as a consequence of a constant and unavoidable blurry effect. The only case where the intensified fast visible camera has provided improved results when the optical filters have been employed is the tracking of disruption mitigation gas. As a mix of Deuterium and a inert gas is injected, filtering the latter (usually Argon) guarantees that only the mitigation gas can be tracked spatially during the disruption. Unfortunately, few of these cases have been successfully recorded as a consequence of several communication errors with the filter wheel controller. But the high luminosity of the disruptive events suggests that even without the image intensifier, Ar-filtered images would provide enough signal for a fast analysis.

Part IV

Appendices

Appendix A

Developing a Matlab library for KL8A

A.1 Motivation

When it comes to analysing experiments from JET from an outer location, there are two basic ways to access the data.

- **Remote connection** through a SecurID token. It is possible to access JET's cluster (called JACs) via remote desktop. This allows the use of all the JET's specific tools for data visualisation and analysis, but with the common bias of remote desktop connections (i.e. slow response). Downloading this data to an external computer to avoid working on remote is not a trivial matter, as manual upload to an external server is the only way.
- **MDSplus** (http://www.mdsplus.org) is a software tool that allows hieratic storage and access to scientific data from tens of fusion laboratories. It is the most widely used system for data management in the magnetic fusion energy program. It can be invoked through a variety of programming languages, like Python, IDL, C++ or Matlab.

Before the beginning of this thesis there were two basic ways of accessing and interacting with KL8A produced videos, and both depended on JET's remote desktop:

- **Pinup and then Juvil.** Pinup was the general video managing took at JET til 2015, when it was substituted by Juvil (developed by Valentina Huber at JET). Both are useful tools to easily access data from all the visible and infrared cameras at JET, run basic analysis and statistics and compare data from different sources and points of view.

- **IDL Libraries.** These codes were developed by Arturo Alonso and updated by Alfonso Baciero and Gabor Cseh and allow checking KL8A's data availability, extract movies and frames, rapidly visualise large videos and create basic PPFs with KL8A's integrated signal. (See http://users.euro-fusion.org/openwiki/index.php/KL8A#KL8A_software_tools for more information).

Although the mentioned codes were reliable and useful, there were a few desirable features that they didn't cover:

- Extraction of full time resolution time traces.
- Production of two dimensional light maps to track the signal along a certain direction.
- Production of tailored PPFs to share KL8A's processed data with other experimentalists who require it at JET.
- Download raw data from KL8A to an external computer (video compressing is very likely to imply losses of information).
- Manipulation and reproduction of videos from KL8A with a consistent time vector to compare them with the time evolution with other signals from JET.

Although custom coding has already been done by Gabor Cseh and Gabor Kocsis, it has mainly been focused to analyse pellet injection via IDL using JET's terminals, on site or through remote connection. Systematic analysis of ELMs at the divertor like the one shown in Sec. 7.2 and production of tailored PPFs during experiments has required a considerable amount of code development that has finally turned into two versions of the same library: one is aimed to be used at the JAC machines from JET and, the other, to be used in computers independent from JET.

- **KL8A Matlab library at JET's JACs.** Although Matlab is not commonly used as an analysis tool by scientists at JET, there is an old license for the R14 2005 version (without extra toolboxes). It is not optimal and crushes sometimes, but it is useful and enough for Matlab users that want to run some basic data analysis from the KL8A data without using IDL. The reason for using Matlab for this purpose is simply: chronologically, the Matlab library for external computers was the first to be developed so a great part of its code was recycled to be used at the JACs. This is the reason why many of the functions and capabilities will be similar in both libraries.

  No toolboxes are needed to run the library (that's why it is so simple), but you will need to have Adrian Capel's modified `getdat` library in your path. All the functions add the needed folders to the path automatically when they are executed, but in case you want to add them manually or export them to use the library somewhere else, the files that you need are in `/home/ajc/matlab/jpf/native` and `/home/ajc/matlab/jpf/native/linux2.i686`.

  All the functions can be used by adding `/home/amda/public/KL8A_library/` to the path.

- **JET and KL8A Matlab library for external computers.** This version of the library is a little bit wider and visual than the one installed at the JACs, although it uses some toolboxes. It is designed to work under PC and UNIX systems, although an operational installation of MDSplus is mandatory in all the cases. The functions are designed to try to add the necessary MDSplus folders to Matlab's path, but if they are not located at a "predictable" location, the user will have to add these folders to the path manually. The latest version of the library can be requested via email to adrianamdeaguilera@gmail.com or downloaded trough `https://drive.google.com/drive/folders/0B9AIoGs2odhNaVJzS2dGWENEMHc?usp=sharing`.

All the programming has been done in Matlab for being this language the most frequently used at CIEMAT. None of this work would have been possible without the assistance of Adrian Capel.

A.2 General functions

A.2.1 Reading and saving raw data

We will provide a short description of the functions involved in the libraries. For detailed information about the input and output in each function, check the help files in the corresponding scripts.

- **Read recording settings** `[GenPar, err] = KL8A_read_par(shot)`
  When provided a valid JPN, checks KL8A data availability and, if possible, will produce a structure with information about the camera's exposure time, frame speed, size and position; the II's gaining and time width and the filter wheel position.

- **Download raw data** `[KL8A_raw, GenPar, TimeVector, camData, telapsed, err] = KL8A_save_raw(shot, save_folder, video)`
  As the JACs can access directly JET's database, there is no point on using this function there. It was designed for external computers and is capable of producing two sets of files: one with the raw data (hundreds of MB), time vector and camera settings (saved in a `/data/` subfolder in the designed destination); and an optional avi video (saved, to ease the search, in a `/video/` subfolder). The development of this key function wouldn't have been possible if Adrian Capel hadn't improved the `getdat` routine, so that saturated pixels could be downloaded with a 256 value instead of the default 0, that made impossible any light tracking analysis of videos with saturated phases (which is pretty common in KL8A).

- **Access downloaded videos** `[frame, err] = KL8A_read_raw(shot, frame_number, source_folder)`
  The raw file produced by `KL8A_save_raw` is too large for it to be loaded in any computer's RAM memory. This script is only available for the external computers version of the library and given a JPN, a frame number and the address where the raw file is stored, provides a matrix with the correctly formatted raw image. This function is normally meant to be used sequentially.

- **Save a clip** `[kl8_video, telapsed] = KL8A_save_clip(shot, window_type, window, output_type, save_folder, corrector, correction_video,`

`source_folder, roi_folder, roi_set, roi_family)`

It is designed to extract short clips, not complete videos, as RAM can be problematic when this function is used in the JACs. When used in an external computer it will use `KL8A_read_raw` to read the previously downloaded raw and save time. Both Juvil and the IDL libraries provide this ability, but this function includes a few extra capabilities:

. The selected window can be defined with the initial and final frames to be extracted or the time limits.

. The output can be a video or a list of images (all Matlab supported formats are available).

. Rotation and vibration can be corrected on demand (see Sec. A.4), although this consumes more time and resources. A video describing the correction process can also be produced.

. ROIs (defined according Subsec. A.2.2) can be superimposed on the resulting video or images, mostly for eduactional and reference purposes.

– **Produce a mean image** `[mean_image, data_mean, err] = KL8A_mean_image(shot, window_type, window, source_folder, colorsc, colorlim, corrector)`

This is a simple routine to plot and save an averaged image from a sequence of frames. Colour map and limits can be chosen for better visualisation. If requested, vibration and rotation correction can be applied. The resulting image will be offered as a figure for saving and as a matrix for data analysis.

– **Integrated light time trace** `[TimeVector, fulltrace, err] = KL8A_fulltrace(shot, source_folder)`

The simplest analysis that one can provide when dealing with a video is the total sum of light in the sensor frame by frame. This script produces a column with the time vector and another one with the corresponding integrated light trace (see Fig. A.1 c)).

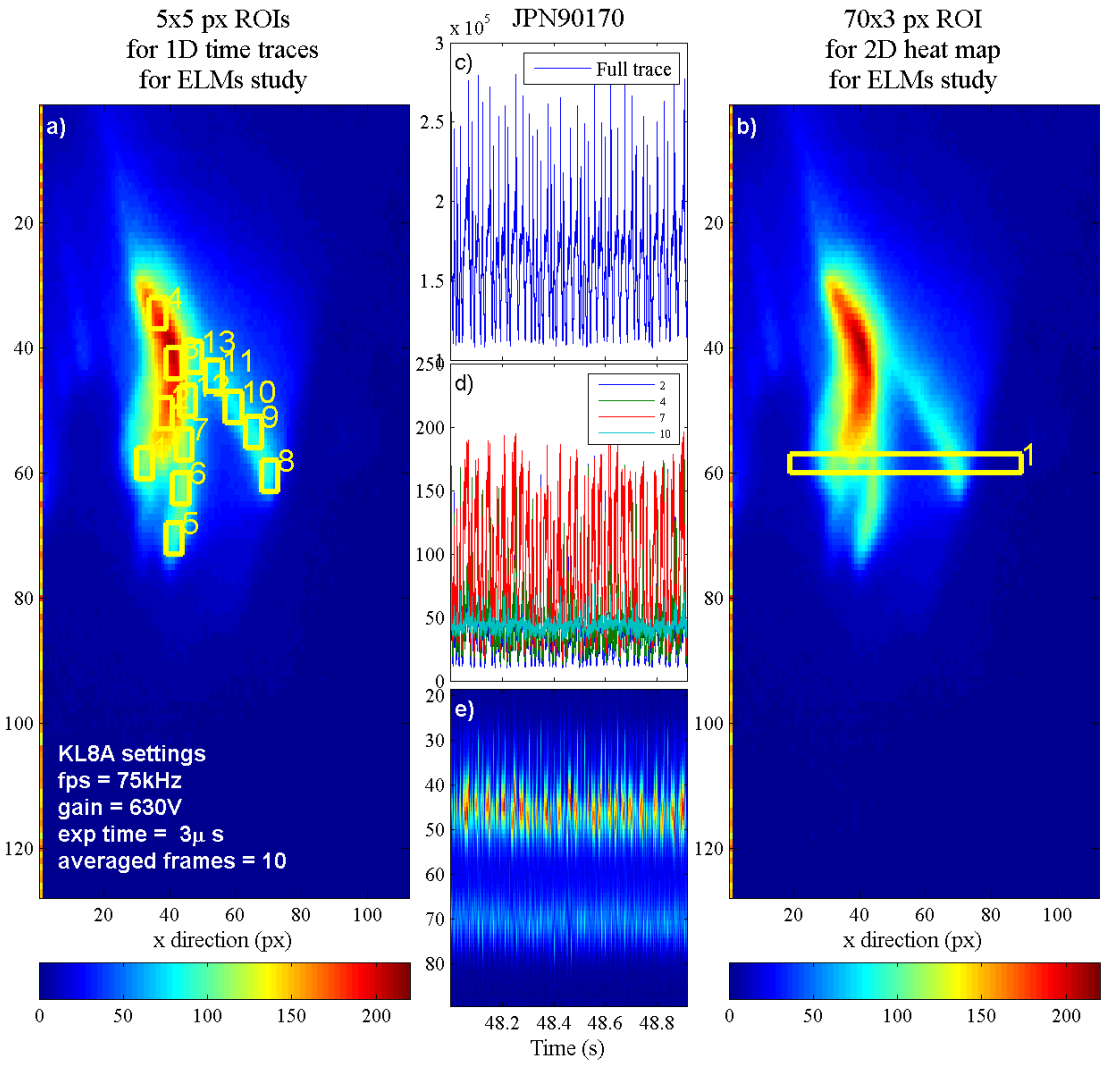

Figure A.1: An example of ROI analysis in KL8A on JPN90170. a) Averaged image (created with `KL8A_mean_image`)) with 13 squared ROIs designed specifically to track light on the divertor strike points. b) Same average with a long horizontal ROI designed to map the complete divertor section vs. time. c) KL8A integrated signal. d) Averaged time trace for four of the ROIs represented in a). e) Heat map for the x-direction involving the divertor strike points vs. time.

A.2.2 Defining and analysing ROIs

Once we have all the tools to access KL8A's raw data in a systematic way, we can start defining regions of interest and extract the time evolution of light in these areas.

– **Draw ROIs with one's mouse** `rects = draw_rects(shot, image, type, x_width, y_width, save_rois, save_fig)`

This routine allows, given an initial image (like one generated using `KL8A_mean_image`),

dynamically define rectangular ROIs on it. These ROIs can have a fixed size (optional input, see Fig. A.1 a)) or can be drawn freehand (see Fig. A.2 a)). In any case, the resulting coordinates will be stored in a desired location with an indentifier name (taking into account that there can be different sets of ROIs defined for the same JPN) so they can be used by the rest of the functions. It is important to mention that the version of this routine installed in the JACs is much simpler than the one for external computers, as the latter makes use of the Image Processing Toolbox (`https://es.mathworks.com/help/images/index.html`).

– **Load and use previously created sets of ROIs** `rects = load_rects( inputrois, saveshot, image, type, load_folder, save_fig)`
When using large shot databases it is normal to deal with lots of different sets of ROIs. This function eases loading each of them when neccesary.

– **1D Time traces** `[TimeVector, ttrace, fulltrace, corrections, err] = KL8A_ttrace(shot, roi, values, source_folder, window_type, window, corrector)`
Once we have defined a set of ROIs, an immediate analysis of the time evolution of light in those areas is one of the first results to provide from a diagnostic like KL8A. This function provides a time vector and a matrix containing the time traces for each ROI. The averaged light in each area, the integrated signal, maximum and minimum values can be selected (see Fig. A.1 d)). Also, on default, the total integrated light in the sensor is provided. An specific time window can be selected for a faster and more specific analysis, and rotation and vibration can be corrected frame by frame.

– **2D Time traces** `[TimeVector, tsurface, fulltrace, corrections, err] = KL8A_tsurface(shot, roi, source_folder, window_type, window, corrector)`
Another common analysis when dealing with video data is the time evolution of light along a certain direction for a 2D colour heat map. A rectangular ($dim_1 \gg dim_2$) set of ROIs has to be provided, so the routine will integrate the signal along the shorter dimension and provide a 2D matrix for each ROI (see Fig. A.1 b) and e)).

– **Normalise KL8A data** `normalized_vector = KL8A_normalize(raw_vector, exp_time, gain)` A rudimentary calibration of KL8A's signal was attempted in

2014, although the exposure times used were two or three orders of magnitude larger than the ones normally used in operation. This function provides a linear normalisation for any time trace provided. II's gain and exposure time are the only inputs needed. This function can be useful to compare shots with different light settings, although it is worth remembering that it will almost always be applied as an extrapolation.

A.3 Writing PPFs

In JET PPFs are the standard for sharing scientific information about a JET pulse. Anyone can request permissions to write PPFs, that can be accessed by any other JET user via JETdsp (the standard time trace visualisation software installed at the JACs) by knowing the creator's `Uid` and the diagnostic's labelling. Tab. A.1 presents a quick guide to the PPFs that can be found under the `Uid:amda`.

Uid	amda
diagnostic id	KL8A
Name	**ROI**
FULL	full trace
Variable size free-hand drawn ROIs for disruptions	
LIM1-3	outer limiters
DIVR	complete divertor
UPCH	top region
TS01-...	2D matrices with light integrated along one direction. In this case, normally vertical labelled from the outer to the inner wall.
Fixed size rectangles, normally used for ELMs at the divertor	
TT01-...	small squares along the strike points
TS01-...	2D matrices with light integrated along one direction. In this case, normally horizontal across the divertor.
Variable size ROIs for IRCH heating and Be migration	
INL1-2	inner limiters
OUL1-4	outer limiters and ICRH antenna

Table A.1: Key to KL8A's PPFs created by amda.

JAC's users can find two functions to write PPFs. In all the cases, the functions are designed to identify the user's ID in order to write the PPFs under his or her `Uid`:

– **1D Time traces** `err = KL8A_write_ppf(shot, TimeVector, TimeTraces, data_types)`
Only allows writing 1D time traces. All the traces must be provided in one single

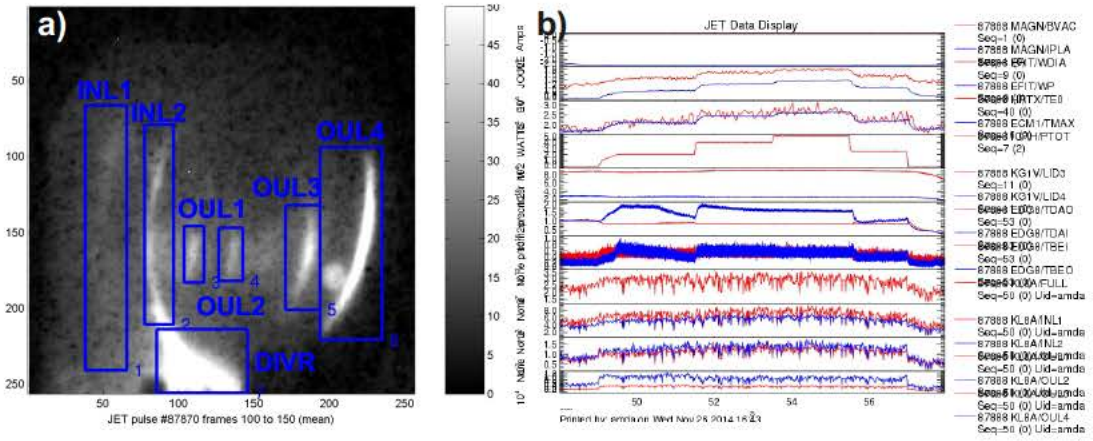

FIGURE A.2: An example of a set of PPFs created with the Matlab library. a) Averaged image of 50 frames during ICRH experiments JPN87870 with the ROIs used for analysis. b) The time traces produced displayed along with another JET signals on JETdsp.

matrix with their proper labelling and a common time vector. Each time that this function runs it will overwrite any previous PPFs saved for the current JPN under the KL8A diagnostic.

– **1D and 2D data simultaneously** `err = KL8A_write_multiple_ppf(shot, TimeVector, TimeTraces, TimeTraces_data_types, TSurfaces, TSurfaces_data_types)`

If 2D direction integrated signals are required, the syntax becomes more complicated, as all the signals need to be written in the same order, but their dimensions and characteristics are different. This function requires the introduction of the time traces as a single matrix and the time surfaces as a stack of 2D matrices. The labelling for each kind of data needs to be introduced separately.

Although these functions are designed to be used once the ROI selection and data extraction from KL8A's video has been executed and previously saved, JAC's users can find a set of useful routines in `/home/amda/public/util/` that automate this whole process. This can be useful to rapidly create PPFs during an experiment, by request, for a first analysis and tuning of the camera's settings. An example of the PPFs shared with these functions can be seen on Fig. A.2.

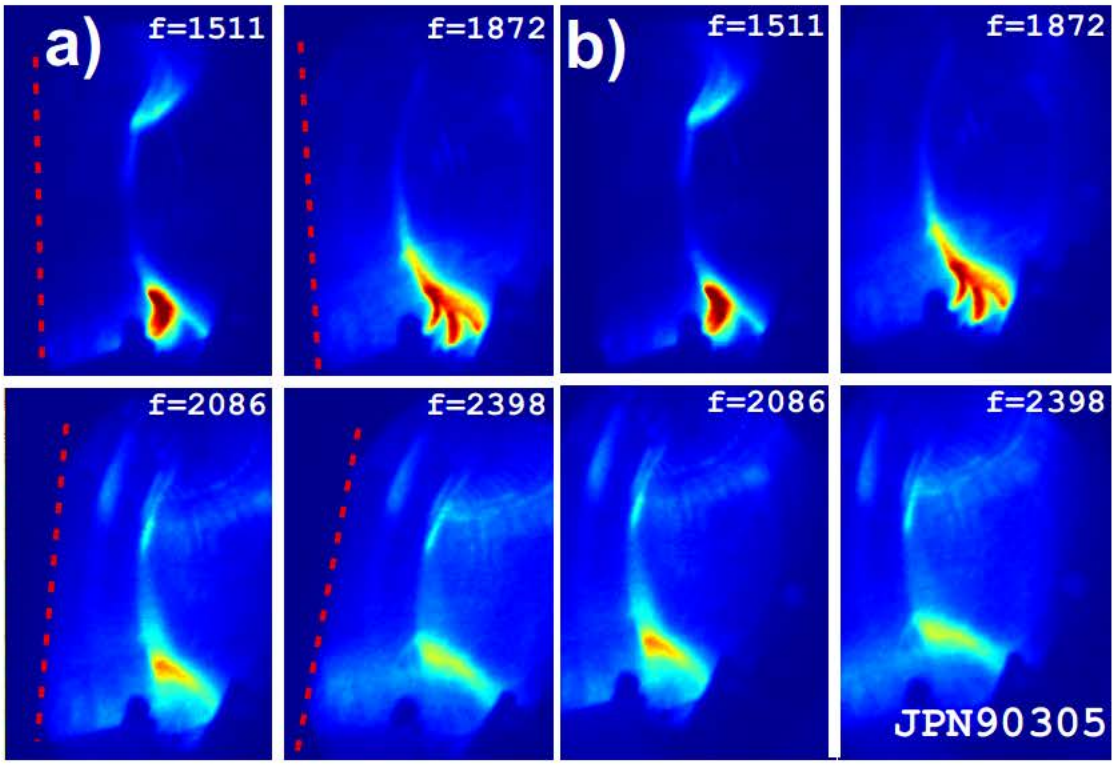

FIGURE A.3: For the MGI mitigated disruption in JPN90305. a) Four frames selected during the current quench that show both rotation and horizontal displacement. The red dotted line has been added to help the eye to follow the rotation. b) The same four frames after the correction script is applied on them.

A.4 Correcting rotation and vibration

As we explained in Subsec. 4.1.3, KL8A's II is protected by a μ-metal cage to minimise the incidence of JET's magnetic field on the accelerated electrons trajectory. The solution works most of the time, although during disruptions it is not enough because:

1. The sudden change in the plasma current produces a magnetic field that cannot be shielded by the cage. In consequence, the image registered in the sensor rotates in an uncontrolled and unpredictable way.

2. Although MGI mitigation, disruptions imply a severe mechanical stress on the elements of the tokamak. The plasma's vertical displacement during the current quench causes the complete device to shake in an uncontrolled way. Although KL8A is mounted on an optical table, damping in these moments is not enough, resulting in an uncontrolled horizontal and vertical (less intense in this direction) movement of the image.

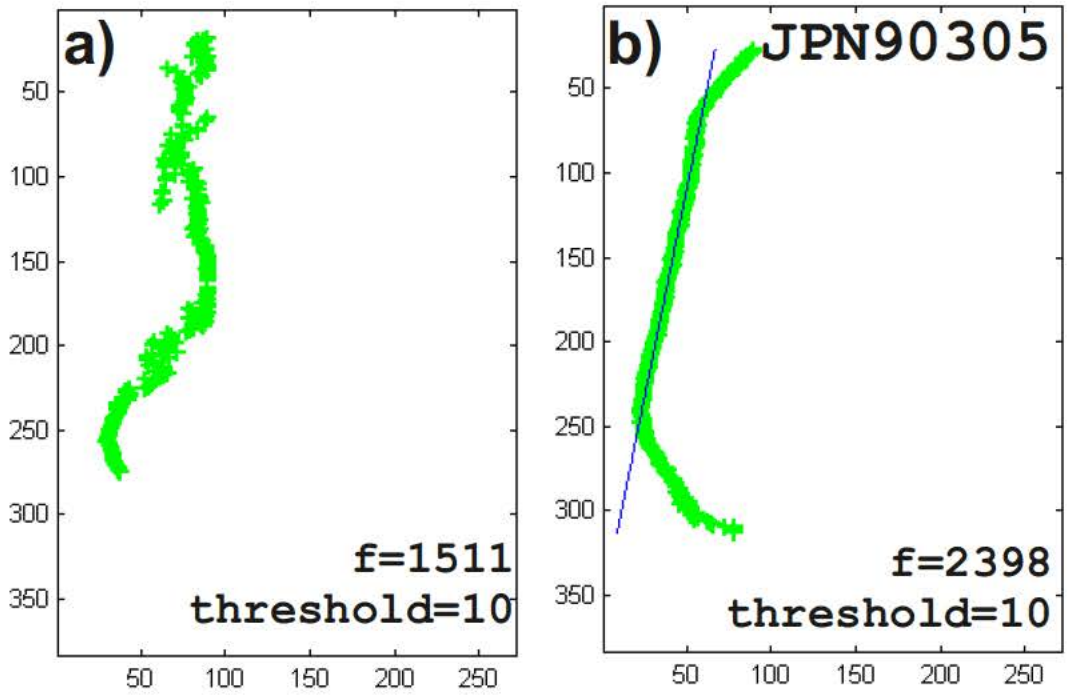

FIGURE A.4: Vertical left edge analysis for two of the frames presented in Fig. A.3 a). The green crosses represent the contour obtained by the threshold analysis and the blue line, the lineal fit to these points. Same threshold used in both cases.

Fig. A.3 a) is a common example of this phenomena. It shows clearly how any ROI analysis on these videos will be biased by the unpredictable movements of the image in the sensor. Several software solutions have been attempted on this problem, and in this section the one developed as part of this library will be presented. The work strategy is the following:

1. **Detect rotation angle** `[corrected_frame, theta, r2, edges_figure] = KL8A_de_rotator(original_frame, threshold, r2_tolerance, previous_theta, video)`

   Following Fig. A.3 a) as an example, it is clear that the recorded image is smaller than the portion of sensor used in this recording. This is useful because it allows us to distinguish the edge (shown as red dotted lines in the mentioned example). As long as there is enough light in the inner wall section to distinguish image from background, a simple threshold detection on each horizontal line of pixels should be able to allow us to draw this contour. Once the contour is drawn one can encounter two situations that will be both covered by the function `[fit, rsq_adj] = fit_edges(edges, r2_tolerance, fit_tolerance)`:

(a) Ideal. The contrast is good enough along the whole contour and time, so the threshold sweep along the y-direction will provide a clear line suitable for a lineal fit to $y = ax + b$ with a high correlation coefficient. This is the case exposed in Fig. A.4 b), which clearly produces a contour to fit. This way only one fit within two reasonable limits for the y coordinate, will be enough to characterise the rotation of the frame. In the JACs library, algebraic rotation of the image matrix is applied in order to avoid the use of toolboxes.

(b) Low contrast. Very commonly, mostly at the beginning of the disruption, only the lower part of the inner wall is properly illuminated. This is the case of the first frame presented in Fig. A.3 a): in these cases a simple threshold analysis won't provide a suitable contour (see Fig. A.4 a)). The way to deal with this situation is to sequentially attempt $y = ax + b$ fittings in different sections of the contour, accepting the one with higher $r2$ coefficient as suitable to be corrected. This sequential fitting consumes much more time (≈ 4 times) than the single fit, but the results are much more reliable.

2. **Rotation correction.** Again, two possible courses of action.

   (a) If a good lineal fit has been accomplished, then the rotation angle is $\alpha_f = \arctan(a)$. This α_f will be considered valid as long as it doesn't imply a sudden change with respect the angle obtained from the previous frame α_{f-1}. The function `imrotate` from Matlab's Image Analysis Toolbox provides a corrected version of the original frame.

   (b) The contour doesn't fit to a line, so α_{f-1} will be implemented as the rotation angle. If there is no previous angle, no correction will be applied.

3. **Detect vertical and horizontal vibration** `[corrected_frame, coords, r2, edges_figure] = KL8A_de_vibrator(original_frame, threshold_x, threshold_y, previous_coords, video)`

   Only when the image has been straightened it becomes clear that coupled with the rotation, the video wonders (like floating) along the sensor. The idea is very similar to the one used to correct rotation: thresholds are employed to detect the left and upper contours and, if possible, fit them to lines with `fit_edges`. A complication arises once one realises that the upper region of the image is normally much darker

than the left contour, so normally different thresholds need to be defined for each coordinate.

4. **Vibration correction.** If successful fits are obtained, the correction will be given by the obtained intercepts, with the abscissa in the x-coordinate correction and with the ordinate for the y-coordinate. The corrected frame consists in a new matrix where the original frame's dimensions have been displaced according with the obtained intercepts.

Global correction of a raw frame can be implemented with the routine `[corrected_frame, corrections, r2] = KL8A_correct_frame(original_frame, rotation, vibration)` which applies sequentially the two available corrections to an original frame when the thresholds for each of them are provided. This function is incorporated in most of the routines previously shown, but its use is optional. When creating a video clip from KL8A data with `KL8A_save_clip` the possibility of creating extra video files with the corresponding sequences of contour extraction and fit analysis is available. An example of the results of the analysis with `KL8A_correct_frame` during a mitigated disruption can be seen in Fig. A.5.

The conditions for data correction are:

1. Contrast between the image and the sensor's background has to be enough to draw reliable contours.
2. Thresholds have to be defined individually for each video.
3. The routine only works with images large enough to show edges. This is why it is not possible to apply it to divertor-focused videos, although they normally experience certain vibration.
4. Running on a 6-core processor with 8GB of RAM, it takes around 30 minutes to correct a disruption clip ($\approx$ 1800 large field of view frames).

Corrections are normally necessary and reliable during current quench: before it, the contrast is so low that the edge detection is faulty, producing erratic corrections. The original video that we have been using as example in this section can be downloaded from https://drive.google.com/open?id=0B9AIoGs2odhNb0ZRQVhTSzltSzQ, and the corrected version, from https://drive.google.com/open?id=0B9AIoGs2odhNZFZwOUZER2RjRW8.

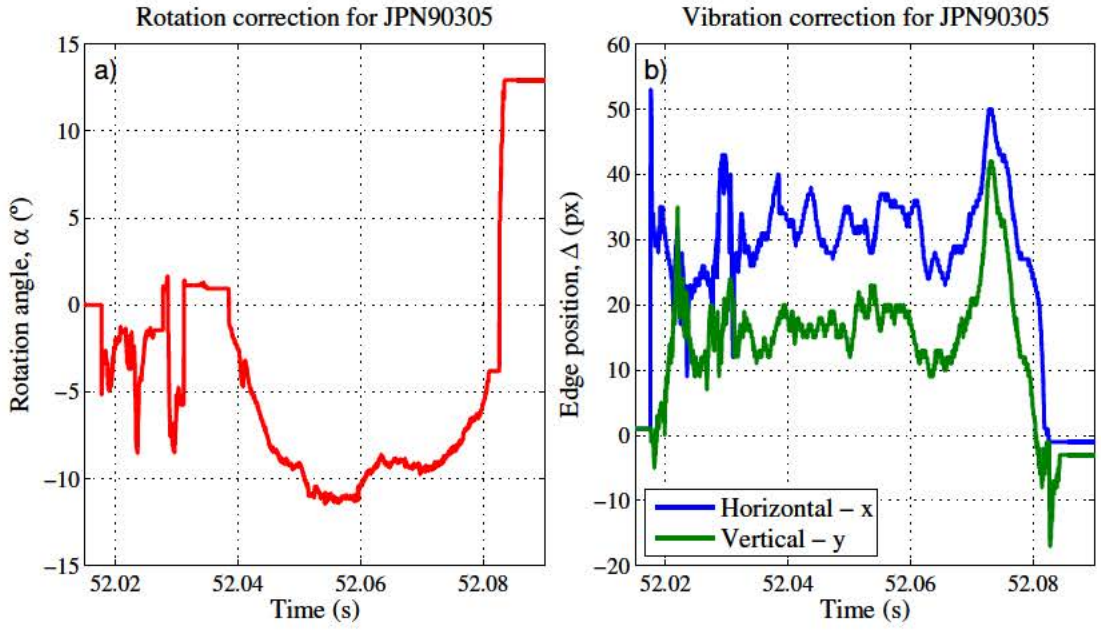

FIGURE A.5: For the mitigated disruption recorded at JPN90305 a) Rotation angle detected using `KL8A_de_rotator`. A video containing this correction process can be downloaded from https://drive.google.com/open?id=0B9AIoGs2odhNTXZOQUl1ZUNyUjA. b) Edge position once the rotation has been corrected extracted for the horizontal and vertical direcitons using `KL8A_de_vibrator`. A video containing this correction process can be downloaded from https://drive.google.com/open?id=0B9AIoGs2odhNekx0NDRrUGNvUEk.

A.5 Playing KL8A data

Most of the functions mentioned in the previous section lack any visual interface, and must be invoqued using Matlab's command line. Being KL8A's output data a set of bidimensional images, designing a tool to view, manipulate and compare these frames with other signals with a consistent time vector was a reasonable necessity. `KL8A_explorer` is a visual interface developed completely on Matlab (runs on R2013a) that covers the following functions (numbered as in Fig. A.6):

1. Select a JPN and:
   (a) Open the raw file previously downloaded from JET's database.
   (b) Download the raw file if not available on user's hard disk.
2. Check recording settings and manipulate the image:
   (a) Luminosity
   (b) Contrast

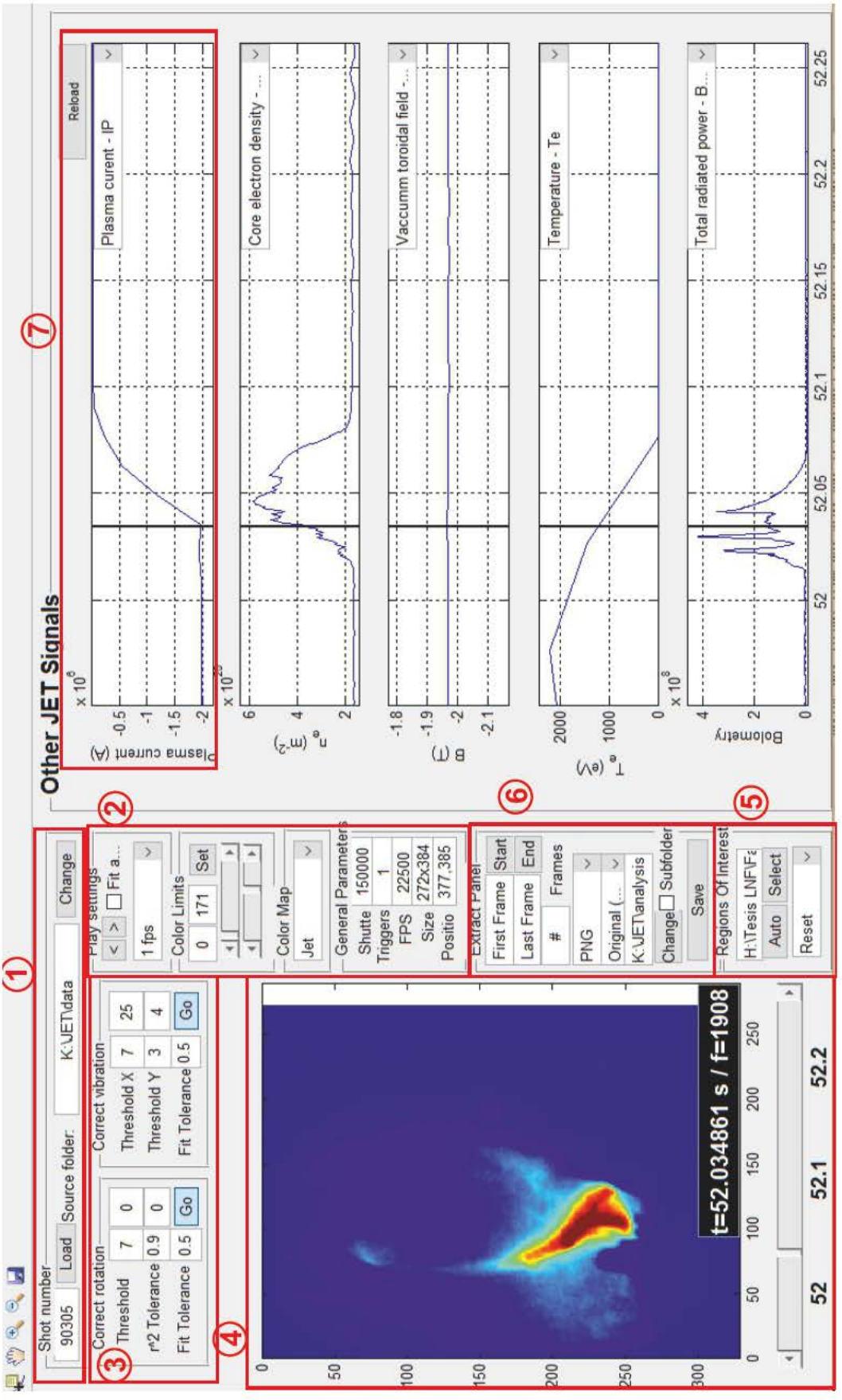

FIGURE A.6: KL8A Explorer running on Matlab R2013a under Windows 10.

(c) Colormap

(d) Zoom

3. Correct rotation and/or vibration with tuneable settings.

4. Display and navigate KL8A's videos and time vectors.

5. Select an initial and final frame to be extracted. Video or single images can be selected and the manipulations implemented previously (light, colour, corrections) can or cannot be included in the output.

6. Load and superimpose a previously created set of ROIs.

7. Download and display up to 5 common JET signals. They will all be plotted within the recording time limits and a dynamic pointer will mark the video's time position on them.

More than an analysis tool, `KL8A_explorer` is designed to help visualisation of the data provided by KL8A and provide a better context for an informed analysis.

A.6 Other useful functions

When analysing KL8A data from external computers, correlation with other diagnostics becomes an extra need. JETdsp at the JAC's allows accessing and saving any signal from any JPN, but its outputs can truncate time resolution, which can be critical for fast diagnostics such as Langmuir probes. Some extra functions are included in the library to help any users to access JET experimental data from Matlab via MDSplus.

- **Access time trace with its time vector** `[Time, Data, err] = JET_signal(shot, JET_address, uid)`
  This is a very simple routine to extract column vectors with a diagnostic's time trace at a given JPN. It works with public PPFs, JPFs and privately created PPFs. The signal's label must be known: otherwise, the function won't return any data. The JET Data Handbook http://users.euro-fusion.org/pages/data-dmsd/jetdatahandbook/php/index.php is the common tool to look for the correct naming for any diagnostic at JET.

- **Download and save a list of signals** `err = JET_signals_saver(shot_list, signal_list, name_list, save_folder, format)`

  As simultaneous work with different signals and pulse numbers is a common practise, and taking into account that accessing constantly to JET data via MDSplus consumes time and resources, a dynamic function was created in order to access and download large sequences of data. The signals can be saved as Matlab files or text columns ready to be exported to any other analysis software. Eight-digit time resolution is guaranteed in the output.

- **DMV Injection parameters** `[DMVPar, err] = DMV_read_par(shot)`

  Lots of work has been carried in Sec. 7.3 related with disruption mitigation. The injection conditions from the three DMVs active at JET is stored as private PPFs for each JPN. This routine provides a fast and simple way to produce structures (one per each active DMV during the required plasma pulse) with basic information about the gas injection process.

Appendix B

Publications and contributions to international conferences

Publications

- Edge turbulence and magnetic well depth in TJ-II
  - de Aguilera, A. M., Castejón, F., Ascasíbar, E., Blanco, E., De la Cal, E., Hidalgo, C., Velasco, J. L., and the TJ-II Team. (2015). Magnetic well scan and confinement in the TJ-II stellarator. Nuclear Fusion, 55(11), 113014.
  - Castejón, F., de Aguilera, A. M., Ascasíbar, E., Estrada, T., Hidalgo, C., López-Fraguas, A., and the TJ-II Team. (2016). Influence of magnetic well on electromagnetic turbulence in the TJ-II stellarator. Plasma Physics and Controlled Fusion, 58(9), 94001.
  - van Milligen, B. P., Carreras, B. A., García, L., Martín de Aguilera, A., Hidalgo, C., Nicolau, J. H., and the TJ-II Team. (2016). The causal relation between turbulent particle flux and density gradient. Physics of Plasmas, 23(7), 72307.
  - van Milligen, B. P., Snchez, E., Alonso, A., Pedrosa, M. a, Hidalgo, C., de Aguilera, A. M., Hidalgo, C. (2015). The use of the biorthogonal decomposition for the identification of zonal flows at TJ-II. Plasma Physics and Controlled Fusion, 57(2), 25005.

  - van Milligen, B. P., Fraguas, A. L., Pedrosa, M. A., Hidalgo, C., Martín de Aguilera, A., Ascasbar, E. (2013). Parallel and perpendicular turbulence correlation length in the TJ-II Stellarator. Nuclear Fusion, 53(9), 93025.

- Fast visible imaging in TJ-II

  - de la Cal, E., Martín, A., Carralero, D., de Pablos, J. L., Pedrosa, M. A., Shoji, M., Hidalgo, C., and the TJ-II Team. (2013). Dust observation with a visible fast camera in the TJ-II stellarator. Plasma Physics and Controlled Fusion, 55(6), 65001.
  - de la Cal, E., Semwal, P., Martín Aguilera, A., van Milligen, B., de Pablos, J. L., Khan, Z., Hidalgo, C. (2014). Double imaging with an intensified visible fast camera to visualize the fine structure of turbulent coherent plasma structures (blobs) in TJ-II. Plasma Physics and Controlled Fusion, 56(10), 105003.

- Fast visible imaging in JET

  - Reux, C., Plyusnin, V., Alper, B., Alves, D., Bazylev, B., Belonohy, E., ⋯ Martin de Aguilera, A., and JET contributors. (2015). Runaway electron beam generation and mitigation during disruptions at JET-ILW. Nuclear Fusion, 55(9), 93013.
  - Wiesen, S., Brezinsek, S., Wischmeier, M., de la Luna, E., Groth, M., Jaervinen, A., ⋯ de Aguilera, M. A., Sergienko, G. (2017). Impact of the JET ITER-like wall on H-mode plasma fueling. Nuclear Fusion, IAEA-FEC 2016 (accepted).

Posters

- de la Cal, E., Martín de Aguilera, A., De Pablos, J. L., Manzanares, A., Baciero, A., Arnaux, G., Balshaw, N., ⋯ and JET Contributors. The Visible Intensified Fast Camera with wide-angle view of JET ILW experiment. 39th EPS Conference on Plasma Physics 16th International Congress on Plasma Physics. July 2012, Stockholm (Sweden).

- de Aguilera, A. M., Castejón, F., López Fraguas, A., Pedrosa, M. A., Ochando, M. A., Pastor, I., Estrada, T., de la Cal, E., Hidalgo, C., and the TJ-II Team.

Properties of plasma fluctuations at the stability threshold: Magnetic well scan in the TJ-II stellarator. 41st EPS Conference on Plasma Physics. June 2014, Berlin (Germany).

Contributions to talks

- Castejón, F., de Aguilera, A. M., Ascasíbar, E., de la Cal, E., Hidalgo, C., Lpez-Fraguas, A., Ochando, M. A., Pastor, I., and the TJ-II Team. Influence of magnetic well on electromagnetic turbulence in the TJ-II. 42nd EPS Conference on Plasma Physics. June 2015, Lisbon (Portugal). Oral. stellarator

- Castejón, F., de Aguilera, A. M., Ascasíbar, E., Estrada, T., Hidalgo, C., López-Fraguas, A., and the TJ-II Team. Influence of magnetic well on electromagnetic turbulence in the TJ-II stellarator. 20th International Stellarator-Heliotron Workshop (ISHW). October 5-9, 2015, Greifswald (Germany). Invited talk.

- Castejón, F., the TJ-II Team and collaborators. 3D Effects on Transport and Plasma Control in the TJ-II Stellarator. 26th IAEA Fusion Energy Conference. October 17-22, 2016. Kyoto (Japan). Oral.

Bibliography

[1] *Adoption of the Paris Agreement*. 2015.

[2] Michael J. Ring et al. "Causes of the Global Warming Observed since the 19th Century". en. In: *Atmospheric and Climate Sciences* 02.04 (Oct. 2012), pp. 401–415.

[3] IEA. *Energy Technology Perspectives (Executive Summary)*. Tech. rep. 2015, p. 14.

[4] Omar Ellabban, Haitham Abu-Rub, and Frede Blaabjerg. "Renewable energy resources: Current status, future prospects and their enabling technology". In: *Renewable and Sustainable Energy Reviews* 39 (2014), pp. 748–764.

[5] IAEA. *Climate Change and Nuclear Power 2015*. Tech. rep. Viena: IAEA, 2015, p. 112.

[6] IEA. *Key World Energy Statistics 2015*. Tech. rep. IEA, 2015, p. 81.

[7] Charikleia Karakosta et al. "Renewable energy and nuclear power towards sustainable development: Characteristics and prospects". In: *Renewable and Sustainable Energy Reviews* 22 (June 2013), pp. 187–197.

[8] Vivianne H M Visschers and Michael Siegrist. "How a nuclear power plant accident influences acceptance of nuclear power: results of a longitudinal study before and after the Fukushima disaster." In: *Risk analysis : an official publication of the Society for Risk Analysis* 33.2 (Feb. 2013), pp. 333–47.

[9] Robert Vance. *Uranium 2014: Resources, Production and Demand*. English. Tech. rep. 2014, p. 26.

[10] Nebojsa Nakicenovic. "Part III: Ares sustainable futures possible?" In: *World Energy Assessment: Energy and the Challenge of Sustainability*. Ed. by UNDP. 2010. Chap. 9, p. 35.

[11] H A Bethe. "Energy Production in Stars". In: *Phys. Rev.* 55.5 (Mar. 1939), pp. 434–456.

[12] H. A. Bethe and C. L. Critchfield. "The formation of deuterons by proton combination". In: *Physical Review* 54.4 (Aug. 1938), pp. 248–254.

[13] J D Lawson. "Some Criteria for a Power Producing Thermonuclear Reactor". In: *Proceedings of the Physical Society. Section B* 70.1 (1957), pp. 6–10.

[14] RJ Goldston and PH Rutherford. *Introduction to plasma physics*. 1995.

[15] Jeffrey P Freidberg. *Ideal Magnetohydrodynamics*. 1987, p. 489.

[16] K. Lackner et al. "Tokamak confinement in relation to plateau scaling". In: *Nuclear Fusion* 30.4 (Apr. 1990), pp. 767–770.

[17] T. M. Antonsen et al. "Physical mechanism of enhanced stability from negative shear in tokamaks: Implications for edge transport and the L-H transition". In: *Physics of Plasmas* 3.6 (1996), pp. 2221–2223.

[18] J P Freidberg. *Plasma physics and fusion energy*. Vol. 1. 2007, p. 671. arXiv: arXiv:1011.1669v3.

[19] H Yamada et al. "Characterization of energy confinement in net-current free plasmas using the extended International Stellarator Database". In: *Nuclear Fusion* 45.12 (2005), p. 1684.

[20] R. D. Hazeltine and J. D. Meiss. *Plasma Confinement*. 2003.

[21] A.E. Costley, J. Hugill, and P.F. Buxton. "On the power and size of tokamak fusion pilot plants and reactors". In: *Nuclear Fusion* 55.3 (Mar. 2015), p. 033001.

[22] William P. Thurston and Silvio. Levy. *Three-dimensional geometry and topology*. Princeton University Press, 1997.

[23] K Miyamoto. *Plasma physics and controlled nuclear fusion*. First. Berlin: Springer, 2006.

[24] Jan Mlynár; Milan Ripa. *50 years of tokamaks — EUROfusion*. 2008.

[25] NJ Peacock, DC Robinson, and MJ Forrest. "Measurement of the electron temperature by Thomson scattering in tokamak T3". In: *Nature* (1969).

[26] J Wesson and DJ Campbell. *Tokamaks*. Third. Oxford: Oxford University Press, 2011.

[27] F. Wagner et al. "Regime of Improved Confinement and High Beta in Neutral-Beam-Heated Divertor Discharges of the ASDEX Tokamak". In: *Physical Review Letters* 49.19 (Nov. 1982), pp. 1408–1412.

[28] A. W. Leonard. "Edge-localized-modes in tokamaks". In: *Physics of Plasmas* 21.9 (2014).

[29] D.N. Hill. "A review of ELMs in divertor tokamaks". In: *Journal of Nuclear Materials* 241-243 (Feb. 1997), pp. 182–198.

[30] G.A. Rattá, J. Vega, and A. Murari. "Improved feature selection based on genetic algorithms for real time disruption prediction on JET". In: *Fusion Engineering and Design* 87.9 (2012), pp. 1670–1678.

[31] R. Moreno et al. "Disruption Prediction on JET During the ILW Experimental Campaigns". In: *Fusion Science and Technology* 69.2 (Apr. 2016).

[32] D. G. Whyte et al. "Mitigation of tokamak disruptions using high-pressure gas injection." In: *Physical review letters* 89.5 (July 2002), p. 055001.

[33] "Disruption mitigation by massive gas injection in JET". In: *Nuclear Fusion* 51.12 (2011), p. 123010.

[34] M.N Rosenbluth et al. "Theory for avalanche of runaway electrons in tokamaks". In: *Nuclear Fusion* 37.10 (Oct. 1997), pp. 1355–1362.

[35] C. Reux et al. "Runaway electron beam generation and mitigation during disruptions at JET-ILW". In: *Nuclear Fusion* 55.9 (Sept. 2015), p. 093013.

[36] B.E. Keen and P. Kupschus. *JET Joint Undertaking: Progress Report 1983*. Tech. rep. Abingdon: EURATOM, 1984, p. 148.

[37] P-H Rebut et al. "The JET preliminary tritium experiment". In: *Plasma Physics and Controlled Fusion* 34.13 (Dec. 1992), pp. 1749–1758.

[38] M Keilhacker et al. "High fusion performance from deuterium-tritium plasmas in JET". In: *Nuclear Fusion* 39.2 (Feb. 1999), pp. 209–234.

[39] J. Paméla et al. "An ITER-like wall for JET". In: *Journal of Nuclear Materials* 363 (2007), pp. 1–11.

[40] F. Romanelli et al. "Overview of the JET results with the ITER-like wall". In: *Nuclear Fusion* 53.10 (Oct. 2013), p. 104002.

[41] G.J. van Rooij et al. "Tungsten divertor erosion in all metal devices: Lessons from the ITER like wall of JET". In: *Journal of Nuclear Materials* 438 (2013), S42–S47.

[42] M. Lehnen et al. "Impact and mitigation of disruptions with the ITER-like wall in JET". In: *Nucl. Fusion* 53.9 (Sept. 2013), pp. 93007–13.

[43] Jr. Lyman Spitzer. "The Stellarator Concept". In: *Physics of Fluids* 1.1958 (1958), pp. 253–264.

[44] Per Helander. "Theory of plasma confinement in non-axisymmetric magnetic fields." In: *Reports on progress in physics. Physical Society (Great Britain)* 77.8 (2014), p. 087001.

[45] V D Shafranov. "Magnetohydrodynamic theory of plasma equilibrium and stability in stellarators: Survey of results". In: *Physics of Fluids (1958-1988)* 26.2 (1983), pp. 357–364.

[46] M. D. Kruskal and R. M. Kulsrud. "Equilibrium of a Magnetically Confined Plasma in a Toroid". In: *Physics of Fluids* 265.1958 (1958), p. 265.

[47] Claude Mercier. "A necessary condition for hydromagnetic stability of plasma with axial symmetry". In: *Nuclear Fusion* 1.1 (1960), pp. 47–53.

[48] Claude Mercier. "Equilibrium and stability of a toroidal magnetohydrodynamic system in the neighbourhood of a magnetic axis". In: *Nuclear Fusion* 4.3 (1964), p. 213.

[49] B.A. Carreras et al. "Low-aspect-ratio torsatron configurations". In: *Nuclear Fusion* 28.7 (July 1988), pp. 1195–1207.

[50] C Alejaldre et al. "First plasmas in the TJ-II flexible Heliac". In: *Plasma Physics and Controlled Fusion* 41.3A (Mar. 1999), A539–A548.

[51] Carlos Alejaldre et al. "TJ-II Project: A Flexible Heliac Stellarator". In: *Fusion Science and Technology* 17.1 (Jan. 1990), pp. 131–139.

[52] A. Varias et al. "Ideal Mercier stability for the TJ-II flexible Heliac". In: *Nuclear Fusion* 30.12 (1990), pp. 2597–2609.

[53] F Castejon et al. "Microwave injection in heliac device TJ-II". In: *Plasma Physics and Controlled Fusion* 30.7 (July 1988), pp. 907–911.

[54] José Guasp Pérez and Macarena Liniers. "Theoretical Evaluations of Neutral Beam Injection Efficiency for the TJ-II Helical-Axis Stellarator". In: *Fusion Science and Technology* 24.3 (1993), pp. 251–258.

[55] F. Castejon and the TJ-II Team. "3D effect on transport and plasma control in the TJ-II stellarator". In: *Nuclear Fusion* ().

[56] N.D. Vinogradova and Ksenia Razumova. "Higher-Mode instabilities in a tokamak device". In: *Plasma Physics and Controlled Nuclear Fusion Research*. Culham: IAEA, 1965.

[57] J L Terry et al. "Visible imaging of turbulence in the SOL of the Alcator C-Mod tokamak". In: *Journal of Nuclear Materials* 290-293 (2001), pp. 757–762.

[58] S J Zweben et al. "High-speed imaging of edge turbulence in NSTX". In: *Nucl. Fusion* 44.04 (2004), pp. 134–153.

[59] G. Kocsis et al. "A fast framing camera system for observation of acceleration and ablation of cryogenic hydrogen pellet in ASDEX Upgrade plasmas". In: *Review of Scientific Instruments* 75.11 (2004), pp. 4754–4762.

[60] J. A. Alonso et al. "Fast visible camera installation and operation in JET". In: *AIP Conference Proceedings* 988 (2008), pp. 185–188.

[61] E. de la Cal et al. "The Visible Intensified Cameras for Plasma Imaging in the TJ-II Stellarator". In: *Contributions to Plasma Physics* 51.8 (Sept. 2011), pp. 742–753.

[62] D Carralero et al. "Observation of Filamentary Structures on the Boundary Region of the LHD Stellarator". In: *Contributions to Plasma Physics* 51.1 (2011), pp. 92–98.

[63] M Groth et al. "Diagnosis of edge localized mode evolution in DIII-D using fast-gated CID and infrared cameras". In: *Review of Scientific Instruments* 74.August (2003), pp. 2064–2067.

[64] J.A. Alonso et al. "Fast visible imaging of ELM-wall interactions on JET". In: *Journal of Nuclear Materials* 390-391 (June 2009), pp. 797–800.

[65] J H Yu et al. "Fast camera imaging of dust in the DIII-D tokamak". In: *Journal of Nuclear Materials* 390-391.1 (2009), pp. 216–219.

[66] E de la Cal et al. "Dust observation with a visible fast camera in the TJ-II stellarator". en. In: *Plasma Physics and Controlled Fusion* 55.6 (June 2013), p. 065001.

[67] J. H. Yu et al. "Visible imaging and spectroscopy of disruption runaway electrons in DIII-D". In: *Physics of Plasmas* 20.4 (2013), p. 042113.

[68] E De La Cal et al. "The Visible Intensified Fast Camera with wide-angle view of JET ILW experiment". In: *39th EPS Conference on Plasma Physics 16th International Congress on Plasma Physics*. Vol. 31124. 8. 2012.

[69] R. Albanese et al. "Experimental results with an optimized magnetic field configuration for JET breakdown". In: *Nuclear Fusion* 52.12 (Dec. 2012), p. 123010.

[70] P.T. Lang et al. "ELM pacing and trigger investigations at JET with the new ITER-like wall". In: *Nuclear Fusion* 53.7 (July 2013), p. 073010.

[71] I. H. Hutchinson. *Principles of Plasma Diagnostics*. 2005, p. 460.

[72] M. A. Pedrosa et al. "Fast movable remotely controlled Langmuir probe system". In: *Review of Scientific Instruments* 70.1 (1999), pp. 415–418.

[73] S P Hirshman and J C Whitson. "Steepest-descent moment method for three-dimensional magnetohydrodynamic equilibria". In: *Physics of Fluids* 26.1 (1983), pp. 3553–3568.

[74] A. M. de Aguilera et al. "Magnetic well scan and confinement in the TJ-II stellarator". en. In: *Nuclear Fusion* 55.11 (Sept. 2015), p. 113014.

[75] V D Pustovitov. "Diamagnetic measurements and plasma energy in toroidal systems". In: *Plasma Physics and Controlled Fusion* 52.8 (2010), p. 85005.

[76] C Hidalgo et al. "On the radial scale of fluctuations in the TJ-II stellarator". In: *Plasma Physics and Controlled Fusion* 43.12A (Dec. 2001), A313–A321.

[77] C Hidalgo, M A Pedrosa, and B Gonçalves. "Fluctuations, sheared radial electric fields and transport interplay in fusion plasmas". In: *New Journal of Physics* 4.1 (July 2002), p. 351.

[78] J. Castellano et al. "Magnetic well and instability thresholds in the TJ-ii stellarator". In: *Physics of Plasmas* 9.2 (2002), p. 713.

[79] D. López-Bruna et al. "First dynamic magnetic configuration scans in ECRH plasmas of the TJ-II Heliac". In: *Nuclear Fusion* 49.8 (Aug. 2009), p. 085016.

[80] F Castejón et al. "Influence of magnetic well on electromagnetic turbulence in the TJ-II stellarator". In: *Plasma Physics and Controlled Fusion* 58.9 (Sept. 2016), p. 094001.

[81] Masahiro Wakatani. *Stellarator and Heliotron devices*. 95. Oxford University Press, 1998.

[82] A Teubel, J Guasp, and M Liniers. "Monte Carlo simulations of NBI into the TJ-II helical axis stellarator". In: *Report IPP* 4.268 (1994), p. 264.

[83] E Ascasíbar et al. "Magnetic configuration and plasma parameter dependence of the energy confinement time in ECR heated plasmas from the TJ-II stellarator". In: *Nuclear Fusion* 45.4 (Apr. 2005), pp. 276–284.

[84] J.M. Fontdecaba, F. Castejon, and R. Balbin. "Ion heat transport analysis in TJ-II plasmas". In: *14th international stellarator workshop and IAEA technical meeting on innovative concepts and theory of stellarators*. 2003.

[85] Jose M Carmona et al. "A Systematic Study of Impurity Ion Poloidal Rotation and Temperature Profiles Using CXRS in the TJ-II Stellarator". In: *Plasma and Fusion Research* 3.S1044 (2008), pp. 1–5.

[86] F. Medina Yela. "Caracterización de los plasmas de TJ-II y sus poblaciones supratérmicas con diagnósticos de rayos x". PhD thesis. 2007.

[87] C. J. Barth et al. "High-resolution multiposition Thomson scattering for the TJ-II stellarator". In: *Review of Scientific Instruments* 70.1 (1999), p. 763.

[88] C Hidalgo et al. "Plasma fluctuations near the shear layer in the ATF torsatron". In: *Nuclear Fusion* 31.8 (1991), p. 1471.

[89] C. Hidalgo et al. "Dynamical coupling between gradients and transport in fusion plasmas". In: *Physical Review Letters* 108.6 (2012), p. 65001.

[90] B. Ph. van Milligen et al. "The causal relation between turbulent particle flux and density gradient". In: *Physics of Plasmas* 23.7 (July 2016), p. 072307.

[91] A.V. Melnikov et al. "Internal measurements of Alfvén eigenmodes with heavy ion beam probing in toroidal plasmas". In: *Nuclear Fusion* 50.8 (Aug. 2010), p. 084023.

[92] A.V. Melnikov et al. "Plasma potential and turbulence dynamics in toroidal devices (survey of T-10 and TJ-II experiments)". In: *Nuclear Fusion* 51.8 (Aug. 2011), p. 083043.

[93] A.V. Melnikov et al. "Study of NBI-driven chirping mode properties and radial location by the heavy ion beam probe in the TJ-II stellarator". In: *Nuclear Fusion* 56.11 (Nov. 2016), p. 112019.

[94] T. Happel et al. "Doppler reflectometer system in the stellarator TJ-II". In: *Review of Scientific Instruments* 80.7 (2009), p. 073502.

[95] A.V. Melnikov et al. "Effect of magnetic configuration on frequency of NBI-driven Alfvén modes in TJ-II". In: *Nuclear Fusion* 54.12 (Dec. 2014), p. 123002.

[96] D López-Bruna et al. "Effects of Ohmic current in the TJ-II stellarator". In: *Nuclear Fusion* 44.5 (May 2004), pp. 645–654.

[97] Francisco Castejón Magaña et al. "Influence of low-order rational magnetic surfaces on heat transport in TJ-II heliac ECRH plasmas". In: *Nuclear Fusion* 44.5 (May 2004), pp. 593–599.

[98] C. R. Cook and C. C. Hegna. "Analytical theory of the shear Alfv??n continuum in the presence of a magnetic island". In: *Physics of Plasmas* 22.4 (Apr. 2015), p. 042517.

[99] B.J. Sun, M.A. Ochando, and D. López-Bruna. "Alfvén eigenmodes including magnetic island effects in the TJ-II stellarator". In: *Nuclear Fusion* 55.9 (Sept. 2015), p. 093023.

[100] J L Velasco et al. "Damping of radial electric field fluctuations in the TJ-II stellarator". In: *Plasma Physics and Controlled Fusion* 55.12 (Dec. 2013), p. 124044.

[101] T. Estrada et al. "Limit cycle oscillations at the LIH transition in TJ-II plasmas: triggering, temporal ordering and radial propagation". In: *Nuclear Fusion* 55.6 (June 2015), p. 063005.

[102] D. A. Spong, R. Sanchez, and A. Weller. "Shear Alfvén continua in stellarators". In: *Physics of Plasmas* 10.8 (2003), pp. 3217–3224.

[103] A. Huber et al. "Development of a mirror-based endoscope for divertor spectroscopy on JET with the new ITER-like wall (invited)". In: *Review of Scientific Instruments*. Vol. 83. 10. AIP Publishing, 2012, p. 10D511.

[104] G. F. Matthews. "Plasma operation with an all metal first-wall: Comparison of an ITER-like wall with a carbon wall in JET". In: *Journal of Nuclear Materials* 438.SUPPL (2013), S2–S10.

[105] L. Frassinetti et al. "Effect of nitrogen seeding on the energy losses and on the time scales of the electron temperature and density collapse of type-I ELMs in JET with the ITER-like wall". In: *Nuclear Fusion* 55.2 (Feb. 2015), p. 023007.

[106] C. Giroud et al. "Impact of nitrogen seeding on confinement and power load control of a high-triangularity JET ELMy H-mode plasma with a metal wall". In: *Nuclear Fusion* 53.11 (Nov. 2013), p. 113025.

[107] C.F. Maggi et al. "LH power threshold studies in JET with Be/W and C wall". In: *Nuclear Fusion* 54.2 (Feb. 2014), p. 023007.

[108] A. Huber et al. "Impact of the ITER-like wall on divertor detachment and on the density limit in the JET tokamak". In: *Journal of Nuclear Materials* 438.SUPPL (2013), S139–S147.

[109] S. Wiesen et al. "Impact of the JET ITER-like wall on H-mode plasma fueling". In: *Nuclear Fusion* IAEA-FEC 2016 (submitted), EX/P6–6.

[110] M. Wischmeier et al. "High recycling outer divertor regimes after type-I ELMs at high density in ASDEX Upgrade". In: *Journal of Nuclear Materials* 363-365.1-3 (2007), pp. 448–452.